

GROWTH AND CHARACTERIZATION OF GRAPHENE AND
GRAPHENE/COPPER OXIDE NANOCOMPOSITES BY
HOT-FILAMENT THERMAL CHEMICAL VAPOR DEPOSITION
FOR FLEXIBLE PRESSURE SENSOR APPLICATION

SYED MUHAMMAD HAFIZ BIN SYED MOHD JAAFAR

THESIS SUBMITTED IN FULFILMENT OF THE
REQUIREMENTS FOR THE DEGREE OF
DOCTOR OF PHILOSOPHY

FACULTY OF SCIENCE
UNIVERSITY OF MALAYA
KUALA LUMPUR

2017

UNIVERSITI MALAYA
ORIGINAL LITERARY WORK DECLARATION

Name of Candidate : **SYED MUHAMMAD HAFIZ BIN SYED MOHD JAAFAR**

Registration/Matric No : **SHC130099**

Name of Degree : **DOCTOR OF PHILOSOPHY**

Title of Project Paper/Research Report/Dissertation/Thesis ("this Work"):

**"Growth and Characterization of Graphene and Graphene/Copper Oxide
Nanocomposites by Hot-Filament Thermal Chemical Vapor Deposition for Flexible
Pressure Sensor Application"**

Field of Study : **MATERIAL SCIENCE**

I do solemnly and sincerely declare that:

- (1) I am the sole author/writer of this Work,
- (2) This Work is original,
- (3) Any use of any work in which copyright exists was done by way of fair dealing and for permitted purposes and any excerpt or extract from, or reference to or reproduction of any copyright work has been disclosed expressly and sufficiently and the title of the Work and its authorship have been acknowledged in this Work,
- (4) I do not have any actual knowledge nor do I ought reasonably to know that the making of this work constitutes an infringement of any copyright work,
- (5) I hereby assign all and every rights in the copyright to this Work to the University of Malaya ("UM"), who henceforth shall be owner of the copyright in this Work and that any reproduction or use in any form or by any means whatsoever is prohibited without the written consent of UM having been first had and obtained,
- (6) I am fully aware that if in the course of making this Work I have infringed any copyright whether intentionally or otherwise, I may be subject to legal action or any other action as may be determined by UM.

(Candidate Signature)

Date:

Subscribed and solemnly declared before,

Witness's Signature

Date:

Name **PROF. DATIN DR. SAADAH ABDUL RAHMAN**

Designation **PROFESSOR**

Witness's Signature

Date:

Name **DR. HUANG NAY MING**

Designation **SENIOR LECTURER**

ABSTRACT

Graphene is an emerging two-dimensional carbon nanostructure which is composed of sp^2 hybridized carbon atoms arranged in a hexagonal lattice. After the remarkable observations of the unique properties of graphene surfaced in the past decade, tremendous interest in the scientific community on this material has led to various investigations on the preparation techniques as well as its potential application. This thesis reports the top-down and bottom-up approach of fabrication of graphene and its application in gas and pressure sensor devices. Three types of graphene-based materials are produced in this work which includes reduced graphene oxide (GO), high-quality graphene and graphene/ Cu_2O nanocomposites. The top-down approach of graphene fabrication used in this work started with GO where graphite flakes are oxidized using the simplified hummers method. This process initiates exfoliation of graphite layers by weakening the van der Waals forces in between its layers by introducing oxygen functional groups. GO is an insulating material, thus the top-down approach of growing graphene here involves the removal of these functional groups to restore its conductivity which is indeed a challenging task. Hydrogen plasma treatment is employed to reduce the GO into reduced graphene oxide (rGO) as an alternative to using hydrazine solution which is known to be toxic. The effectiveness of hydrogen plasma treatment to remove oxygen functional groups is systematically evaluated in terms of its morphology, topological, structural and elemental composition before and after the reduction process. The optimized rGO is used as the sensing material in a carbon dioxide (CO_2) gas sensor and the sensing capabilities are assessed. The tests are performed in dry and humid environment in the range of 0 to 1500 ppm (parts per million) of CO_2 which match closely to the indoor air quality monitoring environment. The catalytic chemical vapour deposition (Cat-CVD) technique is a simple, low cost, bottom-up approach of growing graphene but have been reported to

have the disadvantage of producing high defect density graphene, In this work, the Cat-CVD system is modified and a novel growth technique of growing graphene and graphene/Cu₂O nanocomposite is introduced. This novel technique is referred to as the hot-filament thermal CVD (HFTCVD). In this technique, a close ended alumina tube wound with tungsten filament is connected to the low voltage connections via the ends of the tungsten coil replacing the hot-filament of the Cat-CVD system. The production of graphene samples by varying the growth duration and hydrogen flow rate is systematically studied with respect to its morphology, topological, structural and elemental composition. The effects of catalytic dissociation of methane and hydrogen gas at tungsten filament temperature above 1500 °C in quasi-static equilibrium copper vapour inside the alumina tube on the properties of graphene are studied and analysed. High quality graphene with I_D/I_G ratio of ~0.1 was successfully produced on Cu foils. The growth mechanism of graphene growth by this technique is proposed. The substrate temperature played an important role in growing graphene/Cu₂O nanocomposites, shown in this work to be a promising material for highly sensitive flexible pressure sensor. The effects of substrate temperature are studied with respect to structure, morphology and electrical properties of the graphene/Cu₂O nanocomposites. The graphene/Cu₂O nanocomposites sample is tested for use as a sensing material in flexible pressure sensor for its sensing capability. The piezoresistive effects are systematically evaluated for applied pressure within a wide range of 0 to 50 kPa. The sensor sensitivity, sensing and recovery time, limit of detection and gauge factor criteria are measured. The sensing mechanism is proposed to provide a better understanding on the use of graphene-based material in highly sensitive piezoresistive-based flexible pressure sensors device.

ABSTRAK

Grafena adalah struktur nano karbon dua dimensi yang terdiri daripada atom karbon hibridisasi- sp^2 tersusun dalam kekisi heksagon. Penemuan penting terhadap sifat-sifat unik bagi grafena sejak sedekad lalu telah meningkatkan minat komuniti saintifik terhadap bahan ini, justru menjurus kepada pengkajian tentang pelbagai teknik penyediaan dan juga kebolegunaan dalam aplikasi. Tesis ini melaporkan mengenai pendekatan ‘top-down’ dan ‘bottom-up’ untuk fabrikasi bahan grafena serta aplikasi bahan ini dalam peranti pengesan gas dan tekanan. Tiga jenis bahan berasaskan grafena dihasilkan dalam kerja ini termasuk grafena teroksida (GO), grafena berkualiti tinggi dan nanokomposit grafena/ Cu_2O . Pendekatan secara ‘top-down’ yang digunakan dalam kerja ini dimulakan dengan penyediaan GO secara pengoksidaan grafit melalui kaedah ‘Simplified Hummers’. Proses ini memungkinkan pengelupasan grafit dalam melemahkan daya van der Waals di antara lapisan-lapisannya dengan memasukkan kumpulan berfungsi oksigen. Pendekatan fabrikasi grafena secara ‘top-down’ melibatkan penurunan semula kumpulan berfungsi oksigen bagi memulihkan sifat konduktor yang dikira sangat mencabar. Rawatan hidrogen plasma telah digunakan bagi menukarkan GO kepada penurunan grafena teroksida (rGO) sebagai alternatif kepada penggunaan larutan hidrazin yang diketahui sebagai bahan toksik kimia. Keberkesanan rawatan hidrogen plasma bagi penurunan kumpulan berfungsi oksigen telah dinilai secara sistematik dari segi morfologi, topologi, struktur dan komposisi unsur sebelum dan selepas proses penurunan. Sampel rGO yang dioptimumkan akan digunakan sebagai bahan pengesan bagi gas karbon dioksida (CO_2) dan keupayaan peranti pengesan akan dinilai. Kajian dilaksanakan dalam persekitaran kering dan lembap dengan konsentrasi CO_2 di antara 0-1500 ppm (bahagian per sejuta), iaitu menyamai persekitaran untuk pemantauan kualiti udara dalam ruangan. Pemangkin pemendapan wap kimia (Cat-CVD) merupakan pendekatan fabrikasi grafena secara

'bottom-up' telah dilaporkan mempunyai kelemahan dengan menghasilkan grafena berketumpatan kecacatan tinggi. Dalam kerja ini, sistem Cat-CVD telah diubahsuai dan teknik pertumbuhan baharu grafena dan grafena/Cu₂O nanokomposit akan diperkenalkan. Teknik baharu ini disebut sebagai pemendapan wap kimia secara haba filamen-panas (HFTCVD). Dalam teknik ini, tiub alumina satu bukaan akan dikelilingi dengan filament tungsten dan hujungnya akan disambung pada punca voltan rendah bagi menggantikan gegelung tungsten seperti dalam sistem Cat-CVD. Penghasilan sampel grafena dengan mengubah kadar tempoh pertumbuhan dan aliran hydrogen telah dinilai secara sistematik dari segi morfologi, topologi, struktur dan komposisi unsur. Kesan daripada pemangkin penguraian oleh gas metana dan hidrogen pada filament tungsten yang mempunyai suhu melebihi 1500 °C pada keadaanimbangan kuasi-statik wap kuprum di dalam tiub alumina akan dikaji dan dianalisa. Grafena berkualiti tinggi dengan nisbah $I_D/I_G \sim 0.1$ telah berjaya dihasilkan di atas kerajang kuprum. Mekanisma pertumbuhan grafena dengan teknik ini telah dicadangkan. Suhu substrat memainkan peranan yang penting dalam menghasilkan nanokomposit grafena/Cu₂O, seperti yang ditunjukkan dalam kerja ini dilihat dapat menjanjikan peranti pengesan tekanan fleksibel yang sangat sensitif. Kesan suhu substrat diselidiki secara sistematik dari segi struktur, morfologi dan sifat elektrik terhadap penghasilan nanokomposit grafena/Cu₂O. Sampel nanokomposit grafena/Cu₂O kemudiannya diuji kebolehpayaannya sebagai bahan pengesan tekanan yang fleksibel. Kesan rintangan piezo dinilai secara sistematik untuk tekanan yang dikenakan dalam julat 0-50 kPa. Kepekaan peranti pengesan, masa tindak balas dan pemulihan, had kriteria pengesanan dan faktor tolok adalah diukur. Mekanisma pengesanan adalah dicadangkan untuk memberi pemahaman yang lebih baik mengenai penggunaan bahan berasaskan grafena dalam menghasilkan peranti pengesan tekanan fleksibel yang sangat sensitif menggunakan kesan rintangan piezo.

ACKNOWLEDGEMENTS

Alhamdulillah (Praise be to Allah), for giving me the energy, strength and health to complete this thesis with the best of my capability. I would like to express my deepest gratitude to the people who have contributed in many ways along the way during my journey as a PhD candidate. My deepest gratitude goes to my supervisors, Prof. Datin Dr. Saadah Abdul Rahman and Dr. Huang Nay Ming. Thank you for the advice, suggestions, encouragements and expert guidance given to me during the difficult times I faced throughout this research. Completion of this thesis would not have been possible without the help of so many people in the Low Dimensional Materials Research Center (LDMRC) in so many ways. My sincere thanks goes to Dr. Richard Ritikos, Dr. Goh Boon Tong, Dr. Thomas Whitcher, Mr. Mohd Arif Sarjidan, Mr. Wong Wah Seng, Ms. Maisara Othman, Ms. Hamizah, Ms. Nur Maisarah, Ms. Fatin Saiha, Ms. Nurul Hazierah and countless others in the center who were always so supportive and helpful to me during my struggle in the course of doing this research. I really appreciate their valuable time in assisting me to complete this PhD work. Thank you to Dr. Prayoon, Dr. Hideki, Dr. Wutthikrai, Dr. Thanit and others at Synchrotron Light Research Institute (SLRI), Thailand for their support on XPS and LEEM measurements as well as the advice rendered to me on the analysis done in this work. I am also very grateful to our collaborators from MIMOS Berhad, especially to Dr. Daniel, Dr. Aniq and Ms. Nadia Mad Razib for the invaluable discussions and advice on this work. Finally, my most sincere gratitude is extended to my late father, Syed Mohd Jaafar and mother, Badariah Yeop Kamarudin, my lovely wife, Shafarina Azlinda and my siblings for their unconditional love and support and also their prayers for my success during the years I was busy pursuing my ambition to obtain my PhD. I would not have been able to complete this thesis without their continuous love and support. I can never repay them enough for their sacrifices.

LIST OF PUBLICATIONS

Related to PhD works:

Chapter 4

- 1) **Hafiz, S. M.**, Ritikos, R., Witcher, T. J., Razib, N. M., Bien, D. C. S., Chanlek, N., ... & Rahman, S. A. (2014). A practical carbon dioxide gas sensor using room-temperature hydrogen plasma reduced graphene oxide. *Sensors and Actuators B: Chemical*, 193, 692-700.

Chapter 5

- 2) **Hafiz, S. M.**, Chong, S. K., Huang, N. M., & Rahman, S. A. (2015). Fabrication of high-quality graphene by hot-filament thermal chemical vapor deposition. *Carbon*, 86, 1-11.

Chapter 6

- 3) Haniff, M. A. S. M., **Hafiz, S. M.**, Wahid, K. A. A., Endut, Z., Lee, H. W., Bien, D. C., ... & Rahman, S. A. (2015). Piezoresistive effects in controllable defective HFTCVD graphene-based flexible pressure sensor. *Scientific Reports*, 5, 14751-14761.

Related to the material and fabrication techniques:

- 1) Omar, F. S., Nay Ming, H., **Hafiz, S. M.**, & Ngee, L. H. (2014). Microwave synthesis of zinc oxide/reduced graphene oxide hybrid for adsorption-photocatalysis application. *International Journal of Photoenergy*, 17685, 1-8.
- 2) Othman, M., Ritikos, R., **Hafiz, S. M.**, Khanis, N. H., Rashid, N. M. A., & Rahman, S. A. (2015). Low-temperature plasma-enhanced chemical vapor deposition of transfer-free graphene thin films. *Materials Letters*, 158, 436-438.
- 3) Yunusa, Z., Rashid, S. A., Hamidon, M. N., **Hafiz, S. M.**, Ismail, I., & Rahmanian, S. (2015). Synthesis of Y-Tip Graphitic Nanoribbons from Alcohol Catalytic Chemical Vapor Deposition on Piezoelectric Substrate. *Journal of Nanomaterials*, 754768, 1-7.

TABLE OF CONTENTS

ABSTRACT.....	iii
ABSTRAK.....	v
ACKNOWLEDGEMENTS.....	vii
LIST OF PUBLICATIONS.....	viii
TABLE OF CONTENTS.....	ix
LIST OF FIGURES.....	xvi
LIST OF TABLES.....	xxvii
LIST OF ABBREVIATIONS.....	xxviii
CHAPTER 1: INTRODUCTION.....	1
1.1 History of Graphene.....	1
1.2 Graphene Properties.....	2
1.3 Graphene as Sensors.....	3
1.4 Research Problem	4
1.5 Research Objectives	8
1.6 Outline of Thesis	9
CHAPTER 2: LITERATURE REVIEW.....	12
2.1 Overview	12
2.2 Unique Properties of Graphene.....	13
2.3 Review on Graphene Fabrication Techniques.....	14
2.3.1 Top-down Method	14
2.3.1.1 Mechanical Cleavage.....	14
2.3.1.2 Chemical Method.....	15
2.3.2 Bottom-up Method.....	17
2.3.2.1 Epitaxial Growth.....	17

2.3.2.2	Chemical Vapour Deposition (CVD).....	18
2.4	Review on Growth Parameter using CVD Technique.....	20
2.4.1	Controllable Growth by Hydrogen Dilution	20
2.4.2	Growth Temperature.....	22
2.4.3	Seeded Growth.....	23
2.4.4	Vapour Trapping Growth.....	24
2.5	Review on Graphene Transfer Process	26
2.5.1	Common Transfer Process	26
2.6	Review on Gas Sensors Technology.....	29
2.6.1	Graphene as a Potential Candidate for Gas Sensor Application...	30
2.6.2	Graphene-based Carbon Dioxide Gas Sensor.....	31
2.7	Review on Pressure Sensors Technology	32
2.7.1	Graphene as a Potential Candidate for Pressure Sensor Application.....	34
2.7.2	Pressure Sensor Performances Criteria.....	35
2.8	Types of Pressure Sensor	38
2.8.1	Piezoresistive Effect in Graphene-Based Material.....	40
2.8.1.1	Structural Deformation.....	41
2.8.1.2	Percolating Conductive Networks.....	42
2.8.1.3	Tunnelling Mechanism.....	44
CHAPTER 3: EXPERIMENTAL AND ANALYTICAL TECHNIQUES...		46
3.1	Overview.....	46
3.2	Hot-filament Thermal Chemical Vapour Deposition Technique (HFTCVD).....	47
3.2.1	System Overview	47
3.2.2	Sample Preparation Process	50

3.2.3	Deposition Process.....	52
3.2.4	Transfer Process.....	55
3.3	Device Fabrication	58
3.3.1	Interdigitated Electrode (IDE) on Polyimide Substrate.....	58
3.4	Measurement and Characterization.....	60
3.4.1	Morphological and Topological Study	60
3.4.1.1	Field Emission Scanning Electron Microscopy (FESEM).....	60
3.4.1.2	Low Energy Electron Microscopy (LEEM).....	62
3.4.1.3	Atomic Force Microscopy (AFM).....	64
3.4.2	Structural Properties.....	67
3.4.2.1	Raman Spectroscopy	67
3.4.2.2	High Resolution Transmission Electron Microscopy (HRTEM)	72
3.4.3	Elemental Composition Study.....	74
3.4.3.1	X-ray Photoemission Spectroscopy (XPS).....	74
3.4.4	Electrical Analysis	76
3.4.4.1	Van der Pauw Method	76
3.5	Pressure Sensor Application	78
3.5.1	Test Set-up	78
3.5.2	Simulation of Pressure Sensor Device.....	80
3.5.2.1	Finite Element Analysis.....	80
CHAPTER 4: REDUCED GRAPHENE OXIDE BY HYDROGEN PLASMA TREATMENT.....		84
4.1	Overview.....	84
4.2	Synthesis of Graphene Oxide: Top-down Method.....	87

4.2.1	Simplified Hummers Method	87
4.2.2	Characterization	88
4.2.2.1	Structural Properties.....	88
4.2.2.2	Elemental Composition Properties.....	89
4.2.2.3	Morphological and Topological Properties.....	90
4.3	Reduced Graphene Oxide by Plasma-Enhanced CVD Technique.....	92
4.3.1	System Overview	92
4.3.2	Sample Preparation Process	94
4.3.3	Room-temperature Hydrogen Plasma Treatment Process.....	94
4.3.4	Results and Discussion.....	96
4.3.4.1	Structural Properties.....	96
4.3.4.2	Elemental Composition Properties.....	97
4.3.4.3	Morphological and Topological Properties.....	100
4.3.5	The Role of Hydrogen Plasma Parameters in Reduction of Graphene Oxide.....	104
4.4	Carbon Dioxide Gas Sensor Application	107
4.4.1	Gas Sensor Set-up	107
4.4.2	Gas Sensor Measurement	108
4.4.3	Performance Criteria	109
4.4.4	Results and Discussion	111
4.4.4.1	Sensing Range and Sensitivity of Designed Sensor....	111
4.4.4.2	Stability in Target Working Environment.....	112
4.4.4.3	Repeatability and Response Time	113
4.4.5	Proposed Sensing Mechanism	115
4.5	Summary.....	116

CHAPTER 5: GROWTH OF HIGH-QUALITY GRAPHENE ON	117
COPPER FOIL.....	
5.1 Overview	117
5.1.1 Set 1: The Effect of Growth Duration.....	119
5.1.1.1 Observation of Initial Growth of Graphene.....	119
5.1.1.2 Identification of Nanoparticles.....	122
5.1.1.3 The Role of Nanoparticle Size in Graphene Growth.....	125
5.1.2 Set 2: The Effect of Hydrogen Flow Rate.....	128
5.1.2.1 Growth and Etching effect on Graphene.....	128
5.1.2.2 Determining the Number of Graphene Layers.....	132
5.1.2.3 Tiered Graphene Island Nucleates by Cu ₂ O	134
Nanoparticle.....	
5.1.2.4 Growth of Bi-layer Graphene.....	137
5.2 Formation of High-quality Graphene	141
5.2.1 The Synergistic Role of Vapour Trapping and Hot-filament	141
Reactions.....	
5.2.2 Controlled Experiment.....	146
5.2.3 Comparison of Graphene Deposited using Cat-CVD Techniques.	147
5.3 Proposed Growth Mechanism	149
5.4 Graphene Transfer	150
5.4.1 Preferred Transfer Process for Device Fabrication.....	150
5.4.1.1 Effect on Defect Density, Transfer Coverage and I-V	151
Characteristic.....	
5.5 Summary	155

CHAPTER 6: GROWTH OF GRAPHENE/COPPER OXIDE	156
NANOCOMPOSITES AND FLEXIBLE PRESSURE	
SENSOR APPLICATION.....	
6.1 Overview.....	156
6.2 One-step Process Growth of Graphene/Copper Oxide Nanocomposites..	158
6.2.1 The Effects of Growth Temperature.....	158
6.2.1.1 Morphology.....	159
6.2.1.2 Crystallinity.....	165
6.2.1.3 Electrical Properties.....	166
6.2.2 Formation Mechanism of the Graphene/Cu ₂ O Nanocomposites..	168
6.3 Characterization of Graphene-based Flexible Pressure Sensor Device....	170
6.3.1 Stability.....	170
6.3.2 Sensing Range and Sensitivity.....	173
6.3.3 Repeatability, Limit of Detection and Response Time.....	175
6.3.4 Gauge Factor.....	177
6.4 Proposed Sensing Mechanism.....	180
6.5 Comparison of Graphene-based Pressure Sensor in Literature.....	186
6.6 Summary.....	191
CHAPTER 7: CONCLUSION AND FUTURE WORKS.....	192
7.1 Conclusion.....	192
7.2 Summary of Contribution.....	195
7.3 Future Works.....	196
7.3.1 Plasma Doping of rGO for Enhancement in Gas Sensor	
Sensitivity.....	197
7.3.2 Transfer-free of Graphene Fabricated Assisted by Trapped	
Copper-Vapour.....	197

7.3.3 Electronic Skin.....	197
REFERENCES.....	198
APPENDIX 1.....	214
APPENDIX 2.....	215

University of Malaya

LIST OF FIGURES

Figure 2.1:	Crystal structure of graphene and its electronic band structure. (a) Graphene has a honeycomb structure with a lattice constant of 2.46 Å. The inset is the unit cell. (b) Band structure of graphene. It has a linear dispersion around the K and K' points in reciprocal space (Sprinkle et al., 2009).....	15
Figure 2.2:	(a) FESEM images of mechanical exfoliation using HOPG with peeled away layer ranged between 30-600 graphene stacked using an AFM tip (Zhang et al., 2004). (b) Graphene is detached from a graphite crystal using adhesive tape. After peeling off the graphite, multiple-layer graphene remains on the tape. By repeated peeling the multiple-layer graphene is cleaved into various flakes of few-layer graphene (Novoselov et al., 2004)	17
Figure 2.3:	Chemical oxidation method to obtain monolayer graphene oxide followed up by reduction process to remove back the oxygen functional group attached to the basal and edges of graphene layer.....	18
Figure 2.4:	Epitaxial growth of graphene on silicon carbide substrate by thermal decomposition process. A structural model of bilayer graphene and buffer layer grown on silicon carbide, as indicated by the blue lines and broken line, respectively (Norimatsu et al., 2014).....	19
Figure 2.5:	A typical graphene growth process by thermal chemical vapour deposition (T-CVD) method (Mattevi et al., 2011).....	21
Figure 2.6:	(Up) Graphene islands fabricated by CVD technique at 1000 °C on Cu foil using 1 mTorr of methane and different partial pressures of hydrogen. (Bottom) The average size of graphene grains is shown as a function of partial pressure of hydrogen. Note that the hexagons shape of graphene islands are observed only at high hydrogen pressures. Scale bars are 10 µm (Vlassiuk et al., 2011)	23
Figure 2.7:	FESEM images of graphene growth depending on the growth temperature at (a) 940, (b) 980, (c) 1000, and (d) 1030 °C. (Hwang et al., 2011).....	25
Figure 2.8:	Schematic representation of the silicon oxide impurity mediated growth kinetics of multilayer graphene on the copper surface (Kasap et al., 2015).....	26
Figure 2.9:	(Up) Schematic drawings of favourable gas phase surface reaction mechanisms of methane precursor for dehydrogenation, hydrogenation, and radical coupling on bulk Cu surface. (Bottom) Additional gas phase reaction of atomic carbon dehydrogenation mediated by Cu vapour, which will be redeposited on Cu surface and completes the graphene growth (Lin et al., 2015).....	27

Figure 2.10:	PMMA polymer-supported metal etching transfer process that typically required for graphene fabricated using CVD technique on rigid substrate (Batrakov et al., 2014).....	29
Figure 2.11:	Schematic of the roll-based production of graphene films grown on a copper foil for industry scale production. The process includes adhesion of polymer supports, copper etching (rinsing) and dry transfer-printing on a target substrate (Bae et al., 2010)..	30
Figure 2.12:	General applications of pressure sensor in various major industries.....	35
Figure 2.13:	(a) PMMA/graphene ribbons film attached to a mechanically pre-strained PDMS substrate with ribbon alignment along the pre-strain direction (Wang et al., 2011). (b) Schematic representing the operating mechanisms in applied vertical pressure (Chun et al., 2015b).....	44
Figure 2.14:	(a) Fabrication of graphene woven fabric (GWF) by CVD method. (b) Current pathway through a fractured GWF. (c) The equivalent circuit model for estimating the resistance of GWF with specified cracked density (Li et al., 2012).....	45
Figure 2.15:	(a) Schematic structure of polycrystalline graphene with the islands size denoted as L_1 and L_2 while the overlapping region between these two islands denoted as W_0 . These parameters would control the change of resistance upon deformation of the sensor (Li et al., 2012). (b) Schematic showing the working principle of the graphene quantum dots (GQDs) mixed with polymer microfiber pressure sensor. The external pressure concentrates stress at the contact spots, deforming the matrix medium, which in turn causes an increase in the contact area and the tunnelling currents (Sreepasad et al., 2013).....	47
Figure 3.1:	(a) Schematic diagram of HFTCVD system and (b) photograph of HFTCVD system. The inset picture shown the glowing of hot-wire at temperature $> 1000\text{ }^{\circ}\text{C}$. (c) Photograph of rolled Cu foil inside the coiled alumina tube from the opening side. (d) Side view of top plate of HFTCVD system.....	51
Figure 3.2:	Photograph of freshly cut Cu foil with dimension of $3.0 \times 2.0\text{ cm}$ (6.0 cm^2).....	54
Figure 3.3:	Temperature profile of the Cu foil acquired from thermocouple along the fabrication process using HFTCVD system. For Set 1, the deposition time is varying at 5, 10, 20, 30 and 40 minutes. In Set 2, the $\text{H}_2:\text{CH}_4$ flow rate is vary at 10:10, 25:10, 50:10, 75:10 and 100:10 ratios. While in Set 3, the deposition temperature is vary at 750, 850 and $1000\text{ }^{\circ}\text{C}$. Note that only the parameter in deposition process will be varied for this work while the heating, cleaning and annealing, and cooling processes are keep the same.....	57
Figure 3.4:	Photograph of fabricated samples on Cu foils.....	57

Figure 3.5:	Schematic representation of typical graphene transfer process on SiO ₂ /Si and polyimide flexible pressure sensor substrate employed in this work.....	59
Figure 3.6:	Fabrication process flow of the IDE array on the polyimide substrate film by UV photolithography method.....	62
Figure 3.7:	(a) Photograph of the fabricated IDE array and terminal electrode on flexible polyimide substrate. The effective sensing area of 5 x 5 mm ² as indicated in a square box. (b) FESEM image of the electrode finger (500 μm) and gap (200 μm).....	62
Figure 3.8:	FESEM images of graphene on Cu foil. (Kochat et al., 2011).....	64
Figure 3.9:	(a) Schematic of the electron optics of the LEEM system. (b) Variation of electrons reflected from the graphene surface and graphene/substrate (SiC substrate) interface which interfered and causes the electron reflectivity to change periodically as a function of the electron energy and graphene thickness. (c-d) The LEEM images of multilayer graphene that vary from 1 to 8 layers denoted by the number in the boxes. (e) Electron reflectivity or intensity voltage (I-V LEEM) plot with respect to the electron energy. The number of the graphene layers can be determined from the analysis of the reflectivity oscillations in I-V LEEM plot (Hibino et al., 2008).....	66
Figure 3.10:	(a) Schematic diagram of AFM set up. (b) Force-curve (or Force-distance curve) as a function of probe-sample separation. They are three region of force which determined the mode of AFM used; contact mode, tapping mode and non-contact mode. (c-d) The tapping mode used in this work is operated via the principle of amplitude-modulation detection. The tapping AFM mode has the advantage with minimum sample damage. This is particularly important in graphene topological mapping and analysis with no surface alteration (Voigtländer, 2015).....	68
Figure 3.11:	Topological AFM mapping of graphene deposited on decorated nanoparticle substrate with (a) height and (b) phase imaging. (Pacakova et al., 2015).....	69
Figure 3.12:	(a) Electronic Brillouin Zones (BZs) of graphene (black hexagons), the first phonon BZ (red rhombus), and schematic electronic dispersion (Dirac cones). The vertical arrow illustrates the electron energy (E) which the energies of the intermediate states are given by the difference in energies of electrons in the empty π^* and filled π bands. The Dirac cones intercept at Fermi level (E_F) for monolayer graphene. The phonon wave vectors connecting electronic states in different valleys are labelled by red Greek letters (Γ , K and K'). (b) Typical Raman spectra of graphite (bottom), graphene (middle) and defective graphene (top) which shown the D, G, G', 2D and D+D' peaks taken using 514.5 nm laser source (Malard et al., 2009).....	71

Figure 3.13:	The prominent features in the Raman spectra of monolayer graphene due to the Raman scattering process denoted as (a) G, (b) D', (c) D and (d) 2D peaks. This would involve the electron excitation due to absorption of photon (laser source), elastic (defect) and inelastic (phonon) electron-phonon scattering and electron-hole recombination which then gave out the photon emission (Raman spectra). The inter-valley transitions process is due to the connected points of electron scattering that circles around at K and K' points in the first BZ of graphene. On the other hand, the intra-valley process is due to the connected points of electron scattering inside the same circle around the K point (or the K' point) (Malard et al., 2009).....	73
Figure 3.14:	Schematic view of the electron dispersion of bilayer graphene near the K and K' points showing both π_1 and π_2 bands. The four Raman scattering process is indicate by: (a) P_{11} , (b) P_{22} , (c) P_{12} , and (d) P_{21} of electrons scattering. (e) The measured 2D peak, $\sim 2700\text{ cm}^{-1}$ of Bernal (AB) stacked bilayer graphene will be deconvoluted into four Lorentzian peaks of peak frequencies at 2658, 2688, 2706, and 2721 cm^{-1} , respectively. This is correspond to the broadened in the $2D_{FWHM}$ peak as compared to monolayer graphene which can be fitted with single Lorentzian peak of $\sim 24\text{-}30\text{ cm}^{-1}$ (Malard et al., 2009).....	74
Figure 3.15:	(a) TEM analysis of platinum/graphene nanocomposites (Aldrich Prod. No.803693). (b) HRTEM image of platinum nanoparticle with lattice spacing, d of 0.23 nm corresponds to (111) plane. (c) The corresponding SAED pattern of platinum/graphene nanocomposites (Marquardt et al, 2014).....	76
Figure 3.16:	Electronegativity effect in (a) pure element and (b) carbon-oxygen bond. (c) High resolution XPS C1s spectra of (from up to bottom) untreated HOPG, HOPG after 10 minutes ozone treatment and HOPG after 60 min ozone treatment. The spectra highlight the significant increase in chemisorbed oxygen upon ozone treatment at pre-existing defect sites on the carbon element presents on the HOPG surfaces. (Webb et al., 2011).....	79
Figure 3.17:	(a) Picture of sample board holder. The sample board shows 4 probe tip, A, B, C and D (top view) which will be connected with the sample edges by spring loaded clamps (side view). (b) Schematic of a rectangular Van der Pauw configuration used in the determination of the two characteristic resistances, R_{AB} (left) and R_{BC} (right) of the sample.....	80
Figure 3.18:	Schematic diagram of pressure sensor set up.....	82
Figure 3.19:	Photograph of pressure sensor set up.....	82
Figure 3.20:	Illustration of (a) steady state and (b) under deformation state of flexible pressure sensor device. The deflection of pressure sensor device would change the initial resistance (R_0) into the resistance value measured under deformation (R).....	83

Figure 3.21:	(a) Plot of maximum deformation, d with respect of applied pressure obtained from FEA for fabricated flexible pressure sensor platform shown in Section 3.3.1. (b) Nonlinearity as a function of applied pressure. (c). Calculated strain, ε (%) exerted due to the deformation of the fabricated sensor when applied to a pressure range of 0-50 kPa. The solid lines are given as guides to the eye.....	86
Figure 4.1:	Flow chart showing the progression of graphene fabrication using top-down approach and its potential application as a gas sensor.....	90
Figure 4.2:	(a) Raman spectra of graphite and graphene oxide. Note that the significant increase of D peak, the broadening of D and G peak as well as appearance of D+D' peak denoted the graphite has been successfully converted into graphene oxide.....	92
Figure 4.3:	Deconvoluted XPS spectrum of C1s narrow scan peak for GO sample.....	94
Figure 4.4:	FESEM morphological images of graphite (left) and graphene oxide (right).....	95
Figure 4.5:	AFM topological image of graphene oxide on SiO ₂ /Si substrate (left) and corresponding cross-sectional height profile with an average thickness of 0.947 nm (right).....	95
Figure 4.6:	(a) Photograph and (b) schematic diagram of the custom-made plasma enhanced chemical vapour deposition (PECVD) chamber used for room-temperature hydrogen plasma reduction.....	97
Figure 4.7:	Raman spectra of the graphene oxide and reduced graphene oxide with different degrees of structural evolution. The spectra consists of D, G, 2D and D + D' peaks located at 1343, ~1590, 2700 and 2930 cm ⁻¹ , respectively. Note that the D + D' peak monotonously increase in intensity and broadens with the spectra stacking order shown above, due to ion-bombardment effect.....	101
Figure 4.8:	(a) Comparison of typical wide scan XPS spectra of GO and rGO sample. Note that the difference in intensity of the O1s and C1s peaks between GO and rGO sample. (b) Deconvoluted O1s narrow scan of a typical GO and rGO sample.....	102
Figure 4.9:	X-ray photoelectron spectrometry analysis with different degrees of reduction illustrating the deconvoluted spectra in the C1s peak region at around 284.8 eV; C–C=C, 286.4 eV; C–OH, 287.8 eV; C=O 288.9 eV; O=C–OH for (a) graphene oxide, (b) rGO-F50, (c) rGO-P20, (d) rGO-F40, (e) rGO-F20 samples. The intensity of the y-axis increases from (a) to (e) indicated by the multiplication factor in each graph.....	103
Figure 4.10:	Photograph of (a) GO, (b) rGO-F20 and (c) overly-exposed rGO samples on quartz substrate.....	104
Figure 4.11:	Higher magnification FESEM images of (a) GO, (b) rGO-P40, (c) rGO-F20 and (d) overly-exposed rGO sample on SiO ₂ /Si substrates.....	105

Figure 4.12:	AFM images of the (a) rGO-P40 and (b) rGO-F20 samples. The height profile is taken along the line (blue) presented on the right and measure to be 0.758 and 0.663 nm, respectively.....	107
Figure 4.13:	Illustrations of (a) energetic species presents in between parallel-plate PECVD configuration, (b) reduction of oxygen functional groups at basal and edges of GO flakes and (c) restoration of C=C backbone structural of graphene with different degree of reduction.....	110
Figure 4.14:	(a) Photograph and (b) schematic diagram of the gas sensor set-up.....	111
Figure 4.15:	(a) Photograph of the CO ₂ gas sensor device. The size of pre-pattern silicon die on the device is 3.1 mm×3.8 mm. The images of CO ₂ gas sensor device taken from; (b) optical microscope and FESEM at (c) low magnification or (d) high magnification of the reduced graphene oxide sheet on 3 μm electrode fingers width and separation distance.....	112
Figure 4.16:	I–V curve obtained for the fabricated graphene gas sensors.....	114
Figure 4.17:	Room-temperature CO ₂ gas sensor response, $(R_{N_2}-R_x)/R_{N_2} \times 100$ (%) on the GO, rGO-P40 and rGO-F20 samples from 0 ppm to 1500 ppm in an N ₂ environment at 37% RH. Note that the sensing response of all the sensors is based on the changes of resistance when exposed to CO ₂ gas with respect to the initial resistance measured in N ₂ environment at 23 °C.....	116
Figure 4.18:	(a) The CO ₂ gas sensor response, $(R_{Air}-R_x)/R_{Air} \times 100$ (%) on the rGO-F20 sample from 300 ppm to 1500 ppm in an air environment at 68% RH. Note that the sensing response of the sensor is based on the changes of resistance when exposed to CO ₂ gas with respect to the initial resistance measured in air environment at 23 °C.....	117
Figure 4.19:	The change of sensing response versus time when the CO ₂ concentration is switched from 350 ppm to 750 and 769 ppm. The response and recovery time can be determined from the figure about ~4 minutes.....	118
Figure 4.20:	Schematic representations of the proposed sensing mechanism in reduced graphene oxide CO ₂ gas sensor.....	119
Figure 5.1:	Flow chart showing the progression of graphene fabrication using bottom-up approach using HFTCVD technique.....	123
Figure 5.2:	FESEM images of graphene grown on Cu foils with different deposition times: (a) 5, (b) 10, (c) 20, (d) 30, and (e) 40 minutes at 1000 °C. The CH ₄ :H ₂ flow rate was fixed at 10:50 sccm. The graphene patch (b) and corrugated copper substrate (e) are shown in rectangular boxes. Wrinkles and nanoparticles are indicated by arrows and circles, while tension caused from a bump of corrugated surface is indicated by dotted arrows.....	125

Figure 5.3:	(a) Raman spectra of samples deposited for time duration of 5 and 30-minutes on Cu foil. The inset shows a typical Cu ₂ O spectrum. Note that copper does not have a Raman active mode. Thus, no Raman peak was observed. (b) HRTEM images of Cu ₂ O nanoparticle on graphene transferred onto square copper mesh TEM support grids further proved that these Cu ₂ O nanoparticles are the nucleation sites for the graphene growth.....	128
Figure 5.4:	Phase diagram of the copper-oxygen system for pressure versus temperature. (Ito et al., 1998).....	129
Figure 5.5:	FESEM images and size distribution diagram of graphene grown on Cu foils at different deposition times: (a) 5, (b) 10, (c) 20 and (d) 30 minutes at 1000 °C. The Lorentz fitted curved shifted to lower particle size with respect of deposition time shown by red arrow. Two groups of nanoparticles size were indicated by star and circle shape that increased or decreased as the deposition time was prolonged.....	131
Figure 5.6:	Evolution of Cu ₂ O nanoparticle size that initiates the graphene growth. Graphene would start to grow after the size of nucleation seed is favourable. The duration that takes for the patch-like graphene to be observed to grown is called the induction time....	132
Figure 5.7:	FESEM images of graphene grown on Cu foils with different H ₂ flow rates: (a) 100, (b) 75, (c) 50, (d) 25, and (e) 10 sccm at 1000 °C. The CH ₄ flow rate was fixed at 10 sccm with a 30 minutes deposition time. The branch-like graphene grown around the nanoparticle at the centre of each domain was indicated by a hexagonal and circle shapes respectively in the magnified image on the right (a). Merging of two branch-like graphene was indicated by dotted square, while exposed graphene under-layer was differentiated from graphene upper-layer indicated by arrows as shown in the magnified images on the right (d) and (e).....	134
Figure 5.8:	Illustration of the formation of graphene layer high and low flow rate of H ₂	136
Figure 5.9:	(a) 514-nm laser excitation Raman spectra of graphene deposited on Cu foils and (b) FWHM _{2D} of transferred graphene onto SiO ₂ /Si substrate at various H ₂ flow rates: 10, 25, 50, 75, and 100 sccm.....	138
Figure 5.10:	(Upper Part) LEEM images collected at 50, 15 and 7.5 μm field of view (FOV) of 10, 25 and 50 sccm H ₂ sample. The images were taken using an energy of ~3.0 eV. This shows that the graphene is homogenously grown on the copper foil by using HFTCVD technique. (Lower Part) The IV-LEEM graph shows different number of dips (3, 2 and 1 dips) as a function of incident-electron bias voltages; V _{Bias} -V _{Vac} that corresponds to the number of graphene layer (1 dip means mono-layer etc.). The colours of arrow (red, blue and green) correspond with the number of dips shown in 7.5 μm FOV. The V _{Bias} and V _{Vac} are defined as the bias voltage applied to the sample and vacuum energy level divided by electron charge, respectively.....	141

Figure 5.11:	The i) until iii) shows the sample of 10 sccm, 25 sccm and 50 sccm H ₂ flow rate, respectively. The LEEM images of (a) and (b) shows a selected area of interest for coalesce between two graphene islands indicated inside the dotted box. (c) The colour coding of certain spots is corresponds to the number of graphene layer; Red is tri-layer, Blue is bi-layer and Green is mono-layer. (d) Illustrated cross-sectional schematics of graphene island formation on a Cu ₂ O nanoparticle seed.....	143
Figure 5.12:	Mechanisms for adlayer graphene growth followed by a) adsorption-diffusion and then b) gas phase penetration mechanism. (Gan et al., 2015).....	144
Figure 5.13:	The colour coding of 10-sccm H ₂ flow rate sample in 7.5 μm FOV. The dominant yellow colour resembles a bi-layer graphene with the coverage up to 60 % of total area.....	145
Figure 5.14:	Schematic of graphene growth deposition in HFTCVD technique and formation of active flux of carbon, hydrogen and hydrocarbon radicals by catalytic reaction of CH ₄ and H ₂ precursors using tungsten filament. The streamline of mixed gas inside the alumina tube from the simulation calculation shows a circumfluence flow which directly adapted from the work of Wang et al. (2014). Note that, this diagram only act as an illustration of circumfluence flow inside the tube with one end sealed.....	147
Figure 5.15:	A typical wide scan of XPS spectra of graphene sample on Cu foil. (Inset) The deconvolution of C1s peak shows the graphene is slightly oxidized due to its high-quality nature.....	150
Figure 5.16:	Raman spectra of controlled deposition experiment with following parameters: (i) 2-cm alumina tube opening at 1000 °C and (ii) 1-cm alumina tube opening at 850 °C substrate temperature. The 1-cm alumina tube opening deposited at 1000 °C substrate temperature was shown for comparison.....	151
Figure 5.17:	Diagram of growth mechanism of graphene on Cu foil assisted by Cu ₂ O nucleation sites using HFTCVD technique.....	155
Figure 5.18:	Typical images of transferred graphene layer observed on SiO ₂ substrate viewed using optical-microscope and FESEM.....	156
Figure 5.19:	Comparison of the Raman spectra of mono-layer and multi-layer graphene transferred using thermal release tape and Poly-methyl methacrylate (PMMA) support. The D peak is presence in all samples after the transfer process compared to the data taken on Cu foil as shown in Fig. 4.8(a). The effect of transfer process of both techniques is more significant on multi-layer graphene.....	157
Figure 5.20:	FESEM images shows a comparison of mono-layer graphene morphology transferred using (a) thermal release tape; TRT and (b) Poly-methyl methacrylate; PMMA support. The images at the right are magnified image at the centre and edge of transferred graphene. Note that the graphene transferred using thermal release tape shows distinct cracks formation compared	159

	to PMMA transfer method.....	
Figure 5.21:	Comparison of the I-V (current-voltage) characteristic of monolayer graphene transferred using thermal release tape and Poly-methyl methacrylate (PMMA) support.....	160
Figure 6.1:	Flow chart showing the progression of graphene/copper oxide nanocomposites fabrication using HFTCVD technique which leads to its integration in flexible pressure sensor device. Note that the device fabrication has been explained in Chapter 3 under Section 3.3.....	163
Figure 6.2:	FESEM images of (a-b) graphene/Cu ₂ O nanocomposites (750 and 850 °C) and (c) graphene (1000 °C) grown on Cu foils at different deposition temperature. The FESEM images of 750, 850 and 1000 °C sample was further magnified and shown in (d), (e) and (f) respectively. The circle, triangle and rectangular shapes indicate Cu grain domain sizes, nanoparticles and wrinkles.....	165
Figure 6.3:	FESEM images of overlapping region of sample grown at (a) 750 °C (b) 850 °C and (c) 1000 °C on SiO ₂ /Si (100) substrates. The magnified images of the overlapping region are shown on the right. Note that the overlapping region is decreased from 0.30 to 0.20 μm and then at ~0.05 μm with an increase of growth temperature from 750 to 850 and 1000 °C, respectively.....	167
Figure 6.4:	Illustration showing how the overlapping regions are controlled by the nucleation density of Cu ₂ O nanoparticles. At low graphene growth temperature (750 and 850 °C), the nucleation density is expected to be higher compared to sample grown at 1000 °C, thus increase the probability of overlapping between graphene islands.....	167
Figure 6.5:	Flow diagram of graphene/Cu ₂ O nanocomposites transfer process. The PMMA support layer was inferred to protect the decorated Cu ₂ O nanoparticles from the Cu etchant solution.....	169
Figure 6.6:	FESEM and AFM (10 x 10 μm ²) images of transferred (a-b) graphene/Cu ₂ O nanocomposites (750 and 850 °C) and (c) graphene (1000 °C) graphene samples on polyimide substrates. The corresponded AFM topological images with height profiles were shown at the bottom.....	170
Figure 6.7:	Raman spectra of graphene and graphene/Cu ₂ O nanocomposites deposited on (a) Cu foils and transferred on the (b) SiO ₂ /Si (100) substrates grown at 750, 850 and 1000 °C.....	172
Figure 6.8:	Diagram of growth mechanism of graphene/Cu ₂ O nanocomposites using HFTCVD technique. Note that a lower growth temperature (750 and 850 °C) would cause the re-deposited of oxygen-copper vapour reaction due to a low evaporation rate environment thus forming a decorated Cu ₂ O nanoparticles on graphene layer. The growth mechanism of graphene was presented for comparison.....	176

Figure 6.9:	(a) Close up photograph of graphene-based flexible pressure sensor devices. (b) Time-dependence of initial resistance, R_0 at room-temperature and 50-60% relative humidity and reproducibility of I-V characteristic for four samples for each deposition parameters is shown in the inset graph, (c) Temperature-dependence of resistance at ~60% relative humidity, (d) Humidity-dependence of resistance in sensor at room-temperature for 750, 850 and 1000 °C samples.....	178
Figure 6.10:	Relative change in resistance as a function of applied differential pressure for pressure sensor fabricated from 750, 850 and 1000 °C samples. Dashed lines are given as guides to the eye. The sensor's sensitivity, S (kPa^{-1}) was defined by the slope of the graph. The inset shows that the resistance increases as the differential pressure increases.....	180
Figure 6.11:	(a) Multi-cycle operation of repeated loading and unloading at different pressures with graphene grown at 750 °C. (b) Magnified resistance change of 0.24 kPa applied pressure which consider as limit of detection for this device. The inset shows a hysteresis plot of the relative change in resistance of loading and unloading in the wide pressure regime (0-50 kPa).....	182
Figure 6.12:	The response time of multiple loading and unloading at 10.39 kPa with graphene grown at 750 °C. The response time of loading and unloading pressure was measured to be about ~1000 millisecond. The differences in sensing time and recovery time from multiple cycles were measured to be within 150 and 200 millisecond, respectively.....	183
Figure 6.13:	(a) Finite element analysis (FEA) on the fabricated sensor has been conducted using CoventorWare® to demonstrate that the applied pressure from initial condition to 10 kPa and then to 50 kPa applied pressure. A round-shape deformation was formed on the bottom surface of the fabricated sensor which gives maximum deformation of 4.5 μm at 10 kPa and 18.0 μm at 50 kPa. (b) Plot of maximum deformation, d with respect of applied pressure obtained from FEA. (c) Calculated strain, ε (%) exerted due to the deformation of the fabricated sensor when applied to a pressure range of 0-50 kPa. The solid lines are given as guides to the eye.....	185
Figure 6.14:	Changes of relative resistance with respect to the strain, ε exerted due to the deformation of the fabricated sensor when applied to a pressure range of 0-50 kPa. Calculated gauge factor, GF for pressure sensor fabricated from 750, 850 and 1000 °C samples were shown with the value of 50, 30 and 15, respectively. Note that the GF of pristine graphene purchased from Graphene Supermarket was around ~1.9-2.0. Dashed lines are given as guides to the eye.....	186
Figure 6.15:	Schematic representations of the proposed resistance mechanism in graphene/ Cu_2O nanocomposites network.....	188

Figure 6.16:	(a) FESEM images of transferred graphene/Cu ₂ O nanocomposites grown at 750 °C on the IDE structure with different possibilities of resistance changes; (b) Overlapping region between graphene islands, (c) Wrinkle defect structure, (d) Cu ₂ O nanoparticles defect structure and (e) point defects inside graphene lattice.....	189
Figure 6.17:	Schematic representation of circuit model for graphene-based flexible pressure sensor.....	191
Figure A1:	Hot-filament Thermal Chemical Vapour Deposition (HFTCVD) full system set up.....	222
Figure A2:	Transfer-free Graphene Fabrication using HFTCVD Technique. The modification of substrate placement inside the rolled Cu foils is inferred to yield a transfer-free graphene fabrication using HFTCVD technique.....	223

LIST OF TABLES

Table 2.1:	Classification of indoor air quality with respect to CO ₂ concentration.....	34
Table 2.2:	Relative merits and demerits of various types pressure sensor...	41
Table 3.1:	General deposition procedures carried out for HFTCVD technique.....	53
Table 3.2:	Details of the deposition parameters for each set of samples.....	56
Table 3.3:	Comparison of deflection results between MemMECH solver and analytical model by Timoshenko et al. (Timoshenko et al., 1959) for the square diaphragm structure.....	85
Table 3.4:	Comparison of stress results between MemMECH solver and analytical model by Timoshenko et al. (Timoshenko et al., 1959).....	85
Table 4.1:	Flow chart showing the progression of graphene fabrication using top-down approach and its potential application as a gas sensor.....	90
Table 4.2:	General plasma treatment procedures carried out by PECVD technique.....	97
Table 4.3:	Summary of the hydrogen plasma reduction parameters performed by PECVD technique.....	99
Table 4.4:	Summary of Raman and XPS analysis of GO and rGO samples.	108
Table 5.1:	Comparison of results from this work and literature regarding the quality of fabricated graphene on Cu foil based on various CVD techniques.....	153
Table 6.1:	Details of the morphological, topological and electrical properties of graphene and graphene/Cu ₂ O nanocomposites grown at specific temperature. This would then correlate to the electron percolation pathway in the graphene networks.....	173
Table 6.2:	Performance comparisons between graphene-based flexible pressure sensors presented in this work and reported by others...	194

LIST OF ABBREVIATIONS

AFM	Atomic Force Microscopy
ASHRAE	American Society of Heating, Refrigerating and Air Conditioning Engineers
BE	Binding Energy
BLG	Bilayer Graphene
BSE	Backscattered Electron
BZ	Brillouin zone
Cat-CVD	Catalytic Chemical Vapour Deposition
CH ₄	Methane
CO ₂	Carbon Dioxide
Cu	Copper
Cu ₂ O	Copper Oxide
CVD	Chemical Vapour Deposition
E _D	Dirac Point
E _F	Fermi Energy
E-skin	Electronic Skin
FEA	Finite Element Analysis
FESEM	Field Emission Scanning Electron Microscopy
FLG	Few Layer Graphene
FOV	Field of View
FWHM	Full width half maximum
GF	Gauge Factor
GIC	Graphite Intercalation Compound
GO	Graphene Oxide
GQDs	Graphene Quantum Dots

GWF	Graphene Woven Fabric
HFCVD	Hot-filament Chemical Vapour Deposition
HFTCVD	Hot-filament Thermal Chemical Vapour Deposition
HOPG	Highly Ordered Pyrolytic Graphite
HRTEM	High-resolution Transmission Electron Microscopy
HWCVD	Hot-wire Chemical Vapour Deposition
IDE	Interdigitated Electrode
iLO	In-plane Longitudinal Optic Phonon Mode
InSn	Indium-tin compound
iTO	In-plane Transverse Optic Phonon Mode
I-V	Current-Voltage
I-V LEEM	Intensity-Voltage Low Energy Electron Microscopy
L_a	In-plane sp^2 Crystallite Size
LEEM	Low Energy Electron Microscopy
LSG	Laser-scribed Reduced Graphene Oxide
MFC	Mass Flow Controller
PDMS	Polydimethylsiloxane
PECVD	Plasma Enhanced Chemical Vapour Deposition
PMMA	Poly(methyl methacrylate)
ppm	Part per million
PU	Polyurethane
rGO	Reduced Graphene Oxide
RH	Relative Humidity
sccm	Standard Cubic Centimetres per Minute
SE	Secondary Electron
STM	Scanning Tunnelling Microscopy

T-CVD	Thermal Chemical Vapour Deposition
TEM	Transmission Electron Microscopy
TRT	Thermal Release Tape
UV	Ultra-violet
VRH	Variable Range Hopping
XPS	X-ray Photoemission Spectroscopy

University of Malaya

CHAPTER 1: INTRODUCTION

1.1 History of Graphene

Looking back at graphene history, it should probably start with an observation from the work of British chemist named Benjamin Brodie (1859). Brodie has demonstrated a graphite oxidation process by exposing graphite to strong acids to obtain graphene sheets with a dense cover of hydroxyl and epoxide groups. Over the next century, there were several papers published describing the graphite oxide process (Staudenmaier, 1898; Hummers, 1958). However, due to the limitation of the magnification of the microscope at that time, it was not possible to establish that graphite oxide consisted of floating atomic planes. These studies were continued by a group led by Hofmann who reported the thinnest possible fragments of graphite oxide using transmission electron microscopy, TEM by counting the number of folding lines and identifying some of them as monolayers (Boehm et al., 1962). Furthermore, Hofmann's group was the first to introduce the term graphene, deriving it from the combination of the word "graphite" and the suffix that refers to polycyclic aromatic hydrocarbons.

Ultrathin graphitic films were first reported to be epitaxially-grown on Ru, Rh and Ni metal substrates (Grant et al., 1970; Blakely et al., 1970). Usually, the grown film was then analysed by surface science techniques like scanning tunnelling microscope, STM that average over large areas and lacks the information on the film's continuity and quality. In 1990, Kurz's group reported optically thin graphite layers obtained by peeling-off parent graphite using a Scotch tape, which was then used to study charge carrier dynamics (Seibert et al. 1990). Even more relevant were earlier attempts to obtain ultrathin films of graphite by the cleavage process. In 1999, Ruoff's group presented one such approach for graphite by using an atomic force microscope (AFM) tip to manipulate highly oriented pyrolytic graphite, HOPG and obtained about

~600 layers (Lu et al., 1999). Later, Kim's group improved the method, which successively obtained graphite layer as thin as 30 layers (Zhang et al., 2004). The first isolation of single layer graphene from HOPG using Scotch tape was demonstrated in 2004 by Geim's group (Novoselov et al., 2004).

In 2005, Geim and Philip's groups both described the all-important observation of quantum electrodynamics in monolayer graphene and successfully published this new highlight on graphene in Nature (Novoselov et al., 2005; Zhang et al., 2005). The single-layered hexagonal structure of graphene makes it the "mother" of all carbon-based systems namely, graphite, carbon nanotubes and buckminsterfullerene (Neto et al., 2006). The graphite material that can be found in pencils is simply a stack of graphene layers; carbon nanotubes are made of rolled-up sheets of graphene; and buckminsterfullerene molecules are nano-meter size spheres of wrapped-up 'graphene-like' structure (comprises of pentagons and hexagons carbon atom arrangements). Recently, scientists decorated various semiconductor or metal nanoparticles on graphene sheet. These graphene-based nanocomposites provide an important milestone to improve the overall performance due to the versatile and tailor-made properties as compared to those of the individual semiconductor/metal nanoparticles (Rathod, 2015).

1.2 Graphene Properties

Graphene's unique properties arise from the collective behaviour of electrons. The interaction between electrons and the hexagonal lattice causes the electrons to behave as if they have absolutely no mass (Novoselov et al., 2005). Because of this, the electrons in graphene are governed by the Dirac equation which gives the quantum mechanical description of electrons moving relativistically. The electrons in graphene are therefore called Dirac fermions which carry one unit of electric charge and so can be manipulated using electromagnetic fields. Since the manipulation of electrons within

materials is available in modern electronics, the unique behaviour of electrons in graphene may allow us to go beyond the limits of silicon-based semiconductor technology (Abergel et al., 2010). Since these remarkable observations on graphene surfaced, tremendous interest in the scientific community on this material led to various investigations on techniques of preparation of graphene as well as its potential application (Geim et al., 2012).

Versatility of graphene as a material in sensor devices arises from its unique electronic and structural properties such as large surface-to-volume ratio, unique optical properties, excellent electrical conductivity, high carrier mobility and density, high elastic stiffness and stretchability, and high thermal conductivity (Zhang et al., 2013; Zhu et al., 2013). The 2D structure of graphene constitutes to an absolute maximum of the surface area to volume ratio in a layered material, which is essential for high sensitivity. Graphene will also enable the fabrication of sensors that are smaller, lighter, flexible and transparent which provide endless design possibilities. The production of graphene from abundant carbon source, e.g. graphite will eventually become less expensive compared to the production of traditional sensors. Graphene-based nanoelectronic sensor devices have also been researched for use in gas sensors; for detection of hazardous gases, strain and pressure sensors; for touch screen devices as well as health and medical application, and many other devices (Ferrari et al., 2015).

1.3 Graphene as Sensors

Recently, prototype and commercial activities in the field of graphene-based sensor devices are increasing rapidly. In 2012, Nokia has filed for a patent for a graphene-based photodetector that is transparent, thin and should ultimately be cheaper than traditional photodetectors (Mertens, 2012). Then, in 2013, Nokia has developed a

humidity sensor based on graphene oxide which is incredibly fast, thin, transparent, and flexible and has great response and recovery time (Borini et al., 2013). In 2014, the AMO GmbH (in collaboration with Alcatel Lucent Bell Labs) has developed a graphene-based photodetector, which is said to be the world's fastest photodetector (Mertens, 2014). In 2014, researchers from Trinity College in Ireland have developed wearable sensors by coating rubber bands with graphene. The idea is that the rubber band would change its electric conductivity when stretched, so even tiny movements (such as breathing or pulse) can be sensed (Boland et al., 2014). In 2015, collaboration between BOSCH GmbH and scientists at the Max-Planck Institute have yielded a graphene-based magnetic sensor that is 100 times more sensitive than an equivalent device based on silicon (Peleg, 2015). Seeing the rapidly emerging trend of graphene's industry in production process as well as nanoelectronic sensor devices prototype or commercialization, this research is driven by the current trend and focuses on the fabrication technique and sensor application of graphene-based material.

1.4 Research Problem

Graphene research has developed at a truly relentless pace. Many efforts have been devoted to develop diverse approaches to fabricate graphene, aiming for the simple, high-throughput and easy functionalization process or large and uniform area synthesis of high-quality graphene which largely depends on specific target application. In general, the approach of graphene fabrication can be classified into two categories: top-down and bottom-up approaches (Tour et al., 2013). The most commonly use top-down and bottom-up methods to grow graphene are by chemical oxidation of graphite flakes and chemical vapour deposition technique, respectively.

The chemical oxidation of graphite flakes weakens the van der Waals forces of graphite by introducing oxygen functional groups thereby promoting a complete exfoliation of graphene oxide (GO) sheets in aqueous media (Ming et al., 2010). The GO solutions could be obtained in a large quantity from a single preparation process. However, the presence of oxygen functional groups on the graphene sheets significantly reduces electron mobility. The removal of these functional groups to restore its conductivity is a challenging task to be explored and is referred to as the reduction process. Reduction of graphene oxide by employing a hydrazine solution is the current and widely used reduction process (Wang et al., 2010). The major drawback of using hydrazine is the issue of its toxicity and potentially explosive nature (Ganguly et al., 2011). In addition, hydrazine reduction process always introduces nitrogen impurity (Pei et al., 2012). As compared to the reduction process by hydrazine, hydrogen plasma discharge offers a unique advantage because the reactions can occur at low temperature, high rate and result in high purity material (Lee et al., 2012).

As for the bottom-up approach, chemical vapour deposition (CVD) technique has been widely used. There are various types of CVD technique: thermal (T-CVD), plasma enhanced (PECVD) and catalytic (Cat-CVD) (Losurdo et al., 2011; Stojanović et al., 2012; Othman et al., 2015). Unlike top-down approach, fabrication of graphene nanocomposites by bottom-up approach is not reported much. Some reported works on the bottom-up approach of growing graphene usually involves the use of CVD technique (Xu et al., 2015; Zhang et al., 2015). The fabrication of graphene by Cat-CVD is not much explored (Wang et al., 2014). Reports on graphene fabricated by Cat-CVD techniques showed presence of high defect density despite of it being a popular industrial process and is already been exploited on a commercial scale by several companies for specific applications (Soler et al., 2013). However, this technique is still attractive in many ways, with the most important advantages being:

- (1) a faster temperature ramp, which holds great potential for the large-scale production and rapid manufacturing of graphene with higher energy efficiency (Piner et al., 2013).
- (2) The deposition of thin films utilizing catalytic cracking reaction in the vicinity of hot-wire/filament which is plasma-free may eliminates the disadvantages produced by energetic ion bombardment to the deposited graphene films (Schropp, 2009).
- (3) A rigid or flexible substrate can be used as it does not have a role in the decomposition process, and it has an excellent step coverage and uniformity, which is a good approach for large area and high-quality graphene (Hawaldar et al., 2012).
- (4) It is an easily scalable method and is already used commercially for specific applications in industry, which is good for realizing the mass production of graphene in the future (Hawaldar et al., 2012).

Graphene remains as an “experimental” material, since it is not yet mass-produced, it is costly and is also difficult to handle, but it is a very attractive candidate to be used in sensors. There is a great potential of graphene-based sensors especially in gas and pressure sensor industry due to its large surface to area ratio, unique electrical and mechanical properties as well as high sensitivity (Bogue, 2014). In the molecular sensing context, for example by detecting extremely low concentration (parts per millions or parts per billions range) of hazardous gases, graphene has shown its potential to yield a high-sensitivity sensors (Schedin et al., 2007). Target gases such as nitrogen dioxide, ammonia, oxygen, carbon monoxide and hydrogen have been extensively studied (Lu et al., 2009; Wu et al., 2010). However, graphene has not been tested much in gas sensors for detecting a colourless, odourless, and tasteless gas carbon dioxide (CO₂) (Yoon et al., 2011). Measuring CO₂ is important in monitoring indoor air quality, the function of the lungs in the form of a capnograph device, and many industrial processes. Therefore, a study on sensing mechanism from the interaction of CO₂ gas molecule with graphene is needed.

In the pressure sensing context, several kinds of graphene-based pressure sensor had been reported in literature by implementing the piezoresistive effect of graphene (Kim et al., 2011; Smith et al., 2013). Although a number of studies have already been published, the piezoresistive effect of graphene is not completely understood yet. Recently, scientists from the Delft University of Technology have reported the use of the piezoresistive effect in graphene (Zhu et al., 2013). The sensor exhibited a gauge factor of approximately 1.6 and operated in a wide range of 0-70 kPa. Although the sensing range is wide, the gauge factor of fabricated pressure sensor shows small gauge factor which hindered the usage of graphene material in pressure sensor technology. In addition, the fabricated pressure sensor is based on rigid silicon substrate which is not flexible, more fragile and relies on high-cost silicon fabrication processes (Yao et al., 2013). Flexibility, highly sensitive and low-cost pressure sensors are highly desirable because of potential applications in structural health monitoring and medicine, which require sensors to be placed in intimate contact with non-planar and curved surfaces (for example human skins). Huge challenges remain in tactile sensing simulation of the human skin characteristics with high resolution, high sensitivity, and rapid response. Continuity in the progress of research in this area is promising for the development of a fully integrated electronic skin in the near future.

1.5 Research Objectives

Graphene has attracted huge interest from the research community in terms of its fabrication technique (Ferrari et al., 2015). In addition, the discovery of new phenomena or mechanism in graphene may pave the way for sensors with novel capabilities. Therefore, its unique properties have been exploited in various prototypes of sensors (Novoselov et al., 2005). Graphene-based sensors are rapidly emerging and exhibit encouraging characteristics which suggest a huge potential to be commercialized in the near future. Therefore, this work will be focuses on the fabrication of graphene and its potential application.

The objectives of the research work can be summarized as follow:

- 1) To explore the possibility of using hydrogen plasma treatment to reduce graphene oxide for gas sensor applications.
- 2) To develop a novel technique using hot-filament thermal chemical vapour deposition (HFTCVD) to grow graphene and graphene/copper oxide nanocomposites.
- 3) To develop a growth mechanism for graphene and graphene/copper oxide nanocomposites by HFTCVD technique.
- 4) To explore the use of fabricated graphene/copper oxide nanocomposites for pressure sensor application.
- 5) To propose a sensing mechanism of graphene and graphene/copper oxide nanocomposites for flexible pressure sensor applications.

1.6 Outline of Thesis

The thesis is divided into seven chapters. Chapter 1 introduces the work done in this thesis highlighting the research problems and objectives of this work. Chapter 2 presents the literature review related to the work done. This chapter presents a simple review which could be broken into four major parts. The first part gives a brief discussion on commonly employed fabrication technique of graphene involving the top-down and bottom-up approaches. For each technique, examples of deposition set up from various references are shown. It is from these examples and review that the catalytic chemical vapour deposition (Cat-CVD) is chosen and a few important deposition parameters are highlighted. The second part discusses briefly on the graphene transfer processes which are necessary for CVD grown graphene on Cu foils samples. The third part presents briefly the background of graphene application as a gas sensor. The selection of carbon dioxide gas as target molecule detection is also reviewed. The final part discusses the background of graphene-based application in flexible pressure sensors technology and its challenges. Key performance criteria of sensor devices are reviewed covering several types of graphene-based pressure sensors. The piezoresistive effects which act as transduction mechanism in graphene-based pressure sensors are also reviewed.

Chapter 3 presents the experimental and details of characterization techniques used in this work. The first part explained the necessary modification of PECVD technique into hot-filament thermal CVD (HFTCVD) to overcome the limitations of the PECVD technique. It is followed by a description on the sample preparation, deposition process and the parameters used in this work are also presented. A short overview of the graphene transfer procedure using thermal release tape (TRT) and poly(methyl methacrylate) (PMMA) that is used for characterization and application purposes are described. The second part briefly explains the step by step process of fabricating the

interdigitated Electrode (IDE) on flexible polyimide substrate for pressure sensor application. The third part covers the various characterization techniques used to evaluate the properties of the grown samples. The final part gives the overview of pressure sensor measurement system setup and its operations to investigate the graphene-based pressure sensor performance criteria.

The experimental results and discussion are presented in three chapters. Chapter 4 presents the preliminary work done on this project involving synthesis of graphene using a top-down approach and its potential application as a gas sensor. The chapter begins with a description on the synthesis of graphene oxide by Simplified Hummers method followed by description on the reduction process of graphene oxide by hydrogen plasma treatment. These sections also include results and discussion on the structural, elemental composition, and morphology and topological properties of each sample. The reduction mechanism by hydrogen plasma treatment is then proposed. Next, results and discussions on the performance tests results on the use of graphene oxide and selected reduced graphene oxide in gas sensor devices are presented. The gas sensing mechanism involved to explain the observed results is proposed.

Chapter 5 presents graphene fabrication using a bottom-up approach, which is the main scope of the work covered in this thesis. The chapter begins with the presentation of the results obtained from the graphene grown on copper foil using a novel hot-filament thermal chemical vapour deposition (HFTCVD) technique. The effects of deposition time and hydrogen flow rate on the morphology and structure of graphene are investigated by Raman spectroscopy, HRTEM, LEEM, XPS and FESEM. For the second part, analyses on these results are then used to explain the growth of high-quality graphene. The proposed growth mechanism of graphene used this technique is next presented. The results and analysis done on the effects of

graphene transfer processes using thermal release tape (TRT) and the poly(methyl methacrylate) (PMMA) support method are also presented in this chapter.

Chapter 6 presents one-step graphene/copper oxide nanocomposites fabrication using HFTCVD technique based on the understanding of growth mechanism discussed in previous chapter. The graphene application as a highly sensitive pressure sensor is also presented. The first part of this chapter presents the results and discussions on graphene/copper oxide nanocomposites grown using the novel one-step process referred to as the hot-filament thermal chemical vapour deposition (HFTCVD) technique. The effects of growth temperatures studied with respect to structural, morphological and electrical properties are presented next. The use of the controllable defect density, decorated nanoparticles density and overlapping graphene region material grown by this technique a high-sensitivity pressure sensor is then presented. The second part begins with the discussion on the fabrication of graphene-based flexible pressure sensor device and the results of the tests involving the stability, sensing range and sensitivity, repeatability, limit of detection, response time and gauge factor are presented. A sensing mechanism is then proposed to provide a better understanding of the use of graphene/Cu₂O nanocomposites in highly sensitive piezoresistive graphene-based flexible pressure sensors. Finally, performance of graphene-based pressure sensors reported in literature are discussed and compared to the performance of the graphene/CuO₂ nanocomposite gas sensor in this work.

This thesis is concluded in Chapter 7 which presents a general conclusion on this work highlighting important results obtained. Also, suggestions for future works related to improvement and extension of the work already done on graphene/CuO₂ nanocomposites and its applications as sensitive as flexible pressure sensors are proposed.

CHAPTER 2: LITERATURE REVIEW

2.1 Overview

Graphene is an emerging 2-D carbon nanostructure which composed of sp^2 hybridized carbon atoms arranged in hexagonal lattice has a wide range of applications for graphene and graphene-based materials due to its unique properties. Many efforts have been devoted to develop diverse approaches to fabricate graphene either by top-down or bottom up approach. For each technique, examples of deposition setups from various references are shown. It is from these examples and review that the catalytic chemical vapour deposition (Cat-CVD) is chosen and a few important deposition parameters are highlighted. Furthermore, two commonly used graphene transfer process of sample fabricated using CVD technique will be reviewed. Next, this chapter also reviewed the background of a gas and pressure sensor technology. The background of graphene-based material in detection of carbon dioxide gas as target molecule is also reviewed. This followed by the background review of graphene-based material in flexible pressure sensors technology, its challenges and key performance criteria of sensor device. The piezoresistive effects which act as transduction mechanism in graphene-based pressure sensors are also reviewed.

2.2 Unique Properties of Graphene

Graphene, a two-dimensional (2D) carbon material consisting of hexagonally packed carbon atoms bonded by sp^2 bonds is shown in **Fig. 2.1(a)**. In an ideal graphene sheet the π and π^* bands disperse linearly $E(\Delta k) = \hbar v_F \Delta k$, where v_F is the Fermi velocity and Δk is the momentum relative to the K points of the hexagonal reciprocal unit cell (Sprinkle et al., 2009). For single layer graphene the Fermi energy, E_F coincides with Dirac point, E_D so that the Fermi surface consists of six points **Fig. 2.1(b)**. The cone and intersection point of the cone are known as the Dirac cone and E_D , respectively. As a consequence of these features, the electrons in graphene behave as massless Dirac fermions (Norimatsu et al., 2014). Immense efforts have been focused on potential applications of graphene in optoelectronics, flexible electronics, transparent conducting electrodes, and sensors due to its unique properties (Zhu et al., 2010; Ferrari et al., 2015). These can be made possible through the exceptional properties of graphene, such as its high optical transmittance (of over 90%), high electron mobility at room temperature ($\sim 250\,000\text{ cm}^2/\text{Vs}$), very large surface area of $2630\text{ m}^2/\text{g}$ and high elastic stiffness of 340 N/m with a stretchability of up to 20% (Novoselov et al., 2004; Ferrari et al., 2015).

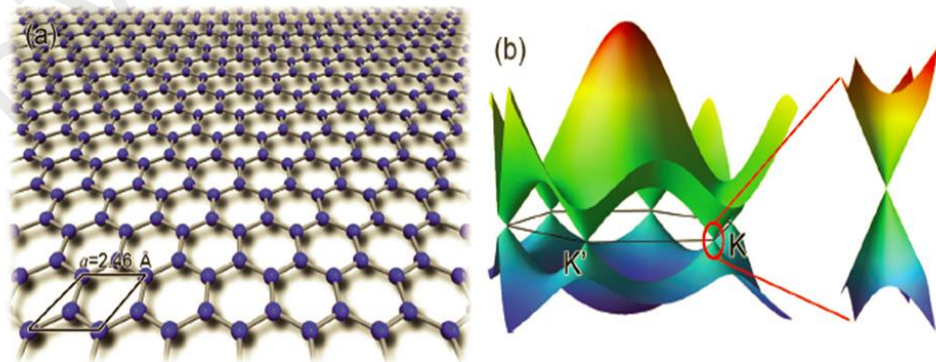


Figure 2.1: Crystal structure of graphene and its electronic band structure. (a) Graphene has a honeycomb structure with a lattice constant of 2.46 \AA . The inset is the unit cell. (b) Band structure of graphene with conduction and valence bands meet at the Dirac points. The E_D is six locations in momentum space, on the edge of the Brillouin zone, divided into two non-equivalent sets of three points. The two sets are labelled K and K'. (Sprinkle et al., 2009).

2.3 Review on Graphene Fabrication Techniques

The preparation methods of graphene can be classified into two categories: top-down and bottom-up methods (Tour et al., 2013). The strategy of top-down methods is to cut down large graphene sheets, carbon nanotubes, carbon fibres or graphite into small pieces of graphene sheet, while in the bottom-up methods, small molecules are used as starting materials to build the graphene layer. For top-down approaches, mechanical cleavage technique (Yi et al., 2015) and acidic oxidation of graphite and followed up by reduction process (Ming et al., 2010; Pei et al., 2012) methods have been used to obtain graphene. As for the bottom-up techniques, graphene can be fabricated using either chemical vapour deposition (Mattevi et al., 2011) or epitaxial growth on silicon carbide (SiC) wafer (Kusunoki et al., 2015).

2.3.1 Top-down Method

2.3.1.1 Mechanical Cleavage

Researchers have used mechanical exfoliation of layered compounds to produce thin samples for some time. In 1999, Ruoff's group presented one such approach for graphite by using an atomic force microscope (AFM) tip to manipulate highly oriented pyrolytic graphite, HOPG (Lu et al., 1999). The thinnest slabs observed at that time were more than 200 nm thick or the equivalent of ~600 layers as shown in **Fig. 2.2(a)**. Later, Kim's group improved the method, which successively obtained slabs as thin as 10 nm or the equivalent of ~30 layers (Zhang et al., 2004). While these elegant methods produced thin samples, it is ultimately a much simpler approach that led to the first isolation of single layer graphene in 2004 by Geim's group, (Novoselov et al., 2004). This method utilizes common cellophane tape to successively remove layers from a graphite flake until multi-layer graphene is obtained as shown in **Fig. 2.2(b)**. Despite tremendous progress with alternatives approach to fabricate

graphene, mechanical exfoliation method with the use of cellophane tape only, still produces the highest quality graphene flakes available to date. The major drawback of this method is it produces a very low yield with a high inconsistency in number of exfoliated graphene layers.

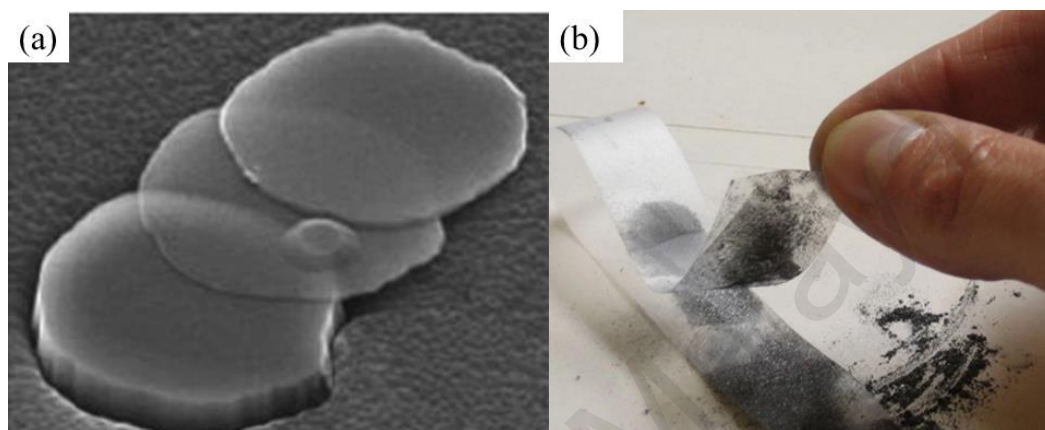


Figure 2.2: (a) FESEM images of mechanical exfoliation using HOPG with peeled away layer ranged between 30-600 graphene stacked using an AFM tip (Zhang et al., 2004). (b) Graphene is detached from a graphite crystal using adhesive tape. After peeling off the graphite, multiple-layer graphene remains on the tape. By repeated peeling the multiple-layer graphene is cleaved into various flakes of few-layer graphene (Novoselov et al., 2004).

2.3.1.2 Chemical Method

Graphene can be synthesized from graphite by introducing intercalating agents that are able to reside between the graphene layers under specific chemical reactions (Chung et al., 2002). This was done by the insertion of additional chemical species between the basal planes of graphite layers. Viculis et al. (2005), has successfully formed the first graphite intercalation compound (GIC) using potassium. The interlayer spacing of GIC would increase from 0.34 nm to more than 1 nm depending on the intercalant, leading to a significant reduction in the van der Waals forces between adjacent sheets (Chung et al., 2002).

Simplified Hummer's method was employed to weaken the van der Waals forces of graphite by introducing oxygen functional groups thereby promoting complete exfoliation of graphene oxide (GO) sheets in aqueous media (Ming et al., 2010). **Fig. 2.3** shows the process involved in the exfoliation of graphite oxide into individual GO sheets. However, the presence of oxygen functional groups on the graphene sheets reduces electron mobility typically becoming an insulator and thus removal of these functional groups to restore its conductivity is a challenging task. To restore the inherent electrical conductivity of graphene, GO should be reduced either in hydrazine solution or hydrogen plasma after films are formed on a substrate (Stankovich et al., 2007; Hafiz et al., 2013). After reduction process, the graphene layer is known as reduced graphene oxide (rGO). It should be noted, however, that hydrazine is highly toxic and potentially explosive, thus a great caution should be exercised when using it. Finally, the weak van der Waals forces make the GIC and GO much easier to be further exfoliated, offering a possible route to fabricate single layer graphene.

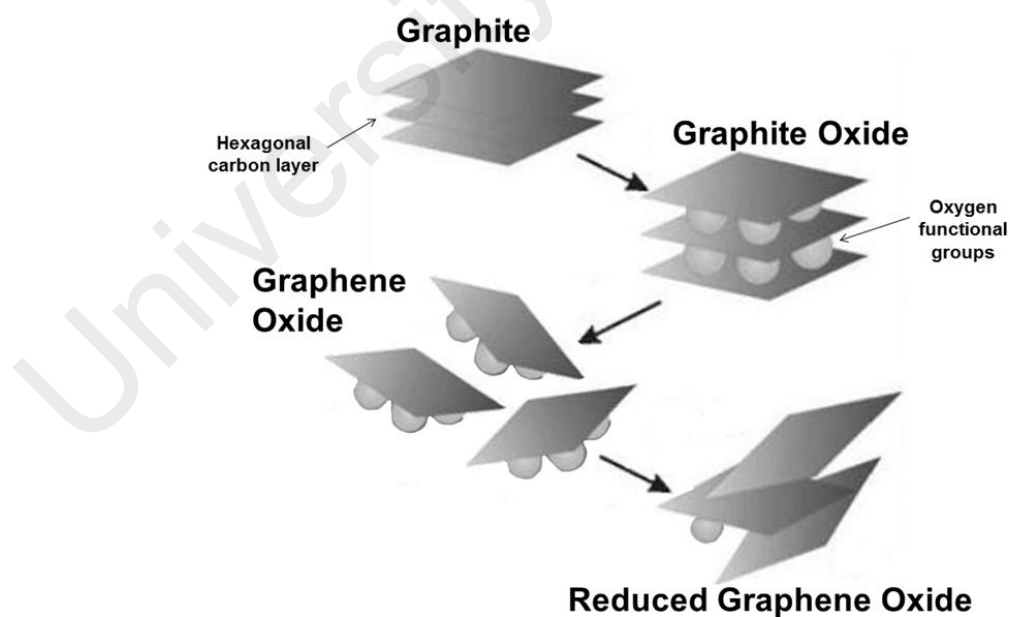


Figure 2.3: Chemical oxidation method to obtain monolayer graphene oxide followed up by reduction process to remove back the oxygen functional group attached to the basal and edges of graphene layer.

2.3.2 Bottom-up Method

2.3.2.1 Epitaxial Growth

The CVD epitaxial growth of graphene on SiC provides a wafer-scale graphene growth, which is appropriate for industrial applications (Wang et al., 2016). The growth of graphene on SiC is transfer-free and it is favourable for device applications. The growth mechanism of graphene on SiC is illustrated in **Fig. 2.4**. In this technique, the SiC is heated to a high temperature above 1000 – 1600 °C in a vacuum or in an argon atmosphere condition (Hibino et al., 2010). At this temperature, the Si atoms desorb from the surface due to the difference in the vapour pressures of Si and C. The remaining C atoms form epitaxial graphene spontaneously on the surface.

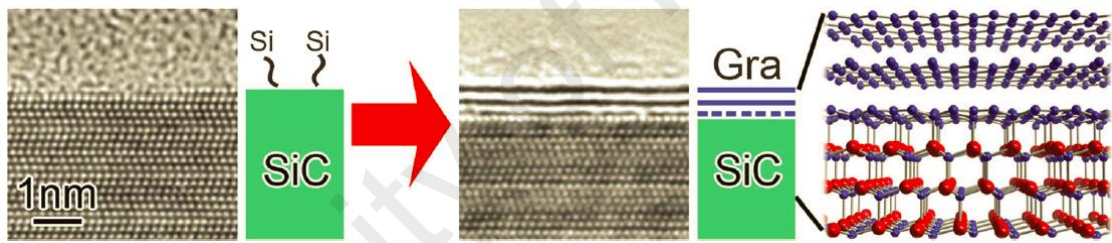


Figure 2.4: Epitaxial growth of graphene on silicon carbide substrate by thermal decomposition process. A structural model of bilayer graphene and buffer layer grown on silicon carbide, as indicated by the blue lines and broken line, respectively (Norimatsu et al., 2014).

The decomposition of SiC surface can result in the growth of large area wafer scale, high-quality and homogeneous graphene with controlled number of layers directly on the semi-insulating substrate (Wang et al., 2016). Furthermore, graphene grown on SiC substrate which is wide band gap semiconductor is certainly very suitable for many optoelectronic applications (Kusunoki et al., 2015). One of the advantages of this technique is that the crystalline structure of graphene on SiC is epitaxially related to the SiC substrate and this makes production of large single-crystal graphene substrate

possible (Norimatsu et al., 2014). However, the major concern in using this technique for graphene growth is the high temperature process and the high cost of the epitaxial SiC wafer.

2.3.2.2 Chemical Vapour Deposition (CVD)

Catalytic decomposition of hydrocarbons on transition metals by using chemical vapour deposition (CVD) technique has been widely used to obtain a large and uniform area synthesis of high quality graphene. CVD growth techniques are widely employed to grow graphene due to their high compatibility with the current complementary metal–oxide–semiconductor (CMOS) technology. There are various types of CVD processes: thermal (T-CVD), plasma enhanced (PECVD), catalytic (Cat-CVD) and many more (Losurdo et al., 2011; Stojanović et al., 2012; Othman et al., 2015). The type of CVD process to be employed depends on the production cost, the graphene quality, the thickness, and the structure needed.

Transition metals such as, Nickel (Ni), copper (Cu), ruthenium (Ru) and gold (Au) have been used as metal substrate but the most common is Cu (Mattevi et al., 2011). In general, the formation of graphene by CVD technique was carried out by introducing carbon sources such as methane (CH_4) diluted with hydrogen (H_2) to be dissociated at high temperature of 900 – 1000 °C or by plasma means (Mattevi et al., 2011). The carbon sources will then decompose to produce active carbon species to be deposited as graphene layer. **Fig. 2.5** shows a typical T-CVD growth process performed on polycrystalline Cu foil.

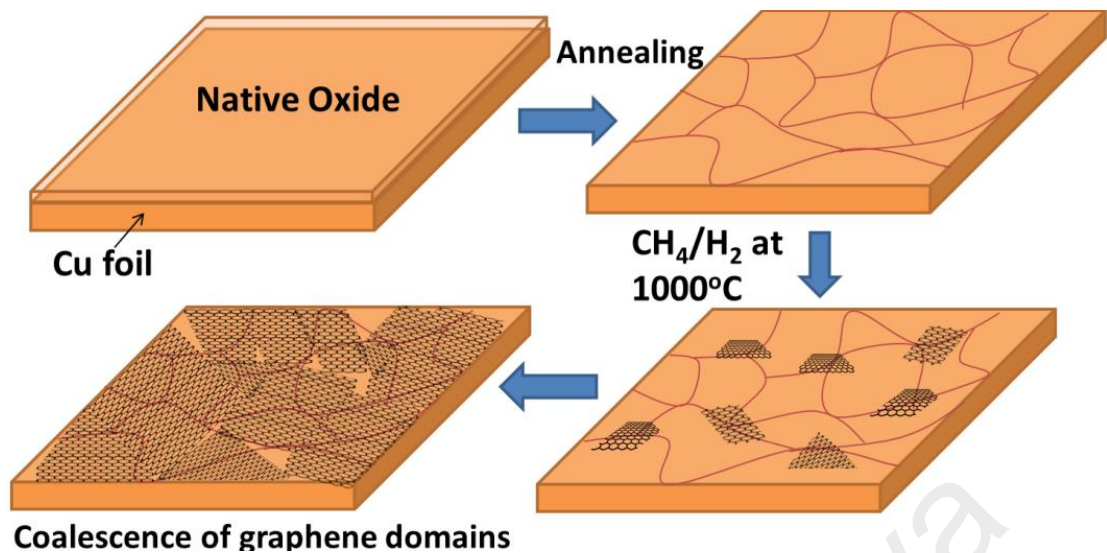


Figure 2.5: A typical graphene growth process by thermal chemical vapour deposition (T-CVD) method (Mattevi et al., 2011).

In 2011, Li et al. (2011a) have successfully fabricated graphene at much low temperature down to 300 °C with excellent quality by using benzene as hydrocarbon source. Despite being able to grow graphene at low temperature, the hydrocarbon source is not environmental friendly. Later, Ruoff's group first reported the growth of high-quality monolayer graphene on the (111) dominant crystal orientation of copper foils at temperature of <900 °C, which attracted great attention due to the advantages of good control of graphene layers, low cost, and ability to transfer (Tao et al., 2012). In 2015, the growth of graphene at temperature of ~400 °C has been successfully demonstrated by Othman et al., using a PECVD technique (Othman et al., 2015). However, the quality of the fabricated graphene was significantly reduced. The creation of plasma of precursor reaction allows deposition at lower temperature with respect to T-CVD. However, since plasma can damage the growing graphene, one needs to design the equipment and select deposition parameters that minimize this damage.

Recently, Hawaldar et al. (2012) have reported the formation of large-area monolayer graphene using Cat-CVD technique. The fabrication was done by using a

heated tantalum filament (Ta) at ~ 1800 °C with a slightly modified version of HFCVD system, namely, a hot-filament thermal chemical vapour deposition (HFTCVD) technique. They found that placing the copper substrate inside the alumina tube would create a gradient in the gas flow and composition and exclude the probability of any nucleation site on Cu, which led to a different graphene growth mechanism compared to the normal HFCVD technique reported by Stojanović et al. (2012). The graphene can be grown directly on SiO_2/Si substrate by this technique which avoids the transfer process that can deteriorate the graphene quality.

2.4 Review on Growth Parameter using CVD Technique

2.4.1 Controllable Growth by Hydrogen Dilution

Controlling the hydrogen in the hydrocarbon precursors has recently been recognized to play a critical role in controlling the size and morphology of graphene (Vlassiuk et al., 2011). **Fig 2.6** shows the effect of hydrogen partial pressure on growth of graphene islands. At low hydrogen partial pressure, the growth of graphene island is dominant (large size) with irregular shape, while at high hydrogen partial pressure, the growth is restricted (small size) with hexagonal shape. This could be explained by the role of hydrogen that acts as an etching agent in the catalytic graphene formation by a copper substrate (Losurdo et al., 2011). In addition, Zhang et al. (2011) has studied the thermodynamics of graphene growth on Cu surfaces and found that carbon atoms are thermodynamically unfavourable on a Cu surface under typical experimental conditions. A possible explanation is that small carbon-containing species are not stable without hydrogen and only when they grow to a certain size they become stable without hydrogen which further aromatizes to the benzene ring on the Cu surface sites (Losurdo et al., 2011).

The hydrogen mixture with hydrocarbon gas can have the following roles:

- (1) a graphene growth promoter by activating a physisorbed surface bound radical $(CH_x)_s$ on the copper substrate, which leads to the agglomeration into multimeric $(C_nH_y)_s$ species and finally forms a hydrogen-free carbon cluster that is thermodynamically favorable compared to the dehydrogenation process of hydrocarbon on Cu; (2) As a graphene growth inhibitor it restricts the growth through selective etching of weakly structured carbon such as the armchair edges of graphene and amorphous carbon from the reactive hydrogen radical $(H^* + \text{graphene} \rightleftharpoons (\text{graphene} + C) + H_2)$ or it limits the hydrocarbon precursor decomposition when excess hydrogen is present in the system $(CH_4 \rightleftharpoons C^* + 2H_2)$. (Celebi et al., 2013).

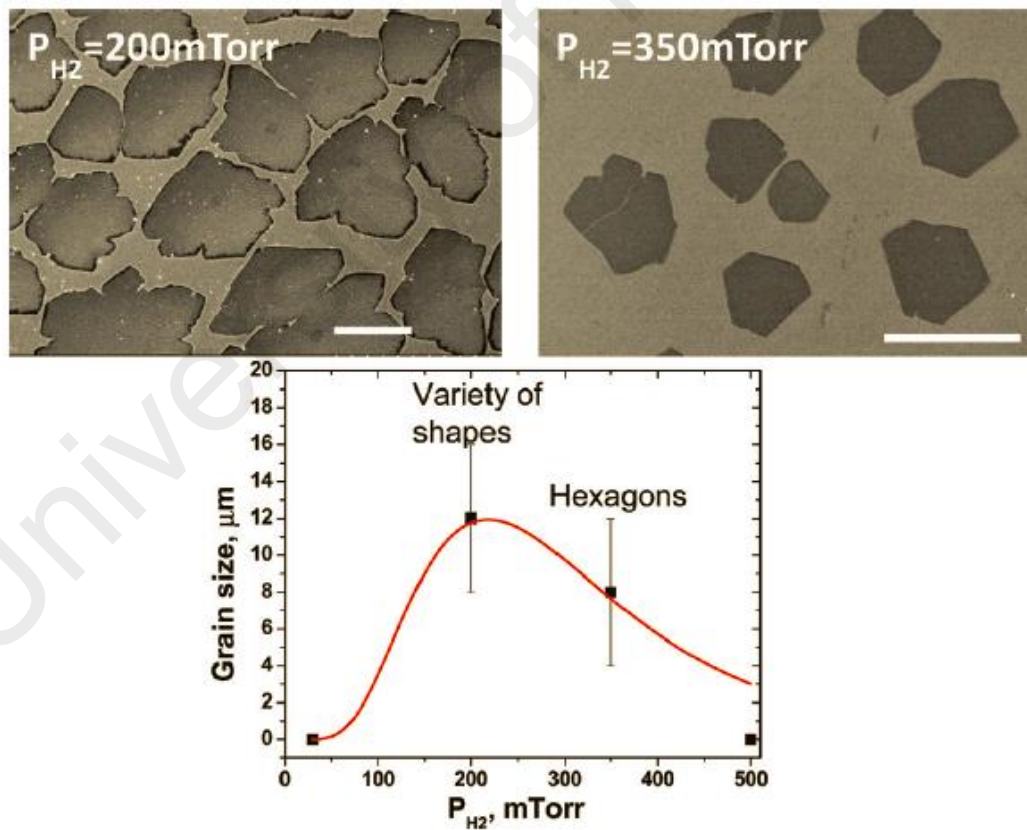


Figure 2.6: (Up) Graphene islands fabricated by CVD technique at 1000 °C on Cu foil using 1 mTorr of methane and different partial pressures of hydrogen. (Bottom) The average size of graphene grains is shown as a function of partial pressure of hydrogen. Note that the hexagon-like shape of graphene islands is observed only at the higher hydrogen pressures. Scale bars are 10 μm (Vlassiuk et al., 2011).

2.4.2 Growth Temperature

The growth temperature of graphene plays an important role in determining the defect density present in graphene structure as well as the nucleation sites on Cu foil. Studies of graphene by CVD technique on Cu have thus far suggested that effects of surface kinetic factors of precursor's gases at specific growth temperature are associated with adsorption, diffusion, dissociation, dehydrogenation, and lattice-attachment steps that will determine the graphene defect density (Li et al., 2009c; Bhaviripudi et al., 2010). Later, thermodynamics of graphene growth has been performed by Zhang et al. (2011) and they found a favourable reaction path of hydrocarbon precursors on Cu surface which can enhance the quality of grown graphene.

The graphene nucleation density is found to be inversely proportional to the growth temperature as shown in **Fig. 2.7**. With an increase of growth temperature, a faster graphene growth rate would occur due to the thermal enhancement of the catalytic reactions (Bhaviripudi et al., 2010). Later, Kim et al. have identified a competing atomic phenomena such as adatom mobility versus desorption which defines the characteristic of nucleation regimes with very different activation energies depending on the growth temperature (Kim et al., 2012). In addition, Celebi et al. (2013) have deduced that the amount of copper sublimation could extend the incubation period of the growth which happened at higher growth temperature, as it can induce carbon reactant desorption and delay the growth until the flakes enlarge.

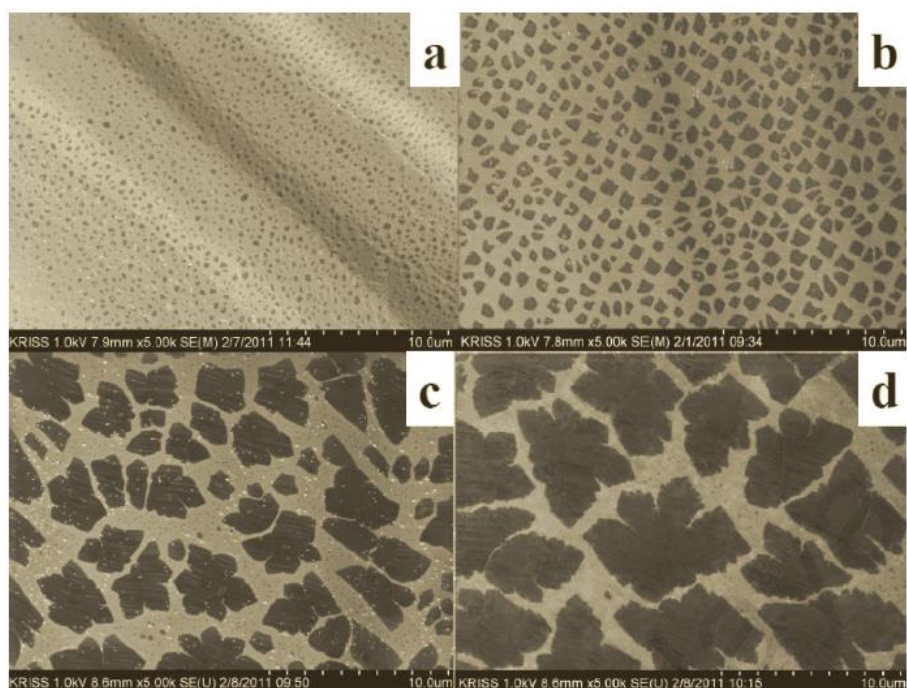


Figure 2.7: FESEM images of graphene growth on Cu foils depending on the growth temperature at (a) 940, (b) 980, (c) 1000, and (d) 1030 °C. (Hwang et al., 2011)

2.4.3 Seeded Growth

Morphology of Cu surface such as roughness, grain boundary, defects, and impurity particles plays a crucial role for forming nucleation seeds of graphene growth (Han et al., 2011). The growth of graphene happened by topochemical reaction which acts as dehydrogenation sites of carbon precursor on copper to produce the active carbon reactants that attach to the edge of the growing graphene lattice (Celebi et al., 2013). However, additional topochemical reaction sites may be introduced from impurity (i.e. nanoparticle) which promotes the growth of consecutive graphene layer (Kasap et al., 2015). **Fig. 2.8** shows a schematic representation of the silicon oxide nanoparticle impurity mediated growth kinetics of multilayer graphene on the copper surface performed by Kasap et al. (2015). The gas pressure was precisely controlled such that the mean free path and the average distance between the activation sites are comparable, to favour the formation of multi-layer graphene at nanoparticle impurity sites. The seeded growth leads to the formation of polycrystalline graphene

which can be manipulated by temperature, hydrogen composition and pressure (Celebi et al., 2013; Gan et al., 2013; Kasap et al., 2015).

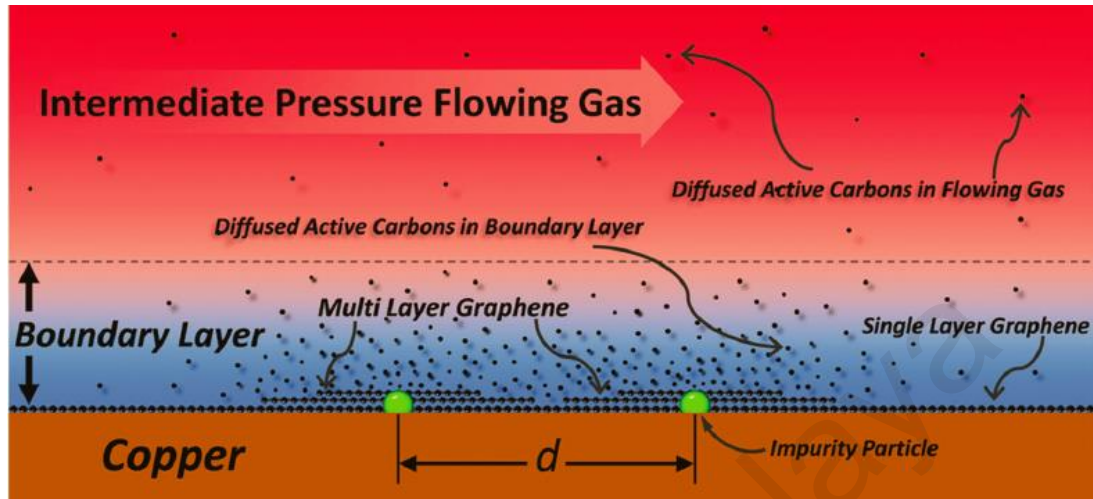


Figure 2.8: Schematic representation of the silicon oxide impurity mediated growth kinetics of multilayer graphene on the copper surface (Kasap et al., 2015).

2.4.4 Vapour Trapping Growth

In 2011, a large-domain graphene growth was observed on the inside of a copper-foil enclosure at high temperature of $\sim 1035^\circ\text{C}$ which enhanced the electrical conductivity of graphene (Li et al., 2011b). The copper-foil enclosure provided an “improved” environment during growth; that is, the Cu vapour is in static equilibrium which then produces a low density of nucleation sites. The role of vapour trapping was then demonstrated by Zhang et al. (2012) and R ummeli et al. (2013), who highlighted the importance of the local environment growth condition, which can lead to a controllable graphene defect density and homogenous growth. This is because of the vapour trapping capability for the Cu species leading to a higher carbon concentration, which then improved the decomposition of hydrocarbon (CH_4) gas. Later, Lin et al. (2015) demonstrated an additional gas phase reaction of atomic carbon dehydrogenation which will be mediated by Cu vapour, in comparison to the gas phase reaction mechanisms at Cu surface (i.e. dehydrogenation, hydrogenation, and radical

coupling on bulk Cu surface) as shown in **Fig. 2.9**. Furthermore, they experimentally showed that the quantity of ambient Cu vapour is the key factor in graphene synthesis, which influences the dropwise condensation for airborne Cu clusters during growth which appear as nanoparticles.

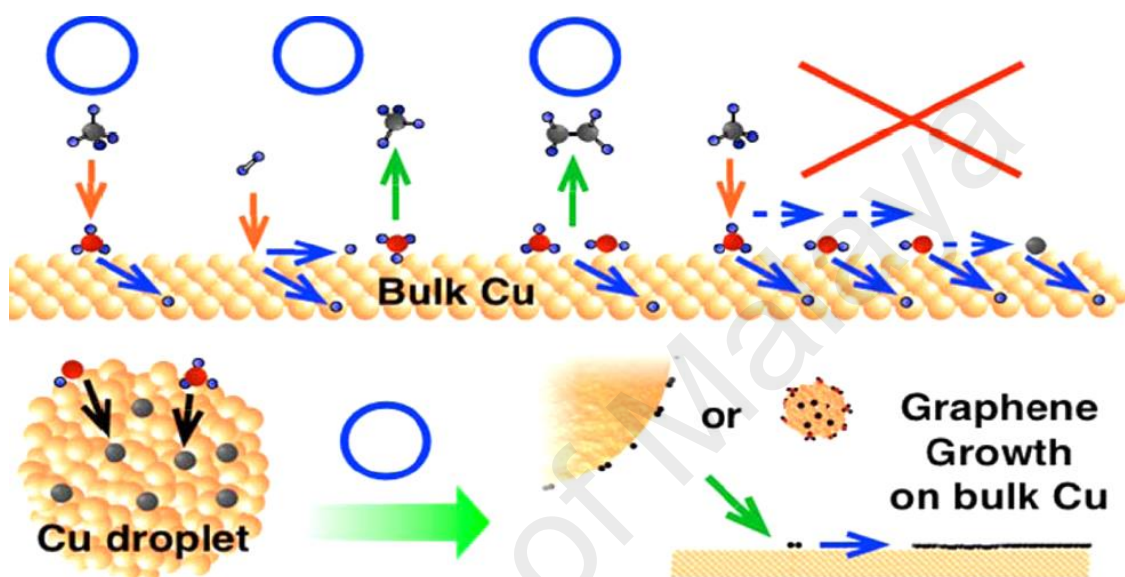


Figure 2.9: (Up) Schematic drawings of favourable gas phase surface reaction mechanisms of methane precursor for dehydrogenation, hydrogenation, and radical coupling on bulk Cu surface. (Bottom) Additional gas phase reaction of atomic carbon dehydrogenation mediated by Cu vapour, which will be redeposited on Cu surface and completes the graphene growth (Lin et al., 2015).

2.5 Review on Graphene Transfer Process

2.5.1 Common Transfer Process

The transfer of graphene grown Cu substrate onto arbitrary substrates is pivotal for characterization and application purposes. The ideal approach is to directly grow it where needed, for example direct growth on SiO₂ substrate. However, to date, the growth process is still far from this goal, especially in the case of non-metallic substrates. The development of a transfer procedure is thus needed.

Wet transfer process by polymer-supported metal etching is often used in graphene transfer technology. In 2008, Reina et al. (2008) first reported the wet transfer process of graphene layers grown by precipitation on rigid Ni substrate, by depositing poly(methyl methacrylate), PMMA support layer and subsequently etching the underlying Ni by an aqueous hydrochloric acid solution. Li et al. (2009b) has demonstrated graphene transfer process grown on Cu by etching using iron(III) nitrite with an introduction of another layer of PMMA on PMMA/Graphene. This improved process has proven to obtain a higher electrical conductivity and high optical transmittance that made them suitable for transparent conductive electrode applications. A typical graphene transfer grown on rigid substrate is shown in **Fig. 2.10**.

Later in 2009, Li and colleagues discovered and demonstrated a CVD graphene growth method which used centimetre-scale copper foil substrates opened a new route to large-scale production of high-quality graphene (Li et al., 2009a). Graphene growth is therefore no longer limited to the use of rigid substrates; instead, large flexible copper foils may be used. The flexibility of the copper foils further allows efficient etching and transfer processes using a time-effective roll-to-roll transfer method as shown in **Fig 2.11** (Bae et al., 2010). In this process, a thermal release tape (TRT) was attached to the graphene/Cu layers at graphene's side, and the Cu was then removed.

The TRT/graphene layers were then attached to a target substrate (e.g. PET) and the supporting TRT was removed by heating, thus releasing graphene onto the target substrate.

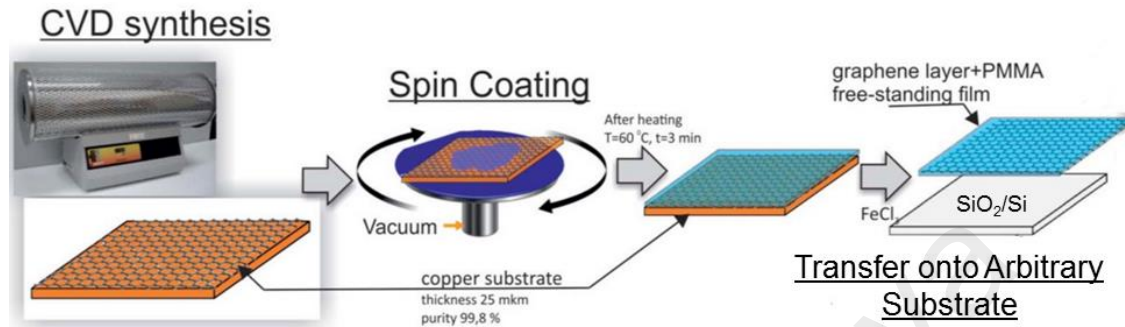


Figure 2.10: PMMA polymer-supported metal etching transfer process that is typically required for graphene fabricated using CVD technique on rigid substrate (Batrakov et al., 2014).

The transfer process usually caused cracks and rips onto the transferred graphene as a consequence of high residual stress during the peeling-off step of the TRT (Gorantla et al., 2014). To avoid mechanically defects caused by TRT transfer, a hot pressing process was developed by Kang et al. by placing the TRT/graphene/substrate between two hot metal plates with controlled temperature and pressure (Kang et al., 2012). This result in the detachment of the TRT with very low frictional stress produces fewer defects as compared to roll-to-roll transfer method. Despite the ease of transfer steps needed for TRT transfer process, this method also served as a fast and industrial scale friendly for graphene transfer.

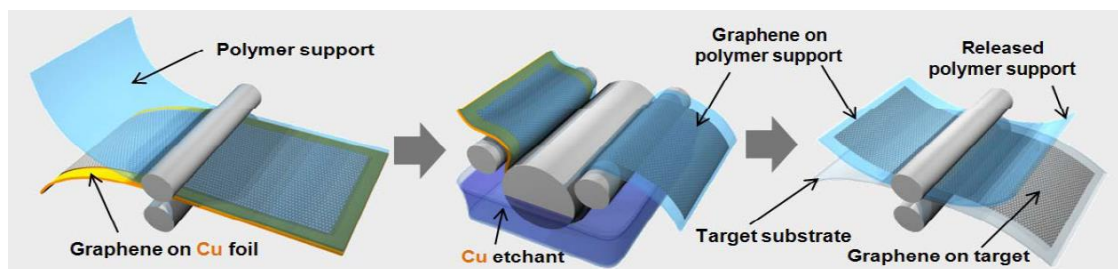


Figure 2.11: Schematic of the roll-based production of graphene films grown on a copper foil for industry scale production. The process includes adhesion of polymer supports, copper etching (rinsing) and dry transfer-printing on a target substrate (Bae et al., 2010).

Cleaning is particularly important when transferring graphene using PMMA polymer support since it may leave some polymer residue after the removal of its layer, as the processes typically involve sacrificial layers, to be chemically dissolved (Gorantla et al., 2014). The polymer residue on the surface of graphene grown on Cu can be compared from the graphene transferred onto SiO₂ by XPS characterization of C1s peak (Chan et al., 2012). The C1s peak was found to be broader than that of graphite and the original graphene on Cu. Thermal annealing in H₂/Ar at 200 - 400 °C is normally used to remove polymer residuals (Pirkle et al., 2011). The high temperature of thermal annealing might limit the type of substrate where the graphene has to be transferred. In contrast, the polymer residuals by chemical removal can be used instead, for example by acetone rinse or hot acetone vapour (at 55 °C) (Li et al., 2009b; Chen et al., 2011). Two methods of commonly transfer routes of graphene transfer have been briefly reviewed, however, these routes are substrate specific and each tends to have its own advantage and disadvantage.

2.6 Review on Gas Sensors Technology

In the last few years there has been an exponential increase in the number of published papers reported as gas sensor using nanomaterials (Llobet, 2013). There is a need for simple, sensitive and stable electronic sensors suited for gas detection in a wide spectrum of applications ranging from production line, health and medical, to environmental monitoring, as opposed to the often employed; expensive, bulky and complicated instrumental methods. Among the difference in nanomaterials, for example; metal oxide, conducting polymers, solid electrolyte and carbon-based materials in developing a gas sensor, carbon-based nanomaterials have attracted to a great deal of interest (Liu et al., 2012). Carbon-based materials with inherent nanoscale features have potential for becoming ideal components for the next generation sensor technology, since they combine excellent detection sensitivity with high capability of surface engineering properties (Llobet, 2013).

Nano-sized carbon structures have most of their atoms exposed to the environment which offer a high specific surface area that is an advantage for achieving high sensitivity (Llobet, 2013). Some carbon-based nanomaterials such as carbon nanotubes or graphene have high quality crystal lattices and show high carrier mobility (e.g. ballistic charge transport) and low signal to noise ratio (Jariwala et al., 2013). In addition, their low power demands make them good candidates for being operated remotely (Baughman et al., 2002). Moreover, the selectivity of carbon nanomaterials can be surface engineered by employing different techniques both to create defects and functional groups to their surface in a controlled way (Basu et al., 2012).

2.6.1 Graphene as a Potential Candidate for Gas Sensor Application

Graphene is a 2-D nanomaterials and every atom of graphene may be considered as a surface atom thus capable of interacting even with a single molecule of the target gas, which eventually results in the ultrasensitive sensor response. The electrical conductivity of graphene will be changed upon exposure to and subsequent adsorption of the target chemical species, owing to change in free electron concentration due to an increase or decrease concentration which depends on the target species that act as donor or acceptor (Leenaerts et al., 2008).

Interestingly, the level of interaction between target gas/vapour molecule may reach the lower limit of even a single molecule, i.e., the smallest quantum of resultant change in conduction could be measured in graphene (Schedin et al., 2006). Therefore, in principle, the dynamic range of detection of gas concentration level may cover from a single molecule to a very high concentration level, which is impossible with the conventionally materials used in 3D gas sensing devices. However, the problem with intrinsic graphene is that it has no dangling bonds on its surface which required for gas adsorption site and therefore to enhance the chemisorptions on graphene surface. Therefore, graphene needs to be functionalized with polymers, metals or other modifiers (Pumera et al., 2010). More importantly, the production of graphene uses graphite raw material or hydrocarbon gases, which is inexpensive and highly abundant (Yavari et al., 2012). These properties make graphene an ideal candidate for practical gas sensors for industrial, environmental, public safety and military applications.

2.6.2 Graphene-based Carbon Dioxide Gas Sensor

Carbon dioxide (CO₂) is a colourless, odourless, and tasteless gas. It is a product of completed carbon combustion and the by-product of biological respiration. The primary source of CO₂ in indoor environment (for example, buildings and laboratories) is from respiration of the indoor occupants (Erdmann et al., 2004). Normal outdoor air and indoor occupied space with good air exchange typically has a CO₂ level of 350 to 800 ppm. High CO₂ levels may indicate a problem with overcrowding or inadequate outdoor air ventilation rates. Adverse health effects from CO₂ may occur since it is an asphyxiant gas which can cause headache, fatigue, eye symptoms, nasal symptoms (sore throat) or respiratory tract symptoms (irritated nose/sinus). According to the American Society of Heating, Refrigerating and Air Conditioning Engineers (ASHRAE) Standard 62-1989, the CO₂ concentration in occupied buildings should not exceed 1000 ppm (Erdmann et al., 2004). While, Building bulletin 101 (Bb101), reported that for the United Kingdom, standards for schools say that CO₂ averaged over the whole day (i.e. 9 am to 3.30 pm) should not exceed 1500 ppm (Erdmann et al., 2004). Therefore, monitoring the levels of CO₂ in indoor air quality can prevent a significant impact on human health. Summary of relationship between CO₂ concentrations with indoor air quality can be seen in **Table 2.1**.

Table 2.1: Classification of indoor air quality with respect to CO₂ concentration.

CO ₂ [ppm]	Air Quality
2100	BAD Heavily contaminated indoor air Ventilation required
2000	
1900	
1800	
1700	
1600	
1500	MEDIOCRE Contaminated indoor air Ventilation recommended
1400	
1300	
1200	
1100	
1000	FAIR
900	
800	GOOD
700	
600	EXCELLENT
500	
400	

2.7 Review on Pressure Sensors Technology

Since a long time, pressure sensors technology have been widely used in fields like automotive, robotic, aviation and aerospace, oil and gas, health and medical measurements etc. Recently, the use of pressure sensor technology has entered a new field in industry including touch screen devices and sports area where the sensor has evolved to be thin and light, high sensitivity and flexible. A few prominent areas where the use of these pressure sensors is inevitable are shown on **Fig 2.12** and briefly explain below;

Touch screen devices: The computer devices, smart phones, home appliances and interactive displays have touch screen panel that come with pressure sensors. Whenever slight pressure is applied on the touch screen through a finger or the stylus, the sensor determines where it has been applied and accordingly generates an electric signal that informs the processor. The usage of this technology has significantly reduced the thickness and weight of the devices compared to the usage of push-button technology.

Automotive: In automotive industry, pressure sensors form an integral part of the engine and its safety. In the engine, these sensors monitor the oil pressure and regulate the power that the engine should deliver to achieve suitable speeds whenever the accelerator is pressed. For the purpose of safety, pressure sensors constitute in part of anti-lock braking system (ABS). This system adapts to the road condition and ensures that in case of braking at high speeds, the tires do not lock and the vehicle does not skid. Furthermore, an air bag system also uses pressure sensors so that the bags get activated when high amount of pressure is applied by the vehicle.

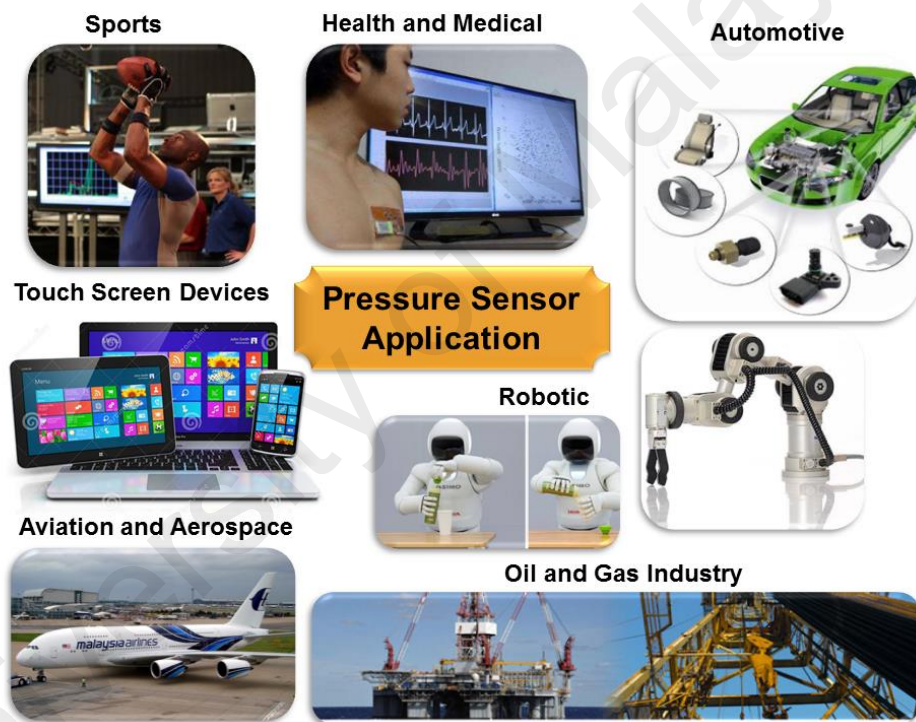


Figure 2.12: General applications of pressure sensor in various major industries.

Sports, health and medical: With an advanced of technology, the sports industry uses pressure sensor to study the performance and the protective gear wear by the athlete. In instruments like digital blood pressure monitors, pressure sensors are needed to monitoring the patient's health. Wearable and lightweight pressure sensing devices could be easily adapted by a patient who requires the sensors to be placed in intimate contact with non-planar and curved surfaces (for example human skins).

Oil and gas: Pressure sensors are used to monitor partial pressure gases in each industrial unit so that a large chemical reaction takes place in precisely controlled environmental conditions. Oil exploration process uses pressure sensor in terms of depth of drilling.

Aviation: In the airplanes, these sensors are needed to maintain a balance between the atmospheric pressure inside the airplanes cabin at higher altitude to provide nominal ground like breathing conditions. In case of emergency, the oxygen mask placed overhead of each passenger seat will drop to manipulate sudden decompression in the cabin environment.

Robotic: The pressure sensors are needed to make a sensitive skin for a robotic arm which could be manipulated for various programmable tasks. For example, the robot that is designed to be perceived the touch to handle object has been used in bomb disposal application, where the area is too dangerous to human life.

2.7.1 Graphene as a Potential Candidate for Pressure Sensor Application

Graphene has been popularly exhibited as a sensing material for sensor devices due to its excellent mechanical and electrical properties. Recently, pressure measurement has made a significance usage in the fields of aerospace engineering, automobile making, robot tactility, etc. (Chun et al., 2015a). In some engineering application, due to the complication of surface configuration and the smallness of interlayer spacing, the pressure sensor is required to be flexible and thin. In addition, the leading material used in pressure sensor device uses silicon. The drawbacks of silicon-based pressure sensor device are not flexible, fragile and rely on high-cost silicon fabrication processes. Flexible, highly sensitive and low-cost pressure sensors are highly desirable because of potential applications in structural

health monitoring and medicine, which require sensors to be placed in intimate contact with non-planar and curved surfaces (for example human skins) (Yao et al., 2013).

The use of graphene material as a potential candidate for pressure sensor measurement was realized in a recent study, where a flexible graphene nanosheets/polyurethane (PU) sponge pressure sensor was reported to be capable of measuring pressure in the low-pressure range of 0–10 kPa (Yao et al., 2013). The detection of high-rate bodily motion such as joint and muscle motion as well and breathing and pulse have been successfully demonstrated by Boland et al. (2014) using graphene-composite for health monitoring purposes. Moreover, a highly sensitive sensing capability for recognizing tactile information beyond the human sense range (<100 Pa) has been demonstrated by Chun's group (Chun et al., 2015b). A wide pressure range of 0-50 kPa with exceptional sensitivity has been obtained recently by laser-scribed graphene by Tian et al. (2015), which further widened the application of graphene in pressure measurement field.

2.7.2 Pressure Sensor Performances Criteria

The performance criteria of fabricated pressure sensor has been typically discussed about the sensitivity, limit of detection, sensing range, repeatability, stability, hysteresis and gauge factor (GF) to determine the quality of the sensor. Each criterion will be briefly reviewed as follows;

Sensitivity of the sensor is defined as the input of parameter change required to produce a standardized output change. In pressure sensor device, the input parameter is the applied pressure while the output will be observed as a change in electrical properties such as resistance or capacitance. The sensitivity pressure sensor could be increased by changing the structural of the sensing element (for example, increase the electrical percolation network) or design of the fabricated sensor (for example, complex

pressure-amplifying design), to manipulate the electrical properties of the fabricated sensor (Boland et al., 2014; Tian et al., 2015).

Limit of detection of the sensor is defined as the lowest input parameter to be applied to the sensor to give a measurable output change. The device is said to be high-sensitivity when a small amount of applied pressure is needed to give a significant change in the measured electrical property which determine by the limit of detection. For example, the highest limit of detection in recognizing a tactile information has been demonstrated by Chun's group by measuring beyond the human sense range (<100 Pa) (Chun et al., 2015b).

Stability of the sensor is defined as the changes that will exist between the actual value (which must be measured in a standard condition) and the indicated value at the output of the sensor from the effect of environmental factors such as temperature, humidity and noise. If the sensor is not stable from the changes of a specific environmental factor which could trigger a false measurement, it should be operated in a tight working condition.

Sensing range is defined as the maximum and minimum values of applied input parameter that can be measured. The sensing range of specific pressure sensor could be varied according to its working region of interest. The pressure required for object manipulation by robotic hand is between 10–100 kPa, which required a high pressure sensor to be able to work in this region. Chun et al. (2015a) has reported a pressure sensor that can operated in general human touch range of 1 to 10 kPa. In addition, some sensor could be measured in a range of perceptual processes of human touch by mechanoreceptors in the skin about 100 Pa–10 kPa (Chun et al., 2015b).

Repeatability of the sensor is defined as the ability of a sensor to reproduce output values when the same input value is applied repeatedly under normal operating conditions. Multi-cycle operation of repeated loading and unloading at different

pressures for a period of time could show the dynamic repeatability performance of the tested sensor. From the repeatability of the measured sensor, the response time of a specific sensing material which further gauges its ability to recover from the structural deformation within a period of time (typically in the range of milliseconds) could be obtained. The response time can be defined as the time required for a sensor output to change from its previous state to a final settled value within a tolerance band (typically ~10% of the minimum and maximum output value) of the correct new value.

Hysteresis of the sensor is defined as the difference in the output reading at an input pressure point when the pressure point is approached first with an increasing pressure (from zero) and then with the decreasing pressure from full sensing range. It is important to note that this criterion is important for flexible thin films pressure sensor as compared to rigid pressure sensor (Ashruf, 2002). The large hysteresis of flexible thin films pressure sensor is due to inheritance of the use of polymer material, which are required for their flexibility and elasticity properties. This might be in the form of composites with the sensing material or flexible support substrates which largely contribute to the hysteresis of the sensor compared to the sensing material itself.

Gauge Factor (GF) of the sensor is defined as the ratio of relative change in electrical resistance R , to the mechanical strain ε as shown in the Equation 2.1 (Yang et al., 2013);

$$GF = \frac{R/R_o}{\varepsilon} \quad (2.1)$$

The higher the gauge factor, the better the sensitivity of the pressure sensor which set as an important criterion for a direct comparison of the sensitivity between various pressure sensors. However, for single layer graphene the GF can be as low as

~6.1 for lateral strain or even less ($GF=2$) for a vertically-applied force (Chun et al., 2015a). This can be a disadvantage for sensors that are detecting and perceiving environmental signals on human skin, where pressing is more critical than stretching. Some attempts have been proposed to increase the sensitivity of force sensors using graphene by complex pressure-amplifying design or manipulate the electrical properties of the graphene structural properties (Li et al., 2012; Tian et al., 2015).

2.8 Types of Pressure Sensor

Pressure sensor can differ in technology, design, performance, application suitability, and cost. There are various types of pressure sensors which can be classified based on various transduction principles such as conductive rubber or composites, capacitive and piezoresistive to name a few. Conductive rubber or composites sensor is based on the changes of the contact resistance between the polymer matrixes (rubber) and conductive filler (sensing material) which is determined by the electrical percolation network. The sensitivity of the sensor could be altered by the amount of infused conductive filler. This type of sensor is capable to monitor the bodily motion sensors, such as monitoring joint and muscle motion as well as breathing and pulse where flexibility is important (Boland et al., 2014). However, due to the inheritance of the use of polymer material that is required for their flexibility and elasticity properties, this type of sensor exhibit a large hysteresis.

Capacitive sensors consist of a plate capacitor, in which the distance between the plates or electrode area is changed when compressed, and it has a suspended structure that can measure the change in the capacitance between these two electrodes. This type of sensor has been most widely used to recognize the tactile input due to its sensitivity. However, they would be inadequate for application to more complex three-dimensional surfaces such as artificial skin-like sensors (Woo et al., 2014).

Piezoresistive pressure sensors use the change of the electrical resistance in a material when it has been mechanically deformed by applied pressure. This type of sensor generally require less electronics as change in resistance can easily be quantified and are therefore easy to manufacture and integrate (Tiwana et al., 2012). In addition, it is also less susceptible to noise and therefore work well in mesh configurations as there is no cross talk or field interactions. However, the piezoresistive sensors suffer from hysteresis and therefore have a lower frequency response when compared to capacitive tactile sensors (Almassri et al., 2015). As a matter of fact, the pressure sensor design is primarily determined by the application requirements by considering the practicalities of its implementation. The relative merits and demerits for various types of pressure sensor are summarized in **Table 2.2**.

Table 2.2: Relative merits and demerits of various types pressure sensor.

Type of Pressure Sensor	Merit	Demerit
Conductive Rubber/Composites	(i) Physically flexible	(i) Mechanical hysteresis (ii) Nonlinear response
Capacitive	(i) Sensitive (ii) Low cost	(i) Hysteresis (ii) Complex electronics
Piezoresistive	(i) Low cost (ii) Good sensitivity (iii) Low noise (iv) Simple electronics	(i) Stiff and frail (ii) Nonlinear response (iii) Hysteresis (iv) Temperature sensitive

2.8.1 Piezoresistive Effect in Graphene-Based Material

The piezoresistive effect describes the change in material's electrical resistivity due to applied mechanical pressure or strain. It was first observed in metal material from the change in resistance with elongation of iron and copper (Thomson, 1856). Later, the term "piezoresistance" was introduced by Cookson, to define the change in conductivity with stress (Cookson, 1935). The resistance change effect was dominated by the geometry change in material. The electrical resistance, R of a physical material under steady and deformation state can be described by the following equation:

$$R = \rho \frac{l}{A} = \rho \frac{l}{(w)(h)} \quad (\text{Steady state}) \quad (2.2)$$

$$R = \rho \frac{\Delta l + l}{(\Delta w + w)(\Delta h + h)} \quad (\text{Deformation state}) \quad (2.3)$$

where ρ , l , A , w , and h is the resistivity, length, cross-section area, width and thickness of material. Later, it was then discovered that semiconductors material, for example silicon, exhibited a much greater piezoresistive effect compared to metals. The piezoresistive effect of silicon semiconductor appeared to be more significant in comparison to the geometry effect due to the presence of the wide energy band gap (~ 1.11 eV), in which the electronic properties can be tuned by the application of pressure (Barlian et al., 2009). This generates a significant interest in semiconductor for pressure sensing devices.

Recently, advance investigations on graphene film technology have been conducted by scientists to further enhance the pressure sensor sensitivity by modified the piezoresistive effect in graphene. A pioneering study by Pereira et al. (2009) proposed that the piezoresistive effect in graphene is related to the graphene lattice

distortion, which leads to a modified electronic band structure. It has been further demonstrated that the piezoresistive effect of graphene can be tuned by changing the density of graphene flakes, widening the tunnelling between graphene islands, or inducing a non-flat graphene ripple structure (Wang et al., 2009; Huang et al., 2011, Jing et al., 2013). By considering this morphological effect, it is therefore crucial to understand the piezoresistive mechanisms in graphene that can improve the sensitivity of a pressure sensor.

2.8.1.1 Structural Deformation

The piezoresistive effect in graphene could be increased by manipulating the structural deformation mechanism. Wang et al. (2011) has demonstrated the buckling graphene ribbons as a potential candidate for a flexible electronic materials under extreme stretching conditions. Prior to that, the flat graphene was transferred on a prestrained PDMS substrate as shown in **Fig. 2.13(a)**. After that, the strain was released and caused a significant deformation in graphene morphology in the form of wrinkles. The resistance of the graphene ribbons will be changed through buckling and stretching process. When compared with the flat graphene, the piezoresistive effect of graphene ripples will be significantly increased. Furthermore, Chun et al. (2015b) has further demonstrated to obtain a higher piezoresistive character by manipulating the contact resistance between two graphene layers as well as the electromechanical properties of graphene itself. The sensor features two ways of contributing sensitivity; 1) positively for the contacting effect (X) and 2) negatively for the electromechanical effect of graphene (Y) as shown in **Fig. 2.13(b)**.

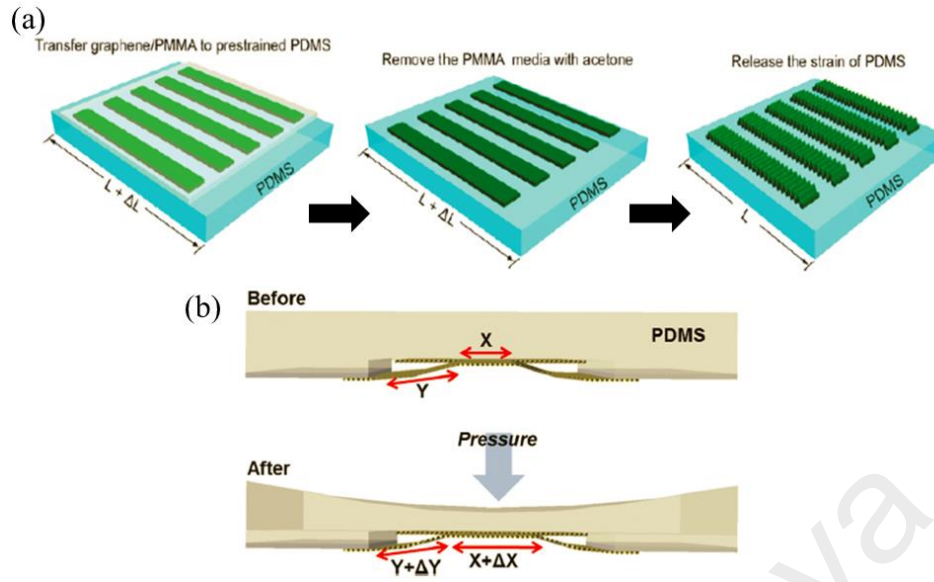


Figure 2.13: (a) PMMA/graphene ribbons film attached to a mechanically pre-strained PDMS substrate with ribbon alignment along the pre-strain direction (Wang et al., 2011). (b) Schematic representing the operating mechanisms in applied vertical pressure (Chun et al., 2015b).

2.8.1.2 Percolating Conductive Networks

Nanocomposite with the fraction of conductive fillers (for example, graphene) closest to the percolation threshold possesses a remarkable piezoresistive effect. Chai et al. (2014), has demonstrated that the formation and destruction of conductive paths between graphene fillers will occur when pressure is applied to the nanocomposite. By controlling the concentration of graphene fillers, the piezoresistive effect could be easily modified, since it directly correlates to the percolating conductive networks inside the nanocomposite. Recently, Li et al. (2012), has fabricated graphene woven fabric (GWF) by employing the Cu mesh structure using CVD technique as shown in **Fig. 2.14(a)**.

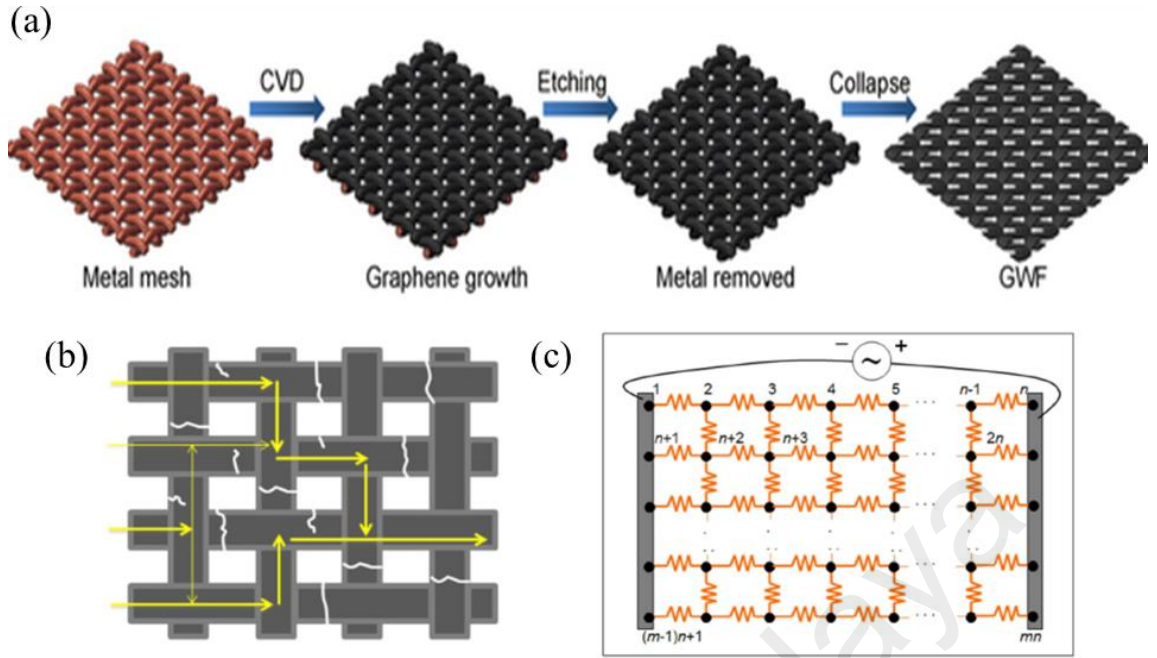


Figure 2.14: (a) Fabrication of graphene woven fabric (GWF) by CVD method. (b) Current pathway through a fractured GWF. (c) The equivalent circuit model for estimating the resistance of GWF with specified cracked density (Li et al., 2012).

It is found that cracks are uniformly distributed in the stretched GWF. A partial crack perpendicular to a pathway will lead to an increase of the resistance while an across crack will result in breaking off the current pathway as shown in **Fig. 2.14(b)**. The percolating conductive network inside the GWF structure can be illustrated by arranging the network with a variable resistor containing M rows and N columns assembled together as shown in **Fig. 2.14(c)**. Since electron will flow in the lowest resistance pathway, these cracks would increase the current pathway length within the GWF which found to be highly sensitive with a small deformation.

The percolating conductive networks can also be precisely controlled by perpendicularly sandwiching two layers of alternating graphene oxide and reduced graphene oxide arrays using a laser-scriber, as demonstrated by Tian et al. (2015). Since reduced graphene oxide is a conductor while graphene oxide is an insulator, the contact between these arrays will create a different current pathway length at specific applied pressure. The sensitivity combined with the pressure sensing range of

pressure sensor fabricated by this method shows the best among all reported pressure sensors to-date.

2.8.1.3 Tunnelling Mechanism

Electron charge transport occurs via variable range hopping (VRH) between intact graphene islands with sizes on the order of several nanometers has been studied by Gómez-Navarro et al. (2007). VRH involves consecutive inelastic tunnelling processes between two localized states and has been frequently observed in disordered systems, including amorphous carbon (Robertson, 1986). This could be observed in reduced graphene oxide electronic system where some of the parts will stay nonconductive unless more clusters of graphitic atoms can be restored by removing oxygen functional groups to decrease the distance between graphitic domains (Lu et al., 2009). At certain degree of reduction, with an adequate amount of restored graphitic cluster, this would resulting in charge transport via electron tunnelling or even to create continuous graphitic “paths” for charge transport, thus becoming a conducting material.

By employing this mechanism, Li et al. (2012) has fabricated a pressure sensor device made from polycrystalline graphene which overlapped together as shown in **Fig. 2.15(a)**. The applied pressure to the device would make the overlapping region (W_o) to decrease or increase with the deformation of polycrystalline graphene structure, hence controlled the tunnelling electron from one graphene island to another island. Later, Sreeprasad et al. (2013) has demonstrated the use of graphene quantum dots (GQDs) mixed with polymer microfiber as pressure sensor by electron tunnelling transport as shown in **Fig. 2.17(b)**. The device leverages the modulation in electron tunnelling distances between the GQDs which caused by the applied pressure across the polymer microfiber. Furthermore, the influence of temperature on the electrical currents in the percolating-GQD device was studied to ensure that the pressure device undergoes

electron-tunnelling process. It was found that the activation energy, E_a , is 3 meV, which is significantly less than the $k_B T$ at room temperature ($= 25$ meV), indicating that the mode of electron transport at room temperature is electron tunnelling, and not thermionic emission (Sreeprasad et al., 2013).

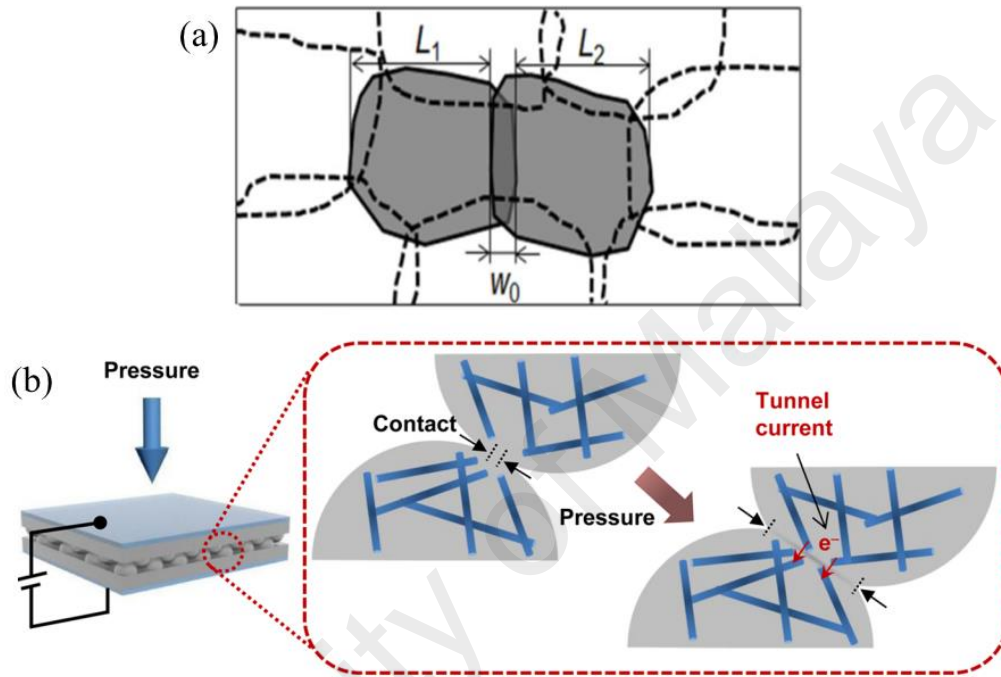


Figure 2.15: (a) Schematic structure of polycrystalline graphene with the islands size denoted as L_1 and L_2 while the overlapping region between these two islands denoted as W_0 . These parameters would control the change of resistance upon deformation of the sensor (Li et al., 2012). (b) Schematic showing the working principle of the graphene quantum dots (GQDs) mixed with polymer microfiber pressure sensor. The external pressure concentrates stress at the contact spots, deforming the matrix medium, which in turn causes an increase in the contact area and the tunnelling currents (Sreeprasad et al., 2013).

CHAPTER 3: EXPERIMENTAL AND ANALYTICAL TECHNIQUES

3.1 Overview

The content of this chapter is divided into four main sections. This chapter begins with a general procedure on the fabrication of graphene and graphene-copper oxide (graphene/Cu₂O) nanocomposites using hot-filament thermal chemical vapour deposition (HFTCVD) technique. This includes the standard procedure of substrate cleaning and parameters involved for the deposition process. The second part covers the transfer process of fabricated sample on Cu foils onto SiO₂/Si and polyimide substrates. The third part of this chapter focusses on measurement and characterization techniques used in this work such as Field Emission Scanning Electron Microscopy (FESEM), Low Energy Electron Microscopy (LEEM), Atomic Force Microscopy (AFM), Raman Spectroscopy, High Resolution Transmission Electron Microscopy (HRTEM), X-Ray Photoemission Spectroscopy (XPS) and Van der Pauw characterization. The final part of this chapter deals with the pressure sensor application. The pressure sensor test set-up and mechanical simulations of the designed flexible pressure sensor by finite element analysis (FEA) are presented.

3.2 Hot-filament Thermal Chemical Vapour Deposition Technique (HFTCVD)

3.2.1 System Overview

The samples are fabricated using a custom-made PECVD system that is slightly modified according to the work of Hawaldar et al., where the alumina tube is placed between the windings of tantalum (Ta) filament that act as a substrate holder (Hawaldar et al., 2012). The configuration of deposition chamber system of HFTCVD used in this work is shown in **Fig. 3.1(a-b)**. The full HFTCVD system set up can be found in Appendix 1. An alumina tube of 1 cm opening and 2 cm length which is sealed at one end is winded with tungsten; (W) filament (99.95% purity, 0.5 mm diameter from Kurt J. Lesker with the copper (Cu) foil substrate rolled and fitted inside it as shown in **Fig. 3.1(c)**. A K-type thermocouple is positioned in between the bottom of the Cu foils and inside wall of alumina tube while still being insulated from the filament throughout the fabrication process to monitor the substrate temperature. The thermocouple is arranged so that the tip touches the copper foil. The filament is hung across two copper rods which is separated 7 cm from the gas inlet and connected to an external power supply (LV 400 model, AC supply with 50/60 Hz from R. D. Mathis Co.) as shown in **Fig. 3.1(d)**. The CH₄ flow rate is controlled by Aalborg mass flow controllers MFCs, which operate in the ranges of 0-10 standard cubic centimetre per minute (sccm). The H₂ gas flow rate varies from 0-100 sccm using an Aera FC-770AC MFC with a display meter (Advanced Energy ROD-4A). These precursor gases are mixed together just before entering the chamber.

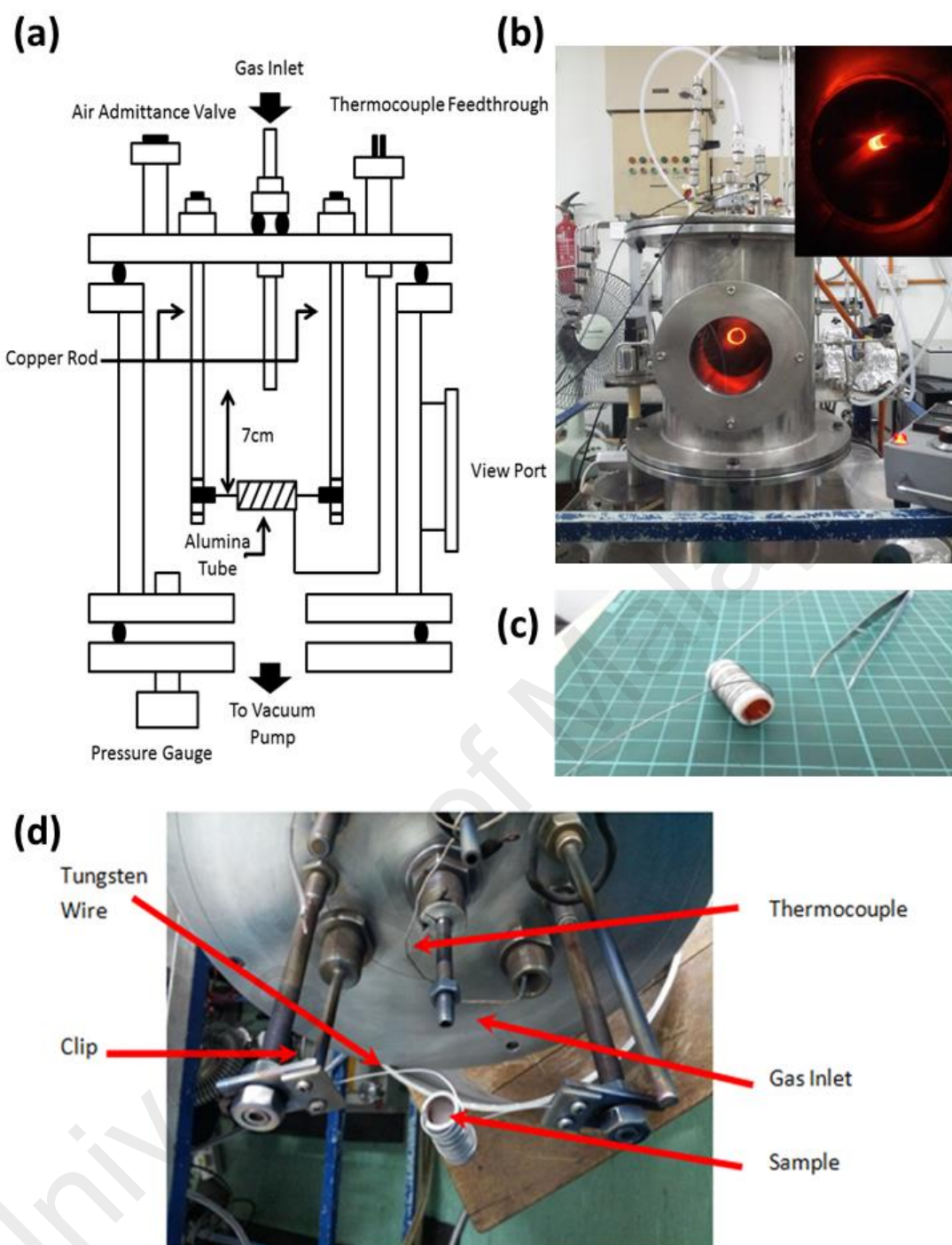


Figure 3.1: (a) Schematic diagram of HFTCVD system and (b) photograph of HFTCVD system. The inset picture shown the glowing of hot-wire at temperature $> 1000\text{ }^{\circ}\text{C}$. (c) Photograph of rolled Cu foil inside the coiled alumina tube from the opening side. (d) Side view of top plate of HFTCVD system.

The gas evacuation sub-system comprises of a single rotary pump (Edwards E2M28) which acts as the low vacuum pumping and a turbo molecular pump (TURBOVAC TW 70H, Leybold) that is directly connected to a single rotary pump

(Edwards E2M5) for high vacuum pumping. These two sets of pumps are separated by throttle valves which allow the flow direction to be selected. The set of turbo molecular and rotary pumps ensure a low base pressure for the chamber which helps to reduce contaminants in the chamber. To achieve good vacuum in the chamber, a certain sequence in the pumping process will be followed. Firstly, the chamber is pumped down to approximately 3×10^{-3} mbar using the low vacuum pumping which is monitored by Pirani gauge (Thermovac TTR-91, Leybold). Then the flow direction is switched towards the turbo molecular pump for high vacuum pumping which enables the chamber pressure to reach approximately 5×10^{-5} mbar by monitoring using Penning gauge (Thermovac PTR-225, Leybold). Just prior to introducing the precursor gas into the chamber, the flow direction is switched back to the low vacuum pumping line, whereby this pump also works as the process pump. Note that the delay between the switch and the gas flow is kept to a minimum to avoid backflow from the rotary pump towards the chamber due to the difference in pressure. In general, there will be three stages namely; pre-deposition, fabrication and post-deposition stages, for the fabrication of graphene and graphene/Cu₂O nanocomposites using HFTCVD technique which is briefly stated in **Table 3.1**.

Table 3.1 General deposition procedures carried out for HFTCVD technique.

Stage	Process	Condition	Remarks
Pre-deposition	Substrate Cleaning Process	Atmospheric	To remove impurities existing on the substrate
	Vacuum Process	Vacuum	Clean deposition environment and minimize contamination in the sample
	H ₂ Treatment Process	Vacuum	To remove the native oxide and increase the Cu grain boundaries
Fabrication	Deposition Process	Vacuum	*Refer to Table 3.2
Post-deposition	Gas-line Cleaning	Vacuum	Safety purposes
	Chamber Cleaning	Atmospheric	To avoid contamination from previous deposition

3.2.2 Sample Preparation Process

In this thesis, the samples are fabricated on 25 μm thick copper (Cu) foil. The Cu foil rim with 150 m x 150 mm (length x width) of 99.99% purity is purchased from Alfa Aesar and then cuts into the dimension of 3.0 x 2.0 cm (6.0 cm²) to perfectly fit the inner of alumina tube as shown in **Fig. 3.2**. The Cu foil is carefully cut using a cutter blade assisted by ruler on a cutting pad to avoid wrinkle at the edges. One of the Cu foil edges is folded to indicate the front and back side of the Cu foil. Next, the Cu foil cleaning is done by immersing in acetone and purged using nitrogen gas. Then, the clean Cu foil will be rolled inside the alumina tube with the folded edge facing the alumina tube side which indicates the back side of Cu foil. The front side of Cu foil is the desired region of sample to be deposited. Note that the handling of Cu foil from the beginning is done by wearing a glove to avoid contamination on the Cu surface.

Next, 0.5 mm diameter of tungsten (W) wire with 99.95% purity (purchased from Kurt J. Lesker) is cut into 50 cm length and then coiled around the alumina tube. Then, the W wire fitted with alumina tube and copper foil is hanging in the deposition chamber. Both end of W wire is clipped to the Cu rods which are later connected to external power supply. The clipping of W wire is adjusted to be not too tight to give freedom for W wire to expand and contract when heating or cooling steps. Finally, the thermocouple was placed on Cu foil to measure the Cu foil temperature throughout the fabrication process.



Figure 3.2: Photograph of freshly cut Cu foil with dimension of 3.0 x 2.0 cm (6.0 cm²).

3.2.3 Deposition Process

Prior to the fabrication process, the W hot-filament is used to heat the Cu foils to the fabrication temperature of ~ 1000 °C. The filament temperature is measured at ~ 1750 °C by using an external optical pyrometer (Raynger® 3i, Raytek). An initial cleaning treatment is done for the Cu foil in H_2 at a flow rate of 50 sccm at 3.3×10^{-1} mbar for 20 minutes to remove the native oxide on the Cu foils. The growth of the graphene films in the Set 1 is carried out in a CH_4/H_2 (10 sccm/50 sccm) gas mixture at 3.7×10^{-1} mbar for 5, 10, 20, 30 and 40 minutes while maintaining the substrate temperature at 1000 °C. For the Set 2 of the samples, the flow rate of the H_2 vary to 10, 25, 50, 75, and 100 sccm ($1.9, 2.4, 3.7, 5.2, 6.3 \times 10^{-1}$ mbar, respectively), while the CH_4 flow is fixed at 10 sccm with the optimum growth condition in the first set (30 minutes deposition time and 1000 °C substrate temperature). The growth of the graphene/ Cu_2O nanocomposites films in the **Set 3** is carried out in a CH_4/H_2 (50 sccm for CH_4 and 10 sccm for H_2) gas mixture for 30 minutes at a pressure of 3.7×10^{-1} mbar. Then, the W filament temperature are adjusted to the required deposition temperature of $\sim 1550, \sim 1650$ or ~ 1750 °C to set the substrate temperature at 750, 850 or 1000 °C, respectively. The details of the deposition parameters are summarized in **Table 3.2**.

After the deposition process, the sample is cooled to 200°C (~ 2 °C/s) by reducing the external power supply. Finally, the fabricated graphene and graphene/ Cu_2O nanocomposites on Cu foils are convectively cooled by adding 100 sccm N_2 gases until room temperature is achieved. A summary of the temperature profile as well as variation of deposition parameters used in these works are shown in **Fig. 3.3**. The photographs of selected sample fabrication are shown in **Fig.3.4**. Note that the distinct purple colour on partially covered graphene on Cu foils is due to oxidation of exposed Cu surface from the environment moisture after some interval of time.

The partially covered graphene appeared to be the same with full coverage of graphene by naked eyes. However, it can be easily distinguished under the view of microscope with the shining part are the uncovered graphene region.

Table 3.2 Details of the deposition parameters for each set of samples.

Set	Study Parameter	H ₂ Plasma Treatment	Deposition Parameters		Type of Sample
			Fix	Vary	
1	Effect of Growth Duration	H ₂ =50 sccm t=20 minutes P _{H2} =3.3 x 10 ⁻¹ mbar	D=7 cm F _{CH4} =10 sccm F _{H2} =50 sccm T _F =1750 °C T _S =1000 °C A= 1 cm P=3.7 x 10 ⁻¹ mbar	t=5-40 minutes	<ul style="list-style-type: none"> Graphene Patch and Graphene Layer
2	Effect of Hydrogen Flow Rate	H ₂ =50 sccm t=20 minutes P _{H2} =3.3 x 10 ⁻¹ mbar	D=7 cm F _{CH4} =10 sccm T _F =1750 °C T _S =1000 °C A= 1 cm t=30 minutes	F_{H2}=10-100 sccm correspond to P _{CH4/H2} =1.9-6.3 x 10 ⁻¹ mbar	<ul style="list-style-type: none"> High-quality and Defective Graphene Monolayer and Multi-layer Graphene
Controlled Sample	Effect of Alumina Tube Opening	H ₂ =50 sccm t=20 minutes P _{H2} =3.3 x 10 ⁻¹ mbar	D=7 cm F _{CH4} =10 sccm F _{H2} =50 sccm T _F =1750 °C T _S =1000 °C t=30 minutes P=3.7 x 10 ⁻¹ mbar	A= 2 cm	<ul style="list-style-type: none"> Defective Graphene Patch
	Effect of Growth Temperature	H ₂ =50 sccm t=20 minutes P _{H2} =3.3 x 10 ⁻¹ mbar	D=7 cm F _{CH4} =10 sccm F _{H2} =50 sccm A= 1 cm t=30 minutes P=3.7 x 10 ⁻¹ mbar	T_S=850 °C correspond to T _F =1650 °C	<ul style="list-style-type: none"> Defective Graphene Layer
3	Effect of Growth Temperature	H ₂ =50 sccm t=20 minutes P _{H2} =3.3 x 10 ⁻¹ mbar	D=7 cm F _{CH4} =10 sccm F _{H2} =50 sccm A= 1 cm t=30 minutes P=3.7 x 10 ⁻¹ mbar	T_S=750-1000 °C correspond to T _F =1550-1750 °C	<ul style="list-style-type: none"> Graphene/Cu₂O Nanocomposites
*D is distance between gas inlet and alumina tube; F _{CH4} is methane flow rate; F _{H2} hydrogen flow rate; T _F is temperature of filament; T _S is temperature of substrate; t is time duration; P is pressure and A is alumina tube opening.					

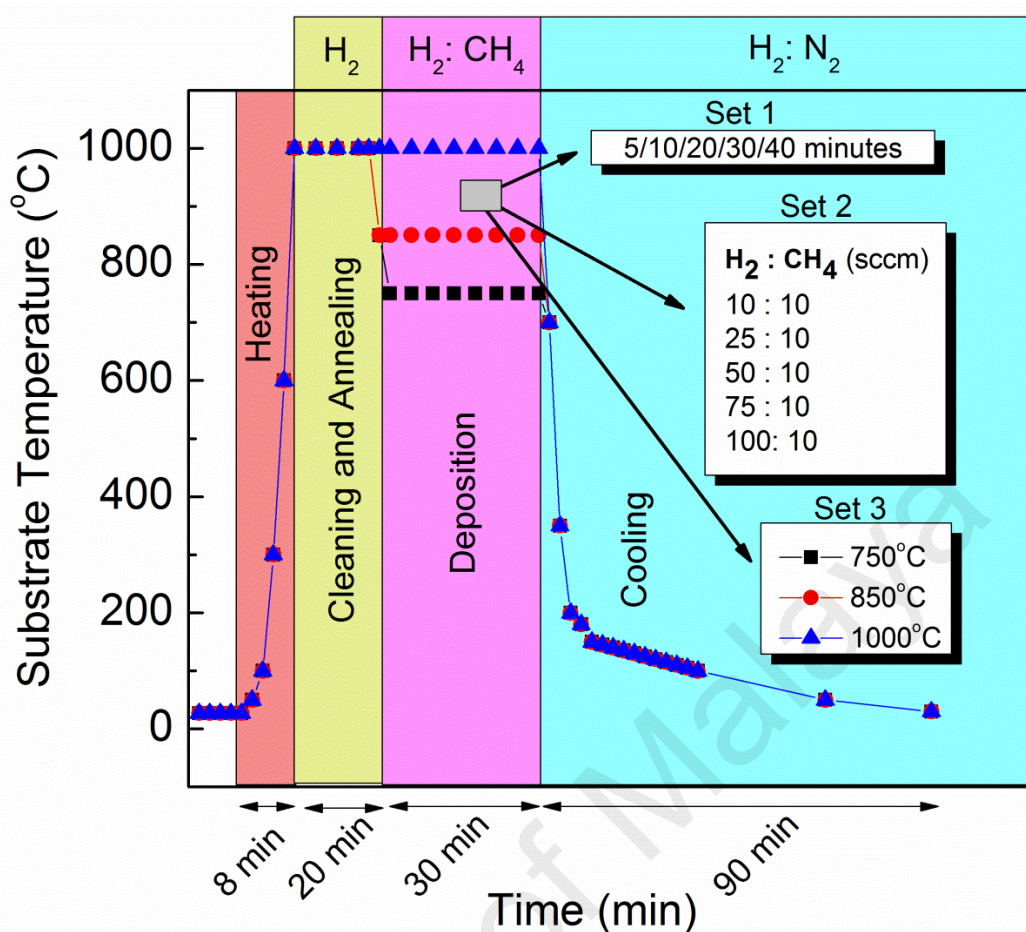


Figure 3.3: Temperature profile of the Cu foil acquired from thermocouple along the fabrication process using HFTCVD system. For Set 1, the deposition time is varying at 5, 10, 20, 30 and 40 minutes. In Set 2, the $H_2:CH_4$ flow rate vary at 10:10, 25:10, 50:10, 75:10 and 100:10 ratios. While in Set 3, the deposition temperature varies at 750, 850 and 1000 °C. Note that only the parameter in deposition process will be varied for this work while the heating, cleaning and annealing, and cooling processes are kept the same.

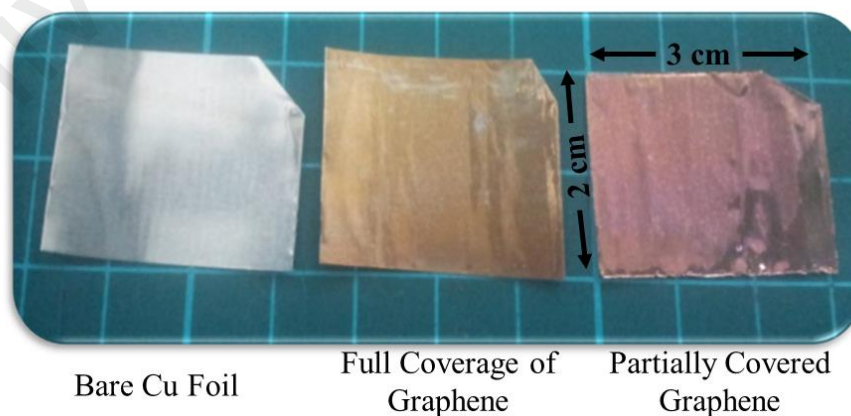


Figure 3.4: Photograph of fabricated samples on Cu foils.

3.2.4 Transfer Process

The fabricated samples on the Cu foils are then transferred to a Si substrate with a 300 nm-thick SiO₂ layer (SiO₂/Si) and interdigitated electrode (IDE) array on polyimide film substrate (IDE/polyimide) via a wet etching transfer process. This process is assisted by using a thin layer of; 1) thermal release tape, TRT (REVALPHA, No. 3196 from Nitto Denko Co.) or 2) poly(methyl methacrylate), PMMA (MicroChem 950 PMMA, 4% in Anisole) methods. The TRT and PMMA assisted layer acted as a support for the graphene sheet. The flow of transfer process onto the target substrate is schematically shown in **Fig. 3.5**.

Prior to transfer process, the as-deposited sample will be unrolled and flattened by sandwiching between two glass slides. Since the graphene would grow on both sides of Cu foils, the graphene grown at the back side needs to be removed by H₂ plasma etching set at 30W for 10 minutes. After the removal of the unwanted graphene at the back side of the Cu foils, the graphene grown on the Cu front side is covered by TRT or PMMA layer. For TRT method, one side of TRT will be peeled-off and carefully sticks on the graphene layer. The air bubble might be trapped between TRT and graphene thus removes the trapped air by rubbing using finger is necessary for a homogeneous and continuous graphene transfer. For PMMA method, the PMMA solutions are spin-coated at 1000 rpm for 15 seconds on Cu foil. The PMMA/Graphene/Cu foil was then cured at 130 °C for 5 minutes to make the PMMA layer stiffer.

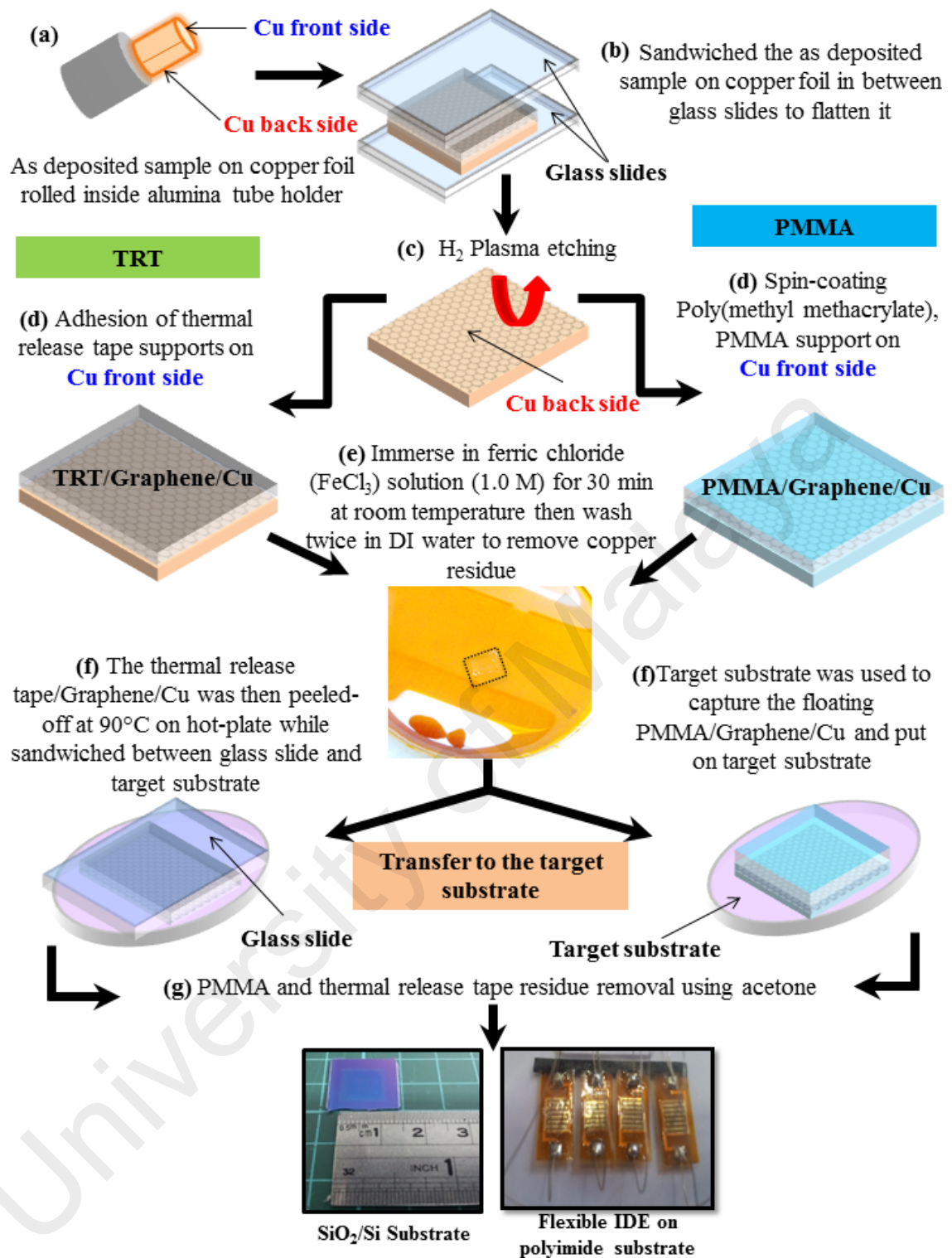


Figure 3.5: Schematic representation of typical graphene transfer process on SiO₂/Si and polyimide flexible pressure sensor substrate employed in this work.

Then, the Cu foil will be removed by immersing the stack of TRT/graphene/Cu or PMMA/graphene/Cu in a ferric chloride (FeCl_3) solution (1.0 mol) for 30 minutes at room temperature. The colour of etching solution turned from brownish to dark brownish. Note that this reaction released a corrosive vapour. The entire process will be performed in a fume hood. After the Cu foils are completely etched away, the graphene supported by PMMA is scooped and then transferred into deionized water a few times to remove any of the Cu residues. Lastly, the graphene is scooped with a SiO_2/Si or polyimide substrate assisted by a tweezer.

For TRT method, the TRT layer are be covered by glass slide and then peeled-off from the graphene by applying a heat at $90\text{ }^\circ\text{C}$ for 10 seconds. An important thing to note is the purpose of glass slide to evenly distribute the tension caused from the loss of stickiness of TRT during the peel-off step for a continuous and homogeneous graphene transfer. The TRT residue and PMMA layer is further removed using acetone and transferred graphene will be ready for further characterization and application purposes.

3.3 Device Fabrication

3.3.1 Interdigitated Electrode (IDE) on Polyimide Substrate

The fabrication method of interdigitated electrode (IDE) array on polyimide film substrate (IDE/polyimide) is shown in **Fig. 3.6**. The IDE array, made of the Cu foil, patterned on a polyimide film substrate using a standard subtractive process based on UV photolithography, in which the unwanted Cu will be removed to leave the desired Cu pattern. The Cu foil is adhered to the polyimide film by using an adhesive applied with heat and pressure in a laminating press. The adhesive epoxy resin is then coated onto polyimide film (DuPont Kapton® 200HN), and then laminated to 35 μm -thick Cu foil at a temperature of 160 °C and pressure of 10 MPa for 1 hour in a vacuum condition. The thickness of the composite film is measured to be about $\sim 105 \mu\text{m}$.

By using the standard UV photolithography method, the Cu foil is first coated with a dry photoresist film (DuPont Riston® GM120) by roll-to-roll lamination at a temperature of 55 °C and a pressure of 0.5 MPa. The photoresist are then exposed to UV light through a mask for 120 seconds and developed in 0.85 wt% sodium carbonate (Na_2CO_3). The undeveloped photoresist are etched away. Then, the unwanted, exposed portions of the Cu are removed in a 1.0 mol ferric chloride etching solution. After the exposed Cu is completely etched away, the remaining photoresist is dissolved slowly in a 3 wt% NaOH stripping solution for 120 seconds to create an IDE array with 500- μm tracks and 200- μm gap widths and two terminal electrodes. The Cu patterns are then finalized with Au electroplating with $0.3 \pm 0.02 \mu\text{m}$ to provide a substantial stable nature towards oxidation. The photographs of final product of flexible pressure sensor device fabrication are shown in **Fig. 3.7**.

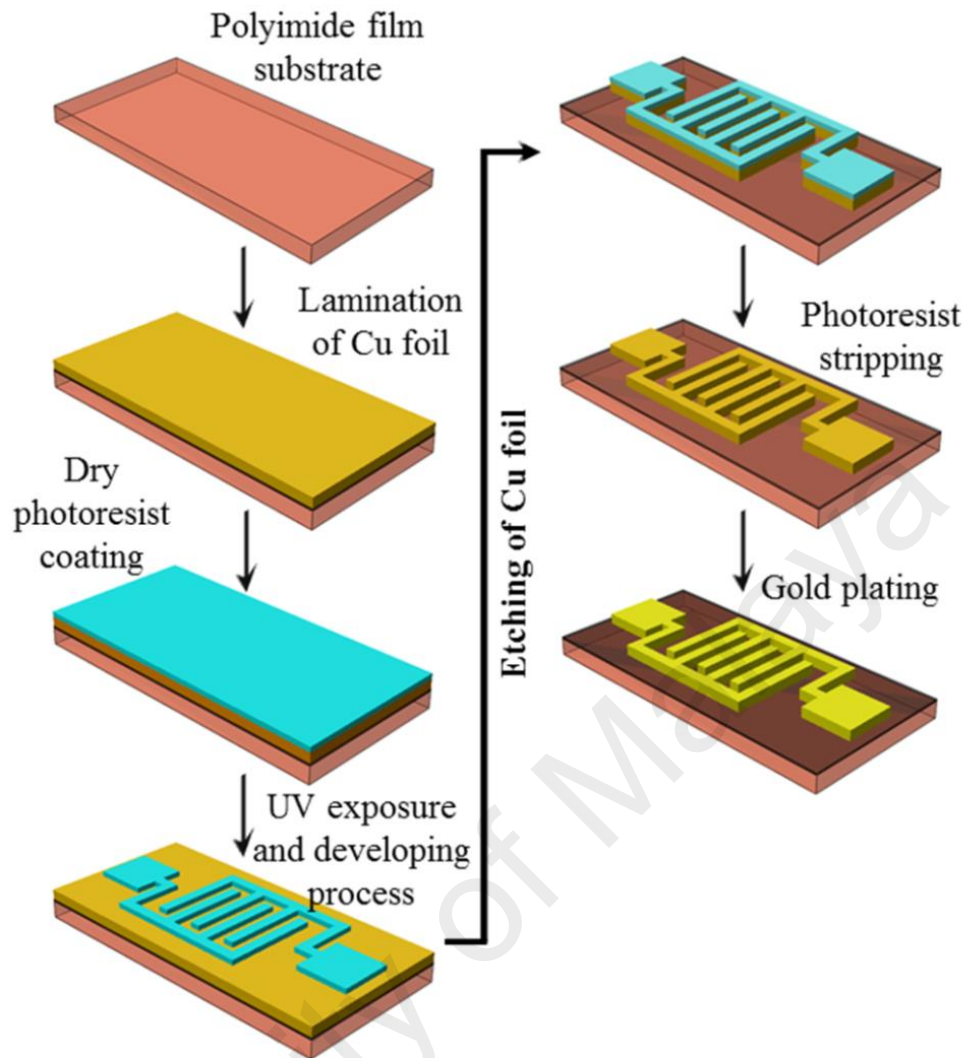


Figure 3.6: Fabrication process flow of the IDE array on the polyimide substrate film by UV photolithography method.

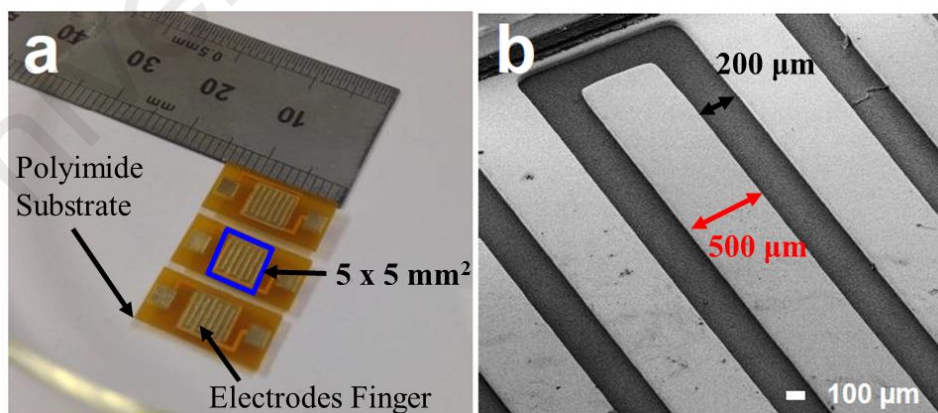


Figure 3.7: (a) Photographs of the fabricated IDE array and terminal electrode on flexible polyimide substrate. The effective sensing area of $5 \times 5 \text{ mm}^2$ as indicated in a square box. (b) FESEM image of the electrode finger (500 μm) and gap (200 μm).

3.4 Measurement and Characterizations

3.4.1 Morphological and Topological Study

3.4.1.1 Field Emission Scanning Electron Microscopy (FESEM)

In this thesis, field emission scanning electron microscopy, FESEM (Hitachi SU8000) will be employed to investigate the morphology of fabricated samples. The images are captured in mixture of secondary electron (SE) and backscattered electron (BSE) modes at 0.5 kV accelerating voltage. An extremely thin and sharp tungsten needle (tip diameter 10^{-7} – 10^{-8} m) functions as a cathode to produce an electron beam. The electron beam will then be confined and focused into a thin focused, monochromatic beam using metal apertures and magnetic lenses to the sample with certain acceleration voltage. When an electron beam impinges on a sample, electron-matter interactions can produce a variety of products such as backscattered electrons (BSE), secondary electrons (SE), auger electrons, X-ray, and cathodoluminescence, which can be selectively collected and combined to generate images.

BSE signal (>50 eV) comes from elastically scattered electron, which scattered differently from different types of atoms. This will result in a different rate of backscattered electrons and hence the contrast of the image will vary as the atomic number (Z) of the specimen changes, usually atoms with higher atomic number will appear brighter than those with lower atomic number. SE signal (<50 eV) comes from inelastic scattered electron, which comes from the ejection of the valence electrons of atoms in the specimen. The angle and velocity of these SE relates to the surface structure of the object. However, unlike BSE, SE is relatively independent of the atomic number of the scattering atoms.

Previously, CVD graphene characterization by SEM was conducted by collecting SE signals, since this technique is highly morphology sensitive, with a

penetration depth of about 5–10 nm (Yang et al., 2012). However, the obtained SE mode image directly on copper could hardly show the exact position of graphene layer due to the Cu substrate being an excellent electrical conductor. Interestingly, by adding the BSE signal into SE signal, graphene grown on Cu substrate reveals clearly various contrasts as shown in **Fig. 3.8**. This is attributing to the difference in penetration depths between the SE signal and the BSE signal. As the number of graphene layers increases, the mean atomic number decreases accordingly, which results in a lower electron yield and thus appear darker contrast in the image (Kochat et al., 2011). Even if there is one layer increases or decreases of the graphene layer, the contrast will be altered. Besides the BSE contribution, SE guarantees images exhibiting surface details clearly in focus. In addition, the electron beam can easily damage the graphene layer, especially when high acceleration voltages or short working distances are used, resulting in burnt spots and unwanted carbonaceous contamination.

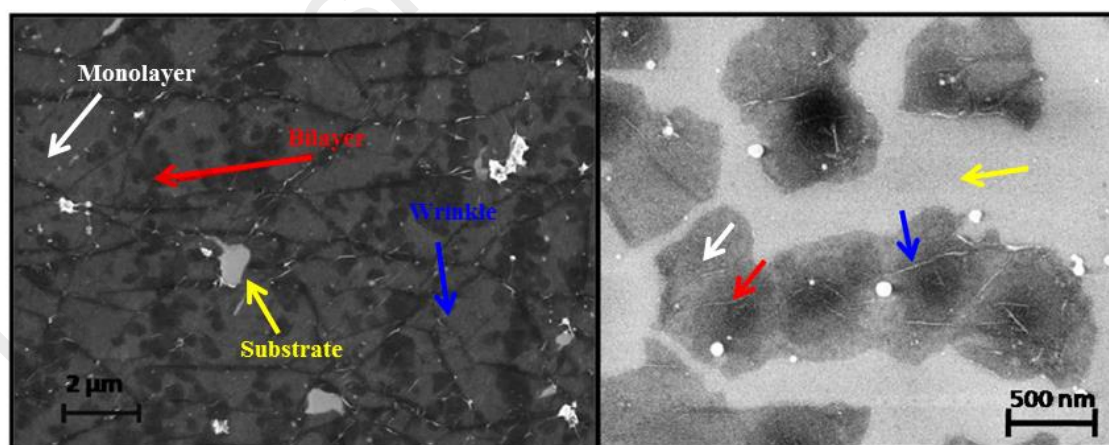


Figure 3.8: FESEM images of graphene on Cu foil. (Kochat et al., 2011).

3.4.1.2 Low Energy Electron Microscopy (LEEM)

In this thesis, low energy electron microscopy (LEEM) are employed to investigate the growth of adlayers between graphene layer and metal substrate as well as number of graphene layers with a sub-micron resolution. The LEEM measurements were performed at the beam-line BL3.2U(b), of the Synchrotron Light Research Institute in Thailand. The LEEM system is equipped with Elmitec LEEM III of hemisphere electron energy analyser with the base pressure during measurement fixed $\sim 3 \times 10^{-10}$ mbar. The sample will be annealed in a vacuum condition at 300 °C for 90 minutes prior to LEEM measurement to clean the sample surface from oxygen contamination.

In LEEM, high-energy electrons (15-20 keV) are emitted from an electron gun, focused using a set of condenser optics, and sent through a magnetic beam deflector as shown in **Fig. 3.9(a)**. The accelerated electrons travel through an objective lens and begin decelerating to low energies (1-100 eV) when they approach the sample surface because the sample was held at a potential near to the potential of the electron gun. The low-energy electrons are now termed “surface-sensitive” and the near-surface sampling depth could be varied by tuning the energy of the incident electrons (difference between the sample and electron gun potentials minus the work functions of the sample and system) as shown in **Fig. 3.9(b)**. The surface-sensitive electrons incident to the surface then will be backscattered are collected by microchannel plate (MCP) and used to form magnified images of the sample surface.

Typical LEEM images of graphene grown on SiC substrate are obtained at two different energies as shown in **Figs. 3.9(c) and (d)** (Hibino et al., 2008). The LEEM image intensity (bright or darker contrast) corresponds to the electron reflectivity. From sequential LEEM images obtained by varying the incident-electron bias voltages between the sample and objective lens; $V_{\text{Bias}} - V_{\text{Vac}}$, the energy dependence

of the electron reflectivity is obtained from specific regions marked as 1 to 8, as shown in **Fig. 3.9(e)**. Periodic oscillations (or number of dips) are indicating that graphene sheets 1 to 8 layers thick are formed on regions marked as 1 to 8, respectively (1 layer shows 1 dip while 8 layers shows 8 dips).

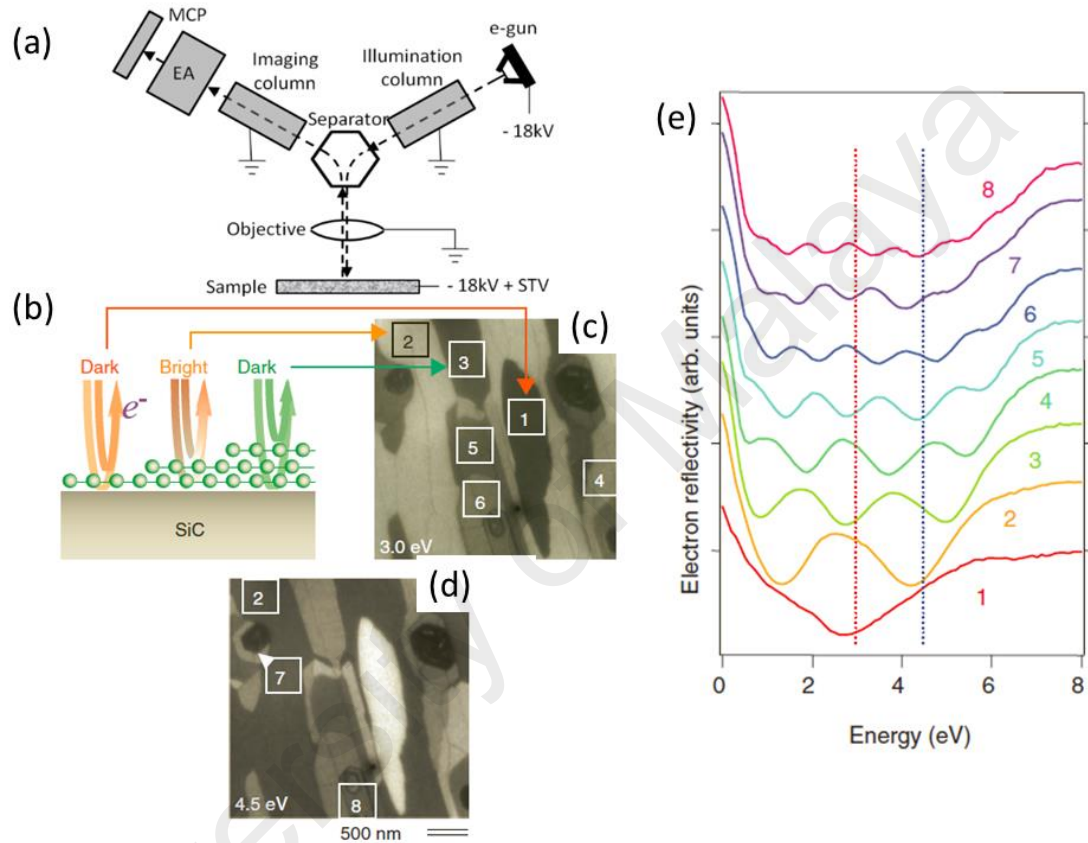


Figure 3.9: (a) Schematic of the electron optics of the LEEM system. (b) Variation of electrons reflected from the graphene surface and graphene/substrate (SiC substrate) interface which interfered and causes the electron reflectivity to change periodically as a function of the electron energy and graphene thickness. (c-d) The LEEM images of multilayer graphene that vary from 1 to 8 layers denoted by the number in the boxes. (e) Electron reflectivity or intensity-voltage (I-V LEEM) plot with respect to the electron energy. The number of the graphene layers can be determined from the analysis of the reflectivity oscillations in I-V LEEM plot (Hibino et al., 2008).

3.4.1.3 Atomic Force Microscopy (AFM)

In this work, atomic force microscopy (AFM) in tapping mode (NTEGRA Spectra, NT-MDT) are employed to investigate the surface topography of the sample. The electron microscopes such as FESEM can easily generate 2D images of a sample surface, with a magnification of $\sim 100,000\times$ (nm range). However, the microscopes cannot measure the vertical dimension (z-direction) of the sample, the height (e.g. wrinkles, particles) or depth (e.g. holes, pits) of the surface features. In contrast, the AFM characterization, which uses a sharp tip to probe the surface features by raster scanning, could image the surface topography with extremely high magnifications that are comparable to the electron microscopes.

An AFM consists of a flexible cantilever containing a sharp probe, laser, photodiode detector, piezoelectric scanner and feedback electronics (not shown) as shown in **Fig. 3.10(a)**. **Fig. 3.10(b)** shows three primary imaging modes of AFM namely; contact, non-contact and tapping mode. During contact mode, the tip of the cantilever is in contact with the sample and repulsive Van der Waals forces prevail, whilst attractive Van der Waals forces are dominant when the tip moves further away from the sample surface. In tapping mode, the tip is not in constant contact with the sample surface. Instead, the cantilever will be oscillated at its resonant frequency, which makes the tip lightly tap on the surface during scanning.

The measurement of an AFM is made in three dimensions, the horizontal X-Y plane and the vertical Z dimension. Resolution (magnification) at Z-direction (up to nm) normally is higher than XY-directions (from μm to nm). The working principle of the tapping mode can be briefly explained by referring to **Fig. 3.10(c-f)**. Firstly, the cantilever will be oscillated near the cantilever's resonant frequency with free amplitude oscillation (A_0) using a piezoelectric crystal and slowly

approaching the sample surface (c). The cantilever motion will be monitored by the piezoelectric scanner. The corresponding detection scheme (tapping mode) exploits the change in the A_0 of a cantilever due to the interaction of a tip with a sample according to the force-distance curve shown by blue (oscillation without contact) and red (oscillation with contact) arrows (d). As the oscillating cantilever begins to tapping the sample surface, the cantilever tapping oscillation (A_{sp}) will be reduced due to energy loss caused by the tip contacting the surface (e). As the tip scans the sample, the forces between the tip and the sample surface cause the cantilever to bend. The reduction in oscillation amplitude is used to identify and measure surface features. A photodiode detector detects the deflection of a laser beam reflected off the back of the cantilever onto a photodiode which transfers the signal into sample surface topology (f).

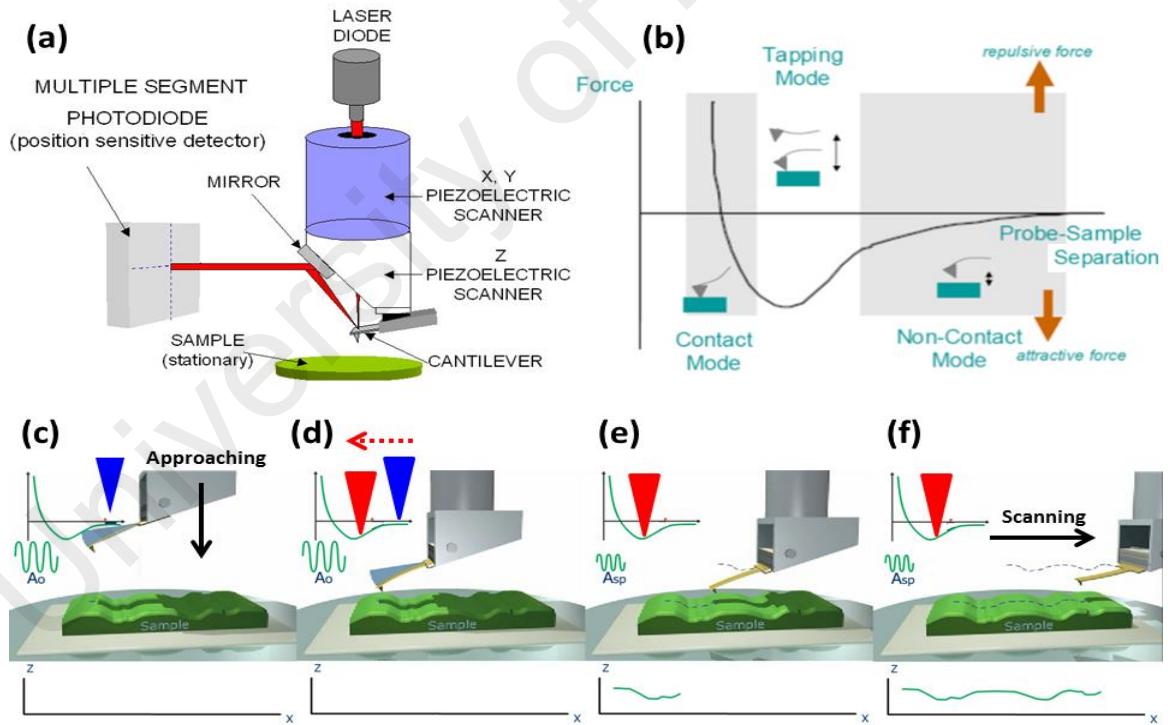


Figure 3.10: (a) Schematic diagram of AFM set up. (b) Force-curve (or Force-distance curve) as a function of probe-sample separation. There are three regions of forces which determined the mode of AFM used; contact mode, tapping mode and non-contact mode. (c-d) The tapping mode used in this work is operated via the principle of amplitude-modulation detection. The tapping AFM mode has the advantage with minimum sample damage. This is particularly important in graphene topological mapping and analysis with no surface alteration (Voigtländer, 2015).

Fig. 3.11 shows an example of topological AFM mapping of graphene deposited on decorated nanoparticle substrate with (a) height and (b) phase imaging. The AFM study is done to study the scattering of the charge carriers is influenced by any topographical inhomogeneity in the graphene layer. From the mapping, the graphene wrinkle can be observed with the height profile that shoots out from the flat surface of graphene. In addition, by employing the phase mapping, there will be a phase change of the probe motion due to the difference of adhesion between the tip and sample surface. This would allow a chemical mapping of surfaces based on these material differences as in this case, the presence of nanoparticle in graphene matrix.

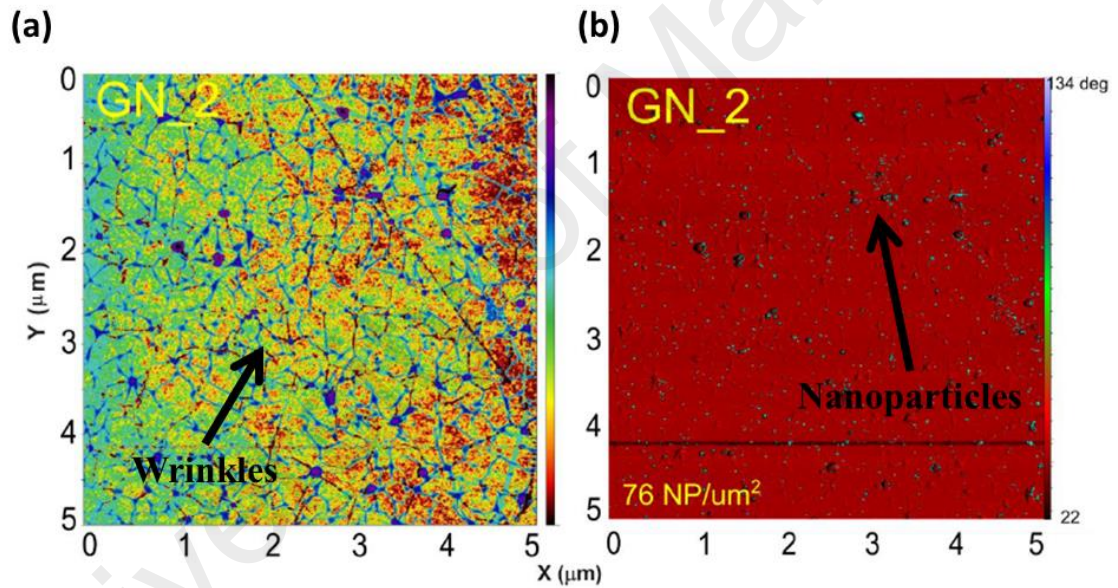


Figure 3.11: Topological AFM mapping of graphene deposited on decorated nanoparticle substrate with (a) height and (b) phase imaging. (Pacakova et al., 2015)

3.4.2 Structural Properties

3.4.2.1 Raman Spectroscopy

In this work, Renishaw inVia Raman spectroscopy with 514 nm laser excitation ($\sim 2 \mu\text{m}$ spot size) are employed to investigate the thickness and crystalline quality of the graphene layers. The wavenumber will be calibrated using the 520.5 cm^{-1} peak of silicon. Raman techniques are particularly useful for graphene characterization and considered as an integral part of graphene research. It is considered as an ideal characterization tool since it would be a simple sample preparation process, non-destructive, able to give structural and electronic information, and applicable to both laboratory and mass-production scales. It is extensively used to determine the number and orientation of layers, the quality and types of edge, and the effects of perturbations, such as electric and magnetic fields, strain, doping, disorder and functional groups in graphene study (Ferrari et al., 2013). In addition, the shapes, intensities and positions of these peaks would give a considerable amount of information, often comparable to that obtained by competing techniques that are more complicated and more destructive.

An understanding of the phonon dispersion of graphene is found to be essential to interpret the Raman spectra of graphene. Graphene could be described as two identical, interwoven hexagonal crystal lattices with a carbon atom at each lattice point as shown in **Fig. 3.12(a)** (Ferrari et al., 2013). The symmetry of electron dispersion inside monolayer graphene created an intersection points where the conduction and valence bands meet at the corners of the BZ, which coincide with the Fermi energy, E_F . Therefore, monolayer graphene is later described as a zero bandgap semiconductor. The corners of the graphene BZ with crystallographic positions at K and K' are known as the Dirac points. Near the Dirac points, the energy-momentum dispersion of electrons is linear and illustrated as a shaded region. This unique band structure causes the charge carriers to move relativistically near the E_F .

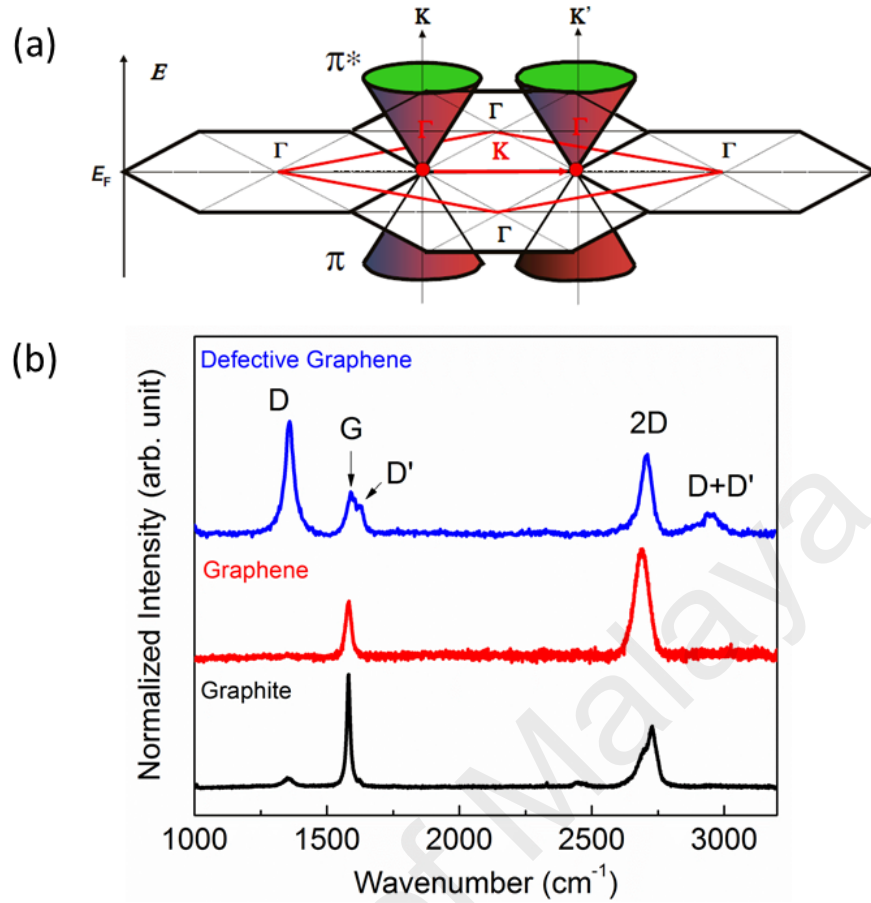


Figure 3.12: (a) Electronic Brillouin Zones (BZs) of graphene (black hexagons), the first phonon BZ (red rhombus), and schematic electronic dispersion (Dirac cones). The vertical arrow illustrates the electron energy (E) which the energies of the intermediate states are given by the difference in energies of electrons in the empty π^* and filled π bands. The Dirac cones intercept at Fermi level (E_F) for monolayer graphene. The phonon wave vectors connecting electronic states in different valleys are labelled by red Greek letters (Γ , K and K'). (b) Typical Raman spectra of graphite (bottom), graphene (middle) and defective graphene (top) which show the D, G, G', 2D and D+D' peaks taken using 514.5 nm laser source (Malard et al., 2009).

A typical characteristic of Raman spectra for graphite, graphene and defective graphene are shown in **Fig. 3.12(b)**. In graphite sample, the G peak at $\sim 1585 \text{ cm}^{-1}$ appear to be prominent which associated with the double-degenerate; in-plane transverse optic (iTO) and longitudinal optic (LO) phonon mode (E_{2g} symmetry) at the Brillouin zone (BZ) center, Γ . The broad 2D peak around $\sim 2700 \text{ cm}^{-1}$ corresponds to a double resonance mechanism that originated from two iTO phonons near the K and K' points in the BZ of graphene. However, for a single layer graphene sample, the 2D peak appears to be prominent with an intense and sharp signal as compared to graphite.

Those peaks such as D, D' and D+D' are presented in from the iTO or iLO phonon modes near the K points in the BZ, indicated to a certain degree of defect density in the structure of graphene sample (Malard et al., 2009).

Fig. 3.13 explains the prominent features in the Raman spectra of monolayer graphene in terms of the Raman scattering process (Malard et al., 2009);

(a) The G peak corresponded to the E_{2g} phonon at the Γ point. The electron initially excited to the π^* band due to the absorption of photon (laser source) leaving a hole at the π band. Then, the excited electron would return to its initial state, recombine with the hole thus emitting a photon which follows the law of conservation energy.

(b) In the case of the D peak, the two scattering processes between K and K' points, consist of one elastic scattering event by defecting of the crystal and one inelastic scattering event by emitting or absorbing a phonon. This mechanism is called an intervalley double resonant process because it connects points in circles around inequivalent K and K' points in the first BZ of graphene.

(c) In contrast to the D peak, the D' peak happens from intra-valley double resonant process. Both D and D' peaks require a defect for its activations. While the D+D' peak is the result from the combination of Raman scattering process of its constituent.

(d) In the case of the 2D peak, both processes are inelastic scattering events and two phonons will be involved. In the special case of graphene, where the valence and conduction bands are almost mirror bands of one another relative to the E_F , this could lead to an important effect called triple resonance Raman scattering process. In triple resonance mechanism, instead of the electron being scattered back by a phonon with wavevector; $-q$ from K to K' point, the hole would also be able to be scattered by an opposite wavevector; $+q$ from K to K' point and finally the electron-hole recombination happened at the opposite side with respect to the K point.

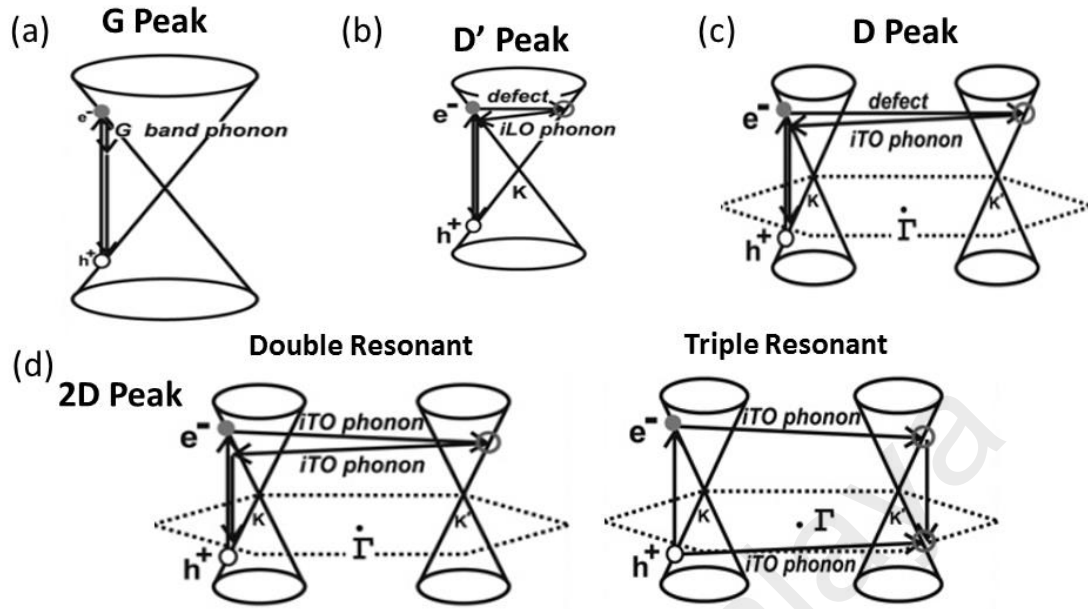


Figure 3.13: The prominent features in the Raman spectra of monolayer graphene due to the Raman scattering process denoted as (a) G, (b) D', (c) D and (d) 2D peaks. This would involve the electron excitation due to absorption of photon (laser source), elastic (defect) and inelastic (phonon) electron-phonon scattering and electron-hole recombination which then give out the photon emission (Raman spectra). The inter-valley transitions process is due to the connected points of electron scattering that circles around at K and K' points in the first BZ of graphene. On the other hand, the intra-valley process is due to the connected points of electron scattering inside the same circle around the K (K') point (Malard et al., 2009).

The band structure of graphene changes when multiple graphene layers are present. The order between successive layers will be determined the nature of the band structure change. It has been observed in literature that bilayer graphene (BLG) or few layer graphene (FLG) that are prepare from graphite using top down techniques, their band structure would splits at the K points into a number of levels commensurate with the number of stacked sheets (Malard et al., 2009; Hao et al., 2010). In the case for Bernal (AB) stacked of bilayer graphene, there would be four Raman scattering process to be taken place as shown in **Fig. 3.14(a-d)**. This would result to an increase of full width half-maximum of the 2D peak ($2D_{FWHM}$) which can be deconvoluted into four Lorentzian peaks, as shown in **Fig. 3.14(e)**. However, when there is no order

between stacked layers (i.e. turbostratic graphene) the electronic interaction between stacked graphene layers is very weak, which then lead to a similar 2D peak shape of monolayer graphene but could be fitted with only one Lorentzian peak of larger $2D_{FWHM}$ ($>40 \text{ cm}^{-1}$). Furthermore, the intensity of the 2D peak relative to the G peak feature, which often presented as I_{2D}/I_G ratio, can also be used to estimate the number of graphene layer. This is due to the intensity of the 2D peak that come from the triple resonance process which inversely proportional to number of graphene layer.

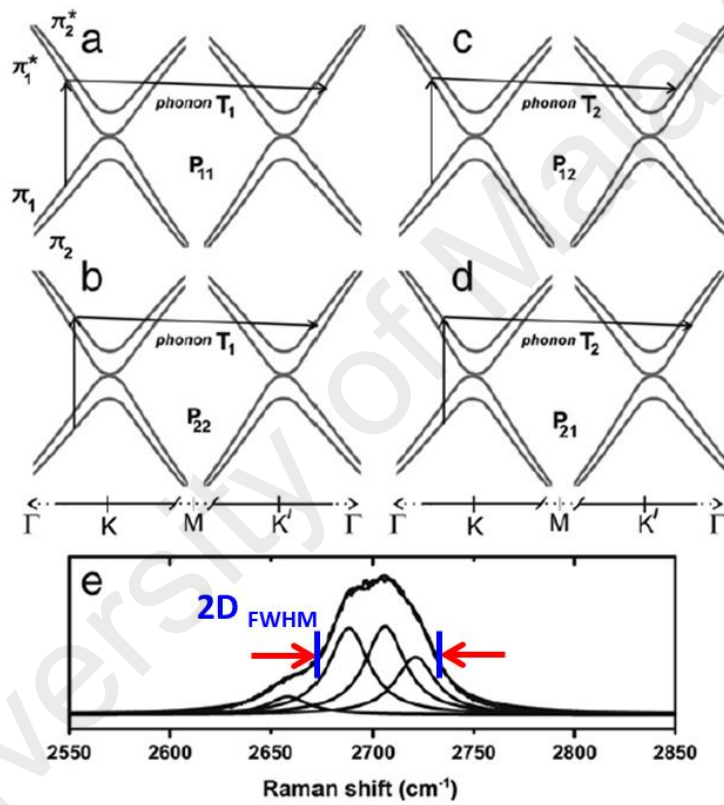


Figure 3.14: Schematic view of the electron dispersion of bilayer graphene near the K and K' points showing both π_1 and π_2 bands. The four Raman scattering process is indicate by: (a) P_{11} , (b) P_{22} , (c) P_{12} , and (d) P_{21} of electrons scattering. (e) The measured 2D peak, $\sim 2700 \text{ cm}^{-1}$ of Bernal (AB) stacked bilayer graphene will be deconvoluted into four Lorentzian peaks of peak frequencies at 2658, 2688, 2706, and 2721 cm^{-1} , respectively. This is correspond to the broadened in the $2D_{FWHM}$ peak as compared to monolayer graphene which can be fitted with single Lorentzian peak of $\sim 24\text{-}30 \text{ cm}^{-1}$ (Malard et al., 2009).

3.4.2.2 High Resolution Transmission Electron Microscopy (HRTEM)

In this work, high resolution transmission electron microscopy, HRTEM (JEOL JEM 2100F microscope) are employed to study the crystallographic structures of the nanoparticles. It is also one of crucial techniques to verify the formation of nanocomposite. The atomic resolution images (lattice image) are used to identify the lattice spacing, d of the nanoparticles. The lattice image of the atoms corresponds to the interference of transmitted beam (TB) and diffracted beams (DBs) of the crystal lattice.

The HRTEM possesses the same basic principle as light microscopy except that the photon source ($\lambda \sim 400$ nm) will be replaced with electron source ($\lambda \sim 4$ pm) which produce much shorter wavelength. Therefore, the resolution will be much higher compared to light microscopy and will be able to image into atomic-scale resolution. The electron gun in TEM system will act as an electron source which then a high voltage is applied in a range of 200 to 300 kV to accelerate the electron and transmitted through the thin sample (< 100 nm).

The transmitted electrons can be classified into three types, namely unscattered, elastically scattered and inelastically scattered electrons. The electrons transmitted through the specimen without any interaction with the sample atoms are called unscattered electrons which mainly contribute to the TEM images. The scattered incident electrons by the sample atoms with no loss of energy are called elastically scattered electrons which follow Bragg's diffraction law. The scattered electron forms a diffraction pattern and the diffraction at a specific area called selected area electron diffraction (SAED) pattern. This can give information on the structure, orientation and atomic arrangement of the sample. Lastly, the inelastically scattered electrons which loss its energy due to interaction with sample atoms provides the information of the compositional and chemical bonding of the sample. Typical results obtained from HRTEM characterization are shown in **Fig. 3.15** (Marquardt et al, 2014).

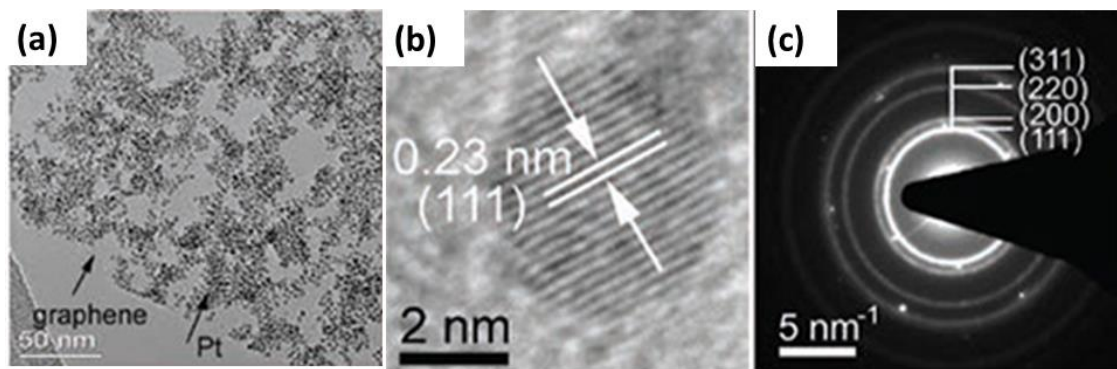


Figure 3.15: (a) TEM analysis of platinum/graphene nanocomposites (Aldrich Prod. No.803693). (b) HRTEM image of platinum nanoparticle with lattice spacing, d of 0.23 nm corresponds to (111) plane. (c) The corresponding SAED pattern of platinum/graphene nanocomposites (Marquardt et al, 2014).

To prepare the samples for the HRTEM analysis, firstly the fabricated sample on Cu foils is floated on the copper etchant to remove the substrate. Note that this process differs slightly from the graphene transfer process shown in **Section 3.2.4**, by removing the TRT and PMMA assisted layer. After the Cu foil is completely removed, the floated graphene sample on copper etchant solution is scooped out using silicon substrate as a support into DI water solution. Next, the graphene will then be scooped out using a copper grid (Formvar on 400 square mesh, Electron Microscopy Sciences, US). The graphene on copper grid is then put inside oven for two days at 60 °C to remove the moisture before it proceeds with the HRTEM characterization.

3.4.3 Elemental Composition Study

3.4.3.1 X-ray Photoemission Spectroscopy (XPS)

In this work, X-ray photoemission spectroscopy (XPS) are employed to investigate the elemental bonding (Carbon and Oxygen) of the samples. The characterization will be performed at the photoemission spectroscopy (PES) beamline, BL3.2a, of the Synchrotron Light Research Institute in Thailand. The PES system is equipped with a Thermo VG Scientific CLAM2 electron spectrometer and operated in the conditions of maximum photon energy 600 eV with an energy step of 0.1 eV. XPS is a surface-sensitive quantitative spectroscopic technique that measures the elemental composition which based on the photoelectric effect.

XPS spectra is obtained by irradiated an x-ray beam to the sample surface which then emitted as photoelectrons. Each of the atom in the surface has core electron with the characteristics binding energy that is conceptually, not strictly, equal to the ionization energy of that electron. When an X-ray beam directs to the sample surface, the energy of the X-ray photon will be absorbed completely by the core electron of an atom. If the photon energy is large enough, the core electron will then escape from the atom and emit out of the surface. The emitted electron from the top of sample surface with the kinetic energy of E_k will be referred as the photoelectron. Each element produces a characteristic set of XPS peaks at characteristic binding energy values that directly identify each element that exists on the surface. The binding energy of the core electron is given by Einstein relationship:

$$h\nu = E = E_b + E_k + \phi \quad (3.1)$$

$$E_b = h\nu - E_k - \phi \quad (3.2)$$

where $h\nu$ is the x-ray photon energy; E_b is the binding energy (B_E) of the electron, E_k is the kinetic energy of the electron as measured by the instrument and Φ is the work function induced by the analyser. Since the work function can be compensated artificially, it is eliminated, giving the binding energy as follows:

$$E_b = h\nu - E_k \quad (3.3)$$

Fig. 3.16 shows the electronegativity effects in (a) pure element and (b) carbon-oxygen bond. This can be described by the tendency of an atom or a functional group to attract electrons towards itself. In pure element, the electronegativity effect can be measured by the electron-nucleus attraction which then can be used to identify the elements (such as carbon, oxygen, copper and etc.) since photoelectron core level peaks in elemental samples occur at the same binding energy. However, when the charge of valence shell increases or decreases due to chemical bond formation (i.e. ionic or covalent bonding), the electrostatic potential is felt by the electron inside the atom will be changed and caused a net charge transfer to maintain charge neutrality. To reflect this change, the binding energy (BE) of the orbitals will be changed (Okpalugo et. al., 2005).

For example, the electronegativity effect of carbon-oxygen bond can be observed with the C1s narrow scan as shown in **Fig. 3.16(c)**. The highly ordered pyrolytic graphite (HOPG) consists of carbon atoms are exposed to various degree of ozone treatment (Webb et al., 2011). The chemisorbed oxygen upon ozone treatment to be bonded with carbon atom has shifted the C1s peak which denoted as C-O-C and O=C-C bonds, while the C-C bond remains at its original position. Due to electron-oxygen atom attraction pulled outwards of carbon nucleus, the core level electron near the carbon nucleus has lost its electronic screening, resulted to a chemical shifting to higher binding energy to maintain the charge neutrality.

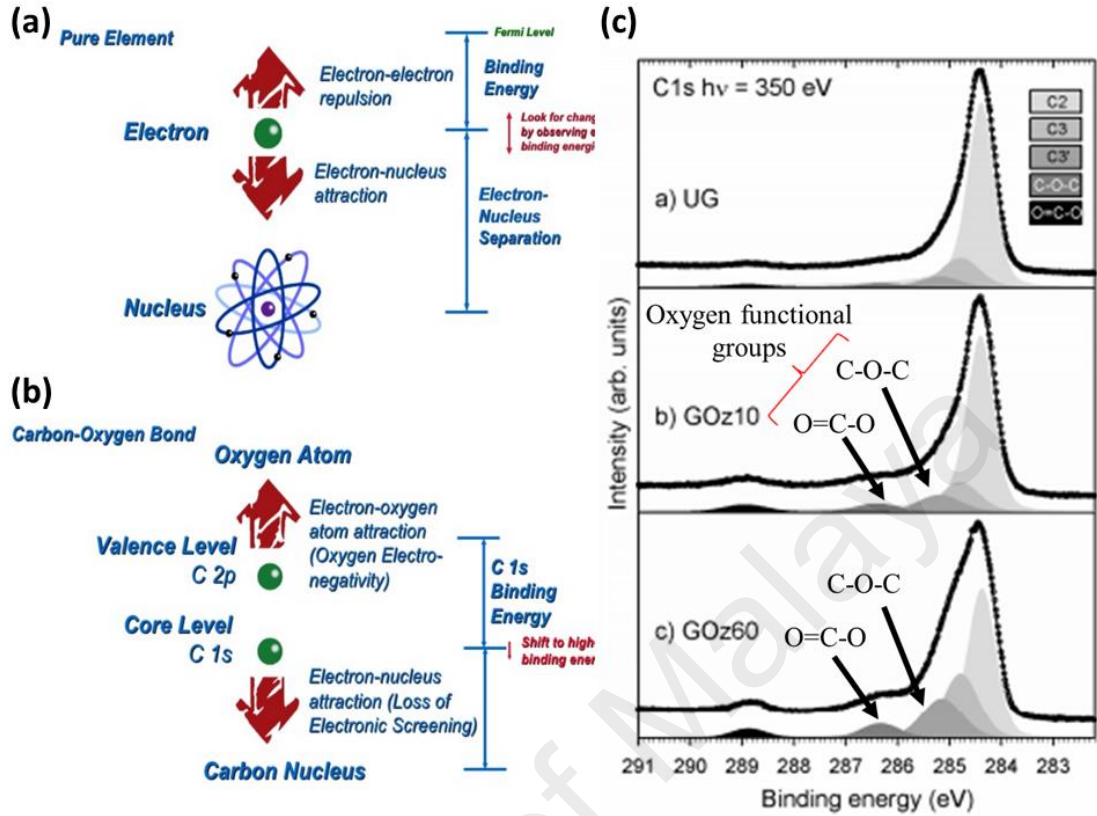


Figure 3.16: Electronegativity effect in (a) pure element and (b) carbon-oxygen bond. (c) High resolution XPS C1s spectra of (from up to bottom) untreated HOPG, HOPG after 10 minutes ozone treatment and HOPG after 60 min ozone treatment. The spectra highlight the significant increase in chemisorbed oxygen upon ozone treatment at pre-existing defect sites on the carbon element presents on the HOPG surfaces. (Webb et al., 2011)

3.4.4 Electrical Analysis

3.4.4.1 Van der Pauw Method

In this work, the sheet resistance of the samples are measured at room temperature with an Ecopia-HMS5300 measurement system based on the van derPauw method under a current excitation of 1mA. The van der Pauw method provides a convenient measurement method for the evaluation of semiconductor thin films. The sample will be mounting on SPCB board without any bonding wires. The spring loaded clamps will help to move probe pin easily x, y, z direction to connect the sample

edges. In addition, indium-tin (InSn) compound will be soldered on 4 point's corner as electro-conductivity materials, to improve the ohmic contact as shown in **Fig. 3.17(a)**.

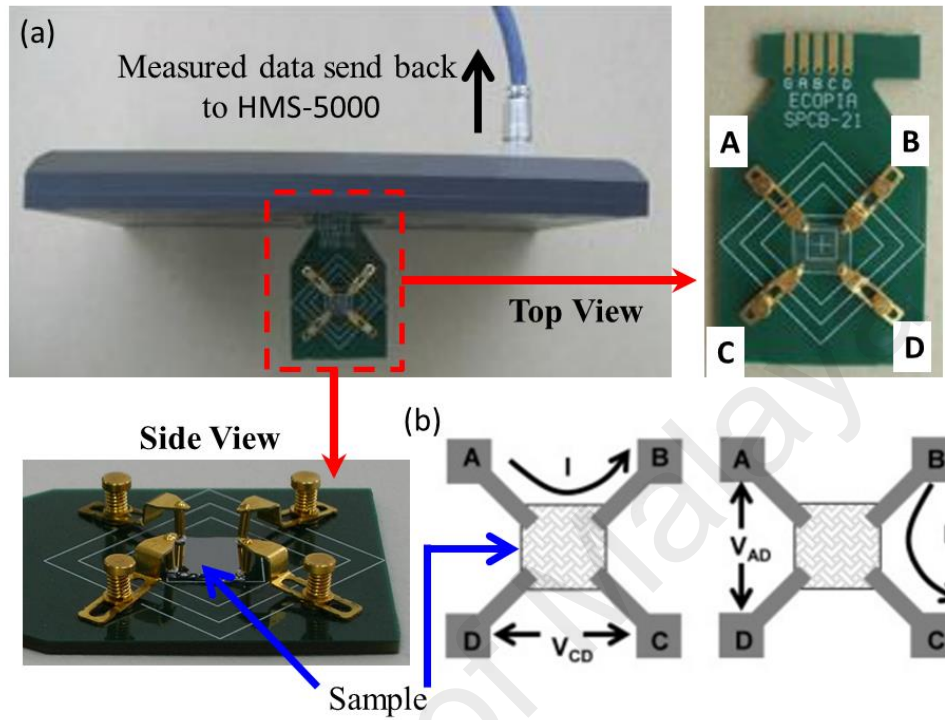


Figure 3.17: (a) Picture of sample board holder. The sample board shows 4 probe tip, A, B, C and D (top view) which will be connected with the sample edges by spring loaded clamps (side view). (b) Schematic of a rectangular Van der Pauw configuration used in the determination of the two characteristic resistances, R_{AB} (left) and R_{BC} (right) of the sample.

In order for the van der Pauw technique to work, the structure must be in uniform thickness, homogenous in composition, and symmetrical (Van der Pauw 1958; Matsumura et al., 2010). In addition, the contacts must be on the perimeter of the structure and much smaller than the area of the structure. Then, when the aforementioned conditions are met, the Van der Pauw showed the following relation holds:

$$e^{\left(-\pi \frac{R_{AB}}{R_S}\right)} + e^{\left(-\pi \frac{R_{BC}}{R_S}\right)} = 1 \quad (3.4)$$

where, R_{AB} and R_{BC} are associated with the resistance of corresponding terminals shown in **Fig. 3.17(b)** and R_S is the sheet resistance of measured sample. To obtain these two characteristic resistances, one applies a direct current, I_{AB} into contact A and out of contact B and measures the voltage V_{CD} from contact D to contact C as shown in **Fig. 3.17(b)**. Next, one applies the current, I_{BC} into contact B and out of contact C while measuring the voltage V_{AD} from contact A to contact D. Then, R_A and R_B are calculated by means of the following expressions:

$$R_{AB} = \frac{V_{DC}}{I_{AB}} \quad \text{and} \quad R_{BC} = \frac{V_{AD}}{I_{BC}} \quad (3.5)$$

3.5 Pressure Sensor Application

3.5.1 Test Set-up

In order to develop a graphene-based flexible pressure sensor, the fabricated samples are incorporated onto an effective sensing area of $5 \times 5 \text{ mm}^2$ with patterned IDE/polyimide film substrate. To demonstrate the pressure sensing performance, the fabricated sensor are initially attached to the substrate with a square cavity area of $5 \times 5 \text{ mm}^2$ using epoxy. It is then sealed and clamped completely on a test jig by epoxy bonding and carbon tape to prevent gas leakage as shown in **Fig. 3.18** and **Fig. 3.19**. A differential applied pressure of up to 50 kPa from an N_2 gas supply system to the cavity is controlled and monitored using an ultralow pressure regulator and a reference pressure sensor (Vernier, gas pressure sensor). The length of pipeline from the valve to the fabricated pressure sensor and the commercial pressure sensor are fixed at 20 cm. In this case, the applied pressure on the fabricated pressure sensor are assumed to be equal to the measurement of the reference pressure sensor. Both the diaphragm and graphene experienced deformation under the applied pressure

(see **Fig. 3.20**), and the resistance changes are simultaneously measured using a source-meter (EA4980A Agilent, LCR meter) at ambient conditions.

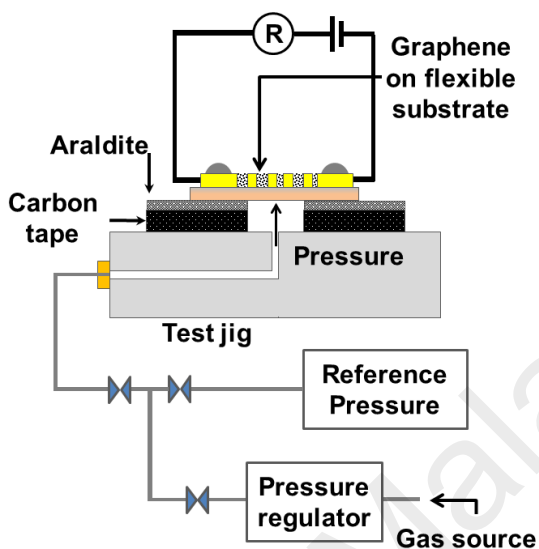


Figure 3.18: Schematic diagram of pressure sensor set up.

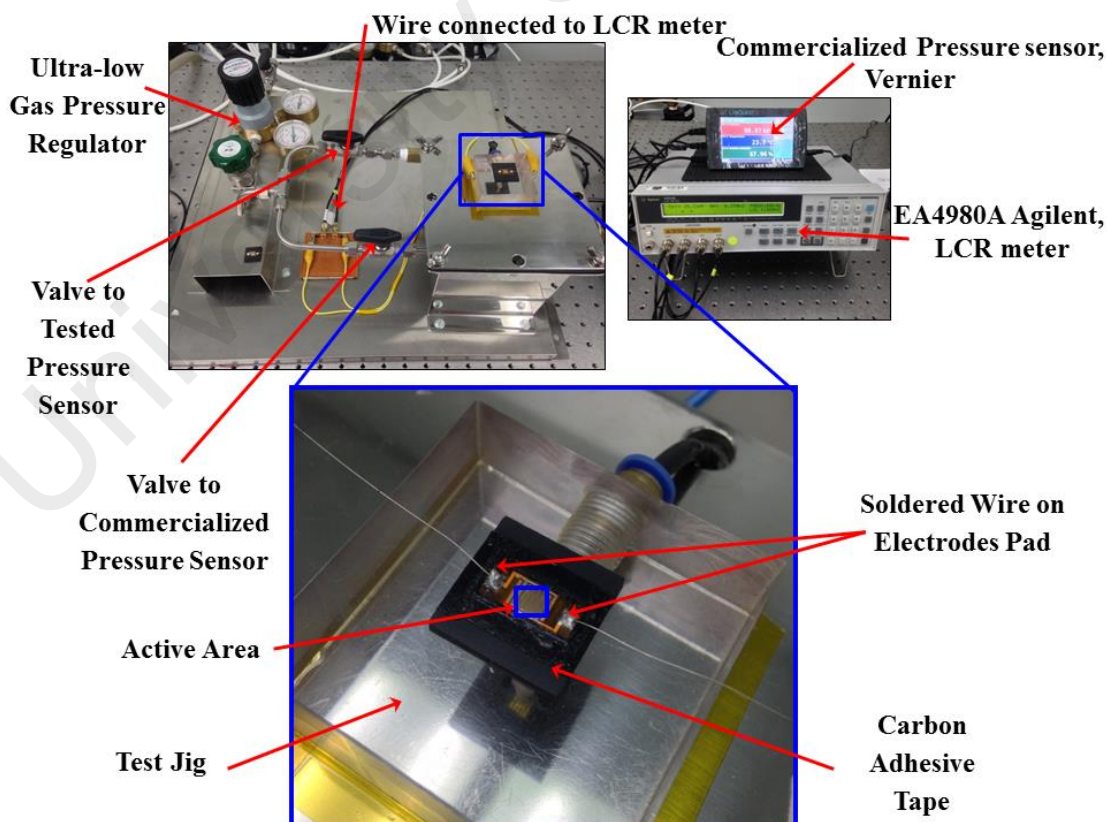


Figure 3.19: Photograph of pressure sensor set up.

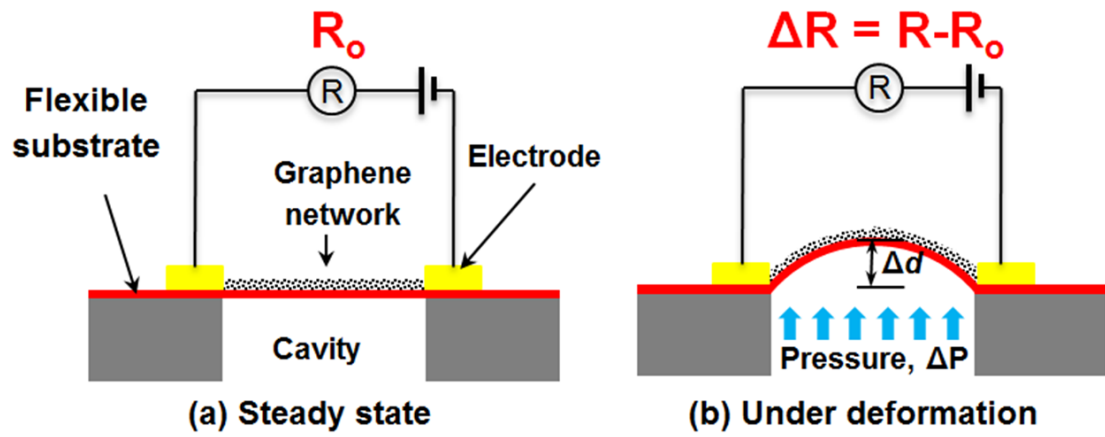


Figure 3.20: Illustration of (a) steady state and (b) under deformation state of flexible pressure sensor device. The deflection of pressure sensor device would change the initial resistance (R_0) into the resistance value measured under deformation (R).

3.5.2 Simulation of Pressure Sensor Device

3.5.2.1 Finite Element Analysis

Finite element analysis (FEA) is a computerized method for predicting how a product reacts to the real-world physical effects such as forces, vibration, heat and fluid flow. FEA shows whether a product will break, wear out, or work the way it was designed. In this section, results from the mechanical simulations of the designed polyimide diaphragm structure incorporated with IDE array for the designed flexible pressure sensor will be presented in order to study its characteristics under a low pressure regime (0 to 50 kPa). The software used for finite element analysis is CoventorWare®. Prior to that, the simulation procedures and results would be validated with existing published results. For the present study, results for the maximum deflection and stress characteristics of the diaphragm structure subjected to a uniform pressure loading obtained via MemMECH solver of CoventorWare® programme would be compared to the analytical model reported by Timoshenko et al. (1959);

$$\omega_0 = 0.0151 \left(\frac{Pa^4}{Eh^3} \right) (1 - \nu^2) \quad (3.6)$$

$$\sigma_{max} = 0.308q \left(\frac{a}{h} \right)^2 (1 - \nu^2) \quad (3.7)$$

where w_0 is the maximum deflection, σ_{max} is the maximum stress, P represents the applied pressure, h is the diaphragm thickness, a is the diaphragm width or length, q is the stress tensor, E is the Young's modulus and ν is the Poisson's ratio.

It should be noted that the diaphragm structure is modelled as a quarter of square plate element with fully clamped around its peripheries, in which the area of the diaphragm (A) is set at $1000 \times 1000 \mu\text{m}^2$ with uniform thickness (h) of $13 \mu\text{m}$. The material constants will be assumed as follows: Young's modulus, $E = 169 \text{ GPa}$ and Poisson's ratio, $\nu = 0.064$. The modelled diaphragm is then subjected to the uniform pressure loading, ranging from 0 to 50 kPa. **Table 3.3** and **Table 3.4** had shown the deflection at the centre of square diaphragm and maximum stress distribution from the different methodologies of interest for verification purposes. The results indicate that the deflection and stress of the diaphragm increase as the applied pressure increases. The obtained results from MemMECH solver show in a good agreement with the results from the analytical model by Timoshenko et al. (1959) obtained from Equation 3.6 and 3.7 with the percentage of variations rated at less than 1%. Therefore, it can be determined that the methodology presented here would be confidently utilized for predicting the mechanical characteristics of the diaphragm.

Table 3.3 Comparison of deflection results between MemMECH solver and analytical model by Timoshenko et al. (1959) for the square diaphragm structure.

Pressure, P (kPa)	Deflection of diaphragm at point (0, 0), w0 (μm)		
	Analytical model – Timoshenko (1959)	MemMECH solver (present study)	[%] Difference
0	0	0	-
10	0.40502	0.40813	0.768
20	0.81004	0.81626	0.768
30	1.21506	1.22440	0.768
40	1.62008	1.63253	0.768
50	2.02511	2.04066	0.768

Table 3.4 Comparison of stress results between MemMECH solver and analytical model by Timoshenko et al. (1959)

Applied pressure, P (kPa)	Maximum stress of diaphragm, $\sigma_{xx} = \sigma_{yy}$ (MPa)		[%] Difference
	Analytical model – Timoshenko (1959)	MemMECH solver (present study)	
0	0	0	-
10	18.2249	18.0818	0.785
20	36.4497	36.1636	0.785
30	54.6746	54.2454	0.785
40	72.8994	72.3272	0.785
50	91.1243	90.4090	0.785

Next, the fabricated flexible pressure sensor platform of interdigitated electrode (IDE) array on polyimide film substrate (**Section 3.3.1**) is further run for FEA. The detail parameters of the fabricated flexible sensor platform are as follows: thickness of polyimide film substrate = 60 μm, thickness of silicon resin adhesive = ~10 μm, thickness of IDE array = 35 μm. The electrode finger width = 500 μm, electrode finger gap = 200 μm, with area of contact pads = 2000 × 2000 μm². The number of electrodes finger are fixed to 8 fingers. From the FEA, the maximum deflection, d shown by MemMECH solver is linearly proportional to the applied pressure, ΔP as shown in **Fig. 3.21(a)**. The nonlinearity as a function of applied pressure for the fabricated flexible pressure sensor platform is shown in **Fig. 3.21(b)**.

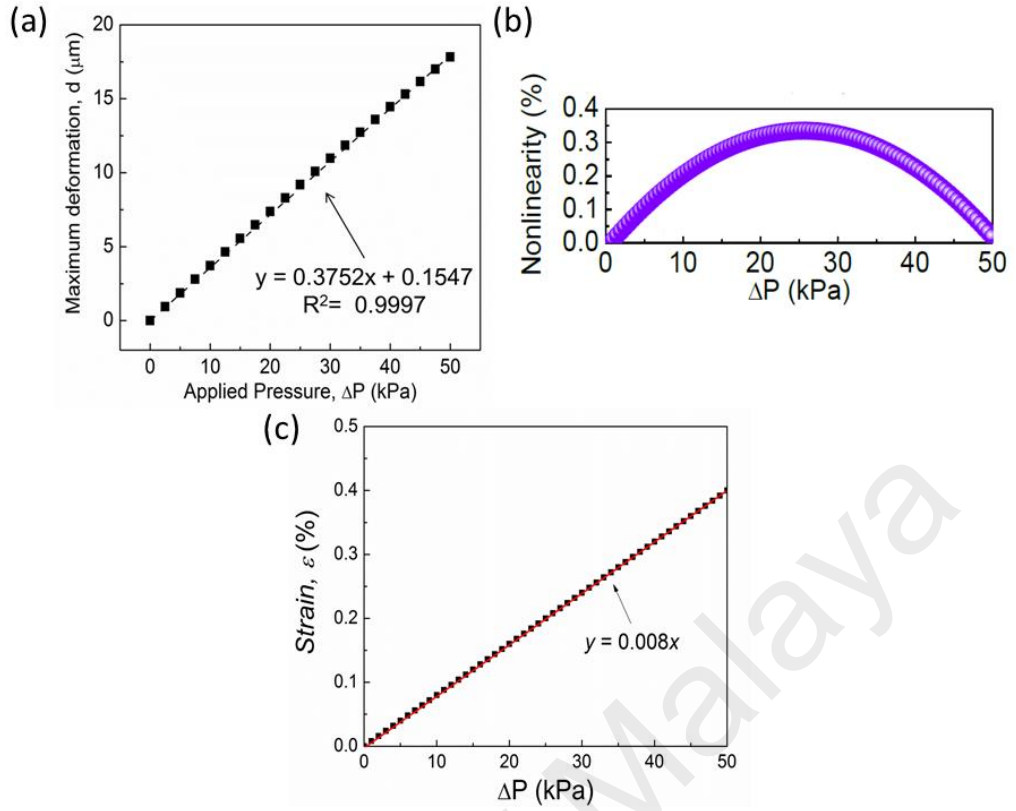


Figure 3.21: (a) Plot of maximum deformation, d with respect to applied pressure obtained from FEA for fabricated flexible pressure sensor platform shown in **Section 3.3.1**. (b) Nonlinearity as a function of applied pressure. (c). Calculated strain, ϵ (%) exerted due to the deformation of the fabricated sensor when applied to a pressure range of 0-50 kPa. The solid lines are given as guides to the eye.

The maximum nonlinearity of the diaphragm deflection happened at applied pressure of 25 kPa. The deflection effect induced a nonlinear stress on the diaphragm in x , y and z -directions due to finite elongation in the central interior of diaphragm plane, which is found to be unavoidable (Timoshenko et al., 1959). The calculated strain, ϵ (%) simulated by MemMECH solver which exert due to the deformation of the fabricated sensor when applied to a pressure range of 0-50 kPa is shown in **Fig. 3.21(c)**. Since the thickness of graphene films are extremely thin ($\sim 0.001 \mu\text{m}$) compared to the fabricated flexible sensor platform ($\sim 100 \mu\text{m}$), it is deduced that graphene will follow the given simulated deformation. From this simulation by FEA, the gauge factor (GF) of fabricated graphene-based pressure sensor devices can be calculated which will be further discussed in Chapter 5.

CHAPTER 4: REDUCED GRAPHENE OXIDE BY HYDROGEN PLASMA TREATMENT

4.1 Overview

This chapter will present preliminary work done on the synthesis and characterization of reduced graphene oxide (rGO) grown using a top-down approach prior to venturing into the actual work done on graphene and graphene/copper oxide nanocomposites grown by hot-filament thermal chemical vapour deposition (HFTCVD) process, a bottom-up approach. Although this work is not in line with the title of the thesis, the results and discussion in this part of the work is important in introducing the other parts of the thesis. The characterization techniques used in this chapter are very important in recognizing that graphene that has been successfully synthesized. Also the application of rGO in this work as a gas sensor introduces important direction in used of graphene in sensor application. This work also gives an opportunity for the existing plasma enhanced chemical vapour deposition (PECVD) system to be tested as an effective system to generate the hydrogen plasma for treating the graphene oxide (GO) surface to produce reduced graphene oxide (rGO). A system called the Hot-Filament Thermal Chemical Vapour Deposition (HFTCVD) system for the growth of graphene and graphene/Cu₂O nanocomposites which are the materials investigated for the actual work of this thesis is developed in the next phase of this work based on the design and operation of the PECVD system used for the hydrogen plasma treatment of GO in this work. Since the work presented in this chapter is not a part of the main focus of this thesis, the synthesis technique used in growing the rGO samples for this work is presented in this chapter and not in Chapter 3, the chapter focusing on the various experimental techniques done as reflected by the title of the thesis.

This work is focused on studying hydrogen plasma treated rGO, its properties and application as a carbon dioxide gas sensor. The oxygen functional groups in GO has the effect of lowering the electrical conductivity of the material. Hydrogen plasma treatment are used to remove the oxygen functional groups at the basal plane and edges of graphene oxide flakes to obtain the rGO. However, sputtering and ion bombardment effects can result in the formation of porous and rougher surface rGO. The effects of the parameters used during the hydrogen plasma treatment are expected to have effects on the morphology, degree of reduction and chemical bonding properties. Gas sensing capability will also be systematically studied using rGO produced from the optimized rGO hydrogen plasma reduction parameters in the second part of this work. The rGO based gas sensors performance are tested in dry N₂ and humid atmospheric environments. The sensing mechanism of rGO will be proposed to explain the observed reaction. The flow-chart showing the progression of the work done in this chapter is shown in **Fig. 4.1**.

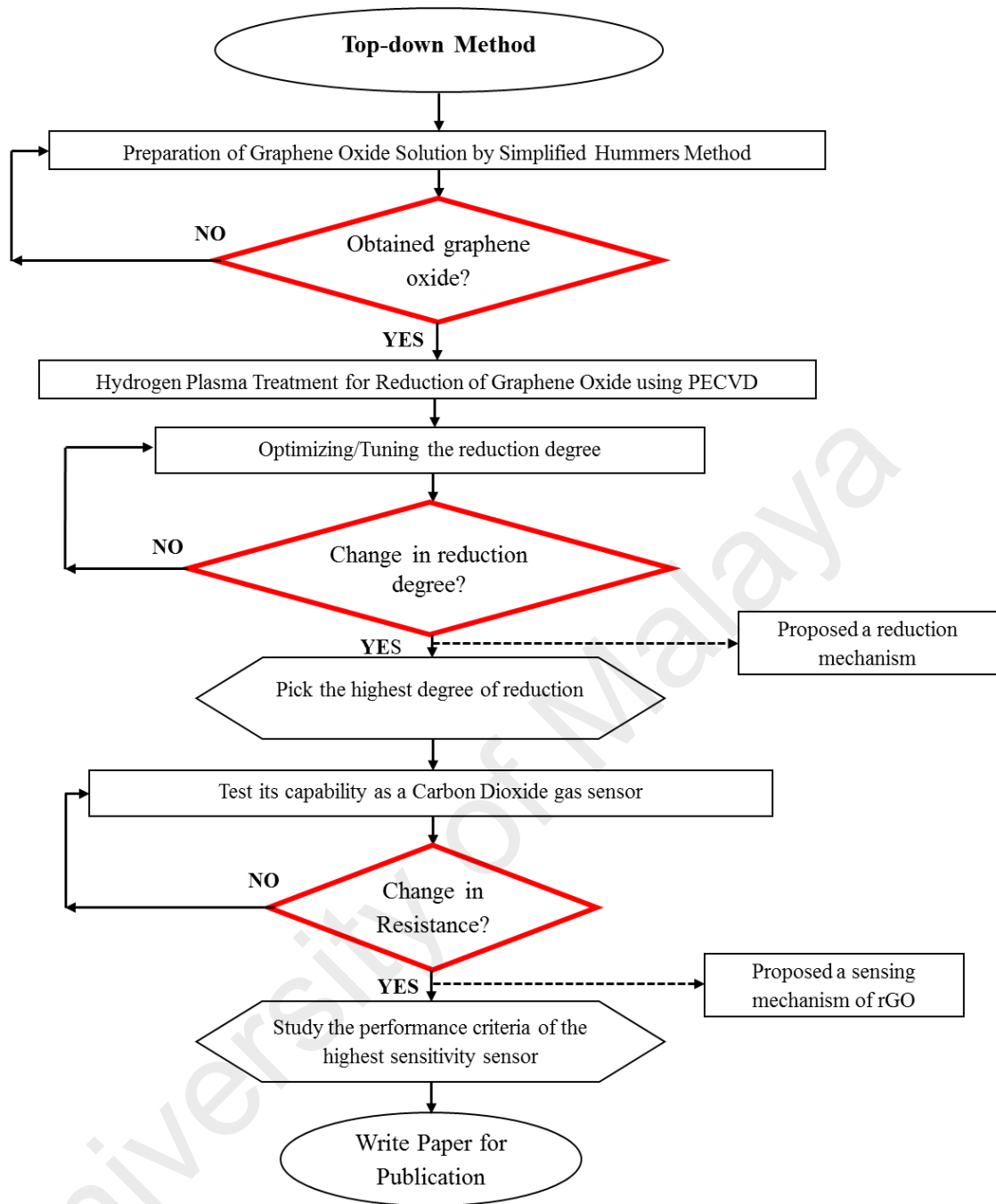


Figure 4.1: Flow chart showing the progression of graphene fabrication using top-down approach and its potential application as a gas sensor.

4.2 Synthesis of Graphene Oxide: Top-down Method

4.2.1 Simplified Hummers Method

The Hummers method is a top-down approach used in producing graphene oxide for this part of the work. The aim of chemical oxidation process, referred to as simplified Hummers method is to exfoliate graphite into monolayer graphene oxide (GO) by strong acids and oxidizing agents. Chemical reactions on the graphite planes attach oxide functional groups onto the graphite planes which in turn weaken the bonds between consecutive layers resulting in the formation of graphite oxide. The oxidation process of graphite involves adding KMnO_4 (18 g, 6 g wt%) gradually to $\text{H}_2\text{SO}_4\text{:H}_3\text{PO}_4$ (320:80, mL) and graphite flakes (Grade 3061, 3 g wt%, Asbury Graphite Mills Ins.) using a stirrer. This one-pot mixture is left to stir for 3 days in room-temperature environment to allow complete oxidation of graphite. The colour of the mixture changes from dark purplish green to dark brown when the oxidation process is completed. Next, solution of $\text{KMnO}_4\text{:H}_2\text{O}_2$ (12:8 mL) in freezing deionized water (400 mL) is added to stop the oxidation process and the colour of the mixture is changed to bright yellow, indicating a high level of oxidation of the graphite flakes. The mixture is left to rest for 10 minutes before proceeding to the next step. The graphite oxide formed is then washed three times in 1 M of HCl (37%, Sigma-Aldrich) aqueous solution and repeatedly with deionized water until a pH of 4–5 is achieved. The washing process is carried out using simple decantation of supernatant via centrifugation (HITACHI model CR21F; Hitachi, Japan) at 6000 rpm for HCl and 11500 rpm for deionized water for 30 minutes each. During the washing process with deionized water, the graphite oxide became exfoliated, which results in the thickening of the graphene solution thus, forming a GO gel. Next, the concentrated GO gel is diluted with ethanol (95%, Merck) to obtain 1 mg/mL GO solution. Finally, 3 μL of diluted GO solution are spin-coated on

SiO₂/Si and pre-pattern silicon die (gas sensor device) substrates at 2000 rpm for 30 seconds.

4.2.2 Characterization

4.2.2.1 Structural Properties

Fig. 4.2 shows the Raman spectra of graphite and GO on SiO₂/Si substrate. Typical D, G and 2D peaks at 1354, 1582 and 2727 cm⁻¹ for graphite and 1343, 1587 and 2700 cm⁻¹ for GO are observed in these spectra. The D+D' peak is only observed in the GO Raman spectrum at 2930 cm⁻¹.

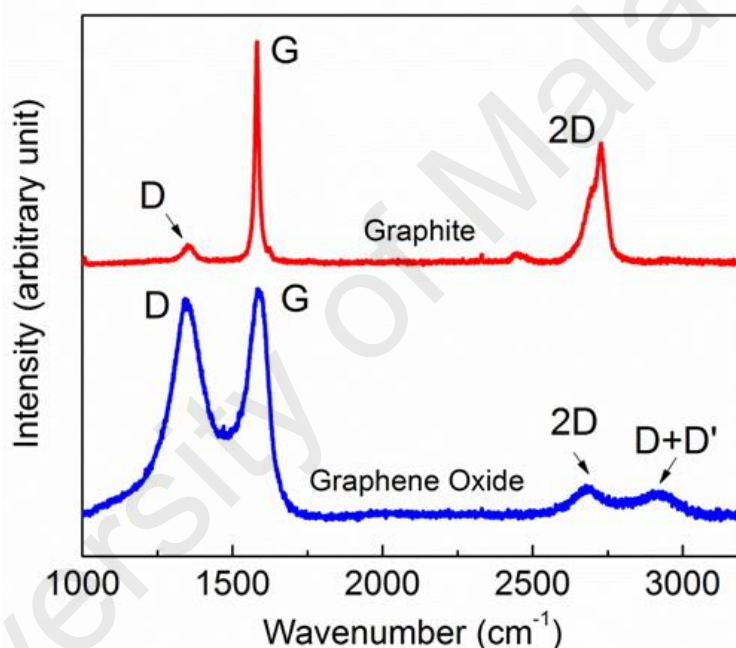


Figure 4.2: (a) Raman spectra of graphite and graphene oxide. Note that the significant increase of D peak, the broadening of D and G peak as well as appearance of D+D' peak denoted the graphite has been successfully converted into graphene oxide.

The D and G peaks are attributed by the out-of-plane breathing mode of the sp² atom due to defects and E_{2g} phonons at the centre of Brillouin zone (BZ) respectively (Malard et al., 2009). The Raman spectrum of the GO revealed a D peak with the intensity comparable to the G peak and the broadening of these peaks are an indicative of significant structural disorders due to the harsh oxidation condition in Hummer's process. The 2D peak originates from a double resonance mechanism of

two iTO phonons near the K and K' points in the BZ of graphene oxide. However, for the graphene oxide sample which contains oxygen functional groups attached to the basal plane which disrupts the triple resonance mechanism, the 2D peak intensity is significantly reduced compared to the graphite sample. The D+D' peak are contributed by the iTO or iLO phonon modes near the K points in the BZ, indicating the presence of a certain degree of defect density in the structure of graphene oxide sample due to attachment of oxygen functional groups.

4.2.2.2 Elemental Composition Properties

XPS is a powerful method to study the bonding properties of the sample. The Simplified Hummers method introduces oxygen functional groups bonded to the carbon backbone inside the graphite, and these changes due to the bonding configurations in the sample can be detected by measuring the C1s narrow scan peak as shown in **Fig. 4.3**. Due to the electronegativity effect of carbon-oxygen bond, the C1s peak appears to be broader (Okpalugo et al., 2005). The C1s peak can be fitted to four deconvoluted components, located at 284.1 eV, 286.4 eV, 287.8 eV, and 288.9 eV (Yang et al., 2009; Wang et al., 2010; Shen et al., 2012). These components are assigned to the graphite backbone; C-C=C and oxygen functional groups; C-OH, C=O and COOH, respectively which confirm the formation of graphene oxide (Ming et al., 2010). Prior to deconvolution of these peaks, Shirley's background subtraction is carried out. This is done to eliminate the effects of inelastic scattering events the photoelectrons undergo as they are transported from the point of excitation to the surface of the sample, thus giving rise to the inelastic background intensity. The C-C=C, C-OH and C=O components are fitted using a Gaussian curve while the O=C-OH peak located at the tail of C1s peak is fitted with a Lorentzian curve because it tends to be wider at higher binding energies. In addition, the peak position has been fixed with respect to their chemical bonding while the FWHM of each deconvoluted

components will be adjusted to a certain extent (the FWHM of each component will not have twice the value from one another) to fit the raw data.

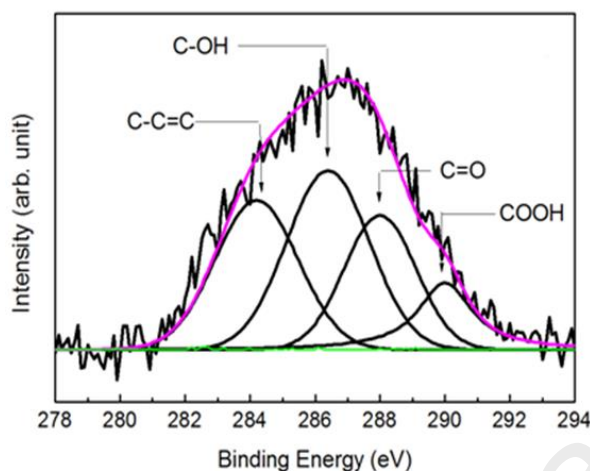


Figure 4.3: Deconvoluted XPS spectrum of C1s narrow scan peak for GO sample.

4.2.2.3 Morphological and Topological Properties

From FESEM images shown in **Fig. 4.4** (left), it is clearly observed that graphite flakes are composed of thick multi-layered structure with average lateral size of 600 μm . The layers of graphite are then exfoliated by chemical oxidation process producing a single layer of graphene oxide with much smaller lateral size ranging from 40 to 100 μm as shown in **Fig. 4.4** (right). The overlapping layer between GO flakes shows a darker contrast as compared to the single graphene layers which appear to be slightly transparent. The topological image of graphene oxide on SiO_2/Si substrate shows non-overlapping image of single layer GO flakes with wrinkles on its surface as shown in **Fig. 4.5** (left). Next, to confirm the successful process of exfoliation from graphite into GO via Simplified Hummers method, the thickness of GO flakes is measured by AFM. The thickness of GO flake is measured to be 0.947 nm as measured from the cross-sectional height profile, confirming the formation of a single-layer structure of GO as shown in **Fig. 4.5** (right) (Gao et al., 2010). This height is somewhat larger than the value of 0.8 nm predicted from theory, but similar results have also been reported by others from AFM measurements (Gómez et al., 2007).

The thickness measured was assigned to individual graphitic sheets bearing oxygen functional groups on both faces (Chen et al., 2010). In addition, the observed ‘spike-like’ features on the flake with heights exceeding the normal GO (> 3 nm) can be attributed to the point defects in the carbon lattice that cause the wrinkling of the sheets in the nanometre scale.

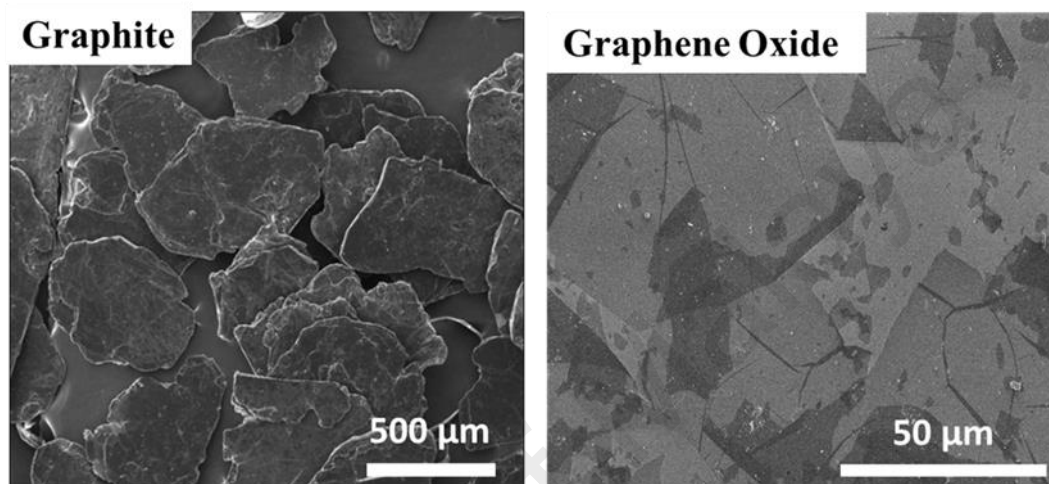


Figure 4.4: FESEM morphological images of graphite (left) and graphene oxide (right).

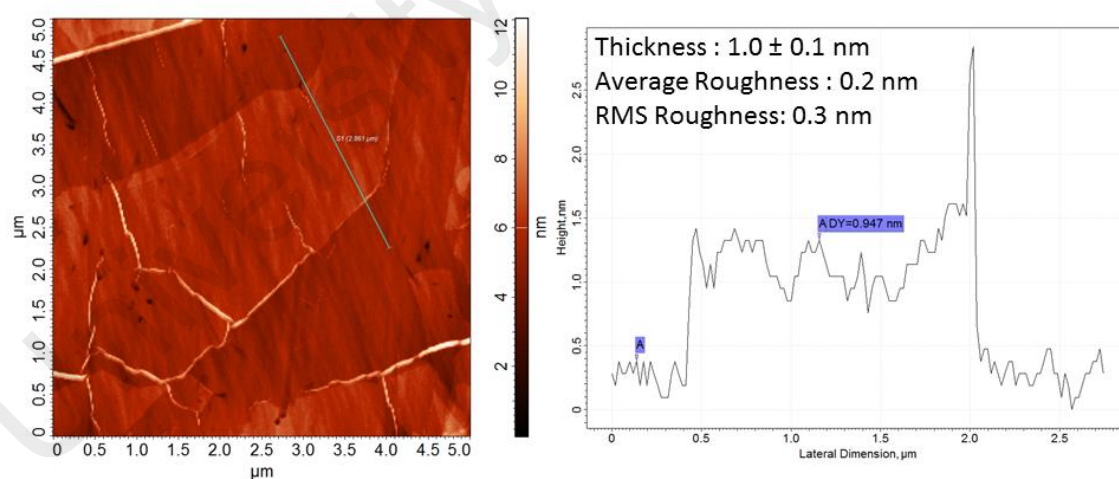


Figure 4.5: AFM topological image of graphene oxide on SiO_2/Si substrate (left) and corresponding cross-sectional height profile with an average thickness of 1.0 ± 0.1 nm (right).

4.3 Reduced Graphene Oxide by Plasma-Enhanced CVD Technique

4.3.1 System Overview

The GO are reduced by hydrogen plasma treatment in a custom-made PECVD system shown in **Fig. 4.6**. The PECVD chamber is made from stainless steel and consists of three parts namely, top-plate, chamber body and bottom-plate. The top-plate carries the feed through carrying the gas inlet and air admittance valve. The radio frequency power supply is also connected to the top-electrode via a feed through on the top-plate. The chamber body holds a view port to observe reaction process. The bottom-plate holds the connections via valves to the pumping system and electrical feed through for the heater, temperature sensor, thermocouple and ground. These three chamber components are sealed by O-rings and tightened by nuts and bolts to achieve the desired vacuum condition for the plasma treatment process. The substrate spin-coated with GO is placed on the substrate holder. The distance between the top electrode which also carries the gas shower head and the bottom electrode is 6 cm. The sample holder is grounded while the shower head is connected to the 13.56 MHz radio frequency power supply. A K-type thermocouple is positioned underneath the substrate throughout the plasma treatment process to monitor the substrate temperature. Different stages of the plasma treatment process are summarized in **Table 4.1**.

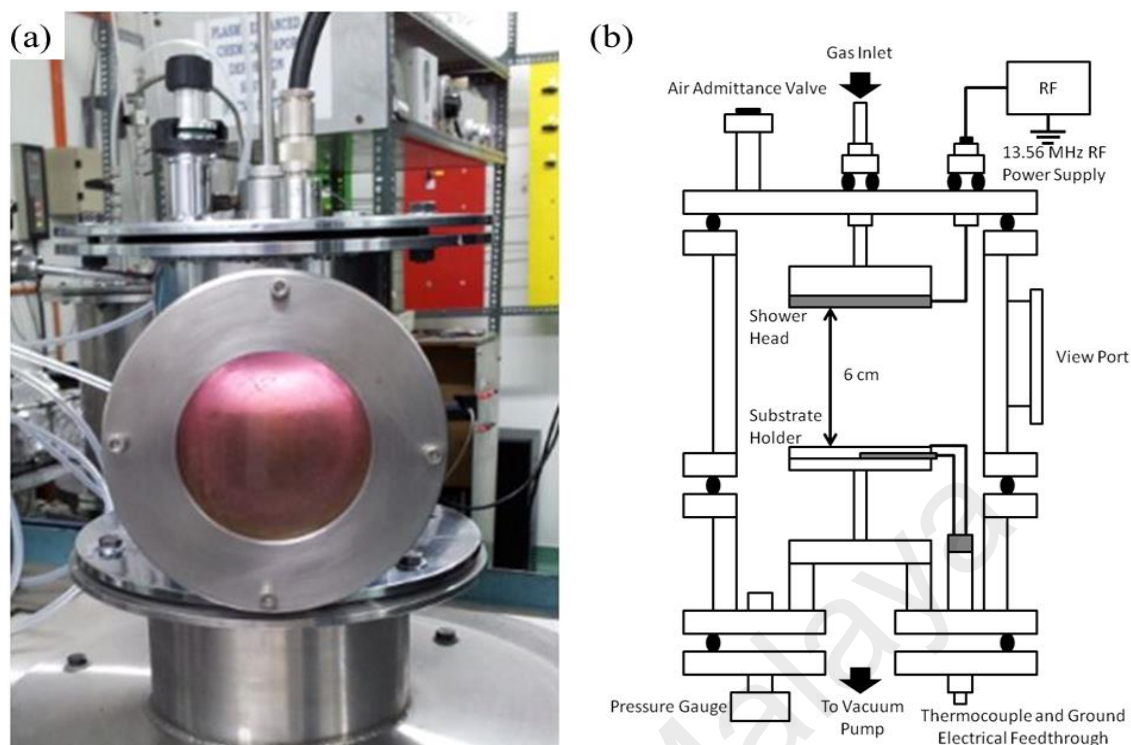


Figure 4.6: (a) Photograph and (b) schematic diagram of the custom-made plasma enhanced chemical vapour deposition (PECVD) chamber used for room-temperature hydrogen plasma reduction.

Table 4.2: General plasma treatment procedures carried out by PECVD technique.

Stage	Process	Condition	Remarks
Pre-treatment	Substrate Cleaning Process	Atmospheric	To remove impurities existing on the substrate
	Vacuum Process	Vacuum	Clean deposition environment and minimize contamination in the sample
Plasma Reduction Process	H ₂ Treatment Process	Vacuum	*Refer to Table 4.3
Post-treatment	Gas-line Cleaning	Vacuum	Safety purposes
	Chamber Cleaning	Atmospheric	To avoid contamination from previous deposition

4.3.2 Sample Preparation Process

The SiO₂/Si substrates used in the experiment are cleaned to remove undesired contaminants. The substrates are handled with tweezers at all time. The SiO₂/Si substrates are first cleaned in deionized water. It is then immersed in a solution of H₂O:H₂O₂:HCl in ratio of 6:1:1 for 10 minutes. Subsequently, the substrates are taken out of the solution and rinsed again in deionized water to remove remaining H₂O:H₂O₂:HCl solution. The substrate is then immersed in the solution of H₂O:H₂O₂:NH₄OH in a ratio of 5:1:1 for about 5 minutes. Deionized water again is used to clean the remaining reagent and purged with nitrogen to dry. The cleaning process is done just before the sample is placed on the sample holder for the hydrogen plasma treatment process.

4.3.3 Room-temperature Hydrogen Plasma Treatment Process

A custom-built plasma enhanced chemical vapour deposition is employed to perform the hydrogen plasma, radical-assisted chemistry method on the samples. The 13.56 MHz radio frequency generator is used to generate the hydrogen plasma in between two metallic-parallel plate electrodes with 10 W radio-frequency power. Two sets of samples are studied for this work. The first set of samples consists of samples reduced at two different treatment times of 20 (rGO-P20) and 40 s (rGO-P40) while the second set of samples are deposited at two different flow-rates of hydrogen, 40 (rGO-F20) and 50 sccm (rGO-F50). The details on the deposition parameters used during the hydrogen plasma treatment for these samples are summarized in **Table 4.3**. The electrode distance and radio-frequency power are fixed at 6 cm and 10 W to minimize sputtering and bombardment effects from energetic hydrogen ions avoid formation of porous and rough rGO surface. A thermocouple fixed on the substrate holder is to monitor the temperature during the reduction process.

The increase in temperature caused by the plasma bombardment effects is measured to be around $27 \pm 1^\circ\text{C}$ (measured from the process with the longest treatment time).

Table 4.3: Summary of the hydrogen plasma reduction parameters performed by PECVD technique.

Set	Study Parameter	Plasma Reduction Process	
		Fix	Vary
1	Effect of Plasma Treatment Time	D=6 cm RF=10 Watt F_{H_2} =50 sccm T_s =27 °C P=0.8 mbar	t=20 and 40 sec
2	Effect of Hydrogen Flow Rate	D=6 cm RF=10 Watt T_s =27 °C t=40 sec	F_{H_2}=20 and 50 sccm correspond to P=0.30 and 0.65 mbar respectively
*D is distance between gas inlet and sample; RF is radio frequency power; F_{H_2} is hydrogen flow rate; T_s is temperature of substrate; t is plasma exposure duration and P is pressure inside the chamber.			

4.3.4 Results and Discussion

4.3.4.1 Structural Properties

In this work, Raman spectroscopy is employed to observe the structural evolution by focusing the changes in D and G peaks due to sp^3 type of defect causes by plasma treatment as shown in **Fig. 4.7** (Felten et al., 2013; Eckmann et al., 2013). Analysis of fitted peak heights ratio of the D and G peaks, I_D/I_G gives an insight into the reduction process by removing oxygen functional groups that create imperfections within the carbon basal plane and can be related to the in-plane sp^2 crystallite size, L_a (Pei et. al., 2012). A low I_D/I_G ratio shows an increase of the L_a due to the disorder associated with oxygen functional groups being diminished (Ganguly et al., 2011). Due to the harsh oxidation process involved from Hummer's method, the D band increases dramatically which resulted in a high I_D/I_G ratio of 0.94 for the untreated sample. This value is close to the value reported for the GO obtained from Wang et al. (2010) and Ganguly et al. (2011). After reduction, the I_D/I_G ratio for the rGO-P20, rGO-P40, rGO-F50 and rGO-F20 are change to 0.89, 0.84, 0.91 and 0.81 respectively. By employing the relation of the I_D/I_G ratio and L_a proposed by Tuinstra and Koenig, the in-plane sp^2 crystallite size is determine using the equation $1/L_a = C(\lambda) \times (I_D/I_G)$, where the coefficient $C(\lambda)$ depends on the excitation wavelength due to resonance effects (Eda et. al., 2010). The Raman wavelength laser, λ used in this work is 514 nm then gives $C(514 \text{ nm}) = 4.4 \text{ nm}$ as reported in literature (Eda et. al., 2010). The L_a values calculated are 4.7, 4.8, 4.9, 5.2 and 5.4 nm for the GO, rGO-F50, rGO-P20, rGO-P40 and rGO-F20 samples respectively. These results indicates that the hydrogen plasma treatment on the GO sample is capable of removing the oxygen functional groups and restores the sp^2 C=C bonds depending on the plasma generating parameters used during the hydrogen plasma treatment.

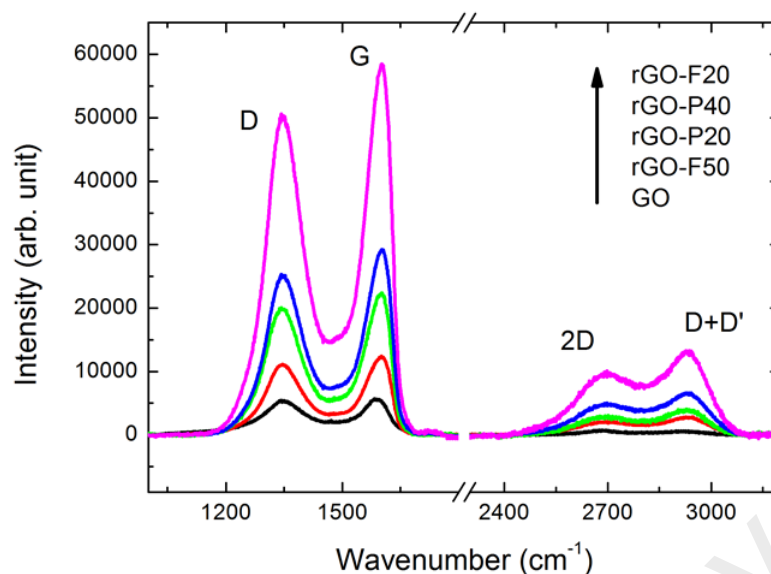


Figure 4.7: Raman spectra of the graphene oxide and reduced graphene oxide with different degrees of structural evolution. The spectra consists of D, G, 2D and D + D' peaks located at 1343, ~1590, 2700 and 2930 cm^{-1} , respectively. Note that the D + D' peak monotonously increase in intensity and broadens with the spectra stacking order shown above, due to ion-bombardment effect.

4.3.4.2 Elemental Composition Properties

XPS is a powerful method to study the bonding properties of a sample, since oxidation introduces functional groups bonded to the carbon atom and reduction will recover the C=C bonds thus changes in the bonding structure in the sample could be determined. The measurements are performed within a wide scanning range for typical GO and rGO material to show the elemental composition present as shown in **Fig. 4.8(a)**. The spectra consists of O, C and Si element which comes from GO and SiO_2/Si substrate. The high-resolution O1s and C1s spectra are measured for detailed analyses on the bonding configurations in the sample as shown in **Fig 4.8(b)**. The deconvoluted O1s peaks for GO and rGO samples show the C-OH, C=O and COOH at 530.7, 532.1 and 533.8 eV, respectively. However, the C=O and COOH bonds present in the rGO sample appears significantly smaller compared to C-OH bonds.

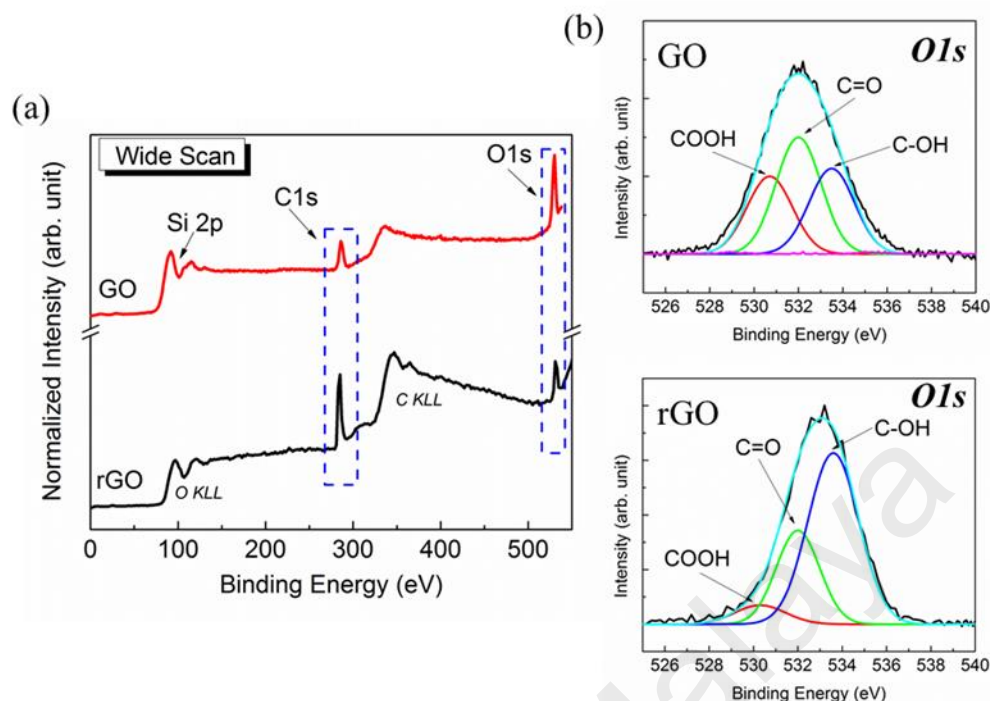


Figure 4.8: (a) Comparison of typical wide scan XPS spectra of GO and rGO sample. Note that the difference in intensity of the O1s and C1s peaks between GO and rGO sample. (b) Deconvoluted O1s narrow scan of a typical GO and rGO sample.

Next, the C1s peak is then deconvoluted into the component C-C=C, C-OH, C=O and O=C-OH peaks at 284.4, 286.4, 287.8 and 288.9 eV, respectively as shown in **Fig. 4.9**. The GO shows a high intensity of individual functional groups and after reduction by hydrogen plasma treatment, a significant decrease in intensity of oxygen functional groups is observed leaving an exceptionally intense C-C=C bond at 286.4 eV. The deconvoluted C-C=C peak appears narrower while the bands assigned for oxygen functional groups broadened after reduction. In addition, the C-C=C peak shifts from 284.1 eV (GO) to 284.4 eV for the reduced samples, approaching 284.6 eV for graphitic C=C species. However, the peak assigned for C-OH that is present for the GO, rGO-F50 and rGO-P20 samples completely disappears for the rGO-P40 and rGO-F20 samples. This may be due to the weaker bonding energy of the C-OH bonds which is 3.72 eV as compared to the stronger C=O bonding energy which is 7.7–8.35 eV (Baraket et al., 2010).

To intuitively evaluate the reduction level, the C/O ratio is estimated by dividing the area of the C1s and O1s peaks and multiplying by the photo-ionization cross section (C=0.15; O=0.4) (Lee et al., 2012). A considerable degree of oxidation are seen from the low C/O ratio (0.81) for GO while the moderate degree of reduction process resulted in the increase of the ratio from 2.11 (rGO-F50), 3.57 (rGO-P20), to a higher degree of reduction at 6.58 (rGO-P40) and 7.9 (rGO-F20). Previous reports show that reduction by Ar/H₂ plasma at 150°C by Lee et al. (Lee et. al., 2012), obtained a C/O ratio at 6.95 which is reasonably close to the value for the rGO-P40 (6.58) and rGO-F20 (7.9) samples even though the hydrogen plasma treatment was done at room-temperature.

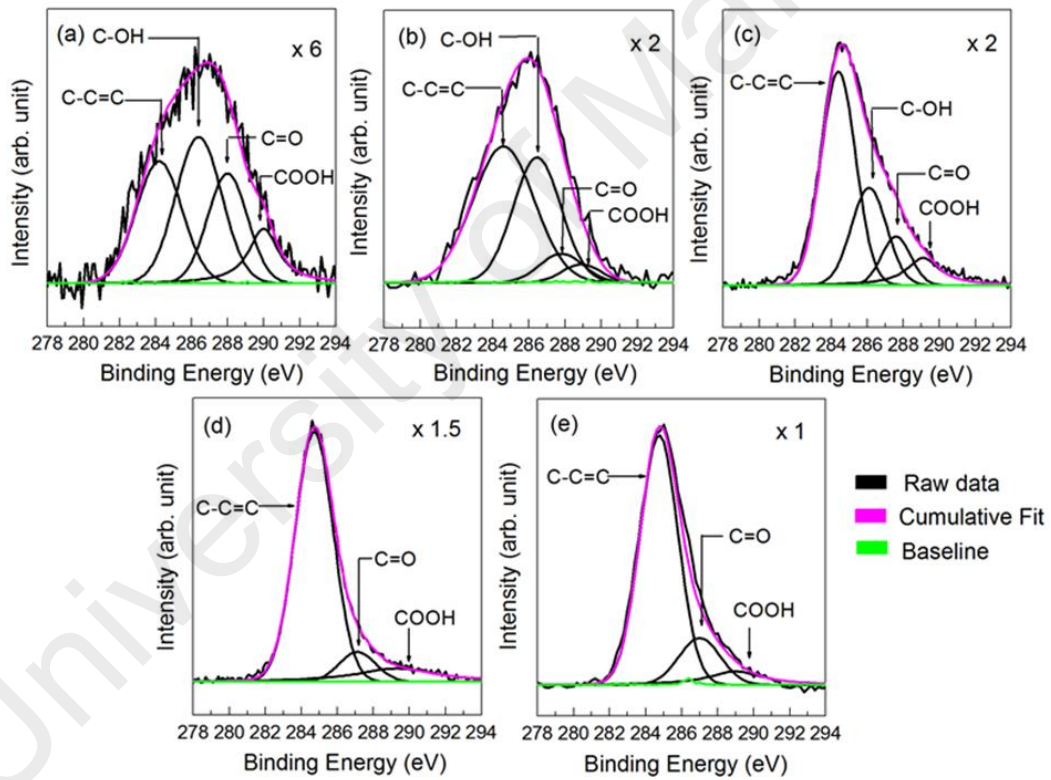


Figure 4.9: X-ray photoelectron spectrometry analysis with different degrees of reduction illustrating the deconvoluted spectra in the C1s peak region at around 284.8 eV; C-C=C, 286.4 eV; C-OH, 287.8 eV; C=O 288.9 eV; O=C-OH for (a) graphene oxide, (b) rGO-F50, (c) rGO-P20, (d) rGO-F40, (e) rGO-F20 samples. The intensity of the y-axis increases from (a) to (e) indicated by the multiplication factor in each graph.

4.3.4.3 Morphological and Topological Properties

The reduction of GO can be easily observed for the sample spin-coated on quartz substrate as shown in **Fig. 4.10(a-b)**. The transformation to a lower degree of transparency and darker colour after undergoing hydrogen plasma reduction treatment of the GO sample can be used as a simple and quick indication of reduction process from GO to rGO. The over-exposure of the GO to hydrogen plasma treatment for a period longer than 40 s produces unevenness in the spread of darker colour of rGO coating due to plasma etching of the rGO coating from the quartz substrate as shown in **Fig 4.10(c)**.



Figure 4.10: Photograph of (a) GO, (b) rGO-F20 and (c) over-exposed GO samples on quartz substrate.

Fig. 4.11 shows the FESEM images of the (a) GO, (b) rGO-P40, (c) rGO-F20 and (d) the over-exposed GO sample on SiO_2/Si substrates. These samples are selected for further characterization by Raman and XPS analysis to show the effects of the reduction process on the GO samples. Not much difference is observed between the FESEM images of rGO-P40 and rGO-F20 samples but the images when compared to the wrinkled and sheet-like morphology of the GO sample showed significant effects of the hydrogen plasma reduction process which results in the removal of oxygen functional groups. It shows that both the rGO samples have a smooth morphology with no observable pits or defects created after the reduction process. The FESEM images are also clearer and sharper compared to GO image showing the expected effect of

increase in conductivity of the rGO sample. As for the case of over-exposed rGO sample, the morphology appeared to be perforated and rougher.

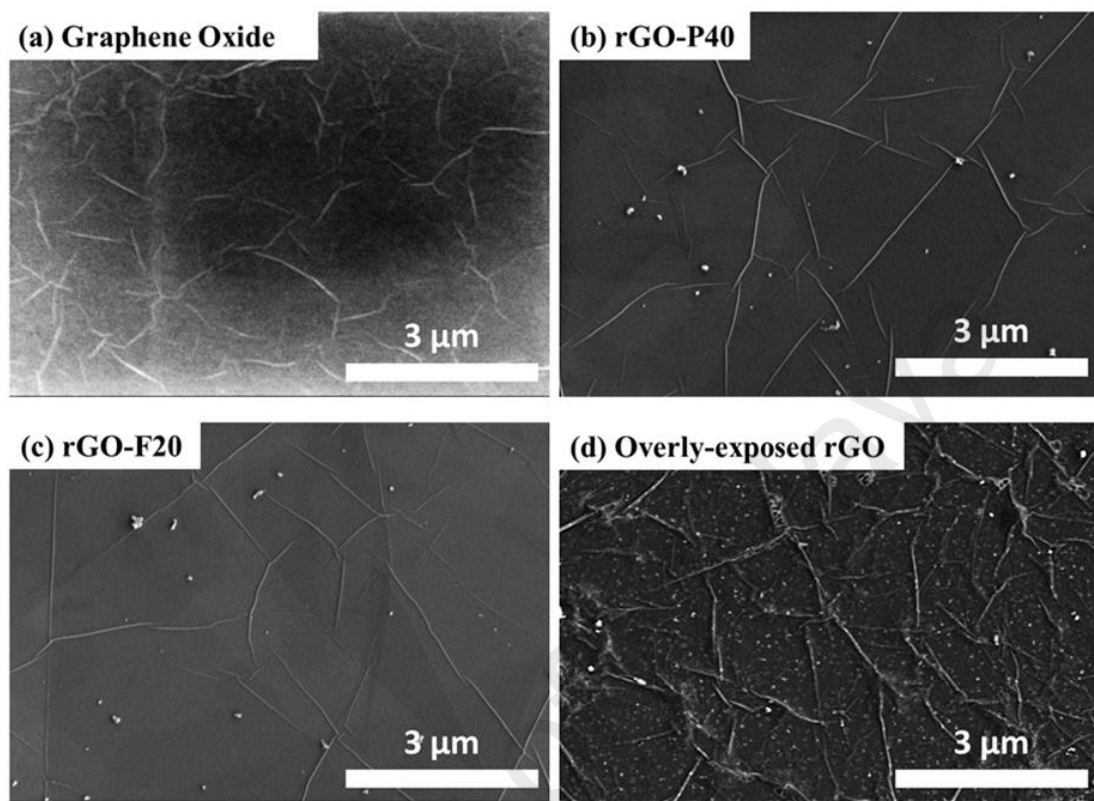


Figure 4.11: Higher magnification FESEM images of (a) GO, (b) rGO-P40, (c) rGO-F20 and (d) overly-exposed rGO sample on SiO₂/Si substrates.

The rGO-P40 and rGO-F20 samples are further characterized using AFM for topological study and images are shown in **Fig. 4.12**. Previous analysis of the AFM images showed that GO heights is of 0.947 nm (see **Fig. 4.5**). It is expected that the reduction process by energetic hydrogen plasma will decrease the thickness of the rGO approaching the thickness of monolayer graphite of 0.3 nm (Chen et al., 2010). Measurements are taken for several GO samples and the thickness are found to be around 1.0 ± 0.1 nm for monolayer GO or a multiplication of 1.0 ± 0.1 nm for multilayer GO. This is done because the decrease in thickness upon the reduction process is dependent on the initial thickness measured from GO samples.

From the topological AFM analysis of the rGO-P40 sample the thickness measured is 0.8 ± 0.1 nm, showing a decrease from the 1.0 ± 0.1 nm thickness for the GO sample as shown in **Fig. 4.12(a)**. The height profile is then investigated for sample with various stacked layers for these reasons:

- 1) SiO_2 and graphene flakes may exert different attraction/repulsion forces on the AFM probe (Paredes et al., 2009)
- 2) Substrate surface roughness may contribute to deviation in the thickness measurements (Paredes et al., 2009) and
- 3) Reduction by plasma usually acts on the surface only, so the layer beneath might not reduce compared to the uppermost layer (Hazra et al., 2010).

Interestingly, it is observed that the thickness between the substrate and the first layer and the first layer with the second layer does not vary indicating that the plasma reduction is not solely confined to the surface. This phenomenon has not been observed before however it may be speculated that energetic hydrogen species can overcome the energy barrier of 3.7 eV to penetrate the centre of the hexagonal carbon (Luo et al., 2009) and then reduce the bottom basal plane. Therefore, it is assumed that the reduction may happen if hydrogen ions gain enough energy and transfer this energy for dissociation of functional groups at the bottom of the graphene basal plane. Next, the other parameters used to produce the rGO-P40 sample is fixed, but then the flow rates of hydrogen fed into the reaction chamber are varied. It was found that the thickness of the rGO-F20 sample is further decreased to 0.7 ± 0.1 nm as shown in **Fig 4.12(b)**. Comparing with thickness reported in literature, reduction via L-ascorbic acid yields a thickness of ~ 0.8 nm (Zhang et. la., 2010), thermal (>900 °C) and chemical reduction

(hydrazine vapour) is $\sim 0.6\text{--}0.7$ nm (Akhavan, 2010; Dubin et al., 2010), mechanical exfoliation is ~ 0.4 nm and pure graphite is 0.45 nm (ideal 0.3 nm).

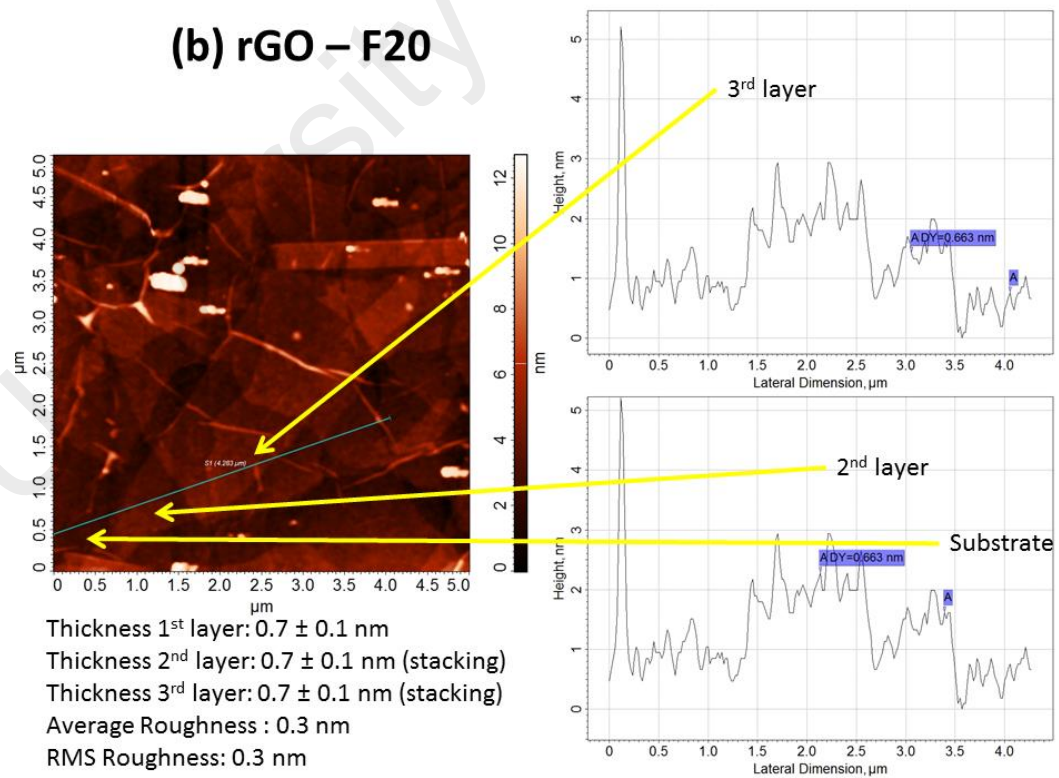
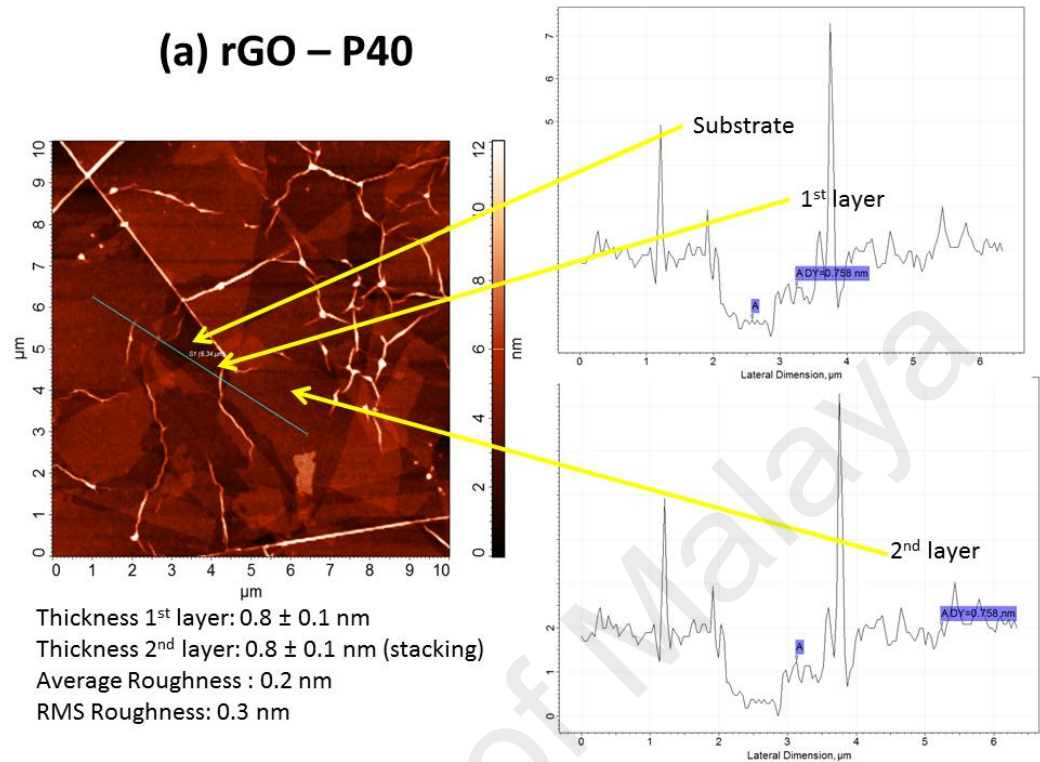


Figure 4.12: AFM images of the (a) rGO-P40 and (b) rGO-F20 samples. The height profile is taken along the line (blue) presented on the right and measure to be 0.8 ± 0.1 nm and 0.7 ± 0.1 nm, respectively.

4.3.5 The Role of Hydrogen Plasma Parameters in Reduction of Graphene Oxide

Reduction of GO to rGO involves removal of oxygen functional groups from the GO sample. **Table 4.4** summarizes the results obtained from analysis done on the Raman scattering spectra and XPS data obtained from the samples studied in this work. Removal of oxygen functional groups removes imperfections within the carbon basal plane and increases the in-plane sp^2 crystallite size, L_a (Eda et. al., 2010). The increase in carbon to oxygen ratio in the sample is a direct implication of the degree of reduction of the GO sample where a higher ratio shows a higher degree of reduction. The influence of the reduction time, hydrogen flow-rate and total pressure in the reaction chamber on these parameters is analysed and the mechanism of hydrogen plasma treatment in the reduction process of GO is proposed.

Table 4.4: Summary of Raman and XPS analysis of GO and rGO samples.

Sample	$\frac{I_D}{I_G}$	L_a (sp^2 crystallite size)	C/O ratio
GO	0.94	4.7 nm	0.81
Set 1-Vary Plasma Treatment Time			
rGO-P20 (Pressure: 0.8 mbar)	0.89	4.9 nm	3.53
rGO-P40 (Pressure: 0.8 mbar)	0.84	5.2 nm	6.58
Set 2-Vary H_2 Flow Rate			
rGO-F20 (Pressure: 0.3 mbar)	0.81	5.4 nm	7.9
rGO-F50 (Pressure: 0.65 mbar)	0.91	4.8 nm	3.57

During the hydrogen plasma treatment process, energetic hydrogen species are produced from reactions between energetic electron collisions and hydrogen molecules. Transfer of energy from the hydrogen radicals and excited hydrogen atoms to carbon atoms and functional groups in the GO sample occurs repeated during

the hydrogen plasma treatment as shown in **Fig. 4.13(a)** (Hazra et al., 2011). Highly reactive hydrogen radicals also react chemically with the hydroxyl and oxygen functional groups resulting in removal of oxygen atoms from the sample as shown in **Fig. 4.13(b)** (Hazra et al., 2011; Lee et al., 2012).

The rGO-P20 and rGO-F50 show the lowest degree of reduction compared to the rGO-P40 and rGO-F20 samples. The samples with the lowest degree of reduction also show insignificant change in the presence of imperfection in the carbon basal plane and very small change in the sp^2 crystallite size as compared to the GO sample. The higher pressure in the reaction chamber during the hydrogen plasma treatment process of these samples result in the low mean free path of the hydrogen radicals resulting in lower energy being transferred to the carbon atoms and functional groups in the sample. The increase in the reduction time to 40 s for the rGO-P40 results in longer hydrogen plasma treatment, thus allowing these low energy hydrogen radicals to react chemically with the hydroxyl and oxygen functional groups to result in significant change in L_a and removal of defects in the sample. The lower pressure during the reduction process for the rGO-F20 sample increases the mean free path of the radicals resulting in higher energy hydrogen radicals and excited hydrogen atoms reacting with the sample on reaching the GO sample. The reduction time as well as the pressure in the reaction chamber plays an important role in the reduction process. Long exposure of hydrogen plasma treatment on the sample increases defects. The XPS results also show an increase in the intensity of the deconvoluted C-C=C peak for the samples with high degree of reduction. Thus hydrogen plasma treatment is able to restore the C=C backbone of graphene structure as shown in **Fig. 4.13(c)**. No external heating was applied during the reduction process by hydrogen plasma treatment thus further confirming the effectiveness of reducing the oxygen functional groups in GO samples using this technique.

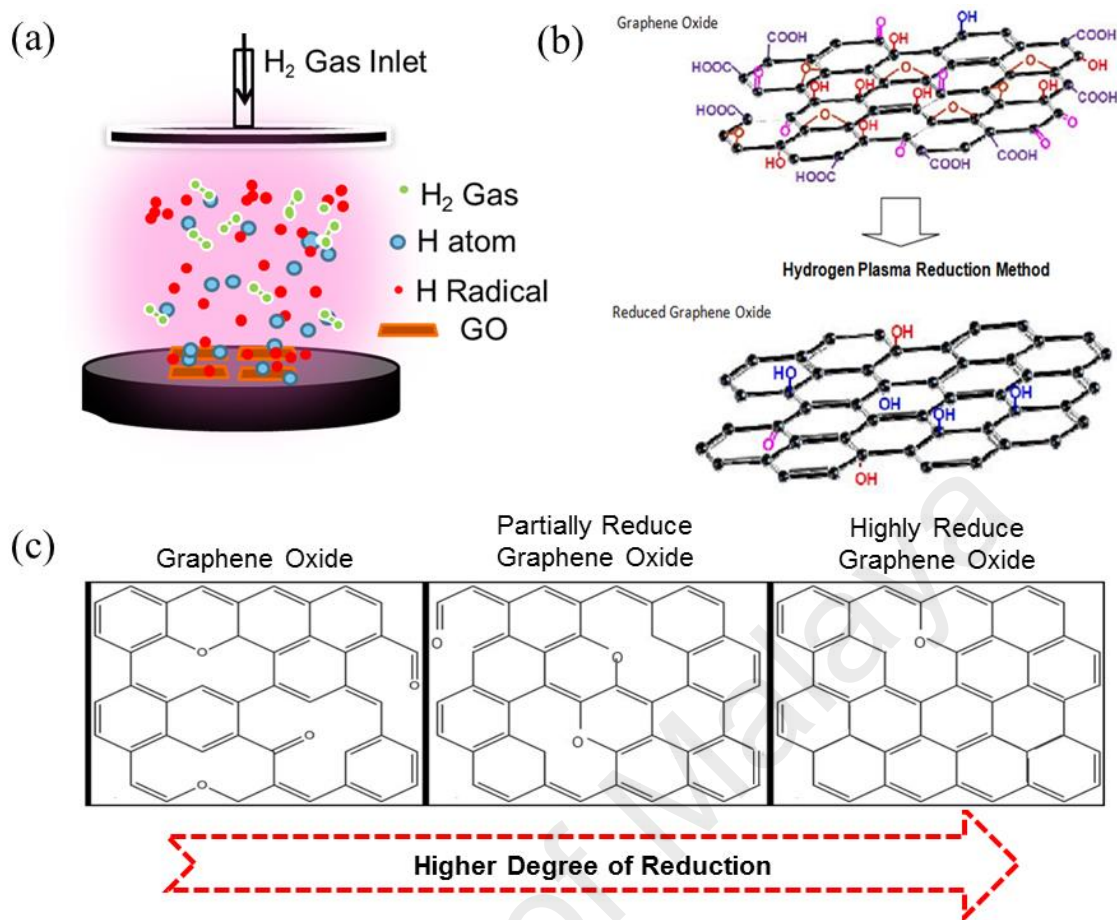


Figure 4.13: Illustrations of (a) energetic species presents in between parallel-plate PECVD configuration, (b) reduction of oxygen functional groups at basal and edges of GO flakes and (c) restoration of C=C backbone structural of graphene with different degree of reduction.

4.4 Carbon Dioxide Gas Sensor Application

4.4.1 Gas Sensor Set-up

The configuration for the gas sensor set-up used in this work is shown in **Fig. 4.14(a-b)**. The prepared sensors are placed on a stage inside a glass chamber and connected to the LCR meter (EA4980A, Agilent) through electrical feed through. The commercial CO₂ sensor (CO2-BTA, Vernier) is also placed inside the chamber to measure the specific gas concentration in part per million (ppm) of the required CO₂ level for this study. By applying a voltage of 1 Volt, the change in resistances for the prepared sensors is collected so the changes over concentration level could be analysed. In order to circulate the CO₂ gas, a small fan is inserted inside the chamber. The CO₂ and N₂ gases are admitted into the chamber through a gas inlet on the base plate. The gap between the stage and the base plate of the chamber is fixed at 2 cm. The pumping system for evacuation of the chamber before admitting the gas is connected via a hose to the base plate of the chamber. The actual gas-sensor system, optical image and FESEM images of prepared sensor device are shown in **Fig. 4.15**.

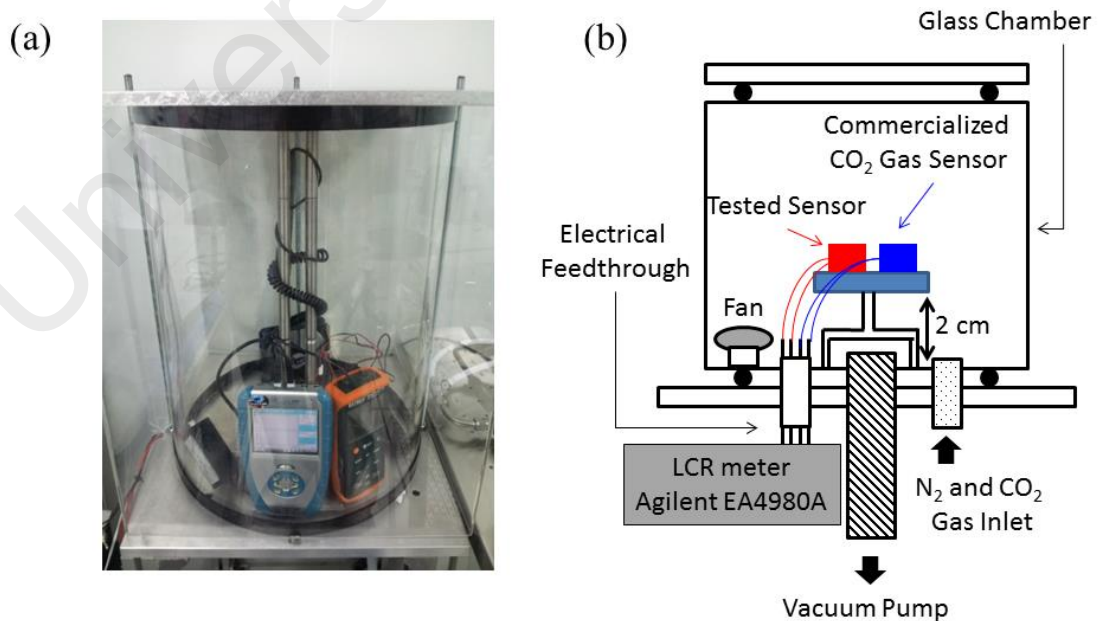


Figure 4.14: (a) Photograph and (b) schematic diagram of the gas sensor set-up.

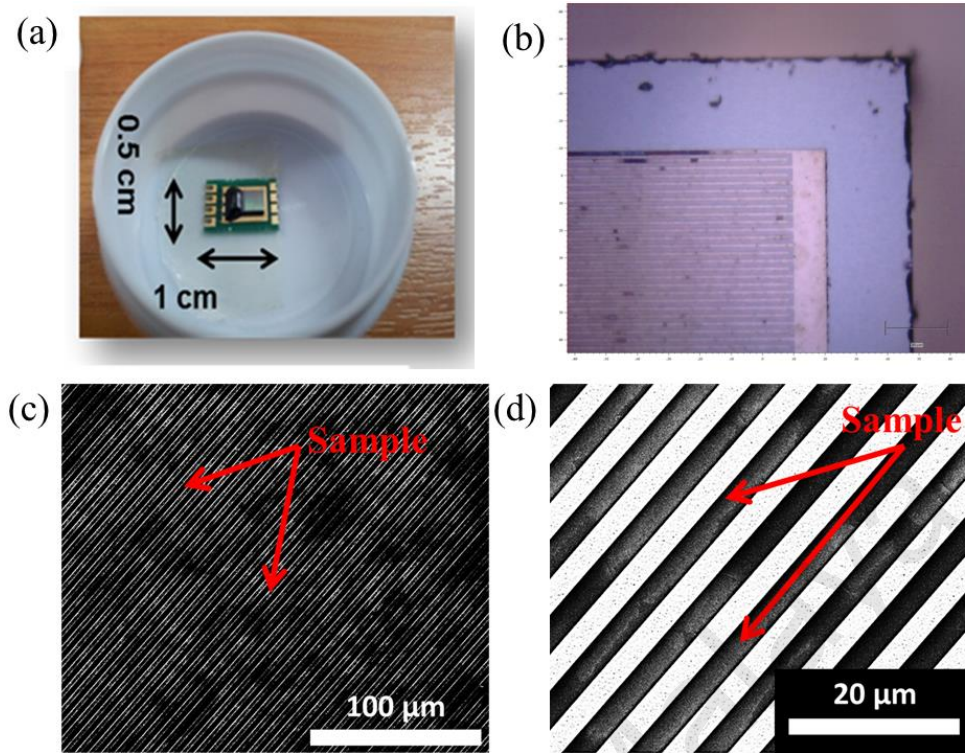


Figure 4.15: (a) Photograph of the CO₂ gas sensor device. The size of pre-pattern silicon die on the device is 3.1 mm×3.8 mm. The images of CO₂ gas sensor device taken from; (b) optical microscope and FESEM at (c) low magnification or (d) high magnification of the reduced graphene oxide sheet on 3 μm electrode fingers width and separation distance.

4.4.2 Gas Sensor Measurement

The electrical behaviour of the graphene sensors is studied by measuring the change in resistance when different concentration of CO₂ measured in parts per million (ppm) at room-temperature are admitted into the chamber. Prior to that, the I-V characteristic of each GO sensor is measured to group GO sensors with almost similar resistance together. The GO samples within the same group are put under hydrogen plasma treatment process together using the reduction hydrogen plasma parameters for the rGO-P40 and rGO-F20 samples. Next, the sensors are placed inside a vacuum chamber and pumped down to a base pressure of $\sim 10^{-2}$ mbar. The CO₂ gas concentrations are varied from 0 to 1500 ppm by controlling the duration time of CO₂ gas being fed into the chamber. The effect of the target gas concentration on the response of the graphene gas sensor in 1 atm N₂ or air environment at 23 °C is studied.

The relative humidity, (RH) in N₂ and air environment is 37% and 68%, respectively. The repeatability of sensing capability of the rGO-F20 sensor response is measured by alternating the concentration of CO₂ gas from 350 ppm to 750 ppm (1st Cycle) or 769 ppm (2nd Cycle) in 1 atm air environment at 23°C and 68% RH. The sensing response is defined as the ratio of the change in the resistance towards CO₂ gas,

$$\frac{R_{N_2 \text{ or Air}} - R_x}{R_{N_2 \text{ or Air}}} \times 100\% \quad (4.1)$$

The initial resistance, R_{N₂} (R_{Air}) is the resistance taken when N₂ (air) is used for the measurement while R_x is the resistance after feeding the CO₂ gas at certain concentration. In addition, the gas concentration is also calibrated against a commercialised CO₂ gas sensor (CO2-BTA, Vernier) to obtain the required gas feeding time duration.

4.4.3 Performance Criteria

The electrical conductance of the GO, rGO-P40 (Set 1) and rGO-F20 (Set 2) samples is measured by varying the voltage source from -1 to 1 V and measuring the current. The parameters of the rGO-P40 and rGO-F20 samples are selected because these samples showed the highest degree of reduction. The I-V characteristics of the sensors exhibit a linear behaviour in an air environment, indicating ohmic contact between the films and electrode fingers. The estimated resistances significantly decreased from 33, 10 and 1.6 kΩ for GO, rGO-P40 and rGO-F20 sensors respectively as shown in **Fig. 4.16**. Increase in the degree of reduction results in decrease in the resistance. After reduction of the graphene oxide by hydrogen plasma treatment, clustering of non-oxidized graphitic domains is restored as indicated by the Raman analysis where the GO and rGO-F20 samples show an increase in the in-plane sp² crystallite size from 4.7 to 5.4 nm. Hence, this shows that the increase in the

distance between graphitic domains will make the charge transport via variable range hopping (VRH) or continuous path results in a more conducting material (Lu et al., 2009). These three devices are next tested for their performance as a CO₂ gas sensor by measuring the sensing range, sensitivity, stability and repeatability in target environment and response time.

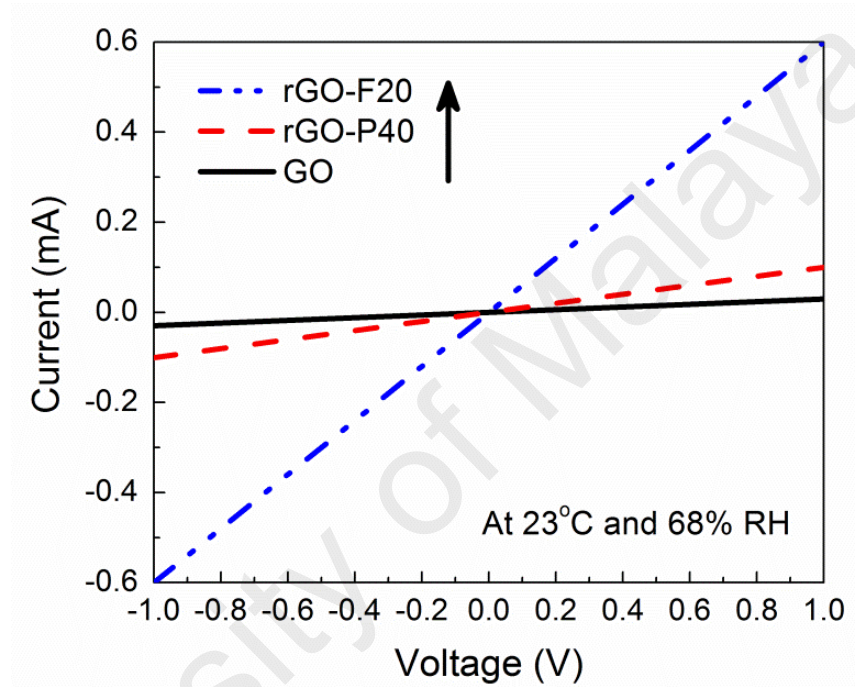


Figure 4.16: I–V curve obtained for the fabricated graphene gas sensors.

4.4.4 Results and Discussion

4.4.4.1 Sensing Range and Sensitivity of Designed Sensor

Fig. 4.17 shows the CO₂ gas sensing response of the GO, rGO-P40 and rGO-F20 gas sensors from 0 to 1500 ppm at 23°C and 37% RH in an N₂ environment. To study the effectiveness of rGO sensors to detect the target gas (CO₂ gas) without interference of other gases, N₂ is used as the base gas. It is observed that the sensing response increases monotonically with the increasing of gas concentration. Furthermore, the slope below 100 ppm is larger compared to that above 100 ppm for all sensors, indicating a high sensing response at lower gas concentrations. Although the sensing response is almost similar for all the sensors, the prominent effect of the hydrogen plasma reduction is shown to enhance the sensing response at low CO₂ gas concentration. In addition, the non-linear sensing response appears to be related to the rate of adsorption of the CO₂ gas molecules on the sp² crystallite sites (adsorption active sites) which has increased after the reduction process (from 4.9 to 5.4 nm sp² crystallite sites for GO and rGO-F20 sensor, respectively). The decrease of sensor response at higher CO₂ concentration may be due to the fact that most of these sites are already covered by the CO₂ gas molecules. The gas sensor response increased from 51% to 60% and 71% at 1500 ppm for the GO, rGO-P40 and rGO-F20 sensors respectively. These results show that the sensor response increased when rGO with higher degree of reduction is used as the sensing material for CO₂.

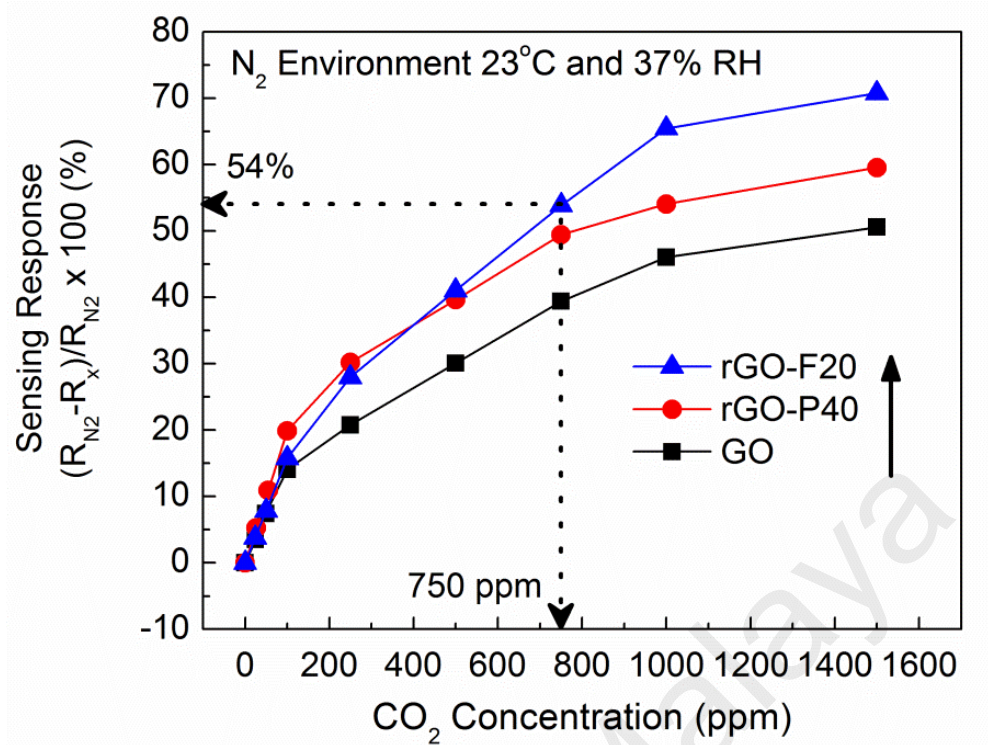


Figure 4.17: Room-temperature CO₂ gas sensor response, $(R_{N_2} - R_x) / R_{N_2} \times 100$ (%) on the GO, rGO-P40 and rGO-F20 samples from 0 ppm to 1500 ppm in an N₂ environment at 37% RH. Note that the sensing response of all the sensors is based on the changes of resistance when exposed to CO₂ gas with respect to the initial resistance measured in N₂ environment at 23 °C.

4.4.4.2 Stability in Target Working Environment

Fig. 4.18 shows the sensing response, $(R_{Air} - R_x) / R_{Air} \times 100$ (%) which is further performed in air environment by using the rGO-F20 sensor due to its highest sensitivity compared to the GO and rGO-P40 sensors. Next, the performances of the sensor are tested in a typically “wet” indoor condition with the highest %RH for the target application. A typical “wet” indoor condition in a hot and humid climate equipped with air-conditioning and mechanically ventilated (ACMV), air-conditioning (AC) and air-conditioned and naturally ventilated (ACNV) usually have RH of 51%, 61% and 68%, respectively (Zuraimi et al., 2007). The sensing responses within 300 to 1500 ppm CO₂ concentration in air environment are observed to still increase monotonically, but with a lower sensing response. The sensing responses are 2%, 6%, 10%, 13% and 15% at 300, 500, 750, 1000 and 1500 ppm of CO₂, respectively.

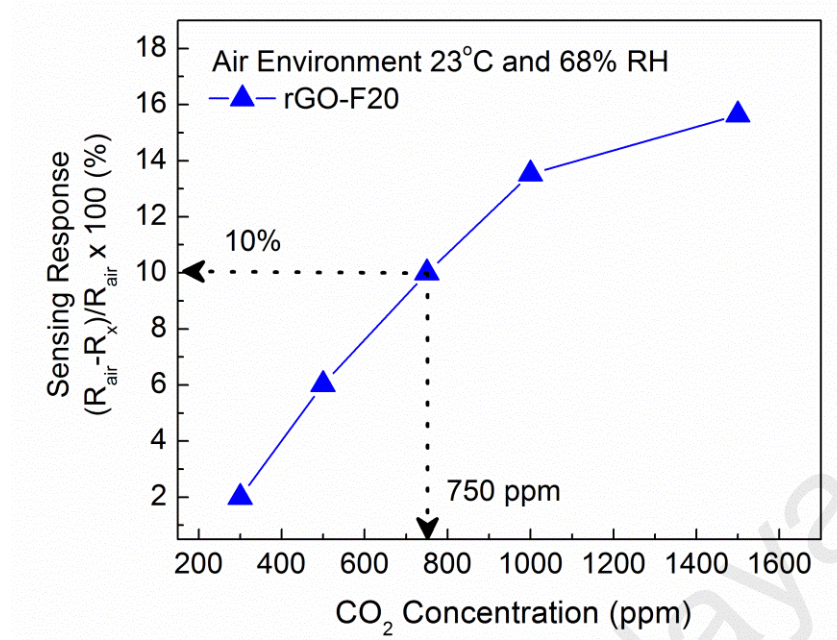


Figure 4.18: (a) The CO₂ gas sensor response, $(R_{\text{Air}} - R_x) / R_{\text{Air}} \times 100$ (%) on the rGO-F20 sample from 300 ppm to 1500 ppm in an air environment at 68% RH. Note that the sensing response of the sensor is based on the changes of resistance when exposed to CO₂ gas with respect to the initial resistance measured in air environment at 23 °C.

4.4.4.3 Repeatability and Response Time

The sensing repeatability $(R_{\text{Air}} - R_x) / R_{\text{Air}} \times 100$ (%) is further measured in atypical “wet” indoor condition of 68% RH air environment by using the rGO-F20 sensor as shown in **Fig. 4.19**. The response and recovery time can be estimated at ~4 minutes from the graph. The response time is defined as the time taken for the relative resistance change to reach 90% of the steady state value after the test gas is injected and the recovery time is taken as the time necessary for the sensor to attain a resistance 10% above the original value in air.

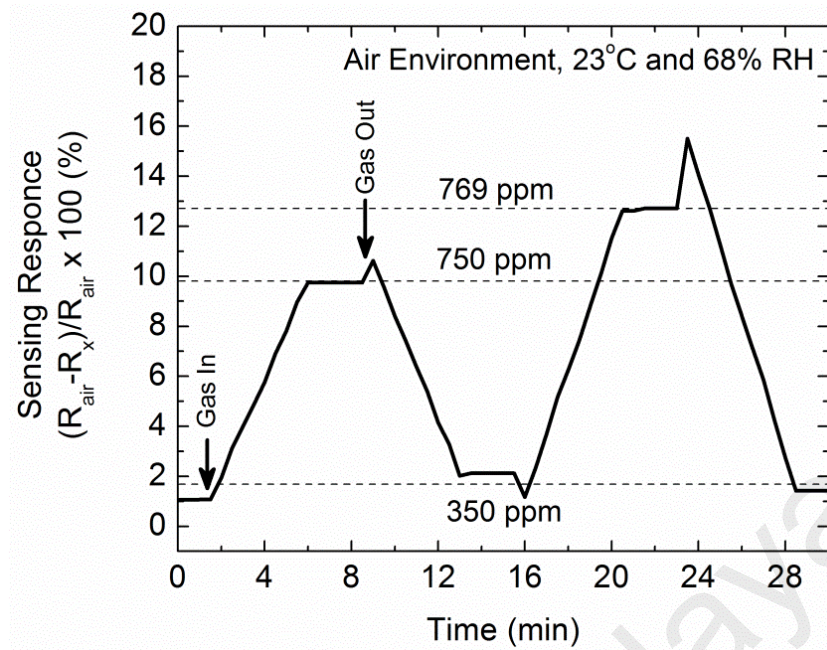


Figure 4.19: (b) The change of sensing response versus time when the CO₂ concentration is switched from 350 ppm to 750 and 769 ppm. The response and recovery time can be determined from the figure about ~4 minutes.

Yoon et al. reported a much lower response and recovery time of ~10 s for 100 ppm CO₂ at 22°C and 44% RH (Yoon et al., 2011) using their graphene sensor from mechanical peeling of highly ordered pyrolytic graphite (HOPG) which has a very low defect density. The slower sensing response and recovery time for the sensor using rGO-F20 as the sensing material is deduced to be due to the presence of higher defect density in the material (Jung et al., 2008). Increasing reduction process time has shown to have the effect of increasing defects due to etching effects by the energetic hydrogen atoms. However, if this sample is reduced by hydrogen plasma treatment for longer period of time at higher pressure, the impact of the energetic hydrogen atom is lower reducing the etching effects. This will result in rGO of high degree of reduction with lower defects density and when used in CO₂ gas sensors with lower response and recovery time. However, the sensing and recovery time of 4 minutes without external assisted recovery performed by rGO-F20 gas sensor is satisfactory for use in environment where the changes of CO₂ concentration is not fast, such as for monitoring indoor air quality.

4.4.5 Proposed Sensing Mechanism

The sensing mechanism can be related to the charge transfer mechanism involving the relative position of the density of state (DOS) of the HOMO and LUMO within adsorbate (Leenaerts et al., 2008). If the HOMO level is above the Fermi level of graphene, there is a charge transfer to the graphene through orbital mixing (hybridization) with graphene orbitals. Adsorbed CO_2 molecules can act as electron donors (Leenaerts et al., 2009) thus shifting the HOMO level further above the Fermi level closer to the LUMO level thus enhancing charge transfers to the LUMO. This enriches the electron concentration in the graphene sheets resulting in an increase in the electrical conductance which is detected from the decrease in the resistance values as shown in **Fig. 4.20** (Schedin et al., 2007). The capability of the sensor to recover without any external assistance is attributed to the weak interaction between the graphene and CO_2 gas molecules (Yoon et al., 2011) as compared to NH_3 or NO_2 gas molecules (Basu et al., 2012) thus making it a better material for CO_2 sensing.

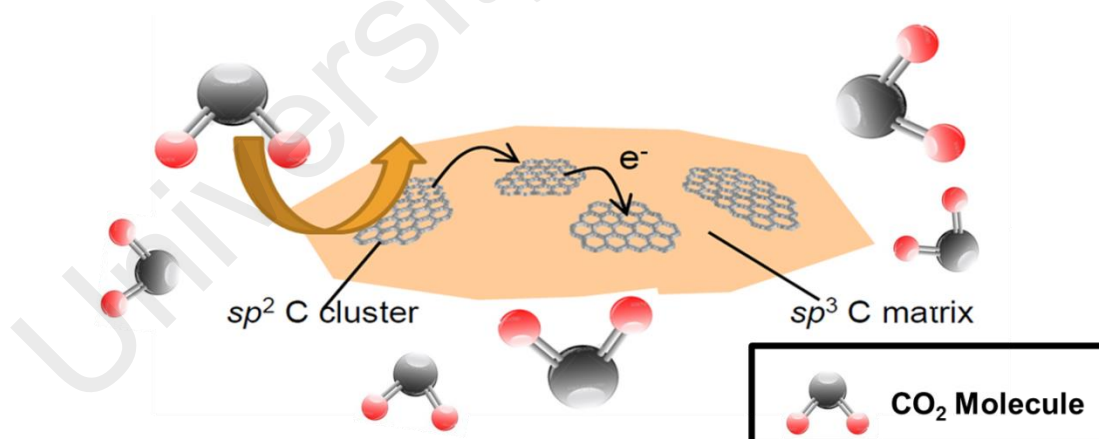


Figure 4.20: Schematic representations of the proposed sensing mechanism in reduced graphene oxide CO_2 gas sensor.

4.5 Summary

In summary, the reduction of GO via hydrogen plasma has been systematically studied. The reduction trend of GO at room-temperature was verified by morphology, topological, structural and elemental composition characterizations. No external heating was applied during the reduction which further confirms the effectiveness that hydrogen plasma alone was capable to reduce the oxygen functional groups. The lowest resistance measured was 1.6 k Ω for the rGO-F20 sample obtained using 20 sccm of hydrogen gas and then exposing the GO for 40 s in 10 W hydrogen plasma environments. The rGO-F20 sensor showed the highest sensing response of 71% at 1500 ppm in N₂ environment and 37% RH comparing to other fabricated sensors. This further supports the reduction process which increases the sp² crystallite sites (adsorption active sites) for the adsorption of the CO₂ gas molecules. However, the rGO-F20 sensing response measured in air environment (68% RH) at 1500 ppm was decreased to 15%. The sensor shows a good repeatability performance with a sensing and recovery time of about 4 minutes when exposed to 750 and 769 ppm CO₂ concentration. The repeatability was measured in air environment at 68% RH without an external assisted recovery. Nevertheless, the sensing performance of the rGO-F20 sensor reported is very encouraging for practical applications when considering the room-temperature reduction process and sensing capability, low cost fabrication of this sensor and the potential opportunities for optimization.

CHAPTER 5: GROWTH OF HIGH-QUALITY GRAPHENE ON COPPER FOIL

5.1 Overview

In this chapter, the results and discussions based on the growth of graphene on copper foil using a novel hot-filament thermal chemical vapour deposition (HFTCVD) technique are presented. The novelty of the HFTCVD technique is the use of a quasi-static condition created during the growth process via vapour trapping mechanism by placing the copper foil inside an alumina tube which is sealed at one end. The effects of deposition time and hydrogen flow rate on the morphology and structure of graphene are investigated by Raman spectroscopy, HRTEM, LEEM, XPS and FESEM. Analysis on these results is then used to propose the growth mechanism of graphene specifically for this technique.

This chapter also presents the results and analysis done on the effects of graphene transfer processes using two different techniques that is the wet transfer method by thermal release tape (TRT) and the poly(methyl methacrylate) (PMMA) support method. The comparison between the qualities of graphene transferred by these techniques is done based on defect density, transfer coverage and electrical property of the graphene. The transfer process producing the expected quality of graphene most suitable for the fabrication of flexible pressure sensor will be implemented in the fabrication of device presented in Chapter 6. The progression of the work done in this chapter is depicted in **Fig. 5.1**.

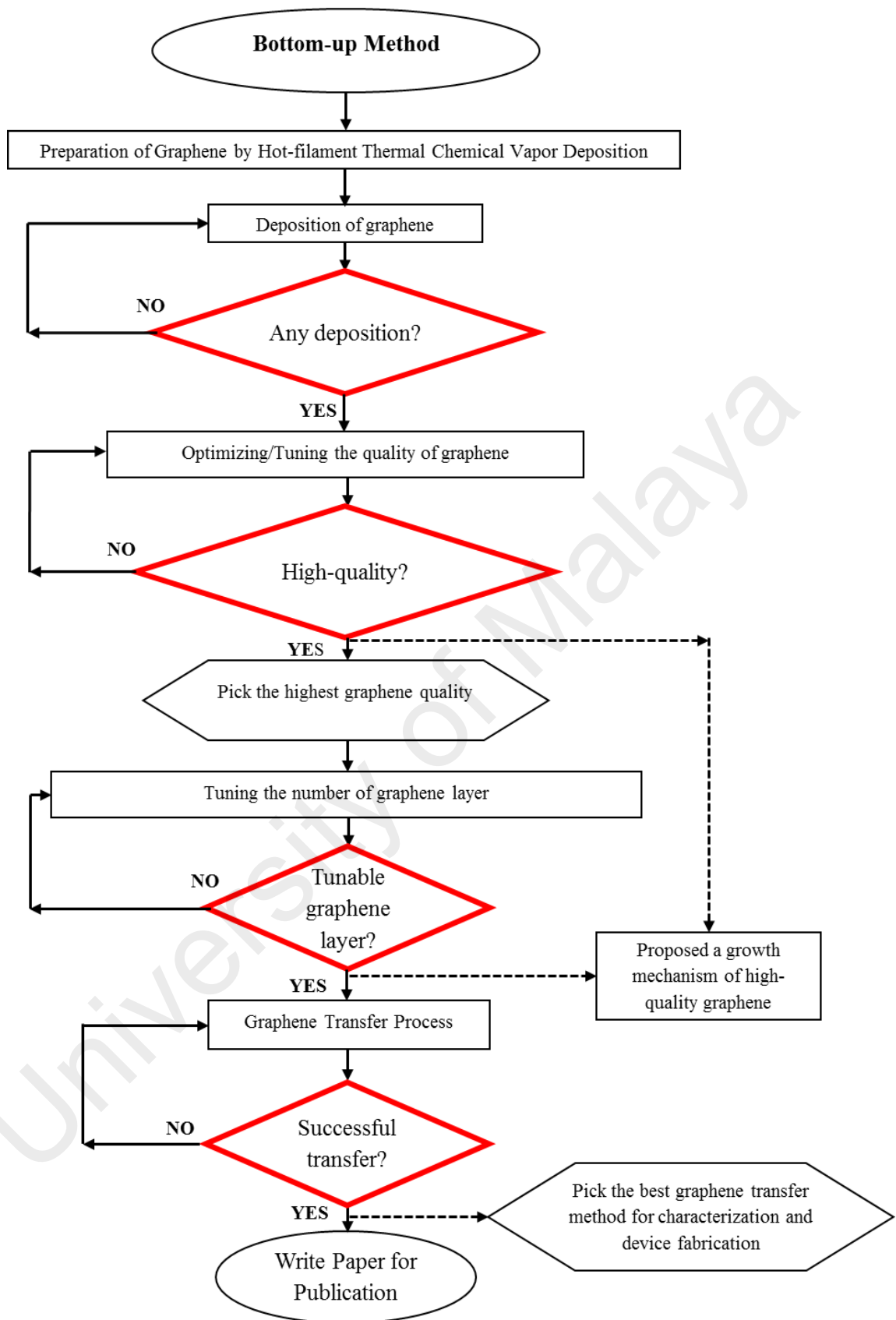


Figure 5.1: Flow chart showing the progression of graphene fabrication using bottom-up approach using HFTCVD technique.

5.1.1 Set 1: The Effect of Growth Duration

5.1.1.1 Observation of Initial Growth of Graphene

Fig. 5.2(a-e) shows the FESEM images of the graphene grown at different deposition time on Cu foils. The figures on the right correspond to the higher magnification of the images on the left. During the initial 5 minutes deposition time shown in **Fig. 5.2(a)**, nanoparticles are observed to be formed on the surface of the copper substrates as indicated by the circle area. No graphene layer is formed during this short deposition period as confirmed by the absence of the typical graphene signal from the Raman spectrum of this sample (see **Fig. 5.3(a)**). Next, the patch-like graphene morphology (highlighted by the area within the rectangular box) is observed on the sample grown for time duration of 10 minutes as shown in **Fig. 5.2(b)**. This patch-like graphene structures appeared to consist of wrinkle-like structures with nanoparticles coexisting within the same area as marked by arrows in the magnified image of this sample on the right. In the region where there is no graphene growth, the presence of nanoparticles is not observed. Note that the region of the image in mixed secondary electron (SE) and backscattered secondary electron (BSE) modes covered by the graphene patch appeared to be brighter as compared to the exposed region of the copper substrate. This could be attributed to the oxidation reaction process on the exposed region of copper substrate. Unlike the copper region beneath the graphene which has been preserved from this oxidation reaction (Topsakal et al., 2012), a lower signal intensity is produced by the oxidized copper which resulted in a darker contrast in the FESEM image (Yang et al., 2012).

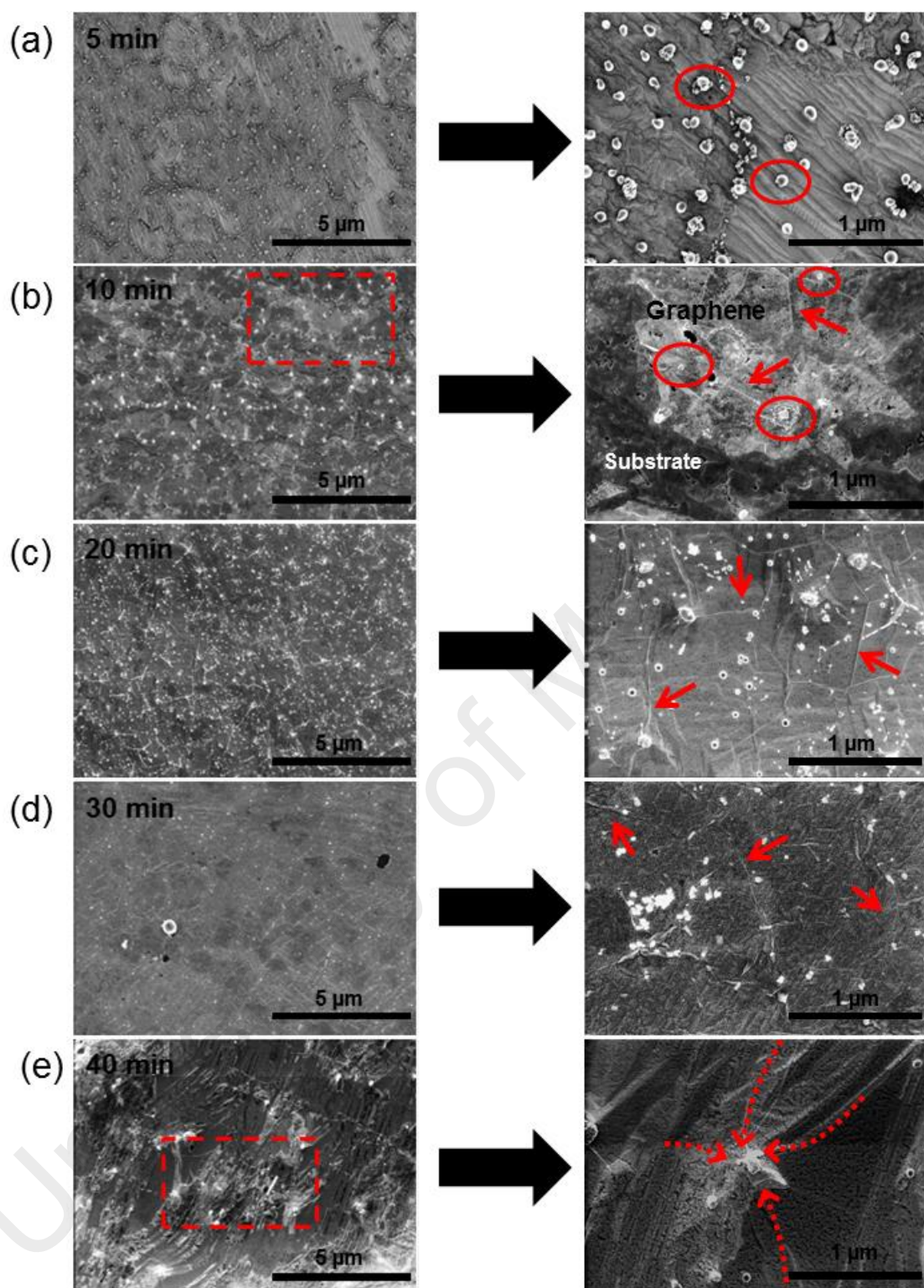


Figure 5.2: FESEM images of graphene grown on Cu foils with different deposition times: (a) 5, (b) 10, (c) 20, (d) 30, and (e) 40 minutes at 1000 °C. The CH₄:H₂ flow rate was fixed at 10:50 sccm. The graphene patch (b) and corrugated copper substrate (e) are shown in rectangular boxes. Wrinkles and nanoparticles are indicated by arrows and circles, while tension caused from a bump of corrugated surface is indicated by dotted arrows.

Fig. 5.2(c) and **(d)** show the morphology of the graphene deposited for time durations of 20 and 30 minutes respectively. For these samples, graphene are observed to completely cover the surface of the copper foil. The magnified images of these samples on the right show that the presence of wrinkle-like structures on the whole surface of the samples are indicative of formation of graphene layer. The formation of wrinkle-like structure is due to the difference in the thermal expansion coefficients (a) of the graphene ($\alpha_{\text{Graphene}} = -6 \times 10^{-6}/\text{K}$) and copper ($\alpha_{\text{Copper}} = 24 \times 10^{-6}/\text{K}$) during the cooling process (Mattevi et al., 2011). However, when the deposition time is extended to 40 minutes, it is observed that the copper foil beneath the graphene layer is rougher and corrugated, as indicated by the region within the rectangular box shown in **Fig. 5.2(e)** on the left. The corrugated surface seemed to be underneath the graphene layer, as demonstrated by the presence of tension on the graphene layer towards the centre of the bump of the corrugated surface as shown by the image on the right.

The time evolution of the graphene growth shown in **Fig 5.2(a-e)** reveals two important implications. First, the transition from 5 to 10 minutes deposition time can be referred as “induction period”. This induction period could have resulted from the nucleation seed (i.e. nanoparticle) size dependence of an initiation of graphene growth which will be further discussed in **Section 5.1.1.3**. Secondly, the transition from 30 minutes to 40 minutes deposition time can be referred as graphene growth-limiting from surface-catalysed process of copper substrate. It has been reported that the decrease in growth rate of graphene domains during the growth process brought about by the decreasing reactivity of the Cu substrate due to the deactivation of topochemical reaction sites at high graphene coverage that eventually stop the growth process (Hsieh et al., 2014). The topochemical reaction acts as dehydrogenation sites of carbon precursor on copper to produce the active carbon reactants that attach to the edge of the

growing graphene lattice (Celebi et al., 2013). However, additional topochemical reaction sites may be introduced from impurity (i.e. nanoparticle) which promotes the growth of consecutive graphene layer (Kasap et al., 2015). This will be further discussed in **Section 5.1.2.3**.

5.1.1.2 Identification of Nanoparticles

Generally, nanoparticles are ubiquitously present on the surface of graphene films prepared by chemical vapour deposition (Fan et al., 2014). The origins of these nanoparticles have been reported to come from the following events;

- (a) Introduction of impurity particle, Cu particle and/or Si particle during polishing/cleaning process of Cu foils or evaporated SiO_x species from quartz tube (Han et al., 2011; Kasap et al., 2015).
- (b) Surface oxidation of deposited Cu nanoparticle into CuO nanoparticle (Magnuson et al., 2014).
- (c) Production of Cu or Cu_2O nanoparticle via precipitation from the sublimation of copper foil during high-temperature annealing (Gan et al., 2013).

Therefore, the nanoparticles observed in Set 1 need to be identified first. To confirm this, the Raman spectra within the $100\text{--}800\text{ cm}^{-1}$ regions are measured, and rich Raman features at 115, 150, 217, 417, 515, and 635 cm^{-1} are found, as observed in **Fig. 5.3(a)**. These peaks were attributed by the cuprous oxide (Cu_2O) crystals in the cuprite structure (space group O_h^4), and the following peaks would be expected from group theory: one Raman active phonon (T_{2g}) at 515 cm^{-1} ; two infrared allowed modes (T_{1u}) at 150 and 635 cm^{-1} ; and three phonons normally nor Raman neither infrared active (IR) modes (T_{2u} , E_u , A_{2u}) at 115, 217 and 417 cm^{-1} , respectively (Debbichi et al., 2012). Further investigation on the nanoparticle by HRTEM images

revealed a lattice spacing of 0.21 nm, which correspond to the (200) plane of Cu_2O as shown in **Fig. 5.3(b)** (Dubale et al., 2014). This further confirmed the Raman results that these nanoparticles are indeed Cu_2O nanoparticles.

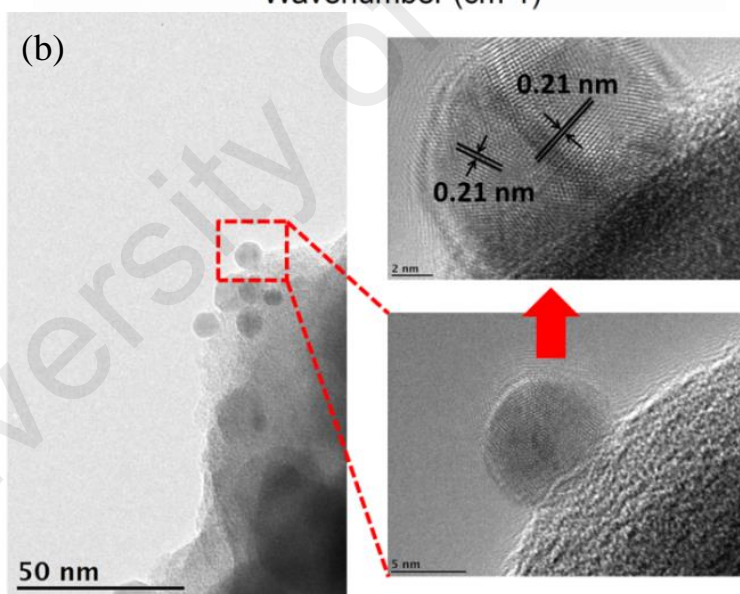
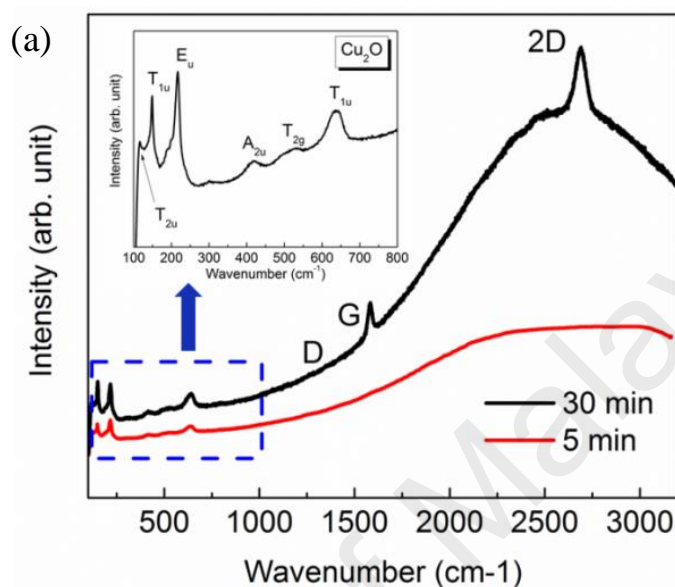


Figure 5.3: (a) Raman spectra of samples deposited for time duration of 5 and 30 minutes on Cu foil. The inset shows a typical Cu_2O spectrum. Note that copper does not have a Raman active mode. Thus, no Raman peak was observed. (b) HRTEM images of Cu_2O nanoparticle on graphene transferred onto square copper mesh TEM support grids further proved that these Cu_2O nanoparticles are the nucleation sites for the graphene growth.

The formation of Cu₂O nanoparticle might be due to the sublimation of Cu at a high temperature, where it reacted with the remaining oxygen in the deposition chamber (Hawaladar et al., 2012). Ito et al. (1998) reported that when copper is heated at temperatures of 700 to 1050°C with the oxygen partial pressure below 10⁻¹ mbar (0.1 mbar ≈ 0.075 torr), Cu₂O or Cu phases are more preferred to be formed as indicated by the phase diagram of the copper-oxygen system shown in **Fig. 5.4**.

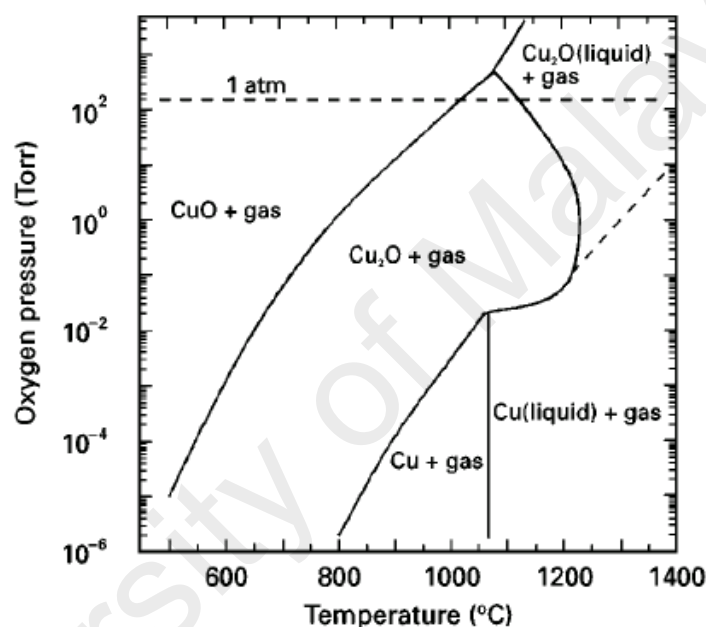


Figure 5.4: Phase diagram of the copper-oxygen system for pressure versus temperature (Ito et al., 1998).

Since the whole fabrication process starting from pre-treatment until deposition stage, the base pressure inside the process chamber is maintained around ~10⁻⁵ mbar (high vacuum region) and no direct oxygen gas is introduced during the process; it is assumed that the oxygen partial pressure is below 10⁻¹ mbar. In addition, the probability of Cu nanoparticles to be deposited instead of Cu₂O nanoparticles is very low since a very low oxygen partial pressure of <10⁻⁴ mbar at 1000 °C is needed to make this possible. The methane gas used in this study is of 99.995% purity (~5 ppm of O₂ and H₂O impurities) which could contribute to an increase in oxygen partial pressure in the

system. However, the oxygen impurities in the system were not enough to increase the partial pressure beyond 10^{-1} mbar. Meanwhile, the deposition of Cu nanoparticle have been reported when operated under ultra-high vacuum (UHV) base pressure; $\sim 10^{-7}$ and/or using a higher methane gas purity; 99.9995% (~ 0.5 ppm of O_2 and H_2O impurities) (Gan et al., 2013; Robinson et al., 2013; Magnuson et al., 2014). In addition, the gas phase nucleation and growth of copper oxide nuclei between Cu vapour and oxygen has been shown by Nasibulin et al. (2001; 2002).

5.1.1.3 The Role of Nanoparticle Size in Graphene Growth

A quantitative study for the diameter distribution of Cu_2O nanoparticle with respect to the deposition time is performed by measuring the nanoparticle diameter from FESEM images of **Fig. 5.5(a-d)** using ImageJ software plotted by histogram as shown at the right side of each figure. The analysis shows that the distribution of nanoparticles is divided into two ranges of diameters for all samples prepared at different deposition time. The first group of nanoparticle diameter range is below 150 nm (indicated by star shape) while the second group is observed for nanoparticles of diameter larger than 350 nm (indicated by circle shape). As the deposition time is increased, the average diameter of nanoparticles in the first group is increased while the average diameter in the second group is decreased. Recently, Gan et al. (2013) has reported that only nanoparticle with a certain set of diameters (~ 20 nm) will become nucleation sites for the formation of graphene. In this work, graphene only start to grow at deposition time of 10 minutes (induction period) as observed in **Fig. 5.5(b)**, this coincided with the formation of Cu_2O nanoparticles of diameter less than 150 nm. This is due to the higher probability of nucleation process in area close to the nanoparticles as compared to the copper edges, boundaries, or even graphene edges.

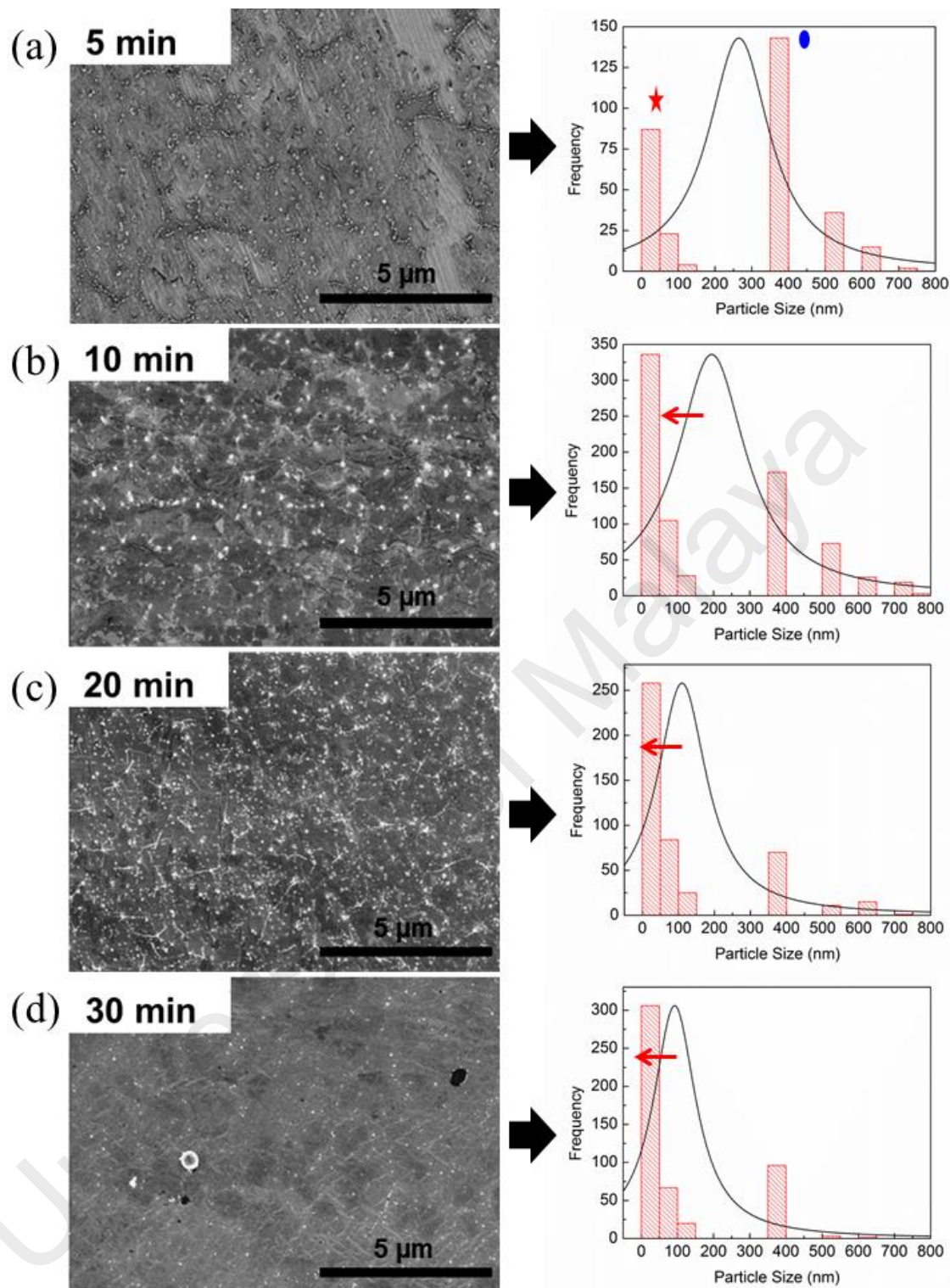


Figure 5.5: FESEM images and size distribution diagram of graphene grown on Cu foils at different deposition times: (a) 5, (b) 10, (c) 20 and (d) 30 minutes at 1000 °C. The Lorentz fitted curved shifted to lower particle size with respect of deposition time shown by red arrow. Two groups of nanoparticles size were indicated by star and circle shape that increased or decreased as the deposition time was prolonged.

In addition, the probability of smaller nanoparticles acting as nucleation sites is increased due to the increase in surface-to-volume ratio and subsequently enhanced the surface free energy. This enhanced its ability to carburize more carbon adatoms (become more soluble) as compared to nanoparticles of larger diameter size. This effect has been observed in the growth of carbon nanotube via the metal-catalytic CVD deposition process where “nearly carbon-insoluble” transition metal, like gold nanoparticle (Takagi et al., 2008) shows an efficient capture of the carbon feedstock from the hydrocarbon precursors. Meanwhile, Lin et al. (2015) has calculated the carbon solubility in Cu nanoparticles of 50 nm diameter at 1020 °C to be 8.42677 at. ppm (atomic parts per million) which has significant differences compared to bulk Cu (0.0076 at. ppm). The evolution of Cu₂O nanoparticle size with respect to graphene growth is illustrated in **Fig. 5.6**. Therefore, high surface-to-volume ratio (smaller) of Cu₂O nanoparticle with enhanced surface energy resulted in a much higher carbon solubility which could initiate the growth of graphene.

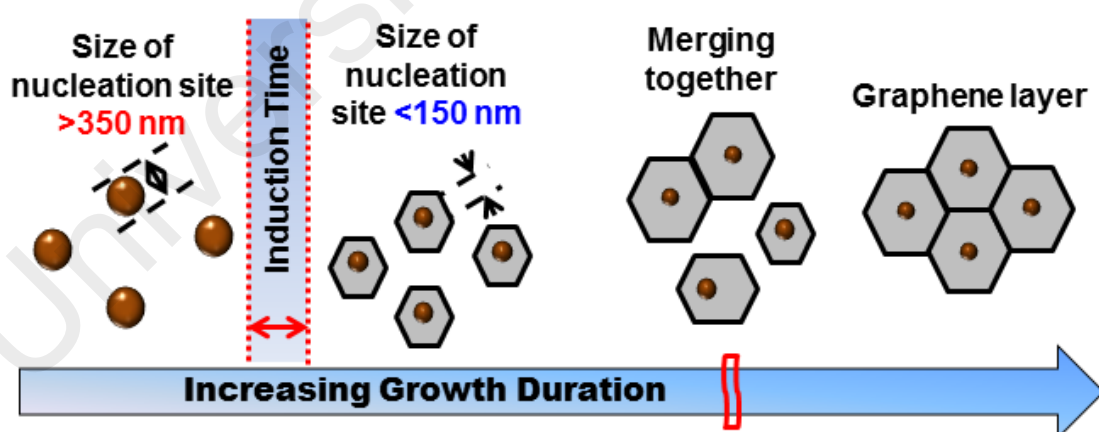


Figure 5.6: Evolution of Cu₂O nanoparticle size that initiates the graphene growth. Graphene would start to grow after the size of nucleation seed is favourable. The duration that takes for the patch-like graphene to be observed to grown is called the induction time.

5.1.2 Set 2: The Effect of Hydrogen Flow Rate

5.1.2.1 Growth and Etching effect on Graphene

Next, the graphene sample deposited for time duration of 30 minutes is selected from Set 1 (see **Section 5.1.1**) to further study the role of hydrogen flow rate on the graphene growth mechanism. This sample is selected because of the large coverage of the graphene layer observed from FESEM images. The hydrogen mixture with hydrocarbon gas play important roles as follows: (1) As a graphene growth promoter by activating a physisorbed surface bound radical $(CH_x)_s$ on the copper substrate leading to the agglomeration into multimeric $(C_nH_y)_s$ species and finally forming a hydrogen-free carbon cluster that is thermodynamically favourable compared to the dehydrogenation process of hydrocarbon on Cu; (2) As a graphene growth inhibitor by restricting the growth through selective etching of weakly structured carbon such as the armchair edges of graphene and amorphous carbon from the reactive hydrogen radical $(H^* + \text{graphene-CH} \rightleftharpoons (\text{graphene-C}) + H_2)$ or by limiting hydrocarbon precursor decomposition when excess hydrogen is present in the system $(CH_4 \rightleftharpoons C^* + 2H_2)$. (Losurdo et al., 2011).

All reactions happen simultaneously during the growth process; however the overall growth rate (or etching rate) is controlled by either one of the reactions above depends on which one is more dominant and strongly depends on the H_2 to CH_4 flow rate ratio. To make this study simpler, the carbon feedstock from CH_4 precursor is fixed at 10 sccm in Set 2, while varying the H_2 precursor from 10 to 100 sccm. This is done based on the fact that CH_4 has a lower sticking coefficient for physisorption onto active surface sites (topochemical reaction sites) on copper surface as compared to chemisorption of H_2 .

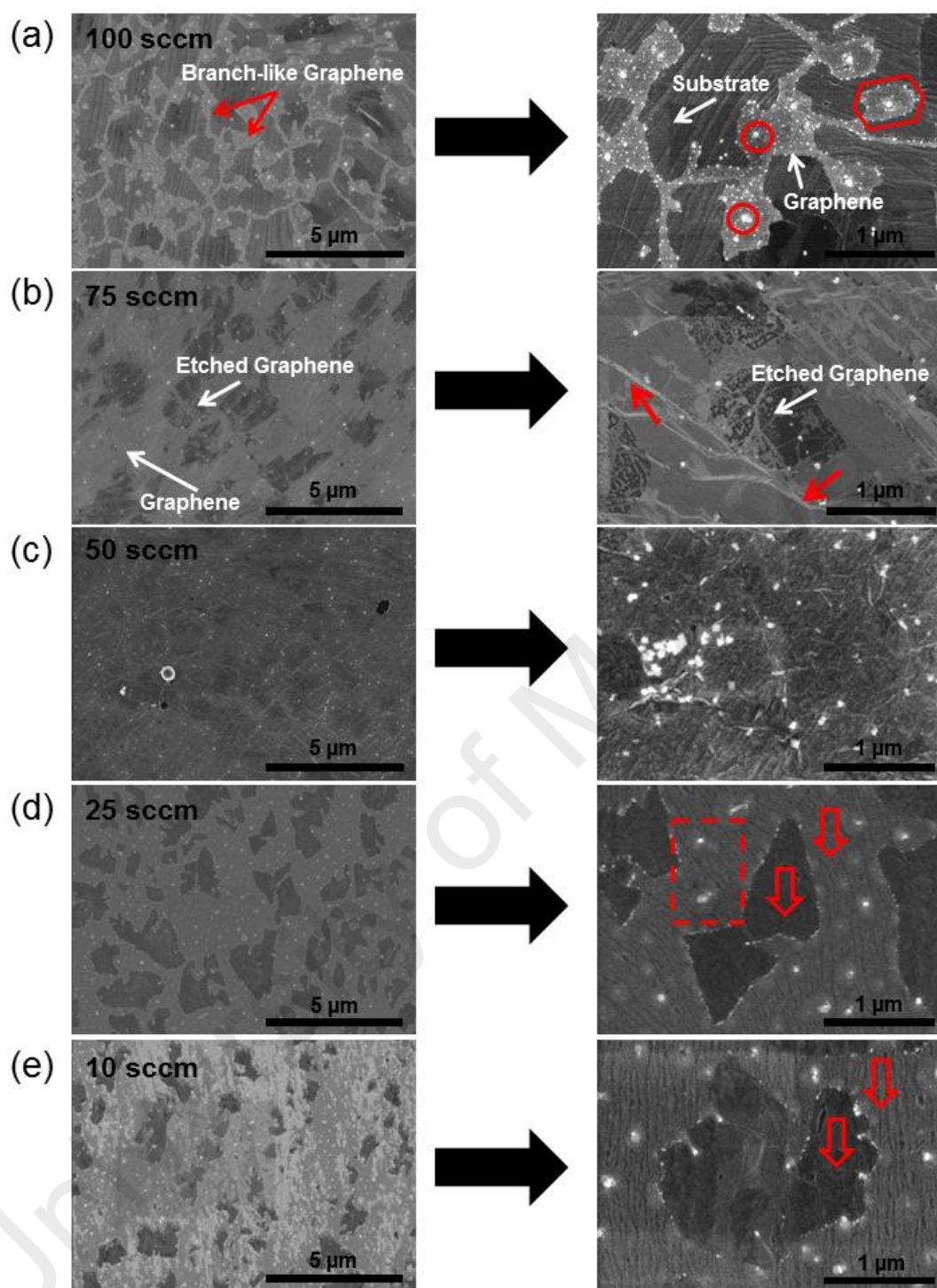


Figure 5.7: FESEM images of graphene grown on Cu foils with different H_2 flow rates: (a) 100, (b) 75, (c) 50, (d) 25, and (e) 10 sccm at 1000°C . The CH_4 flow rate was fixed at 10 sccm with a 30 minutes deposition time. The branch-like graphene grown around the nanoparticle at the centre of each domain was indicated by a hexagonal and circle shapes respectively in the magnified image on the right (a). Merging of two branch-like graphene was indicated by dotted square, while exposed graphene under-layer was differentiated from graphene upper-layer indicated by arrows as shown in the magnified images on the right (d) and (e).

Fig. 5.7(a–e) shows the morphology of the graphene grown on the Cu foils at different H_2 flow rate without changing the other fabrication process conditions as in Set 1. The formation of the graphene layer could be clearly seen for all the samples, except that for 100 sccm (**Fig. 5.7(a)**), which only shows the growth of branch-like graphene domains with a size of $\sim 0.5 \mu m$ (enclosed inside the hexagon) and interconnected with each other. The presence of nanoparticles that appeared at the centre of each graphene domain (enclosed inside circles shape) signified the role of the nanoparticle as a nucleation centre. In contrast to the graphene grown for 10 minutes at the 50 sccm H_2 flow rate (refer to **Fig. 5.2(b)**), which appeared to have an irregular shape, a high H_2 flow rate is observed to trim the edges of the graphene and allowing it to form a more regular shape as shown in the magnified image. The growth is suppressed by an apparent etching of the graphene layer grown at H_2 flow rate of 75 sccm as shown in **Fig. 5.7(b)**. The growth rate decreased as a result of the etching effect of the hydrogen, which is observed to be prominent at higher hydrogen flow rates. Among these factors, controlling the hydrogen flow rate in the hydrocarbon precursors has recently been recognized to play a critical role in controlling the size of graphene patch and its morphology (Zhang et al., 2013; Celebi et al., 2013). In addition, it acts as an etching agent in the catalytic graphene formation by a copper substrate (Zhang et al., 2013).

A stable graphene growth is observed for the sample grown at 50 sccm H_2 flow rate as shown in **Fig. 5.7(c)**. A continuous graphene sheet is formed on the Cu foil and shows the presence of wrinkle-like structures on the whole surface of the samples as marked by the arrows. The growth rates of the graphene are significant at the low H_2 flow rates of 10 and 25 sccm, as shown in **Fig. 5.7(d)** and **(e)**, respectively. The arrows indicated the growth of an under-layer and upper-layer graphene as shown in the magnified images on the right. In addition, the merging of two graphene domains is shown inside a rectangular box. It could be deduced that by tailoring the etching effect of the hydrogen, mono-/multi-layer graphene could be formed by merging with the neighbouring graphene domains as illustrated in **Fig. 5.8**.

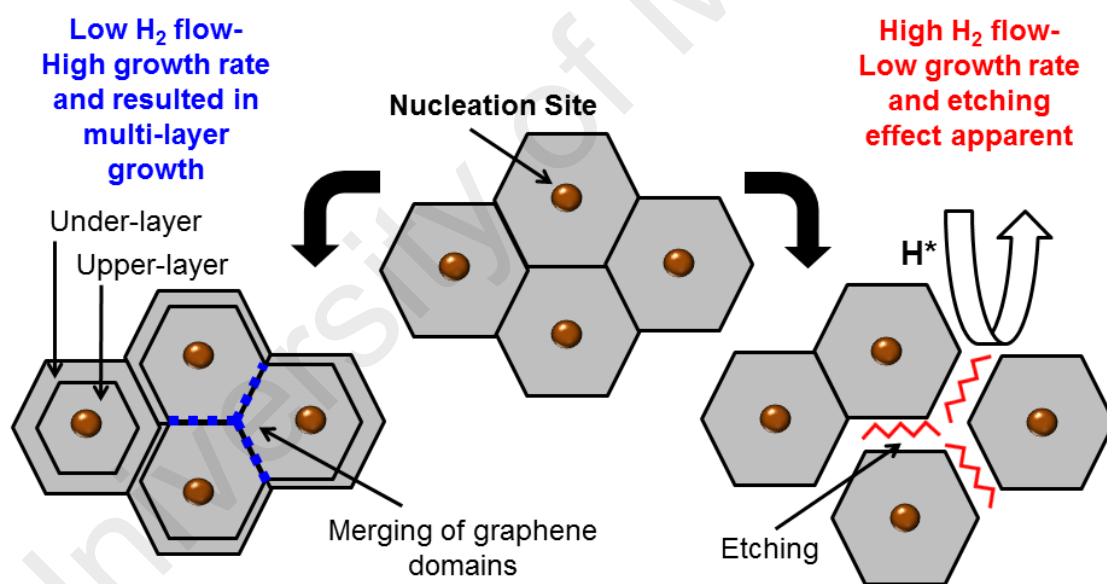


Figure 5.8: Illustration of the formation of graphene layer high and low flow rate of H_2 .

5.1.2.2 Determining the Number of Graphene Layers

Raman spectra measurements have been carried out for the graphene on the Cu foils to confirm the number of layers of the fabricated graphene. A typical graphene spectrum is found for more than 90% of the Cu foil area (more than 20 spots were analysed). **Fig. 5.9(a)** shows the Raman spectra of the graphene on Cu foils grown at different H₂ flow rates. A linear baseline fit has been applied to all the spectra. The spectra show two major Raman peaks for graphene: the G and 2D peaks located at ~1585 and ~2700 cm⁻¹, respectively. The G peak is associated with the double-degenerate; in-plane transverse optic (iTO) and longitudinal optic (LO) phonon mode (E_{2g} symmetry) at the Brillouin zone center. The 2D peak originates from a double-resonance (inter-valley process) mechanism involving two iTO phonons near the K and K₀ points in the first Brillouin zone of graphene (Malard et al., 2009). No D peak is observed in the spectra indicating high-quality graphene for all samples even when changing the hydrogen flow rate. The I_{2D}/I_G ratio is commonly used to determine the number of graphene layers (Malard et al., 2009). Lu et al. (Lu et al., 2012) suggested that the ratio for monolayer graphene should be more than one and a half (I_{2D}/I_G > 1.5) on Cu substrates for a single layer of graphene. According to that, the graphene deposited on the Cu foil shows a few-layers characteristic at 10 and 25 sccm, and a monolayer characteristic at 50, 75, and 100 sccm H₂.

In addition, considering the fact that the number of graphene layers based on the I_{2D}/I_G ratio alone may sometimes be misleading because it is determined empirically and acted as an independent metric to estimate the graphene layers, direct evidence is needed to support the previous estimation. Because the 2D peak originates from the double resonance process, a splitting in the electronic bands caused by the induced interlayer coupling can be detected (Malard et al., 2009). The FWHM_{2D} data are

obtained by fitting the 2D peak with a single Lorentzian line shape for the transferred graphene on the Si/SiO₂ substrate, as shown in **Fig. 5.9(b)** (graphene transfer process will be discussed later in this chapter). Generally, monolayer graphene has an FWHM_{2D} value of approximately 30-40 cm⁻¹ and broader for subsequent layers, which is in good agreement with the I_{2D}/I_G ratio results on Cu foils. The FWHM_{2D} value is found to be inversely proportional to the I_{2D}/I_G ratio (I_{2D}/I_G = 0.75, 1.33, 1.93, 1.95, and 2.42 for 10, 25, 50, 75, and 100 sccm, respectively), which indicates a decrease in the number of graphene layers with an increase in the H₂ flow rate. Note that we did not compare the FWHM_{2D} value of the graphene on the Cu foils because no direct correlation of the I_{2D}/I_G ratio is observed. This was inferred to be due to the strain effect of the underlying polycrystalline Cu facets compared to the amorphous nature of the Si/SiO₂ substrate (Wood et al., 2011). Thus, the effect of the underlying substrate is assumed to be minimal. The Raman results correspond well with the FESEM images shown in **Fig. 5.7**.

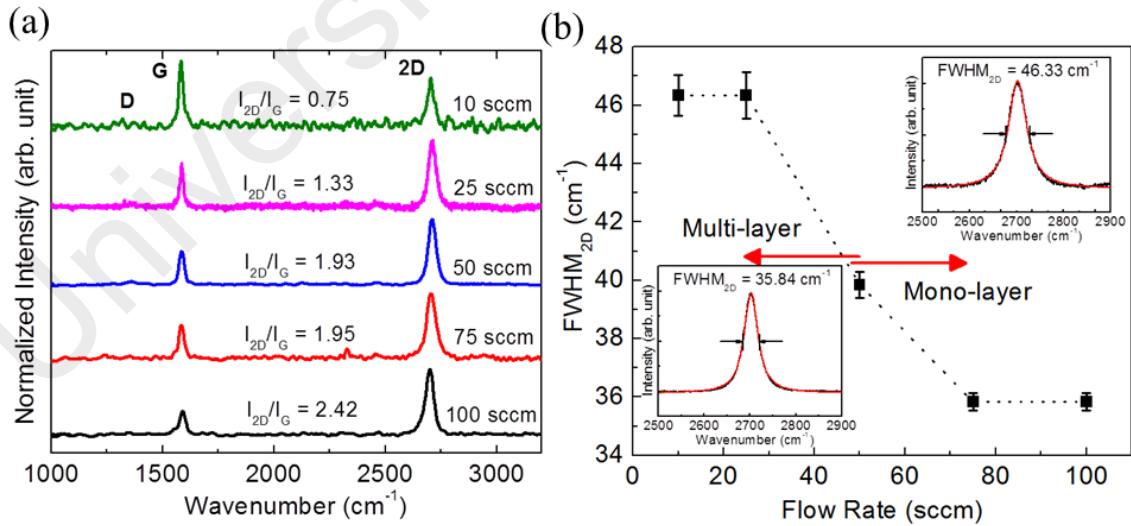


Figure 5.9: (a) 514-nm laser excitation Raman spectra of graphene deposited on Cu foils and (b) FWHM_{2D} of transferred graphene onto SiO₂/Si substrate at various H₂ flow rates: 10, 25, 50, 75, and 100 sccm.

5.1.2.3 Tiered Graphene Island Nucleates by Cu₂O Nanoparticle

Typically, FESEM and Raman spectroscopy (including Raman mapping) are used to map the morphology of graphene films. However, with FESEM imaging only the topmost layer of graphene are observed and cannot view the presence of adlayers or under-layer growth, while micro-Raman mapping is so time consuming that it is limited to small regions of a graphene film with major drawback from a low lateral resolution (micron scale). Most of previous studies have reported that the graphene grown by conventional CVD on copper suggested being surface mediated and self-limiting (Mattevi et al., 2011) which contradicts the results presented in **Fig. 5.9**. It means that once the monolayer graphene is completed, the process did not propagate anymore, since the catalytic Cu surface (topochemical site) is blocked.

However, recent study of graphene growth using isotopic labelling aided with Raman mapping has shown that the monolayer graphene may consists of small regions with double- or multi-layers growth stacked like an inverted ‘wedding-cake’ configuration (Li et al., 2013; Nie et al., 2013). The mechanism of the formation of a multi-layer regions is not well understood yet or even controversial. On the other hand, Low Energy Electron Microscopy (LEEM) can be utilized to study the adlayers between graphene layer and metal substrate as well as number of graphene layers with a higher sub-micron resolution (Bauer, 2014). In addition, the LEEM does not require a graphene transfer process which could alter the initial layer condition and also able to scan a large area by simply moving the sample stage.

Next, the LEEM images are further collected from 10, 25 and 50 sccm graphene samples at 50, 15 and 7.5 μm FOV as shown in **Fig. 5.10**. These sample are chosen since the graphene grown is covered all the surface of copper foil and shows mono- to multi-layer graphene from FESEM and Raman spectroscopy results. The graphene sample on copper foil is irradiated with different

electron energies (by varying the incident-electron bias voltages between the sample and objective lens; $V_{\text{Bias}} - V_{\text{Vac}}$), and the electrons are reflected differently based on the number of graphene layers. This is because only electrons with certain discrete energy levels are allowed in the quantum well-potential assigned for the specific graphene layer, thus allowing us to study how the graphene grows at a specific N^{th} graphene layer (Osaklung et al., 2012). From the images of 50 μm FOV, all samples show a homogeneous formation of graphene islands (dark spots) when irradiated with incident-electron bias voltages of ~ 3.0 eV. A slight difference in lighter and darker regions in these images (more prominent for 50 sccm sample as shown by the red arrow) are due to the unevenness of copper foils present during the handling process.

In addition, the graphene islands have grown without appreciable interference from the copper grain boundary (dotted lines) as can be seen in 15 μm FOV for all sample. In contrast, the graphene islands are consistently scattered around the flat copper surface which strongly implies that nanoparticles act as nucleation seeds for the graphene growth. This observation is consistent with the results discussed in **Section 5.1.1.3** and further confirms the FESEM image in **Fig. 5.7(a)**. By further zoom-in around the flat copper surface up to 7.5 μm FOV, the graphene islands can be clearly seen. Several spots are then extracted from different locations indicated by red, blue and green arrows with respect to the alternating bright and dark patterns. By measuring the oscillations in the LEEM image intensity as a function of electron energy (I–V LEEM analysis) it shows that the number of graphene layers in a certain spots can be clearly differentiated; tri-layer (red), bi-layer (blue) and mono-layer (green) graphene with respect to the colour of arrows.

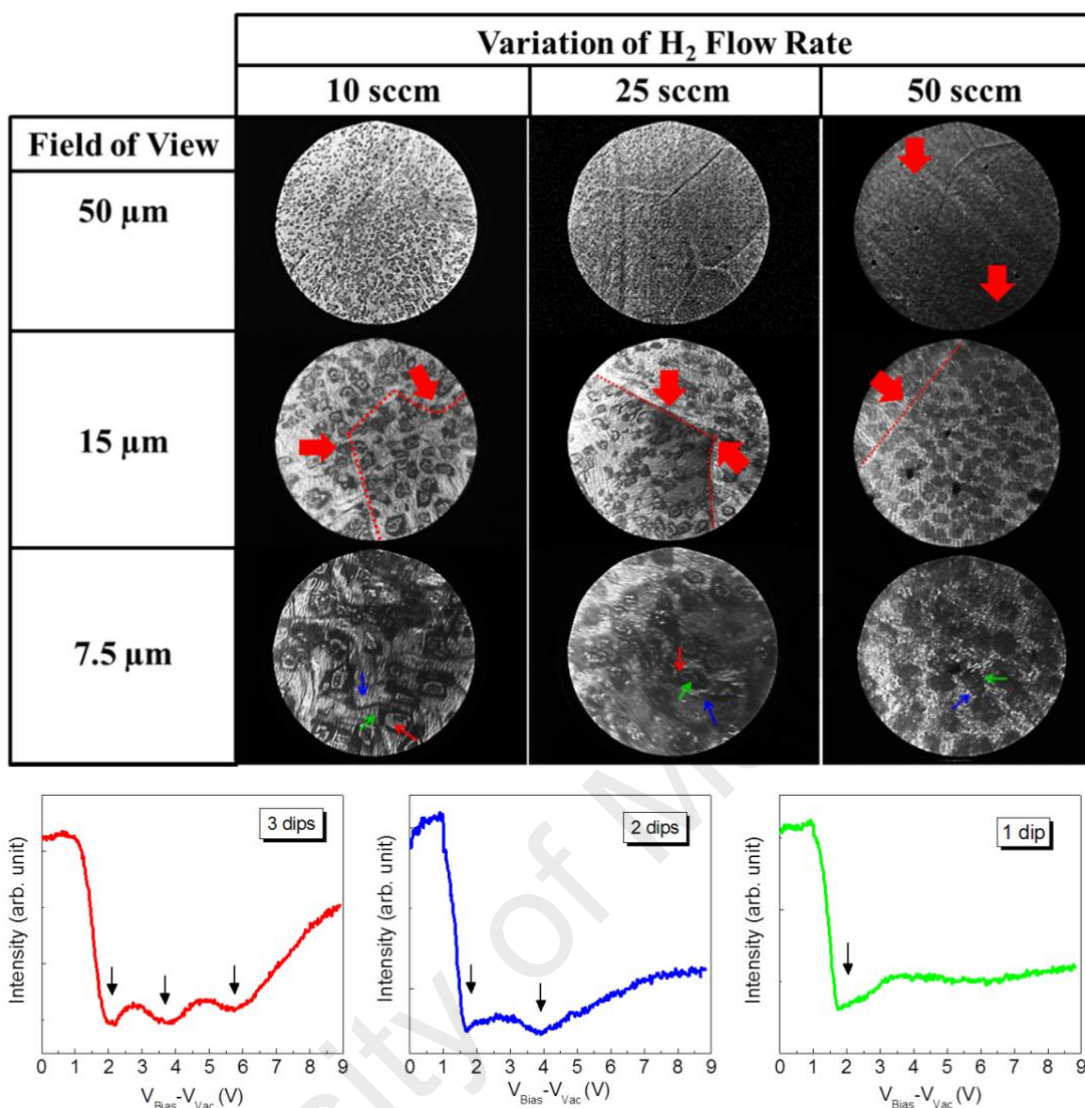


Figure 5.10: (Upper Part) LEEM images collected at 50, 15 and 7.5 μm field of view (FOV) of 10, 25 and 50 sccm H₂ sample. The images were taken using an energy of ~ 3.0 eV. This shows that the graphene is homogenously grown on the copper foil by using HFTCVD technique. (Lower Part) The IV-LEEM graph shows different number of dips (3, 2 and 1 dips) as a function of incident-electron bias voltages; $V_{\text{Bias}} - V_{\text{Vac}}$ that corresponds to the number of graphene layer (1 dip means mono-layer etc.). The colours of arrow (red, blue and green) correspond with the number of dips shown in 7.5 μm FOV. The V_{Bias} and V_{Vac} are defined as the bias voltage applied to the sample and vacuum energy level divided by electron charge, respectively.

5.1.2.4 Growth of Bi-layer Graphene

Coalescence of two graphene islands are analysed with the IV-LEEM graph starting from the centre of each graphene island towards each other which enclosed by dotted box are shown in **Fig. 5.11(a)** and further magnified at **(b)** and **(c)**. The spots are carefully selected from each alternating light and dark bands which represent maxima and minima interference in the electron reflectivity, respectively therefore gives accurate determination of number of graphene layer in tiered graphene island configuration. At the centre of graphene island as observed for 10 sccm sample (**Fig. 5.11i**), mono-layer graphene is formed, and then moving to the next band it shows the formation of tri-layer graphene. Further in outward direction, bi-layer graphene is found to form in between two graphene islands.

Conversely, for 25 and 50 sccm sample (**Fig. 5.11ii** and **iii**), the formation of mono-layer graphene is found in between two graphene islands but still maintain the mono-layer formation at the centre of each island. The only difference is the number of graphene layer formed in outwards direction from the island centre. The possible stacking orders of the tiered graphene layer are illustrated in **Fig. 5.11(d)**. For 10 sccm, 25 sccm and 50 sccm sample, the formation of a ‘wedding cake’-like configuration contradicts with the results from Li et al. (2013) and Nie et al. (2013). However, our finding is in agreement with the recent work of Kasap et al. (2015) which found that silicon oxide impurity particles (Cu_2O nanoparticle as found in this study) within the copper act as catalysts and the seeds of multi-layer graphene islands.

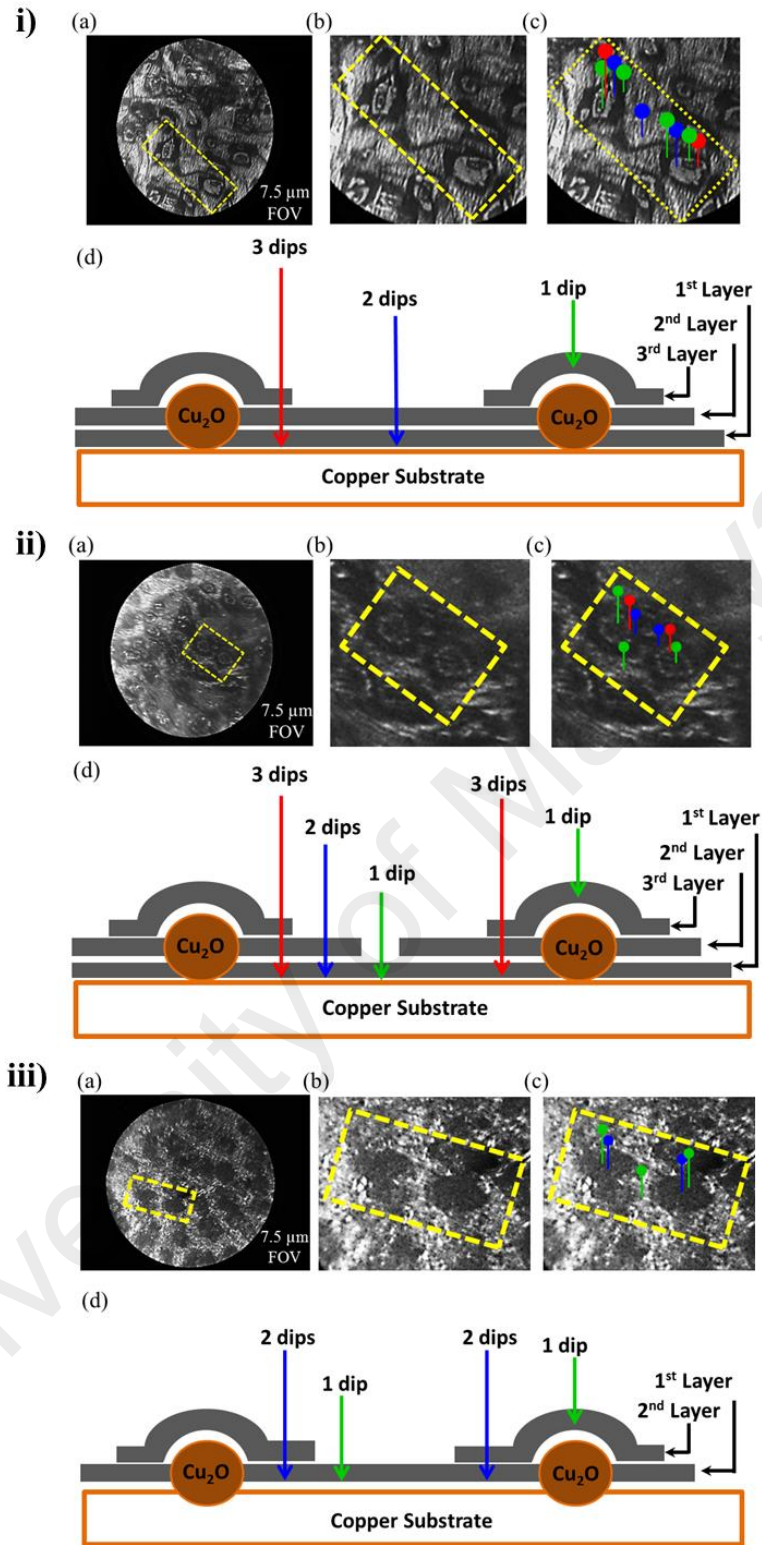


Figure 5.11: The i) until iii) shows the sample of 10 sccm, 25 sccm and 50 sccm H_2 flow rate, respectively. The LEEM images of (a) and (b) shows a selected area of interest for coalesce between two graphene islands indicated inside the dotted box. (c) The colour coding of certain spots is corresponds to the number of graphene layer; Red is tri-layer, Blue is bi-layer and Green is mono-layer. (d) Illustrated cross-sectional schematics of graphene island formation on a Cu_2O nanoparticle seed.

Generally, the growth of second graphene layer is said to be self-limited which contradict with the IV-LEEM results presented earlier. Gan et al. (2015) has described the self-limiting graphene grown mechanism (on Cu foil) as shown in **Fig. 5.12**. This growth consists of a) Adsorption-diffusion mechanism which involves the following three major steps: (1) adsorption, in which precursor gases adsorbed and decomposed on copper surface; (2) diffusion on copper surface; and (3) growth of the second layer underneath the first layer. Under this mechanism, carbon source for under-layer growth are mainly through the edges of top-layer. b) Gas phase penetration mechanism, in which (1) the active carbon species in gas phase directly penetrate the graphene sheet and then (2) providing the carbon source for the under-layer growth. This will leads to the growth of inverted ‘wedding-cake’ configuration as opposed to the proposed growth mechanism earlier (see **Fig. 5.11(d)**). However, this type of growth mechanisms sometimes will seriously constrain the ability to make continuous bi-layer (and even multi-layer) graphene by conventional CVD, where the growth stops once the overlying layer is completed. Hence, the two layers must be completed at the same time, which is a challenge since the edge of the under-layer most certainly grows slower than the overlying layer’s exposed edge.

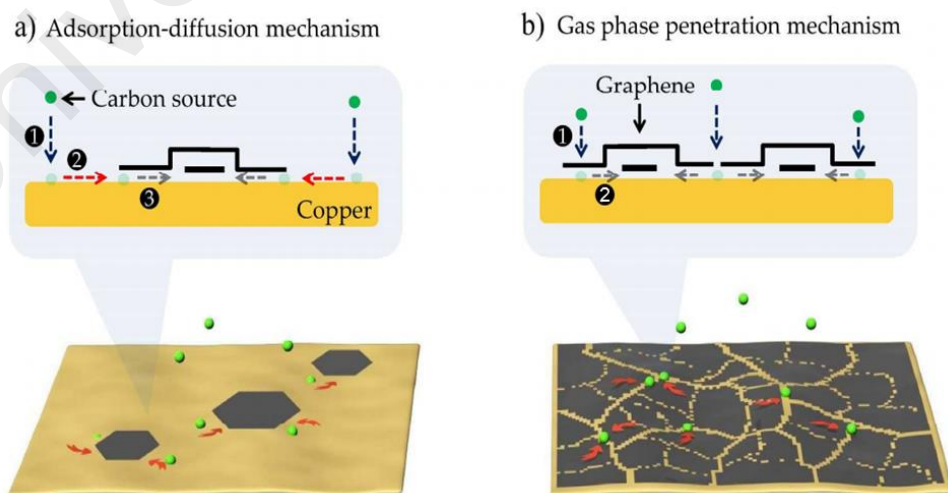


Figure 5.12: Mechanisms for adlayer graphene growth followed by a) adsorption-diffusion and then b) gas phase penetration mechanism (Gan et al., 2015).

To further prove the growth mechanism illustrated in **Fig. 5.11(d)** with the tiered ‘wedding-cake’ graphene configuration, the 10-sccm sample was mapped with a 7.5 μm FOV full-area colour coding as shown in **Fig. 5.13**. The number stated at the upper right edge corresponds to the number of graphene layer(s); for example, 1 bottom means mono-layer graphene and so on. Interestingly, the number of bi-layer and tri-layer graphene covers about ~60% and ~25%, respectively of the 7.5 μm FOV area. This further supported the idea of the first graphene layer is formed by surface adsorption around the nucleation seed and followed up by the consecutive layers on top of the first graphene layer. The growth of consecutive layers stop when the nanoparticle has been covered by graphene as observed by only mono-layer graphene is detected at the centre of each islands while bi-layer or tri-layer graphene grows just besides the centre region. In addition, few pin-holes (about 0.02%) are observed in this sample.

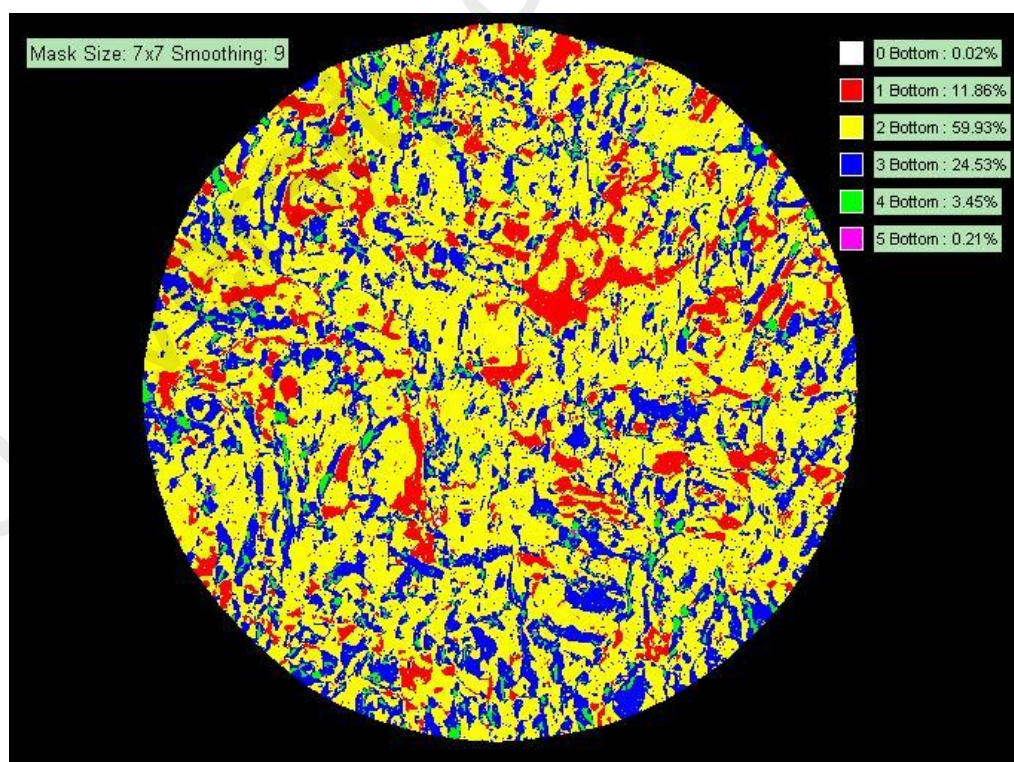


Figure 5.13: The colour coding of 10-sccm H_2 flow rate sample in 7.5 μm FOV. The dominant yellow colour resembles a bi-layer graphene with the coverage up to 60 % of total area.

The growth of bi-layer graphene (10-sccm sample) with tiered ‘wedding-cake’ growth configuration has been shown by the LEEM analysis which signifies the role of Cu₂O nanoparticle seed (nucleation centre) for the growth of subsequent graphene layer. In comparison to the recent work by Mendoza et al. (2015), the largest bi-layer graphene coverage achieved so far is ~90% coverage which far exceed to the value achieved in this work (~60%). In addition, multi-layer graphene growth has been recently reported by Kasap et al. (2015) to be as high as ~98% as compared to this work to be at ~85% coverage. However, with the optimization in the growth duration as well as H₂ flow rate, it is believed that the growth of predetermined number of graphene layer coverage is achievable.

5.2 Formation of High-quality Graphene

5.2.1 The Synergistic Role of Vapour Trapping and Hot-filament Reactions

The key modification in this HFTCVD technique is the vapour trapping mechanism via alumina tube with one end sealed as shown in **Fig. 5.14**. This step is crucial in introducing the circumfluence flow inside the tube with a trapped copper vapour which then initiates the nucleation centres of graphene and consequently enables us to produce a high-quality graphene (refer to **Fig. 5.9**). The role of vapour trapping is first proposed by Li et al. (2011) followed by Zhang et al. (2012) and Rummeli et al. (2013), who highlighted the importance of the local environment growth condition, which can lead to a controllable graphene defect density and homogenous growth. This is because of the vapour trapping capability for the Cu species leading to a higher carbon concentration, which then improved the decomposition of hydrocarbon (CH₄) gas compared to the normal HWCVD and HFCVD configurations.

Pre-cracking of the Precursor Gases at Hot-filament

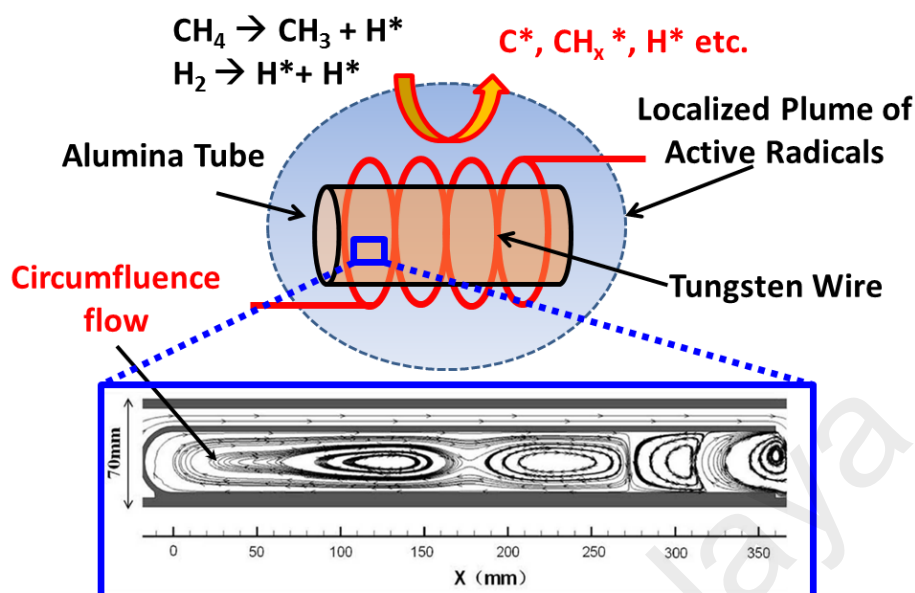


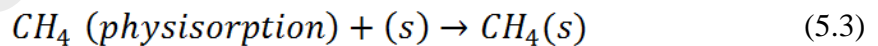
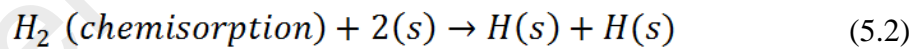
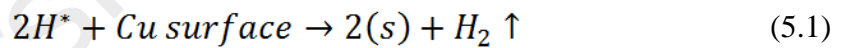
Figure 5.14: Schematic of graphene growth deposition in HFTCVD technique and formation of active flux of carbon, hydrogen and hydrocarbon radicals by catalytic reaction of CH_4 and H_2 precursors using tungsten filament. The streamline of mixed gas inside the alumina tube from the simulation calculation shows a circumfluence flow which directly adapted from the work of Wang et al. (2014). Note that, this diagram only act as an illustration of circumfluence flow inside the tube with one end sealed.

In the conventional HWCVD and HFCVD graphene growth processes, the carbon species in the growth chamber are of high flow velocity, thus only the carbon species molecules adsorbed on the Cu substrate could be pyrolyzed into activated carbon atoms, C^* in addition to the catalytic dissociation at hot-filament surface (Shi et al., 2014). The carbon species molecules far away from the Cu substrate could not convert to activated carbon atoms because of the short residence time and the absence of the catalysis of Cu, which makes the formation high-quality graphene difficult. However, in the HFTCVD system, the assembly of the alumina tube can help to create a quasi-static condition, where the flow velocity of carbon species decreases greatly and some Cu gas molecules might be trapped in the growth chamber (circumfluence flow); thus not only the carbon species can adsorbed on the Cu substrate convert to activated carbon species, but also those far away from the Cu substrate can have enough time to convert to activated carbon atoms with the catalysis of Cu vapour

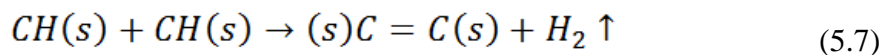
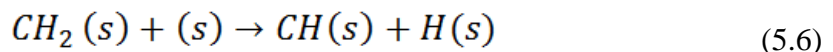
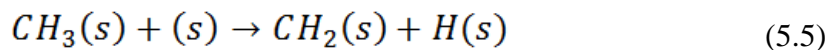
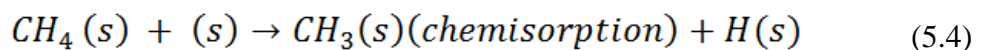
molecules. These activated carbon atoms could be adsorbed onto the Cu substrate or the surface of the grown graphene, promoting the growth of high-quality graphene.

Interestingly, by simply tuning the hydrogen flow rate, the number of graphene layer can be easily manipulated while maintaining its low defect density (see **Section 5.1.2.2**). However, it have been reported by Vlassiouk et al. (2011) and Tao et al. (2012) that there exists an optimum ratio of H₂ to CH₄ precursors to grow a high-quality graphene on Cu foils using conventional CVD technique. These differences in the observed phenomena can be rationalized in light of the different mechanisms for graphene growth using various CVD technique, which have to take into account the different in the surface kinetic factor.

The reaction steps to be considered is the competitive dissociative chemisorption of H₂ and physisorption of CH₄ on copper substrate ‘surface sites’ denoted as (s), which priory created by hydrogen radical; H* (from catalytic reaction at hot-filament). According to Vlassiouk et al. (2011), the reactions can be described as shown in (5.1), (5.2) and (5.3);

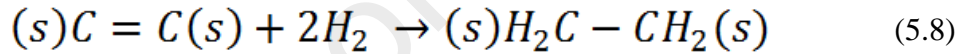


As for the next steps of CH₄ dehydrogenation, the following reactions shows,



which according to previous study by Losurdo et al. (2011), it has been demonstrated that the dissociative chemisorption of $\text{CH}_4(s)$ and (s) on Cu surface are controlled by reaction (5.2) that act as the graphene growth rate limiting step. If the H_2 quantity is high, the subsequently stepwise dehydrogenated according to reactions (5.4) until (5.6) will be significantly decreased. This is due to the etching effect of hydrogen and chemisorption saturation of H_2 at the ‘surface sites’ on the Cu surface (reaction (5.2)).

However, at optimum ratio of H_2 to CH_4 precursors to grow a high-quality graphene, reaction (5.7) will be taken place which further aromatizes into the benzene ring on the Cu surface sites. Conversely, when they are excess of H_2 , reaction (5.8) will be taken place which then contributes to create point defects consisting of hybridized sp^3 C–H bonds as reported by Losurdo et al. (2011).



Nevertheless, in the context of the catalytic reaction at hot-filament to pre-cracking the precursors gases (as well as vapour trapping mechanism) further amplified the C^* concentration and readily react with the excess H_2 present in the system ($\text{C}^* + 2\text{H}_2 \rightleftharpoons \text{CH}_4$) (Vlassioux et al., 2011). This will then reduce the reaction (5.8) to be taken place in the wide variation of H_2 concentration as presented in this work (from 10 sccm to 100 sccm). Therefore, it is deduced that the synergistic role of alumina tube which creates a quasi-static condition as well as the catalytic dissociation of CH_4 and H_2 precursors by hot-filament will promotes the growth of high-quality graphene. As the proof of this concept, even at a low (high) H_2 dilution where the growth rate is prominent (suppressed), the I_D/I_G ratio is observed to be very low ($I_D/I_G \ll 0.1$) for both cases.

Furthermore, an XPS analysis is performed to several sample fabricated in this study (10, 25 and 50-sccm sample due to full coverage of graphene on Cu foil). A typical graphene spectrum on the Cu foils is observed in all samples, with the presence of carbon (indicated by the C1s peak at 284 eV) and a very low oxygen (indicated by the O 1s peak at 532 eV) elemental composition, as shown in **Fig. 5.15**. Since graphene is composed mainly of sp^2 C–C bonds, and a small degree of oxidation is believed to have taken place at the graphene edges and/or defect, the deconvolution of the high-resolution XPS scan for the C1s core level revealed several components assigned to the C=C, C-OH, C-C=O, and C=O bonds at 284.6, 285.7, 287.5, and 288.7 eV, respectively (**Fig. 5.15** inset) (Hafiz et al., 2014). The oxygen- related components of the decomposed peak shown here correspond to ~20% of the total area of the C1s peak, which is close to the value for high-quality graphene material found in the literature since defects in graphene lattice will attract oxygen to be bonded with the carbon atom (Hawaldar et al. 2012).

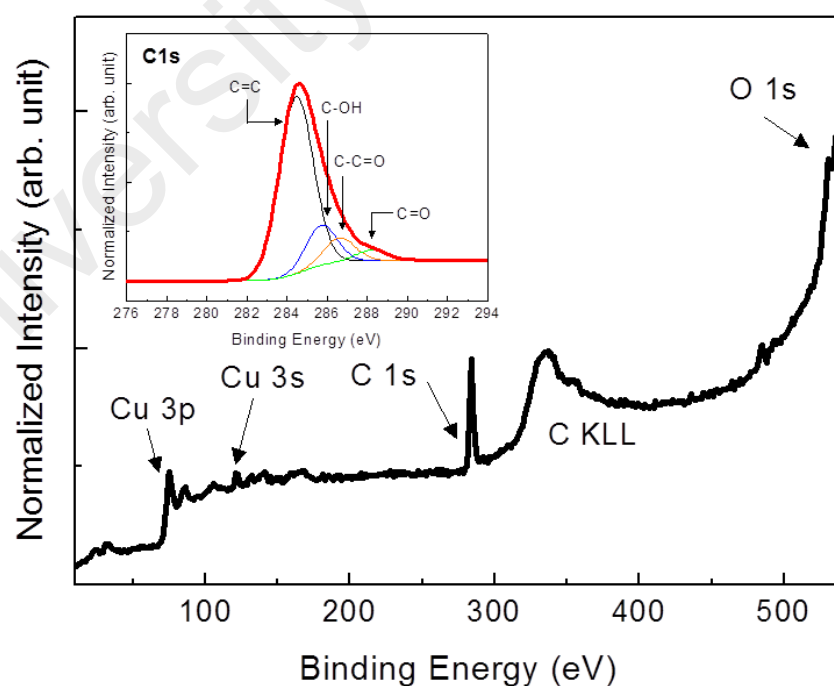


Figure 5.15: A typical wide scan of XPS spectra of graphene sample on Cu foil. (Inset) The deconvolution of C1s peak shows the graphene is slightly oxidized due to its high-quality nature.

5.2.2 Controlled Experiment

A controlled experiment is then conducted, and its Raman spectra are shown in **Fig. 5.16** with the following parameters: (i) a 2 cm alumina tube opening at 1000 °C and (ii) 1 cm alumina tube opening at substrate temperatures of 850–1000 °C. The filament temperature is kept to be >1500 °C for all deposition to maintain the catalytic reaction of tungsten filament. The samples underwent an initial cleaning treatment at 1000 °C for 20 minutes, and then the deposition process for 30 minutes with the CH₄:H₂ flow kept at 10:50 sccm. The opening and length of alumina tube with one end sealed are fixed at 1 cm and 2 cm; respectively. A significantly degraded graphene quality is observed, with an apparent high defect density of D, G', and D + D' peaks at 1354, 1625 and 2957 cm⁻¹, respectively. This is due to the quasi-static equilibrium of copper vapour being distorted with an increase in the alumina tube opening to 2 cm or a decrease in the copper sublimation reaction at 850 °C. These further shows that a suitable vapour trapping condition (Zhang et al., 2012) and surface kinetic factors are necessary to obtain a low-defect ratio in this experimental setup (Bhaviripudi et al., 2010).

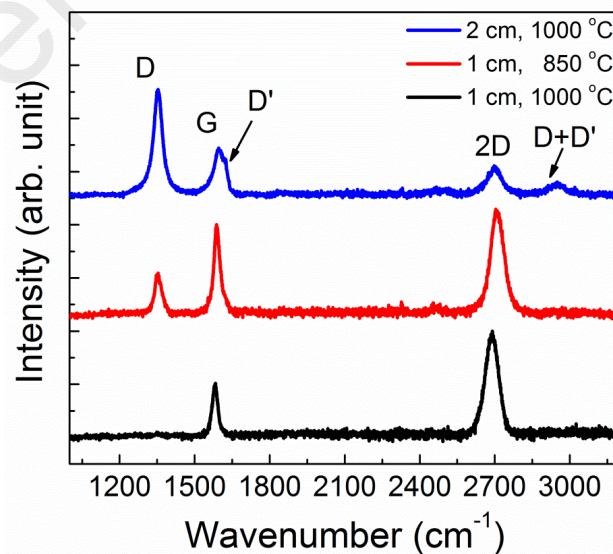


Figure 5.16: Raman spectra of controlled deposition experiment with following parameters: (i) 2-cm alumina tube opening at 1000°C and (ii) 1-cm alumina tube opening at 850 °C substrate temperature. The 1-cm alumina tube opening deposited at 1000 °C substrate temperature was shown for comparison.

5.2.3 Comparison of Graphene Deposited using Cat-CVD Techniques

Many efforts have been devoted to develop diverse approaches to fabricate graphene, aiming for the large and uniform area synthesis of high-quality graphene. Nevertheless, the synthesis of uniform, high-quality and controllable layer of graphene still remains a significant challenge especially by Cat-CVD technique. The progress of Cat-CVD technique to produce the desired graphene criteria has been shown in **Table 5.1**. The work of graphene growth using Cat-CVD technique namely HWCVD is pioneer by Stojanovic et al. (2012) in the mid-year of 2012. However, to the best of our knowledge, the previously reported graphene fabricated by using HFCVD and HWCVD techniques contained a high defect density. In addition, it has been reported by Stojakovic et al. (2012) and Soler et al. (2013) which used the HWCVD techniques for the graphene deposition on Cu foils, they obtained a much higher defect ratio ($I_D/I_G > \sim 0.5$), compared to our results ($I_D/I_G \ll 0.1$). Furthermore, Kataria et al. (2012) has reported that a high-quality mono-layer graphene ($I_D/I_G \ll 0.1$) can be grown using an HFCVD technique with a significantly higher filament temperature of $>2000\text{ }^\circ\text{C}$ compared to our work and that of Hawaldar et al. (2012), which were set at $\sim 1750\text{ }^\circ\text{C}$ and $\sim 1800\text{ }^\circ\text{C}$, respectively. However, with the aid of the proposed vapour trapping configuration, the filament temperature used can be about $200\text{--}250\text{ }^\circ\text{C}$ lower than that with the conventional HFCVD configuration.

Growing full coverage of multilayer graphene on copper substrate with a predetermined thickness still remains as an open problem as the number of layers of graphene and their coverage were not changing much after initial few minutes of growth time. From the recent work of Mendoza et al. (2015), a higher filament temperature ($2300\text{ }^\circ\text{C}$) cannot solely control the formation of continuous bi-layer graphene without the trade-off between the decreases in graphene quality

($I_D/I_G = 0.2-0.3$). However, it has been reported by Kasap et al. (2015) and Gan et al. (2015) that had discussed the important of the nanoparticle nucleation centres during the formation of the first graphene layer and then further attracts the active carbon source for the growth of the successive layers while maintaining the high-quality of graphene structure. By employing the nucleation centre growth condition, this work has been successfully fabricated a continuous high-quality monolayer and bi-layer graphene using HFTCVD technique as shown by the 50 sccm and 10 sccm sample, respectively. It is also important to note that the quality of the graphene deposited using the widely used T-CVD technique typically has a very low defect density ($I_D/I_G \ll 0.1$). Hence, a comparison is only made in the context of the less-explored Cat-CVD technique (e.g. HWCVD and HFCVD), which still has a lot of room for improvement.

Table 5.1: Comparison of results from this work and literature regarding the quality of fabricated graphene on Cu foil based on various CVD techniques.

Year	Ref.	Growth Technique	Substrate Temperature, (°C)	Hot-filament Temperature, (°C)	Vapor Trapping Condition	Seeded Growth	Number of Layer	I_D/I_G Ratio
2012	Stojanovic et. al.	HWCVD	1000	N/A	No	-	Multi-layer	~1.00
2012	Kataria et. al.	HFCVD	1000	>2000	No	-	Mono-layer	$\ll 0.1$
2012	Hawaladar et. al.	HFTCVD	1000	~1800	Yes	-	Mono-layer	~0.5
2013	Soler et. al.	HWCVD	800-900	N/A	No	-	Multi-layer	~0.7
2014	Y. G. Shi et. al.	CVD	1045	-	Yes	-	Mono-layer	$\ll 0.1$
2014	Frank Mendoza et. al.	HFCVD	1000	2300	No	-	Bi-layer	0.2-0.3
2015	Sibel Kasap et. al.	CVD	1000	-	No	SiO _x impurities	Multi-layer	$\ll 0.1$
2015	Lin Gan et. al.	CVD	1000	-	No	Cu	Mono-layer	$\ll 0.1$
2015	This work	HFTCVD	1000	~1750	Yes	Cu ₂ O	Controllable Number of Layer	$\ll 0.1$

5.3 Proposed Growth Mechanism

By corroborating the experimental approach using FESEM, LEEM and Raman analysis as well as models found in the literature, a growth mechanism was then deduced for the growth of the graphene films using the HFTCVD system presented in this study, as shown in **Fig. 5.17** and described below;

- (1-2) At the time of fabrication process, CH_4 and H_2 precursor gases are dissociated with the aid of a hot-filament and created a localized plume of active radicals in the vicinity of the alumina tube.
- (3) Meanwhile, the copper substrate inside the alumina tube was in a state of sublimation, which created a quasi-static equilibrium copper vapour that reacted with the oxygen to form Cu_2O nanoparticle on top of the copper foil.
- (4) The Cu_2O nanoparticle then acted as nucleation sites after the induction period for the active carbon reactants to form a graphene patch and progressively enlarge the graphene domain to form a graphene layer.
- (5) At the apex of nanoparticle, where the growth rate is high, the growth will eventually starts at the borders of the nucleation sites. This will then leave an exposed Cu_2O nanoparticle surface for the tiered ‘wedding-cake’ graphene island formation. Eventually, the growth will stop when the Cu_2O nanoparticle surface has been completely covered up by the graphene layer due to a significant drop in the number of topochemical reaction site. However, the border of the graphene lattice is still chemically active and acts as the incorporation site for the incoming activated carbon atoms (C^*), thus continuing to grow until constituting a complete graphene layer. This has been observed at an early stage of the growth of single-walled carbon nanotube (SWCNT) which has been reported by Homma et al. (2009).

- (6) Finally, H_2 out diffusion reaction will be taken place along the growth process which aromatizes several chemisorption $CH(s)$ into the benzene ring (graphene) on the Cu surface sites for the formation of high-quality graphene.

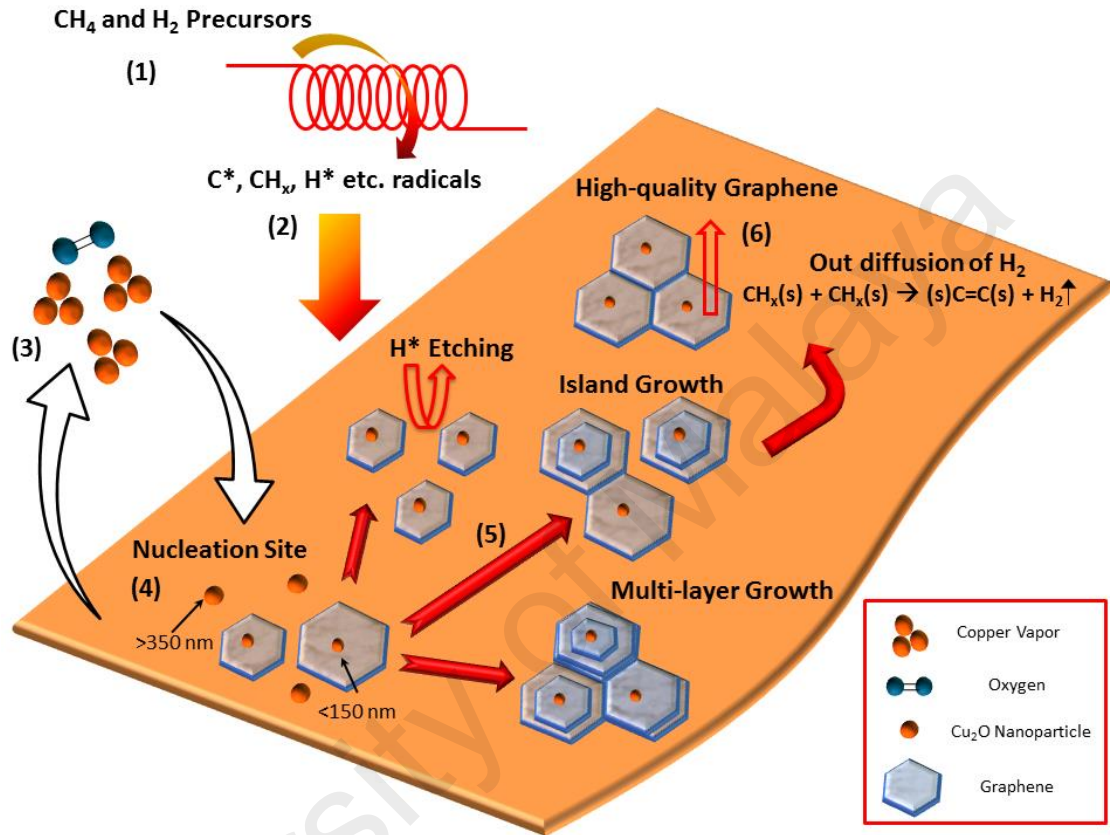


Figure 5.17: Diagram of growth mechanism of graphene on Cu foil assisted by Cu_2O nucleation sites using HFTCVD technique.

5.4 Graphene Transfer

5.4.1 Preferred Transfer Process for Device Fabrication

In general, a transfer step is required for graphene fabricated using CVD technique in order to separate the deposited graphene from the catalyst metal that it grew on and move it to an arbitrary substrate. Typical images of transferred graphene on SiO_2 substrate viewed using optical microscope and FESEM imaging are shown in **Fig. 5.18**. The most widely used transfer method for CVD synthesis is polymer-supported metal etching. The methods are categorized into thermal release tape, (TRT)

and poly(methyl methacrylate), (PMMA) supported. Then, the metal substrate will be etched away by ferric chloride, (FeCl_3) solution as explained in Chapter 3 under **Section 3.4**. The high-quality graphene has been fabricated using HFTCVD technique in this study has shown a significant improvement as compared to the standard Cat-CVD technique. Although a quality improvement can be made during the fabrication steps, it is important to note that most of the time, degradation of the graphene quality occurs during the transfer process due to some tearing and ripping of the graphene sheets. Therefore, the best transfer methods that deliver graphene onto target substrates without significant mechanical damage in terms of defect density, transfer coverage and I-V characteristic are discussed.

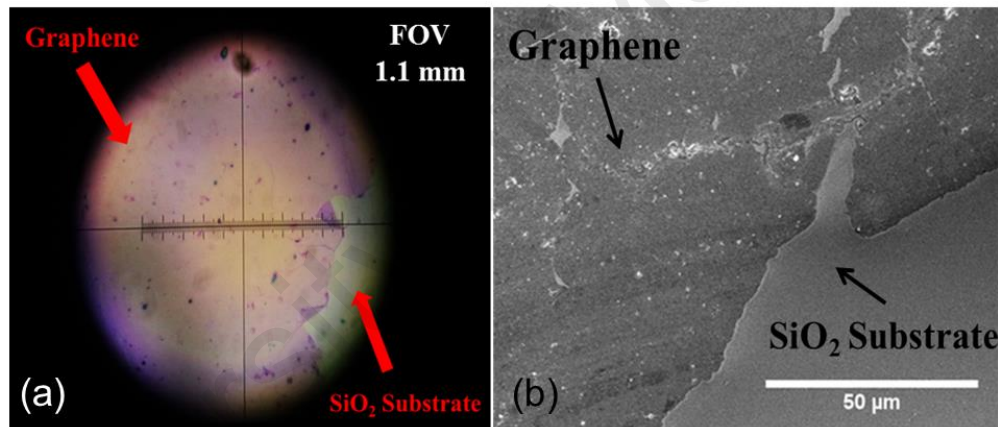


Figure 5.18: Typical images of transferred graphene layer observed on SiO_2 substrate viewed using optical-microscope and FESEM.

5.4.1.1 Effect on Defect Density, Transfer Coverage and I-V Characteristic

The crystallinity of the transferred graphene using TRT and PMMA support method is deduced from Raman spectra measured from mono-layer and multi-layer samples on SiO_2 substrates. In **Fig. 5.19**, the D peak is observed in the spectra at 1337 cm^{-1} along with the presence of G and 2D peaks whose peak positions are unaltered when compared to the Raman spectra of graphene on Cu foil as presented in **Fig. 5.9(a)**. The origin of the D peak is an inter-valley process and its activation requires the presence of defects and is due to the breathing mode of sp^2 atoms in rings and its

intensity is strongly related to the presence of six fold aromatic rings (Malard et al., 2009). The presence of the D peak in the Raman spectrum of the graphene sample indicates the break-down of sub-lattice symmetry of graphene due to topological disorder (Malard et al., 2009). A significant increase of the D peak intensity is observed for multi-layer graphene transferred using TRT. The calculated I_D/I_G ratio for TRT and PMMA transfer method is 0.62 and 0.12, respectively. Both methods transferred the multi-layer graphene without reducing the number of its constituent layers deduced from the unchanged of the I_{2D}/I_G ratio. However, only a slight different in I_D/I_G ratio is observed between mono-layer transferred graphene using TRT and PMMA support of 0.16 and 0.20, respectively. Therefore, the PMMA transfer method may retain the as prepared graphene crystallinity on Cu foil for mono- and multi-layer graphene compared to TRT method which introduced a significant structural defect when transferring a multi-layer graphene.

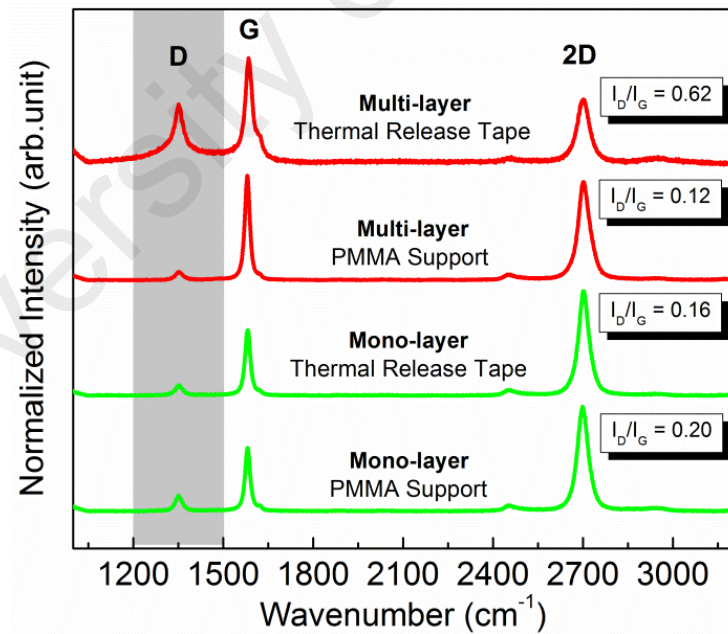


Figure 5.19: Comparison of the Raman spectra of mono-layer and multi-layer graphene transferred using thermal release tape and Poly-methyl methacrylate (PMMA) support. The D peak is presence in all samples after the transfer process compared to the data taken on Cu foil as shown in **Fig. 5.9(a)**. The effect of transfer process of both techniques is more significant on multi-layer graphene.

Next, the physical damage of transferred mono-layer graphene is then compared by observing the FESEM images as shown in **Fig. 5.20**. The graphene transferred using TRT method produces several numbers of cracks in contrast to the PMMA method which observed to be a single crack only (**Fig. 5.20(a)** and **(b)**). However, the PMMA transfer method may leave a residual PMMA on graphene that are visible in the **Fig. 5.20(b)** as shown in the circle area. The clean area of graphene surface can be distinguished as shown by the square area. It is common for the PMMA transfer method to have the PMMA residue but can be easily rinsed away by using acetone followed up by DI water (Gorantla et al., 2014). Higher magnifications of transferred graphene are also investigated at the centre and edge of transferred graphene as shown with the images at the right in **Fig. 5.20**. The centre of transferred graphene using TRT method appeared to have a bigger crack as compared to PMMA method. In addition, the edge of the graphene was incompletely transferred and has a lot of cracks while PMMA transfer method appeared to be a much better condition. This might be caused from the thermal stress on graphene during the peeling-off step where the target substrate and TRT are rapidly heated at elevated temperature ($>100\text{ }^{\circ}\text{C}$) on the hot-plate (Kim et al., 2015).

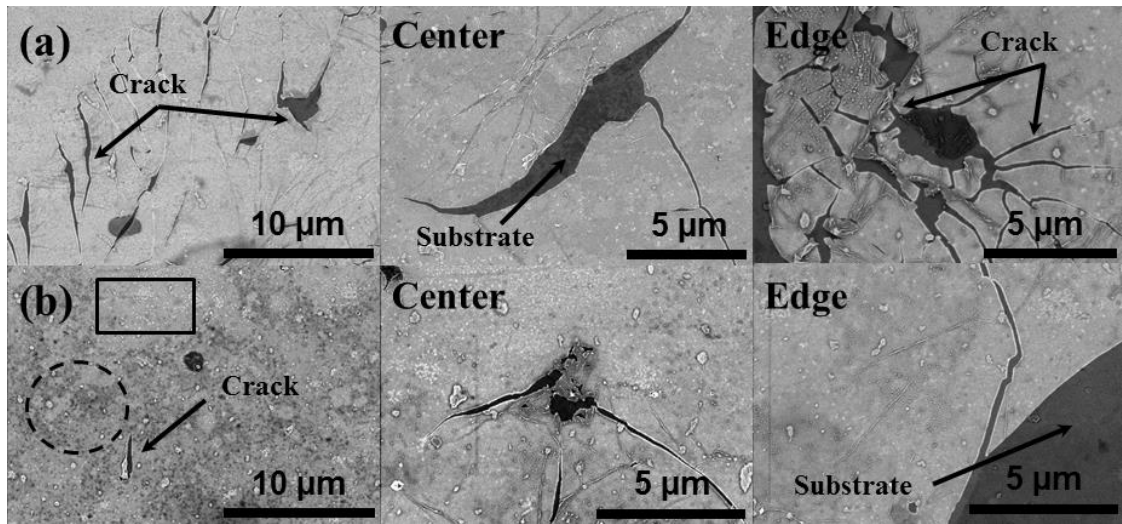


Figure 5.20: FESEM images shows a comparison of mono-layer graphene morphology transferred using (a) thermal release tape; TRT and (b) Poly-methyl methacrylate; PMMA support. The images at the right are magnified image at the centre and edge of transferred graphene. Note that the graphene transferred using thermal release tape shows distinct cracks formation compared to PMMA transfer method.

Furthermore, the transport properties of the transferred graphene on the SiO_2 substrate with patterned Pt electrodes (thickness, $d \approx 100$ nm) are studied using the Van der Pauw method. The graphene channel's width and length are fixed equally at $1000 \mu\text{m}$. The contact resistance of the Pt electrodes is found to be $\sim 3.0 \Omega$. The transferred graphene for TRT and PMMA transfer method shows only a slight different in the resistance of $3.762 \text{ k}\Omega$ and $3.432 \text{ k}\Omega$ respectively as shown in **Fig. 5.21**. The slight difference in the measured resistance is due to the physical damage rather than structural defect caused from the TRT transfer process despite the ease of transfer steps needed, fast and industrial scale friendly. However, the major drawback of TRT method is the use of elevated heating during peel-off process compared to PMMA method that operates at room-temperature which limited the variety of transferable substrate. For example, it is not applicable when the target substrate is made of polymer which will be degraded or damaged upon heating to more than 100°C . This further support that PMMA transfer method is found to be more preferable and will be further implemented to fabricate a flexible pressure sensor device.

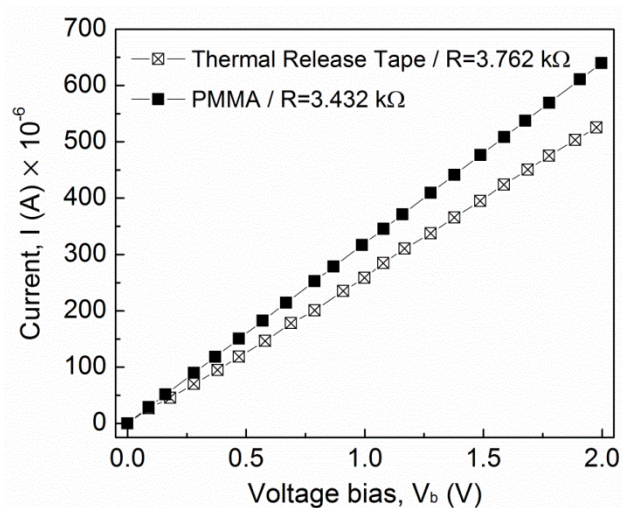


Figure 5.21: Comparison of the I-V (current-voltage) characteristic of mono-layer graphene transferred using thermal release tape (TRT) and Poly-methyl methacrylate (PMMA) support.

5.5 Summary

In summary, challenging issues related to the deposition of a continuous high-quality mono- and bi-layer graphene using the Cat-CVD technique namely HFTCVD on Cu foil has been studied. Very low I_D/I_G ratios (~ 0.1) are obtained for all samples, which reflected the formation of high-quality graphene deposited on Cu foils. This is found to be due to the catalytic dissociation of CH_4 and H_2 precursors at tungsten hot-filament above 1500°C . It is also found that a quasi-static equilibrium copper vapour inside the alumina tube promotes the growth of low defect density graphene. The role of H_2 is found to be important to control the growth rate of graphene. In addition, induction period of graphene is highly dependent on the size of nucleation seed before initiation of growth process. The nucleation seed then promotes the growth of consecutive graphene layers in the form of tiered ‘wedding-cake’ configuration before merge together as a continuous mono- or bi-layer graphene. A growth mechanism is then proposed, where the copper oxide (Cu_2O) acted as a nucleation site for graphene growth. The transfer process using PMMA support is found to be more preferable to fabricate flexible pressure sensor device which will be discussed in the next chapter.

CHAPTER 6: GROWTH OF GRAPHENE/COPPER OXIDE NANOCOMPOSITES AND FLEXIBLE PRESSURE SENSOR APPLICATION

6.2 Overview

In this chapter, a one-step process to grow graphene-copper oxide nanocomposites (graphene/Cu₂O nanocomposites) using hot-filament thermal chemical vapour deposition (HFTCVD) technique is presented. The effects of growth temperatures are studied with respect to structural, morphological and electrical properties. It is found that a circumfluence flow inside the alumina tube during the sublimation state of copper could react with the oxygen to form cuprous oxide (Cu₂O) nanoparticles which will predominantly decorate the graphene layer simultaneously along the growth process at low graphene growth temperature. This chapter also demonstrate; a controllable defect density, decorated nanoparticles density and overlapping graphene region that might increase the probability of electron scattering in the percolating networks which are preferable for a high-sensitivity pressure sensor, simply by controlling the graphene deposition temperature. A linear variation in the change of resistance with the applied gas pressure is obtained in the range of 0 to 50 kPa which shows the piezoresistive effects in graphene and graphene/Cu₂O nanocomposites. The deposition temperature of graphene deposits on copper foil using this technique shows its capability of tuning the sensitivity of the flexible graphene-based pressure sensor. A sensing mechanism is proposed to provide a better understanding in the use of graphene/Cu₂O nanocomposites in highly sensitive piezoresistive graphene-based flexible pressure sensors. The progression of the work is depicted in **Fig. 6.1**.

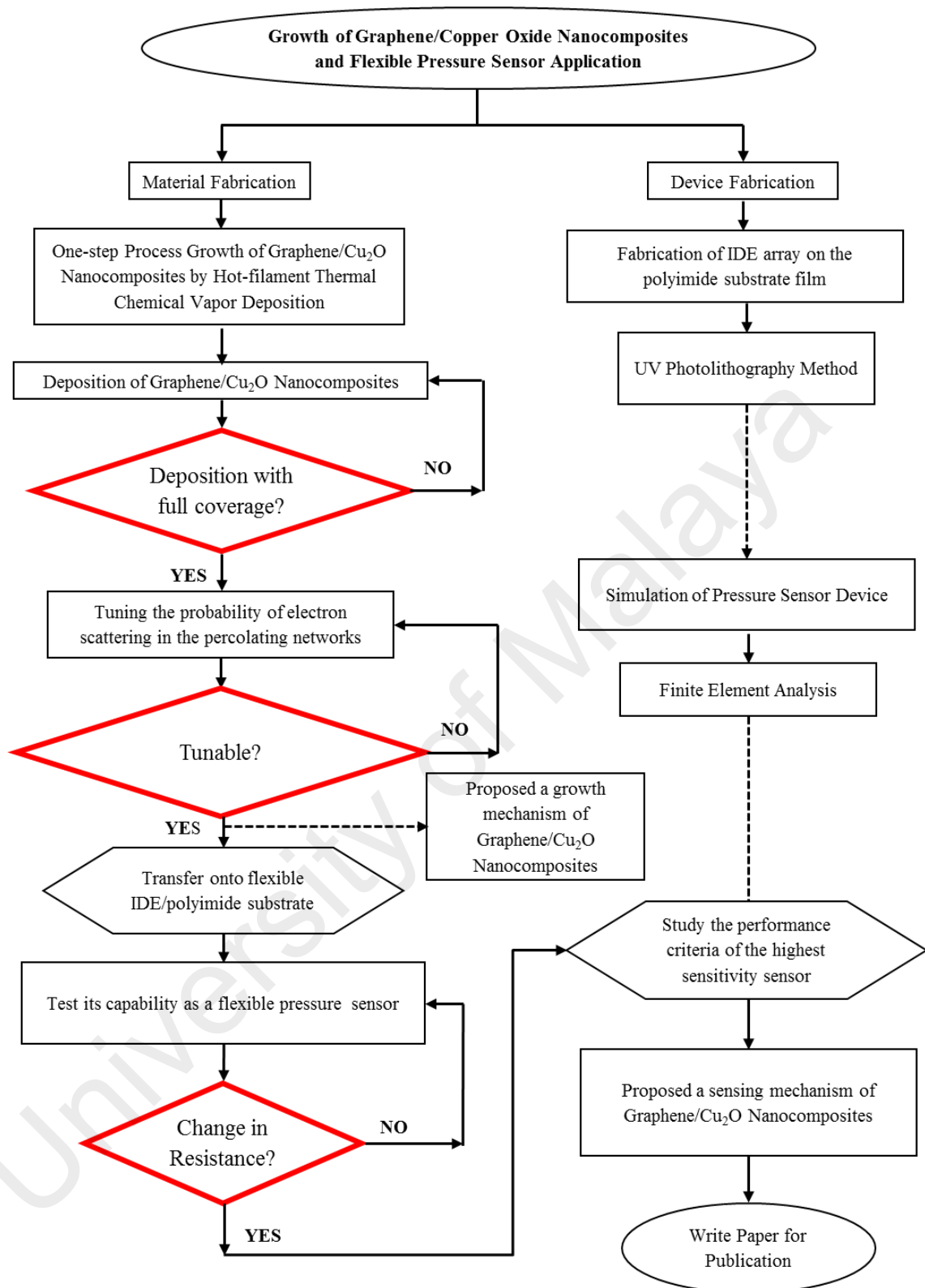


Figure 6.1: Flow chart showing the progression of graphene/copper oxide nanocomposites fabrication using HFTCVD technique which leads to its integration in flexible pressure sensor device. Note that the device fabrication has been explained in Chapter 3 under **Section 3.3**.

6.2 One-step Process Growth of Graphene/Copper Oxide Nanocomposites

6.2.1 The Effects of Growth Temperature

In the previous chapter, the graphene growth is found to depend on the vapour trapping mechanism inside the one end sealed alumina tube. It is also found that circumfluence flow inside the tube with a trapped copper vapour initiated the nucleation of graphene. Kim et al. (2012) has reported the competition between of an atomic phenomena such as adatom mobility versus desorption on copper substrate. This then defines the characteristic of nucleation regimes with different activation energies that depends on the graphene growth temperature. Hence, a lower growth temperature would lead to a higher density of nucleation centre with a smaller graphene lateral size. In addition, it is inferred that the intentionally trapped copper vapour at lower growth temperature ($<920\text{ }^{\circ}\text{C}$) is able to simultaneously decorate the grown graphene which becomes graphene/ Cu_2O nanocomposites (Lin et al., 2015).

Here, the investigation is focused on the formation of graphene/ Cu_2O nanocomposites at substrate temperatures of 750 and 850 $^{\circ}\text{C}$ while graphene grown at 1000 $^{\circ}\text{C}$ is used as a controlled sample. The substrate temperature is refers to the temperature of the Cu foil in the alumina tube placed within the tungsten filament that is coiled around it. The growth duration and $\text{CH}_4:\text{H}_2$ ratio is fixed at 30 min and 10:50 sccm, respectively according to optimize parameters discussed in Chapter 5. The minimum temperature of 750 $^{\circ}\text{C}$ is chosen for various reasons; 1) this is the lowest temperature for favourable hydrocarbon interaction for graphene growth instead of becoming amorphous carbon, 2) it is also the lowest substrate temperature produced by the radiant heat of the heated tungsten (W) filament whereby filament poisoning effect can be eliminated. As reported by Seo et al. (2004), filament poisoning effect can only be eliminated when the filament temperature is above 1500 $^{\circ}\text{C}$.

6.2.1.1 Morphology

Fig. 6.2(a-c) shows the FESEM images of the as-prepared graphene and graphene/Cu₂O nanocomposites on Cu foil substrates at 750, 850 and 1000 °C of growth temperatures. It is observed that the Cu grain boundary size, which is highlighted inside the circles, is directly depends on the growth temperature. It is found that the Cu grain boundaries size has increased from ~50 µm to more than ~200 µm as the substrate temperature is increased from 750 to 1000 °C, respectively. This has been frequently reported for the growth of graphene on Cu foils; an annealing process at 1000 °C will be done prior to the deposition process to increase the Cu grain boundaries and decrease the Cu surface roughness, where the growth of larger graphene grains is required (Mattevi et al. 2011).

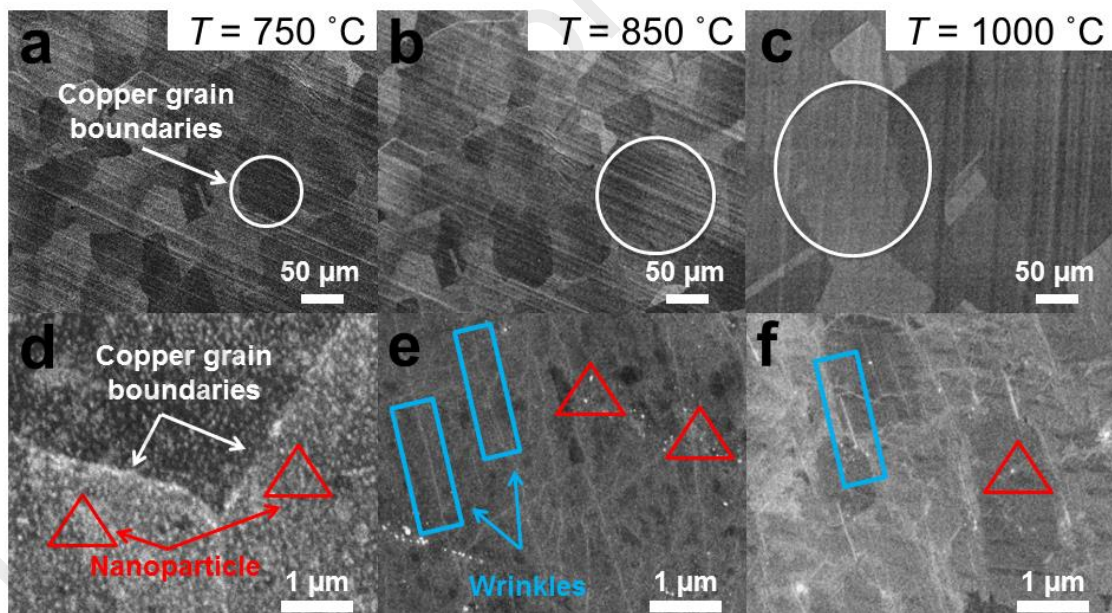


Figure 6.2: FESEM images of (a-b) graphene/Cu₂O nanocomposites (750 and 850 °C) and (c) graphene (1000 °C) grown on Cu foils at different deposition temperature. The FESEM images of 750, 850 and 1000 °C sample was further magnified and shown in (d), (e) and (f) respectively. The circle, triangle and rectangular shapes indicate Cu grain domain sizes, nanoparticles and wrinkles.

Therefore, smaller Cu grain boundaries with high surface roughness leads to an increase in the graphene nucleation density resulting in smaller graphene grain sizes. **Fig. 6.2(d-f)** shows the magnified FESEM images of the sample grown at 750, 850 and 1000 °C respectively. The nanoparticles and graphene wrinkles structure which are highlighted by triangle and rectangular shapes respectively are found to be depending with a specific growth temperature. At a relatively low temperature (750 °C), the density of nanoparticles and graphene wrinkles structure are observed to be much higher compared than the graphene sample grown at 850 and 1000°C. This result is found to be consistent with the results reported by Celebi et al. (2013) and Seah et al. (2014).

The graphene grown at a lower growth temperature of 750 °C has higher overlapping regions as compared to graphene grown at higher temperature of 1000 °C. It is shown from the FESEM images in **Fig. 6.3** that the overlapping region is decreased from 0.30 µm to ~0.05 µm for the samples grown at 750 and 1000 °C of growth temperature, respectively. This could be due to the higher nucleation density observed at 750 °C growth temperature, which induces the graphene islands to grow closer to each other thus results in higher chances of producing the overlapping effect. Illustration on how the overlapping between graphene islands is influenced by the nucleation density is shown in **Fig. 6.4**.

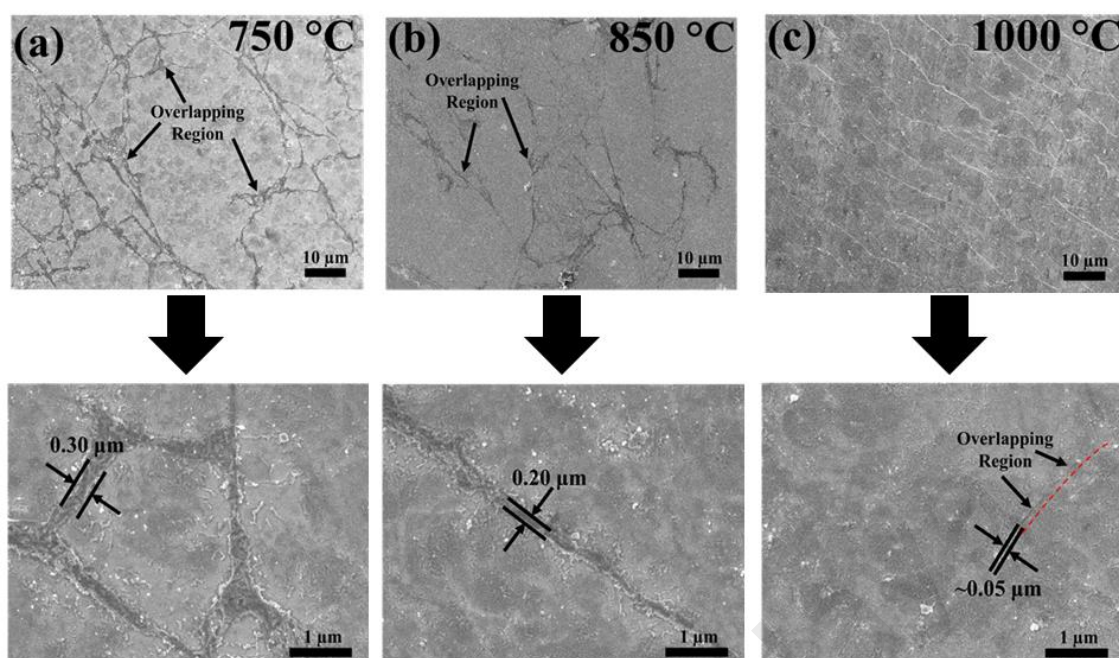


Figure 6.3: FESEM images of overlapping region of sample grown at (a) 750 °C (b) 850 °C and (c) 1000 °C on SiO₂/Si (100) substrates. The magnified images of the overlapping region are shown on the right. Note that the overlapping region is decreased from 0.30 to 0.20 μm and then at ~0.05 μm with an increase of growth temperature from 750 to 850 and 1000 °C, respectively.

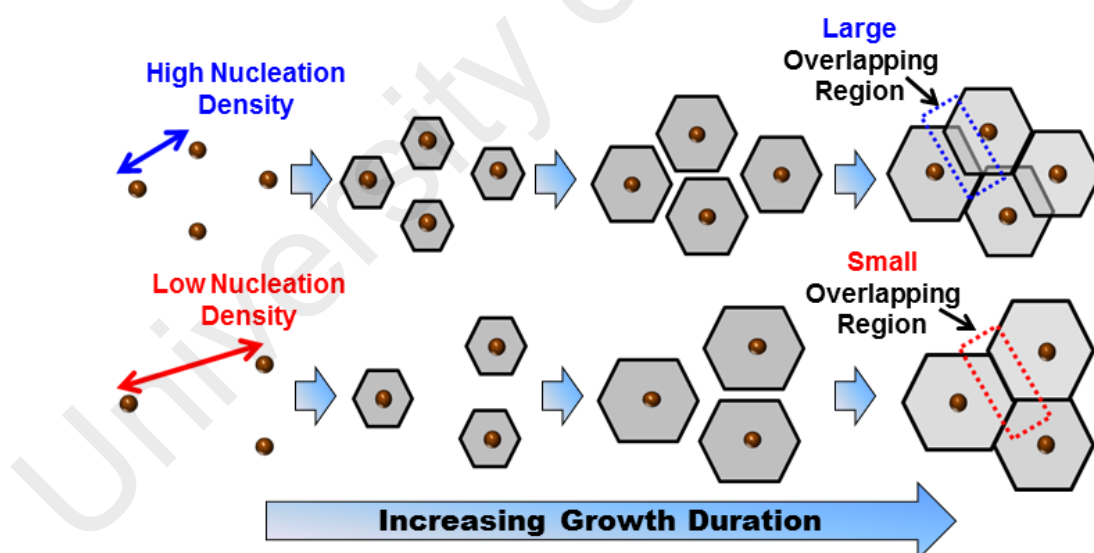


Figure 6.4: Illustration showing how the overlapping regions are controlled by the nucleation density of Cu₂O nanoparticles. At low graphene growth temperature (750 and 850 °C), the nucleation density is expected to be higher compared to sample grown at 1000 °C, thus increase the probability of overlapping between graphene islands.

Lin et al. (2015) reported that snowflake-like dendrite structure of graphene deposited at low graphene growth temperature of 920 °C which results in a low evaporation rate environment. However, since the structure of graphene layer is ultra-thin, it is difficult to distinguish whether the nanoparticles are deposited underneath the graphene layer or on top of the grown layer before it is transferred from the Cu foil substrate to target substrate. The Cu₂O nanoparticles that are deposited underneath the graphene layer as discussed in **Section 5.3** acts as a nucleation centres whereas the nanoparticles on top of the grown layer are formed from the oxygen-copper vapour reaction (Lin et al., 2015) after the growth of graphene layer. To distinguish either the Cu₂O nanoparticles forms above or below the graphene layer, the as-prepared samples are transferred onto a target substrate. After the deposition process, the Cu₂O nanoparticles on top of the graphene layer will remain while the nanoparticles which act as nucleation sites would be etched away during the transfer process as shown in **Fig. 6.5**. The remaining Cu₂O nanoparticles observed after the transfer process referred to as the Cu₂O nanoparticles decorating the graphene layer.

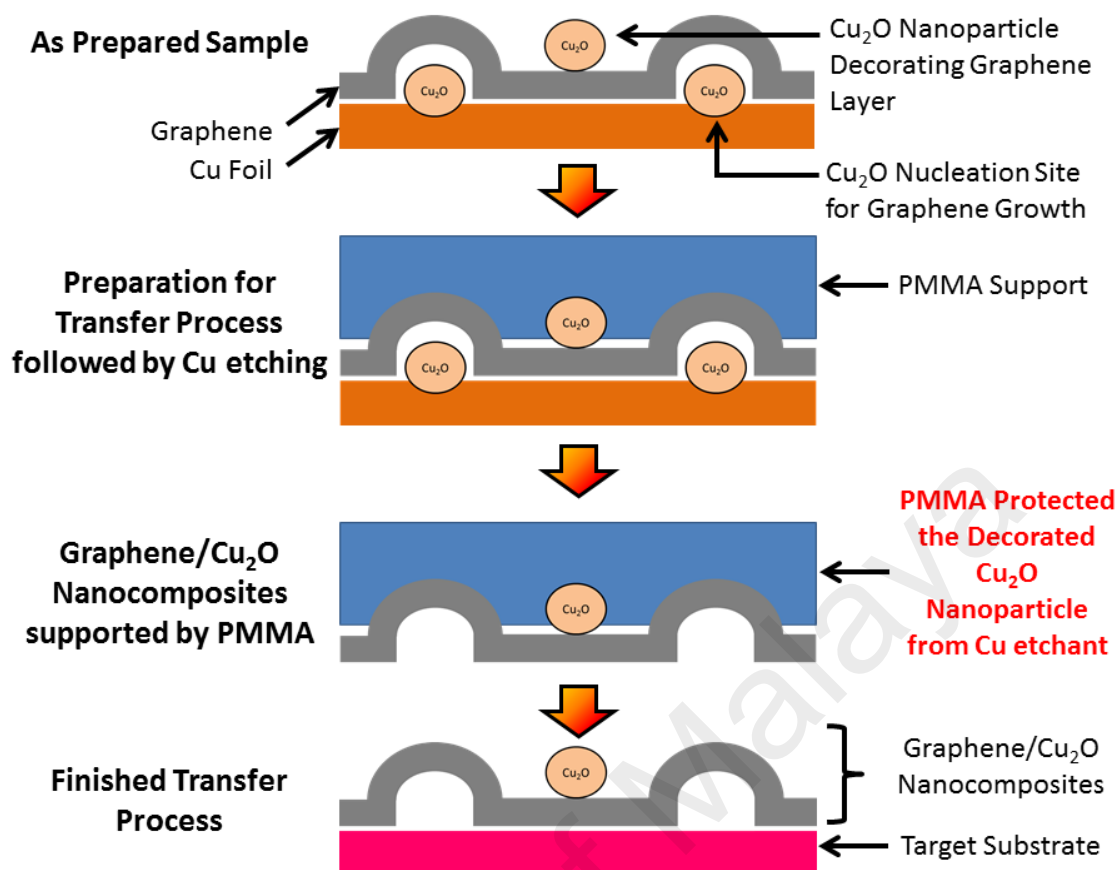


Figure 6.5: Flow diagram of graphene/Cu₂O nanocomposites transfer process. The PMMA support layer was inferred to protect the decorated Cu₂O nanoparticles from the Cu etchant solution.

The morphological and topological characteristics of the resultant transferred graphene and graphene/Cu₂O nanocomposites on the polyimide substrates are shown in **Fig. 6.6**. From FESEM images, samples grown at temperatures of 750 and 850 °C (**Figs. 6.6(a)** and **(b)**), the presence of graphene/Cu₂O nanocomposites are more apparent compared to the sample grown at 1000 °C (**Fig. 6.6(c)**). The presence of decorated Cu₂O nanoparticles after the transfer process is observed in for samples grown at temperatures of 750 and 850 °C. The root mean square (RMS) surface roughness of the resultant transferred graphene calculated by AFM topology images is decreased about ~50% when growth temperature is decreased from 750 °C (7.85 nm) to 850 °C (6.72 nm) and then 1000 °C (3.95 nm). This is due to the decreased in the formations of decorated Cu₂O nanoparticles as well as the wrinkle

structures. In addition, the AFM topological images around the scanning area of $10 \times 10 \mu\text{m}^2$ show that the nanoparticles counts are significantly decreased from 1160 to 768 and 547 for samples grown at temperatures of 750, 850 and 1000 °C, respectively. Furthermore, from the height profiles extracted from the AFM topological images (yellow line), high fluctuation of step height in the sample grown at 750 °C is due to presence of Cu_2O nanoparticles decorating the graphene layer and also wrinkled structures, which are more prominent. The results show that the morphological and topological evolution of graphene with different Cu_2O nanoparticles densities could be tuned by lowering the graphene growth temperature from 1000 to 850 and 750 °C.

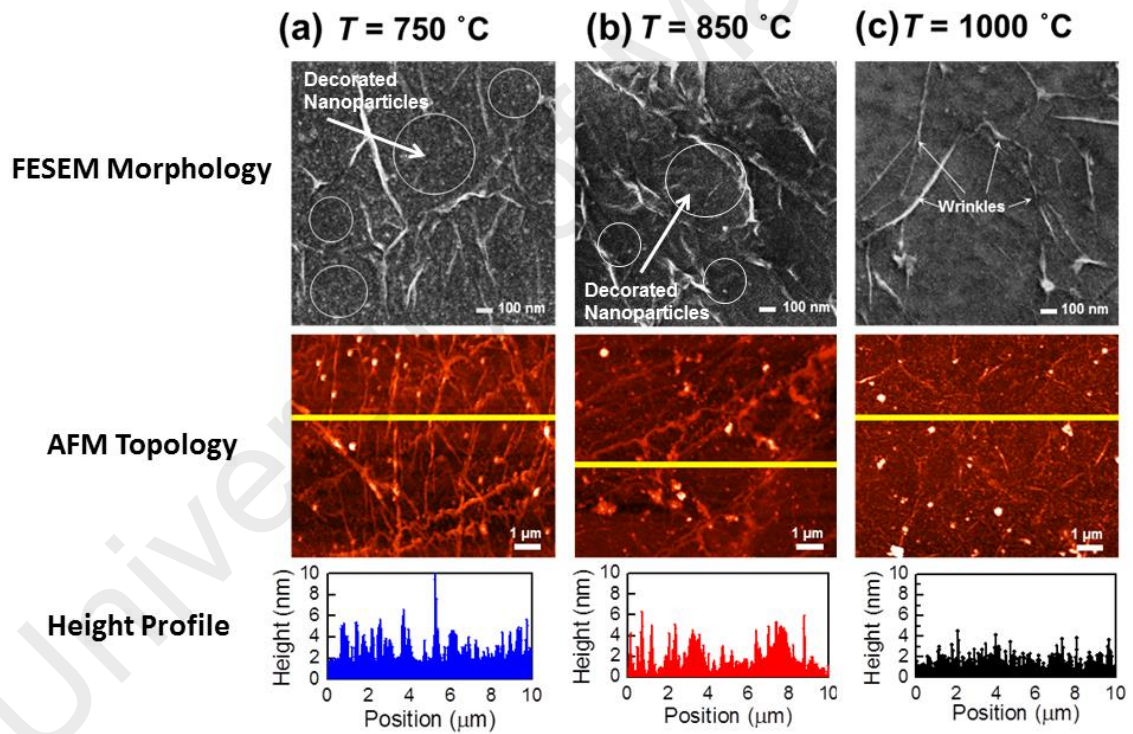


Figure 6.6: FESEM and AFM ($10 \times 10 \mu\text{m}^2$) images of transferred (a-b) graphene/ Cu_2O nanocomposites (750 and 850 °C) and (c) graphene (1000 °C) graphene samples on polyimide substrates. The corresponded AFM topological images with height profiles were shown at the bottom.

6.2.1.2 Crystallinity

Fig. 6.7 shows the Raman spectra of graphene and graphene/Cu₂O nanocomposites on the Cu foil and SiO₂/Si (100) substrates. The spectra show five major Raman peaks for graphene: the D, G, D', 2D and D+D' peaks located at ~1359, ~1590, ~1620, ~2700 and ~2949 cm⁻¹, respectively. As compared to the Raman spectra in Set 2 (see **Fig. 5.9(a)**), the emergence of the D peak in these samples is believed to be due to the breathing modes of six-atom rings from transverse optical (TO) phonons around the K point of the Brillouin zone centre. This peak becomes active because of a double resonance (DR) inter-valley process, and the presence of the D band which indicates large concentration of defects in the graphene (i.e. vacancies and/or dislocation in six-atom rings graphene lattice, bond rotations caused between the merged of graphene islands and decorated nanoparticles). The D' peak occurs via an intra-valley double resonance process in the presence of defects whereas the D+D' is due to the combination mode of two phonons with different momentum.

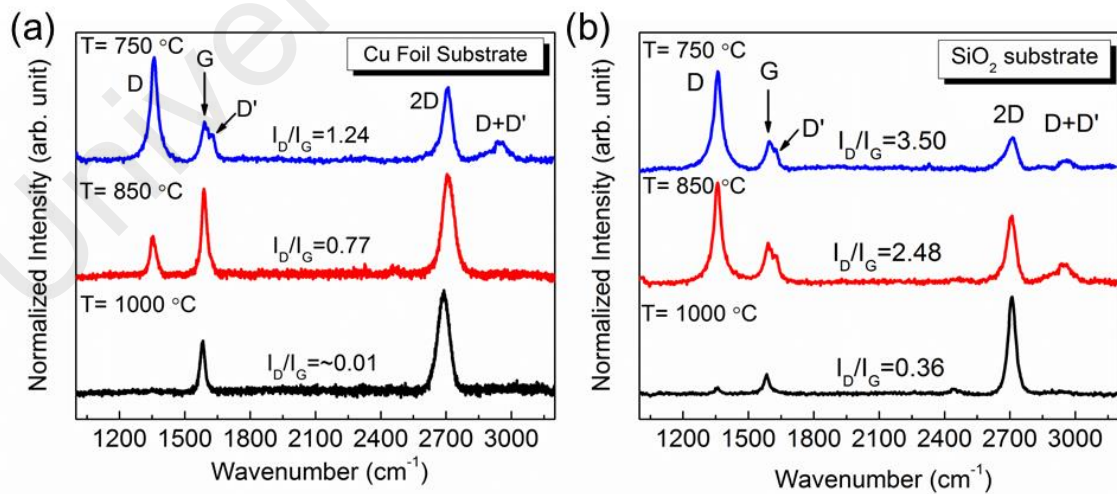


Figure 6.7: Raman spectra of graphene and graphene/Cu₂O nanocomposites deposited on (a) Cu foils and transferred on the (b) SiO₂/Si (100) substrates grown at 750, 850 and 1000 °C.

From the results, it shows that the evolution of the D peak is strongly dependent on the substrate temperature. Before the transfer process, the calculated I_D/I_G ratio on for samples grown at temperatures of 750, 850 and 1000 °C are 1.24, 0.77 and ~0.01, and increased to 3.50, 2.48 and 0.36 after transfer onto the SiO₂/Si (100) substrates. Since the intensity of the I_D/I_G ratio had often been used to identify the defect density inside graphene, given that a higher ratio indicates more defects and vice versa (Malard et al. 2009), this trend suggested that major change in the defect concentration in the graphene structure occurred due to the effect of growth temperature and transfer process. This could probably due to the evolutionary kinetics of the graphene formation on the Cu foil at different growth temperatures resulting from the effects of surface kinetic factors of precursor gases such as the adsorption, dissociation, dehydrogenation and sublimation process (Bhaviripudi et al., 2010; Celebi et al., 2013). The transfer process is shown to introduce more defects in the grown graphene/Cu₂O nanocomposites.

6.2.1.3 Electrical Properties

The electrical properties of the transferred graphene and graphene/Cu₂O nanocomposites are measured on the SiO₂/Si (100) substrate with patterned platinum (Pt) electrodes (thickness, $d \approx 100$ nm) and studied using the Van der Pauw technique. The channel width and length are fixed at 1000 μ m. The contact resistance of the Pt electrodes is determined to be $\sim 3.0 \Omega$. The sample growth at temperature of 750 °C exhibits higher sheet resistance of $1222 \pm 18 \Omega/\text{sq.}$ (ohms per square), as compared to $166 \pm 6 \Omega/\text{sq.}$ for sample grown at temperature of 1000 °C. This is contributed by the morphological evolution of the graphene structure, which includes graphene grain size and topological defects such as dislocations,

grain boundaries, wrinkles, and cracks produced during the growth or transfer processes (Duong et al., 2012; Tsen et al., 2012).

These morphological evolutions towards higher defect density of graphene structure when grown at lower temperature could effectively scatter the charge carriers through the percolating networks as stated in **Table 6.1**. Apart from that, the sheet resistance value of high-quality graphene sample grown at 1000 °C ($166 \pm 6 \text{ } \Omega/\text{sq}$) which produced in this work is higher as compared to that of the pristine graphene ($30 \text{ } \Omega/\text{sq}$.) as reported in literature (Bae et al., 2012). This could be due to the additional electron percolation pathway for electrons tunnelling between the graphene islands as well as to the grain boundaries of polycrystalline graphene (Han et al., 2011; Tsen et al., 2012; Chen et al., 2013).

Table 6.1: Details of the morphological, topological and electrical properties of graphene and graphene/Cu₂O nanocomposites grown at specific temperature. This would then correlates to the electron percolation pathway in the graphene networks.

Growth temperature, T (°C)	I_D/I_G ratio on Cu Foils	I_D/I_G ratio on SiO ₂ /Si (100)	Decorated Nanoparticle Density in $10 \times 10 \text{ } \mu\text{m}^2$ (Counts/ μm^2)	Surface Roughness (nm)	Overlapping Region (μm)	Sheet resistance (Ω/sq .)
750°C	1.24	3.50	~12	7.85	0.30	1222 ± 18
850°C	0.77	2.48	~8	6.72	0.20	761 ± 9
1000°C	~0.01	0.36	~5	3.95	~0.05	166 ± 6

6.2.2 Formation Mechanism of the Graphene/Cu₂O Nanocomposites

By relating the results obtained from FESEM, AFM, Raman spectroscopy and electrical analysis as well as those found in the literature, a growth mechanism for the growth of the graphene/Cu₂O nanocomposites films using the HFTCVD system is then deduced. The proposed growth mechanism is shown in **Fig. 6.8** and described below:

- (1) During the fabrication process, the evaporation of the Cu foil inside the alumina tube results to the Cu atoms to be in a state of sublimation. Whereas, the presence of residual O atoms in the alumina tube results to the interaction between Cu atoms, thus forming the Cu₂O molecules.
- (2) These Cu atoms and Cu₂O molecules are then deposited in the form of nanoparticles on the Cu foil substrates due to the temperature gradient between the vapour and the substrates. These nanoparticles act as nucleation sites for graphene growth.

Growth temperature strongly influenced the growth of graphene/Cu₂O nanocomposites. According to the Robinson and Robins model for graphene growth by CVD, the capture-controlled regime is dominant at growth temperature below 870 °C while desorption-controlled regime is dominant at growth temperature above 870 °C. Competition among the rates of nucleus growth by adatom capture, surface diffusion of C species and desorption of C adatoms, control the nucleation density of graphene growth (Kim et al., 2012). In addition, Cu itself has quite high evaporation rates in vacuum approaching of 4 µm/hour at 1000 °C. This will leads to low nucleation density by promoting desorption of carbon species that already formed on top of the Cu substrates (Vlassiounk et al., 2013).

- (3) The low growth temperatures of 750 and 850 °C decrease the evaporation rate of Cu substrate and thus increase the nucleation density for graphene growth. Higher nucleation density results in higher overlapping events of graphene

layers since the deposition time is fixed for all samples regardless of growth temperature.

- (4) The trapped Cu vapour inside the alumina tube (one end sealed), could be re-deposited or re-evaporated from the growth sites of the graphene layer (Lin et al., 2015). The competition between these processes contributes to the formation of graphene layer decorated with Cu₂O nanoparticles or graphene/Cu₂O nanocomposites. These processes are controlled by the growth temperature, whereby the re-deposition process of Cu₂O nano-particles and capture of C adatoms can be suppressed at high growth temperatures above >850 °C and vice versa.
- (5) High re-evaporation rate of Cu and Cu₂O nanoparticles for high temperature growth of 1000°C prevents the formation Cu₂O nanoparticles decorating the graphene layer.
- (6) Low growth temperature of 750 and 850 °C favours the formation of graphene/Cu₂O nanocomposites which however sacrifice the formations of high-quality graphene structure due to the surface kinetic factors of precursor gases (Bhviripudi et al., 2010; Celebi et al., 2013).

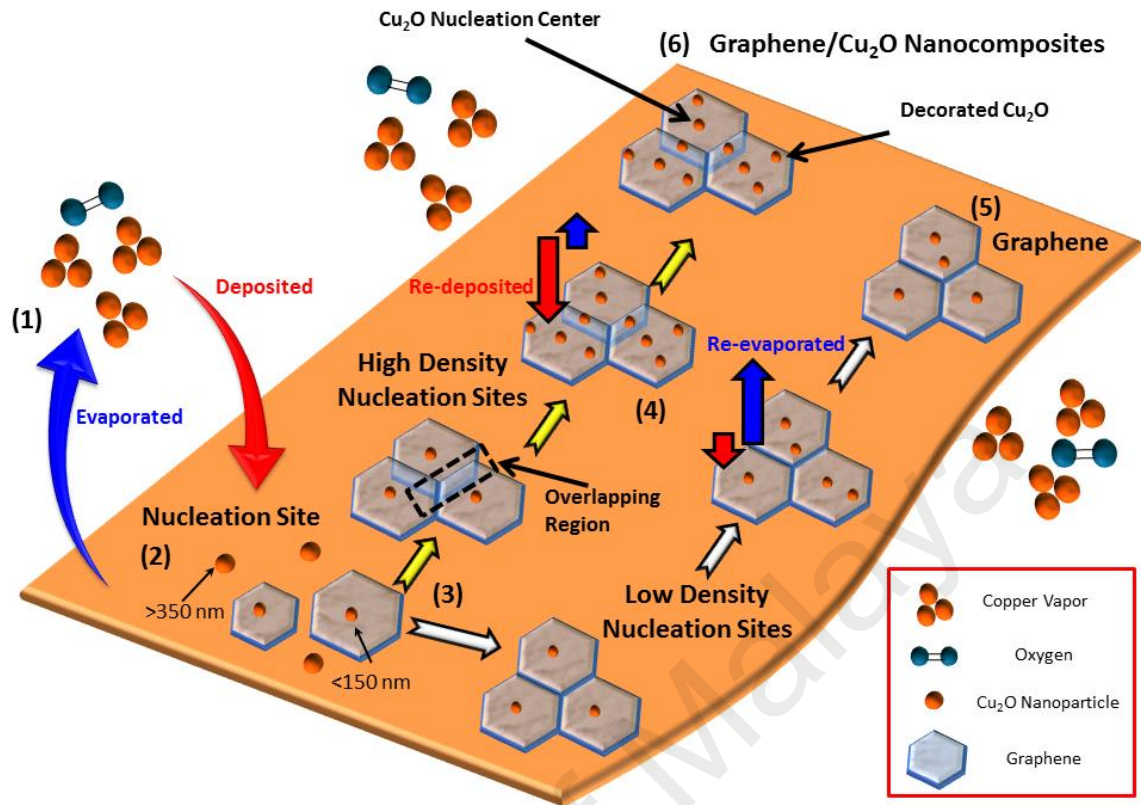


Figure 6.8: Diagram of growth mechanism of graphene/Cu₂O nanocomposites using HFTCVD technique. Note that a lower growth temperature (750 and 850 °C) would cause the re-deposited of oxygen-copper vapour reaction due to a low evaporation rate environment thus forming a decorated Cu₂O nanoparticles on graphene layer. The growth mechanism of graphene was presented for comparison.

6.6 Characterization of Graphene-based Flexible Pressure Sensor Device

6.3.1 Stability

Fig. 6.9(a) shows a close-up photograph of flexible pressure sensor devices which have been soldered to the wire. Three specific morphologies of graphene grown at substrate temperature of 750, 850 and 1000 °C are selected to be incorporated onto the flexible pressure sensors. Their respective morphologies have been characterized using optical microscopy, AFM, FESEM and Raman spectroscopy which have been discussed in **Section 6.2**. The current-voltage characteristics measured at ambient conditions with a temperature of $T = 298$ K and relative humidity of %RH = 60 of the sensor device incorporated with graphene and graphene/Cu₂O nanocomposites grown at

these temperatures are shown as the inset in **Fig. 6.9(b)**. The initial resistances, R_0 determined from these plots are 4.655, 4.076, and 3.432 k Ω for the graphene grown at 750, 850 and 1000 °C, respectively. It shows that each of the transferred graphenes on the sensor devices displayed stable R_0 in the open environment for about 20 days. A slight change in the R_0 may be due to small changes in the surrounding humidity which fluctuates around 50-60 %RH from day to day. It is important to note that the I–V characteristic (inset graph in **Fig 6.9(b)**) from each deposition parameter was measured and then grouped into the same resistance range which is assumed to be identical to other devices of the same deposition parameter. It is only a slight resistance variation observed from each device fabricated from the same deposition parameter due to the transfer process.

However, the R_0 of the sensor devices decreases rapidly with the increase in temperature from 298 to 338 K, and then decreases gradually at an elevated temperature of above 343 K as shown in **Fig. 6.9(c)**. From the results, less than 20% resistance change is observed in the wide temperature range of 298–373 K. The graphene-based pressure sensor device incorporated with the graphene/ Cu₂O nanocomposites grown at 750 °C exhibited a greater temperature-dependence than that of samples grown at temperatures of 850 and 1000 °C. The decrease in the R_0 as the temperature is increased could be explained by the decrease of mean free path which caused by electron–phonon scattering (López et al., 2009), thus shows that a high defect-density graphene sample exhibit a higher temperature-dependence. The operation temperature window of these sensor devices is deduced to be from 298 to 330 K with the margin of R_0 changes to be less than 10% since sensor response are further calculated based on R_0 value. The higher the R_0 sweep as temperature changed, the higher is the error of sensor response. The margin of R_0 changes must be small in order to increase the sensitivity of the sensor.

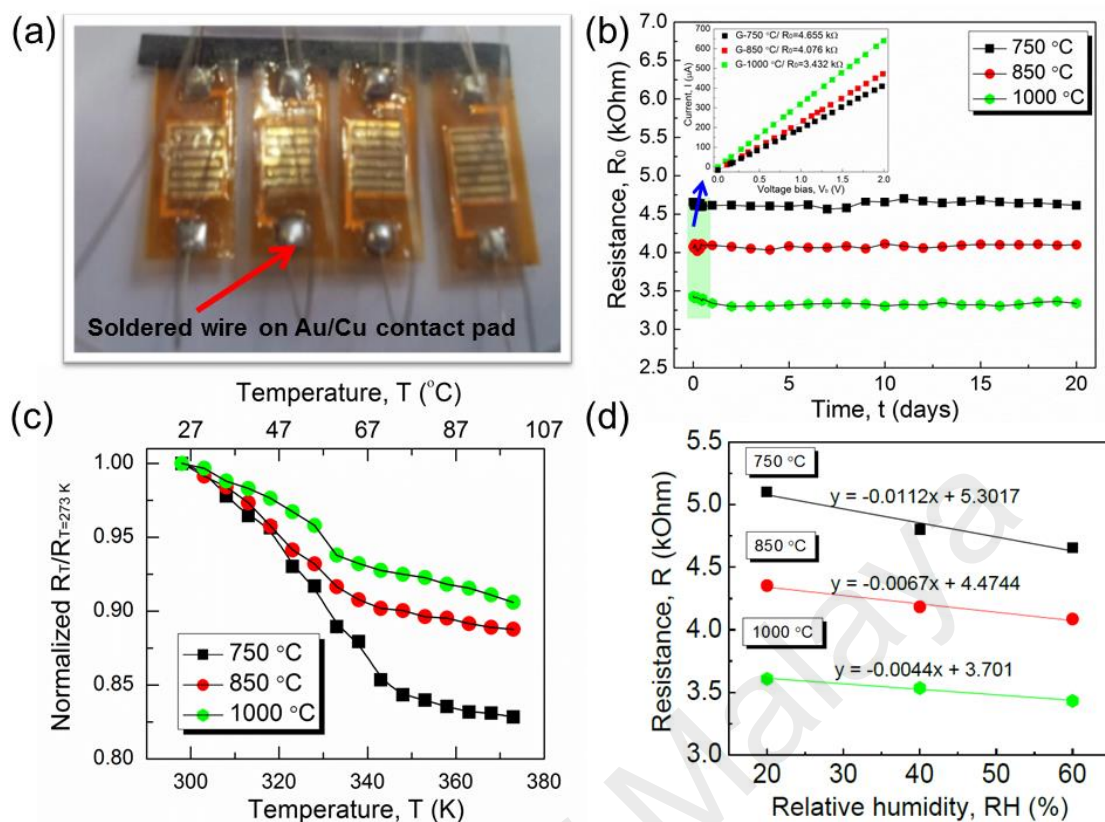


Figure 6.9: (a) Close up photograph of graphene-based flexible pressure sensor devices. (b) Time-dependence of initial resistance, R_0 at room-temperature and 50-60% relative humidity and reproducibility of I-V characteristic for four samples for each deposition parameters is shown in the inset graph, (c) Temperature-dependence of resistance at ~60% relative humidity, (d) Humidity-dependence of resistance in sensor at room-temperature for 750, 850 and 1000 °C samples.

The response of fabricated graphene-based flexible pressure sensors towards the %RH effect is shown in **Fig. 6.9(d)**. Since most of the electronic devices are operated in this humidity range, the tested humidity range is fixed from 20 to 60 %RH. A protection against adverse humidity effect such as encapsulation is necessary if the operation in extreme humidity region is needed. It is observed that the resistance of all fabricated sensors decreases with the increases of %RH for the device incorporated with graphene/ Cu_2O nanocomposite grown at substrate temperature of 750 °C exhibited higher sensitivity towards humidity changes in comparison to the others. This could be due to the presence of a significant amount of defects and impurities which acts as the adsorption sites of oxygen functional groups when in contact with the water molecules

from the environment (Qi et al., 2012). Considering the working environment of fabricated flexible pressure sensor devices have to be; 1) in a close contact with human body or assembled inside a robot parts which normally had a working temperature near a room-temperature and, 2) operated in an open environment with relative humidity usually in the range of 20-60 %RH, all the fabricated sensor in this work have shown a good stability for robotic, health or medical applications.

6.3.2 Sensing Range and Sensitivity

The relative change in the resistance, $\Delta R/R_0$ of the graphene-based flexible pressure sensor with respect to the applied differential pressure, ΔP fabricated from graphene/Cu₂O nanocomposite grown at temperatures of 750, 850 and 1000 °C are shown in **Fig. 6.10**. Note that the piezoresistive effect is based on the change in material resistance due to the applied deformation which in this case is contributed by the deformation caused by the pressure applied to the flexible pressure sensors device. Interestingly, the $\Delta R/R_0$ values for all sensor devices fabricated from 750, 850 and 1000 °C samples show a linear change with respect to the ΔP .

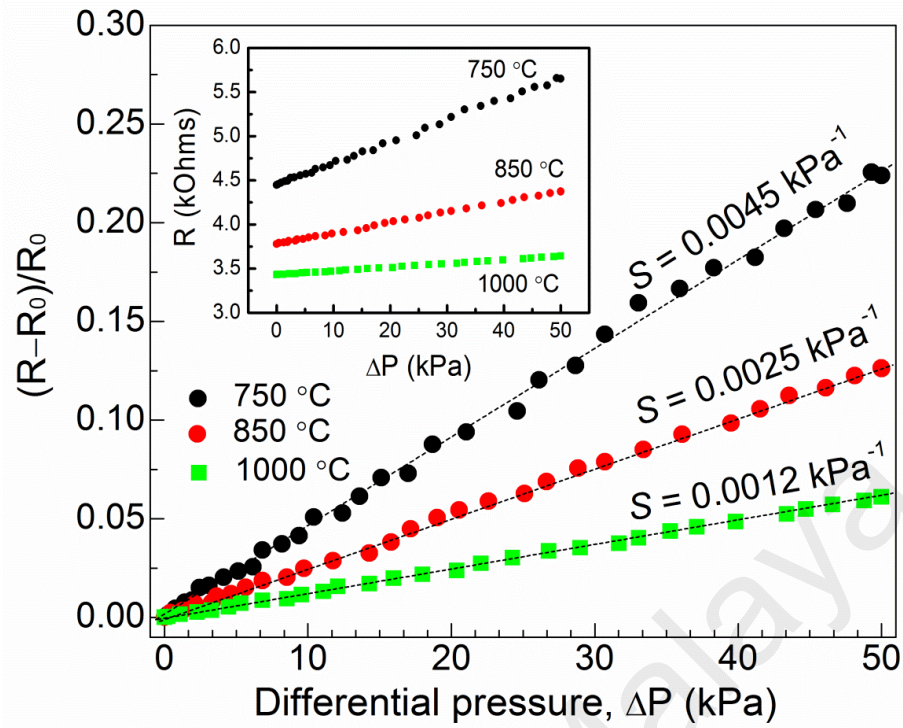


Figure 6.10: Relative change in resistance as a function of applied differential pressure for pressure sensor fabricated from 750, 850 and 1000 °C samples. Dashed lines are given as guides to the eye. The sensor's sensitivity, S (kPa^{-1}) was defined by the slope of the graph. The inset shows that the resistance increases as the differential pressure increases.

The sensitivity of the pressure sensor is defined as $S = (\Delta R/R_0)/\Delta P$ with the kPa^{-1} unit, where ΔR is the change in resistance (Ω), R_0 is the initial resistance ($\text{k}\Omega$), and ΔP was the pressure difference (kPa). The sensitivities for devices fabricated from 750, 850 and 1000 °C samples are based on the slope of the fitted lines are calculated to be at 0.0045, 0.0025 and 0.0012 kPa^{-1} , respectively. These results demonstrate that this piezoresistive effect in the graphene networks could be improved by incorporating the Cu_2O nanoparticles as well as by increasing the overlapping region between graphene islands. As compared to previous works by Li et al. (2012) and Biroju et al. (2014), the incorporation of nanoparticles and overlapping region between graphene islands increases the current pathway length and electrons tunnelling effect, respectively. This could be achieved by simply lowering the graphene growth temperature to 750 and 850 °C. It has also been successfully demonstrated that a higher

sensitivity sensor device is produced by using high defect density graphene compared to previous reported works on flexible pressure sensor such as the rGO–polyurethane sponge (0.001 kPa^{-1}) (Yao et al., 2013), carbon black–silicone rubber nanocomposite (0.001 kPa^{-1}) (Wang et al., 2009), and MWCNT–polyimide nanocomposite ($\sim 0.00025 \text{ kPa}^{-1}$) (Gau et al., 2009).

6.3.3 Repeatability, Limit of Detection and Response Time

The highest sensing response shown in previous section is selected to be further tested for multiple cycle of loading and unloading pressure of different values to evaluate the robustness of the piezoresistive effect. The graphene/ Cu_2O nanocomposite sample that grown at 750°C is chosen as it has shown the highest sensing response. It could be observed in **Fig. 6.11(a)** that the flexible pressure sensor fabricated using 750°C sample is able to give a resolution of the resistance change for a small difference in applied pressure at 10.39, 5.43, 2.06 and 0.24 kPa. The repeated cycling of loading (pressure applied) and unloading (pressure released) at different applied pressures shows to be consistent throughout the 4 cycles.

Interestingly, in **Fig. 6.11(b)** the sensor is shown to be able to detect pressures as low as 0.24 kPa with a good resistance change of $\sim 23 \text{ m}\Omega\text{Pa}^{-1}$ which is defined as a limit of detection for this sensor. The limit of detection shown is comparable to the sensitivity of a discrete pressure sensor. However, the present result mainly relies on the limitation of pressure regulator, in which the target pressure can only be precisely controlled at high pressure range. The hysteresis of loading and unloading for a full measurement scale (0 to 50 kPa) is shown in the inset of **Fig. 6.11(b)**. The hysteresis is found to differ by less than 2% between loading and unloading indicate its ability to give the same output when the same increase and decrease pressures are applied consecutively. This behaviour could be attributed to

the recoverable structure deformation hence it has been proven that the sensor fabricated from 750 °C sample is able to withstand up to 50 kPa.

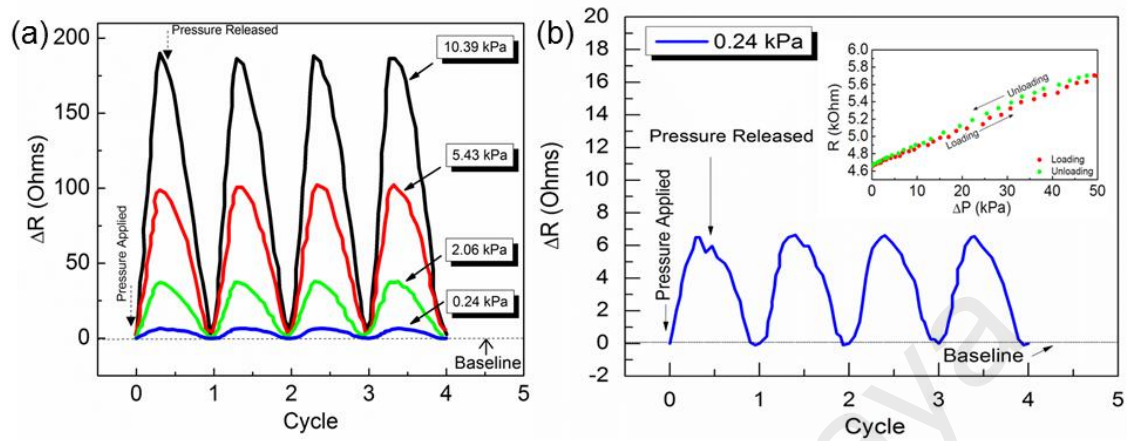


Figure 6.11: (a) Multi-cycle operation of repeated loading and unloading at different pressures with graphene grown at 750 °C. (b) Magnified resistance change of 0.24 kPa applied pressure which consider as limit of detection for this device. The inset shows a hysteresis plot of the relative change in resistance of loading and unloading in the wide pressure regime (0-50 kPa).

The response time of a specific sensing material is further measured. This gauges its ability to recover from the structural deformation within a period of time as shown in **Fig. 6.12** for the sample grown at 750 °C. Multiple cycles of loading and unloading at 10.39 kPa have been stacked in the same time frame so that the difference of sensing and recovery time could be measured. From the graph, the difference of sensing and recovery time is measured to be within 150 and 200 millisecond, respectively. The difference between sensing and recovery time is much smaller when compared to the response time which is measured to be about 1000 millisecond. A slight difference between sensing and recovery time of each cycle for loading and unloading can be attributed to the sample hysteresis for it to be able to recover from a structural deformation upon applied pressure. This is found to be consistent with the hysteresis plot of the relative change in resistance of loading and unloading in the wide pressure regime (0-50 kPa) as discussed earlier.

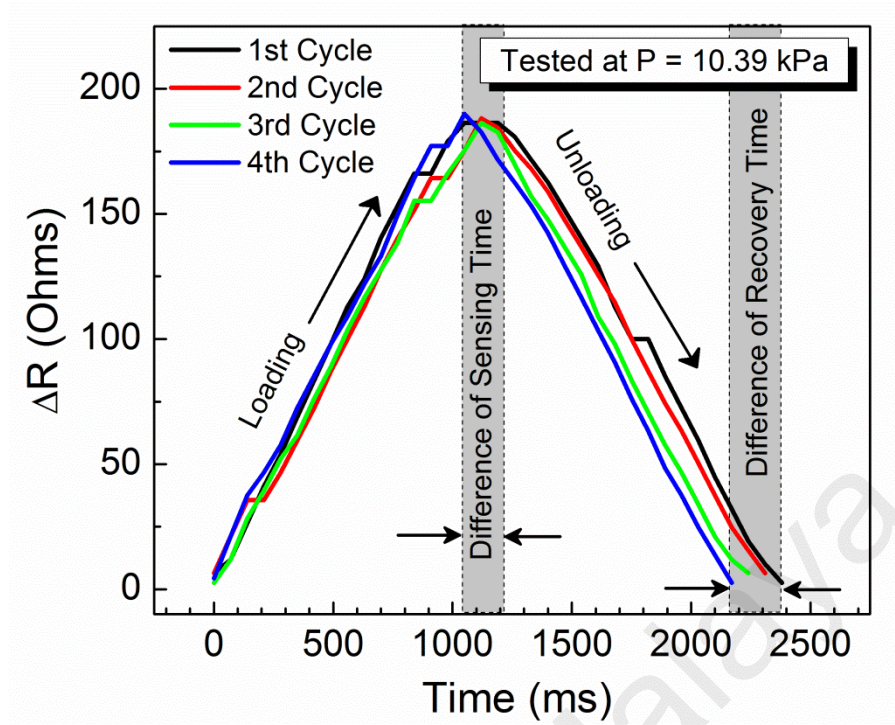


Figure 6.12: The response time of multiple loading and unloading at 10.39 kPa with graphene grown at 750 °C. The response time of loading and unloading pressure was measured to be about ~1000 millisecond. The differences in sensing time and recovery time from multiple cycles were measured to be within 150 and 200 millisecond, respectively.

6.3.4 Gauge Factor

In order to compare the performance of the fabricated graphene-based flexible pressure sensors with other pressure sensors performance found in the literature, it is necessary to calculate their gauge factor (GF). The GF is defined as the changes in relative resistance with respect to the strain, ϵ exerted to the sensing material due to the deformation from the applied pressure. However, the calculation of GF is not straightforward as the flexible pressure sensor with interdigitated electrode (IDE) array has a non-uniform surface, thus resulting in a non-uniform strain distribution. Hence, it is difficult to obtain the actual gauge factor because the exact strain value of piezoresistive components (graphene and graphene/Cu₂O nanocomposites) cannot be determined. By neglecting the contribution of small thickness of the graphene and graphene/Cu₂O nanocomposites (<10 nm) on the effective bending stiffness,

the approximate strain value of the flexible polyimide diaphragm has been considered for the purpose of gauge factor calculation instead of that of the piezoresistive component itself (Park et al. 2006).

Prior to that, the average ε across the flexible polyimide diaphragm with IDE array, which is computed by finite element analysis (FEA) of CoventorWare® simulation, is used to calculate the GF as shown in Equation (2.1). The average ε is defined as the arithmetic average of the principle strains over the finite elements of the diaphragm (Liu et al. 2013). The simulation shown in **Fig. 6.13(a)** demonstrated that a round-shaped deformation is formed when the pressure is applied from the initial condition to 10 kPa and then to 50 kPa. The maximum deformation, d of 4.5 μm at 10 kPa and 18.0 μm at 50 kPa is simulated to have been deflected with respect to the initial condition. A complete plot of d with respect to the applied pressure from 0 to 50 kPa is shown in **Fig. 6.13(b)**. Next, the ε exerted on the flexible polyimide diaphragm with IDE array is calculated from the d as simulated previously. Therefore, the relationship between ε exerted on the flexible polyimide diaphragm with IDE array and applied pressure is established and shown in **Fig. 6.13(c)**. The image in the inset shows the schematic diagram of the tensile ε exerted on the flexible polyimide diaphragm with IDE array which caused the change in the resistance due to the applied pressure.

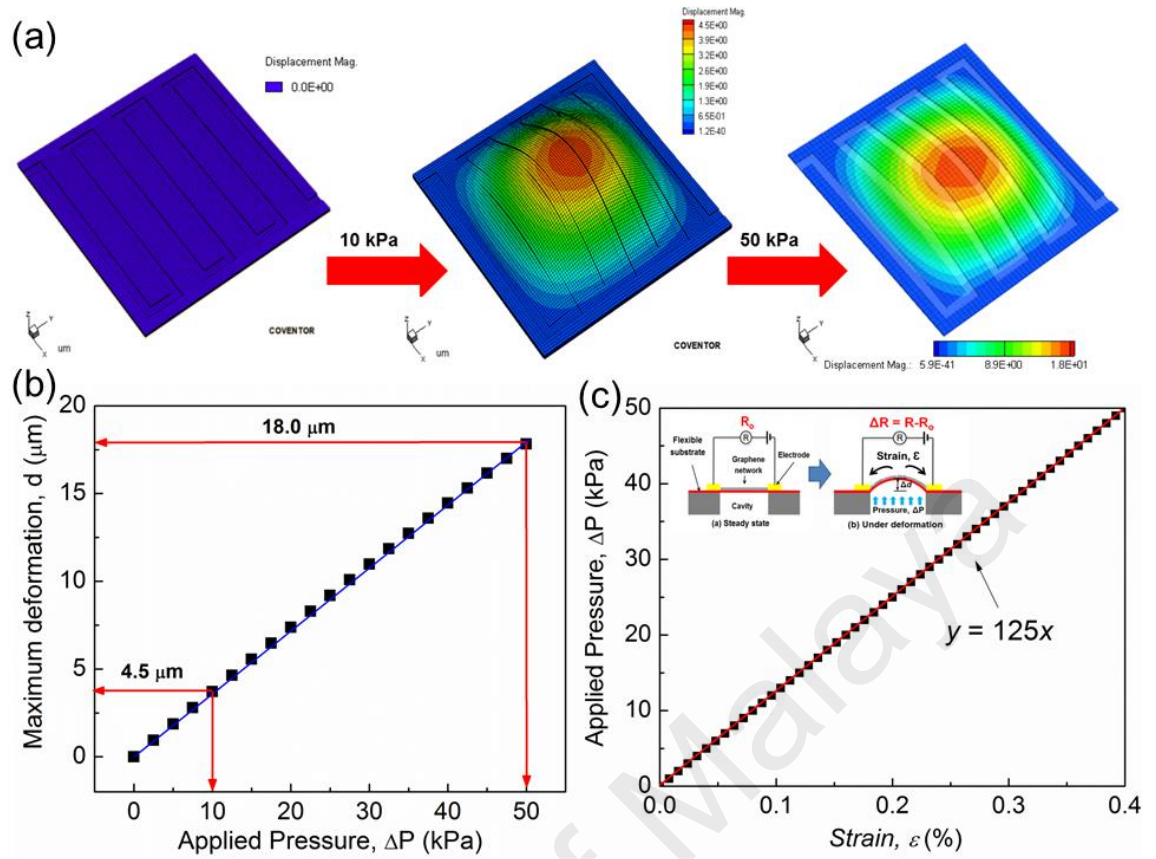


Figure 6.13: (a) Finite element analysis (FEA) on the fabricated sensor has been conducted using CoventorWare® to demonstrate that the applied pressure from initial condition to 10 kPa and then to 50 kPa applied pressure. A round-shape deformation was formed on the bottom surface of the fabricated sensor which gives maximum deformation of 4.5 μm at 10 kPa and 18.0 μm at 50 kPa. (b) Plot of maximum deformation, d with respect of applied pressure obtained from FEA. (c) Calculated strain, ε (%) exerted due to the deformation of the fabricated sensor when applied to a pressure range of 0-50 kPa. The solid lines are given as guides to the eye.

Finally, the relative change in resistance as a function of average strain which directly related to the applied pressure is plotted in **Fig. 6.14** for the sensors fabricated from 750, 850 and 1000 $^{\circ}\text{C}$ samples. The GF is then easily calculated based on the slope of fitted lines. Interestingly, the GF of the graphene/ Cu_2O nanocomposites grown at 750 and 850 $^{\circ}\text{C}$ is calculated to be 50 and 30, respectively which shows much higher values as compared to the graphene sample grown at 1000 $^{\circ}\text{C}$ (GF=15). This further proves that the piezoresistive effect in the graphene networks could be

improved by incorporating the Cu₂O nanoparticles, increasing the overlapping region between graphene islands as well as introducing a highly-dense graphene defects.

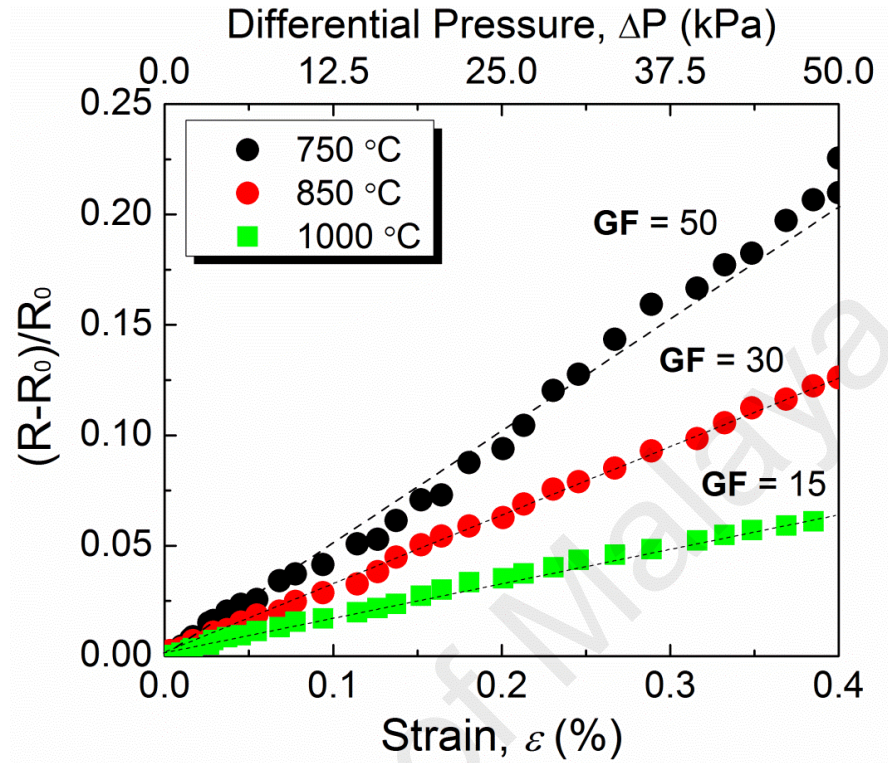


Figure 6.14: Changes of relative resistance with respect to the strain, ϵ exerted due to the deformation of the fabricated sensor when applied to a pressure range of 0-50 kPa. Calculated gauge factor, GF for pressure sensor fabricated from 750, 850 and 1000 °C samples were shown with the value of 50, 30 and 15, respectively. Note that the GF of pristine graphene purchased from Graphene Supermarket was around ~1.9-2.0. Dashed lines are given as guides to the eye.

6.6 Proposed Sensing Mechanism

For pristine graphene grown at a higher growth temperature, the piezoresistive effect under deformation is limited to the structure deformation-dependence of the graphene lattice distortion, which only leads to a modified electronic band structure, so the overall variation of resistance is smaller (Jin et al., 2009). The calculated GF of pristine graphene purchased from Graphene Supermarket is found to be around ~1.9-2.0. The results presented in the previous sections on the properties of graphene/Cu₂O nanocomposites grown by HFTCVD technique performed in this work,

indicate that the transport of charge carriers in this material may differ from that of pristine graphene. The sensing mechanism involved in enhancing the piezoresistive effects under deformation for the graphene/Cu₂O nanocomposites grown by HFTCVD technique is not only limited to changes in the carbon-carbon bond lengths, but also depends on the defective structure in the graphene networks, incorporated Cu₂O nanoparticles and overlapping regions between graphene islands.

Here, four mechanisms contributes to resistance changes in the graphene/Cu₂O nanocomposites as illustrated in **Fig. 6.15** are proposed: (i) contact resistance between adjacent graphene grains (from *a* to *b*) or between their overlapping areas (from *c* to *d*); (ii) resistance to tunnelling or electron hopping effect between neighbouring graphene islands (from *b* to *c*); (iii) resistance to tunnelling through defect-like line disruptions (from *e* to *f*); and (iv) resistance due to point defects-like vacancies or substitutional impurities (from *g* to *h*). Thus, measurable changes in resistance are produced as a result of even small modifications to the lattice distortions in the graphene structure itself, contact area or tunnelling distance between neighbouring islands with structural defects. Note that the mechanism of resistance change for the graphene sample grown at 1000 °C is limited to changes to contact resistance between adjacent graphene grains and resistance due to electron hopping effect between neighbouring graphene islands.

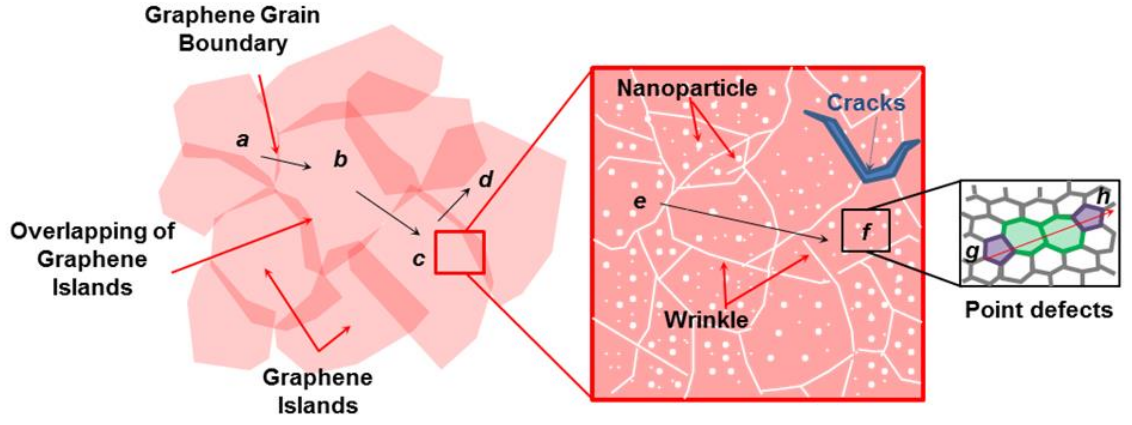


Figure 6.15: Schematic representations of the proposed resistance mechanism in graphene/Cu₂O nanocomposites network.

Fig. 6.16(a) shows an image of the transferred graphene/Cu₂O nanocomposites grown at 750 °C that is fully enclosed on the IDE structure. It is believed that higher initial resistance, R_0 is mainly due to the scattering of charge carriers by small graphene islands with a high topological defect. In this case, the resistance changes, R in these graphene and graphene/Cu₂O nanocomposites networks are contributed by the changes in resistance to tunnelling between graphene islands ($R_{\text{graphene islands}}$), resistance to tunnelling between the defect-like line disruptions structure ($R_{\text{defect-like structure}}$), resistance produced by defects in the graphene lattice itself ($R_{\text{lattice defect}}$) and contact resistance between the graphene and IDE array (R_{contact}). Hence, any changes to these parameters as a function of applied pressure will induce strain in the graphene lattice structure and scatter the charge carriers at increased tunnelling distance, thus resulting in a significant resistance change as shown in **Fig. 6.16(b-e)**.

The total resistance change, R can be written using the expression;

$$R = R_{\text{graphene islands}} + R_{\text{defect-like structure}} + R_{\text{lattice defect}} + R_{\text{contact}} \quad (6.1)$$

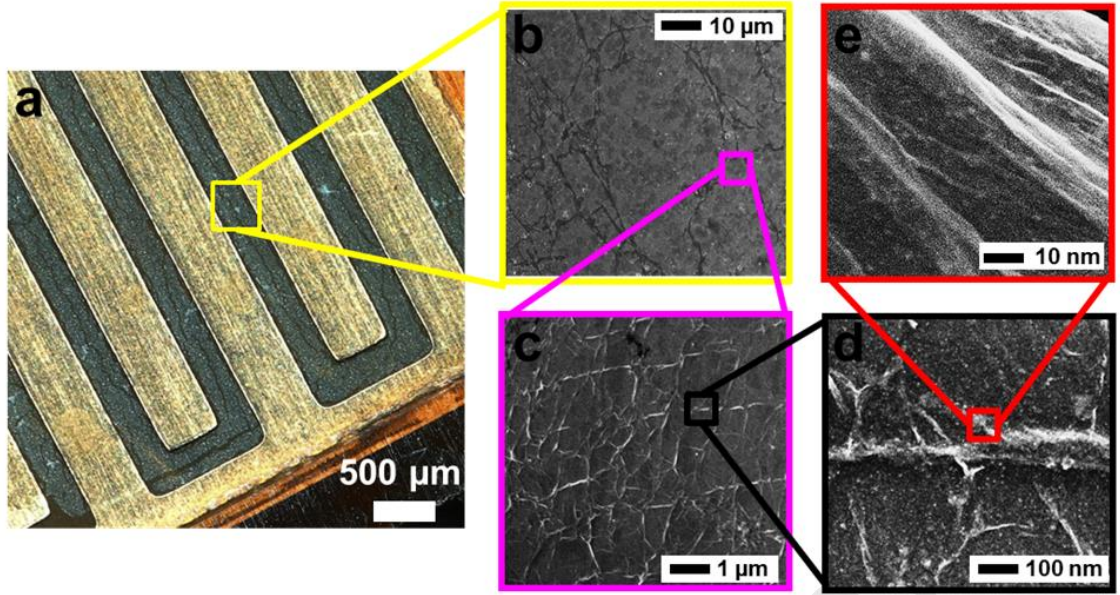


Figure 6.16: (a) FESEM images of transferred graphene/Cu₂O nanocomposites grown at 750 °C on the IDE structure with different possibilities of resistance changes; (b) Overlapping region between graphene islands, (c) Wrinkle defect structure, (d) Cu₂O nanoparticles defect structure and (e) point defects inside graphene lattice.

Furthermore, the equivalent electrical model of sensing mechanism with combination of IDE and graphene or graphene/Cu₂O nanocomposites is illustrated in **Fig. 6.17**. The electrical model of the sensor mechanism without and with applied pressure can be expressed by the following expressions;

1) Without applied pressure

$$R_{eq}^i = R_{graphene\ islands}^i + R_{defect-like\ structure}^i + R_{lattice\ defect}^i + R_{contact}^i + R_{electrode}^i \quad (6.2)$$

$$\frac{1}{C_{eq}^i} = \frac{1}{C_{graphene}^i} + \frac{1}{C_{electrode}^i} \quad (6.3)$$

2) With applied pressure

$$R_{eq}^f = R_{graphene\ islands}^f + R_{defect-like\ structure}^f + R_{lattice\ defect}^f + R_{contact}^f + R_{electrode}^f \quad (6.4)$$

$$\frac{1}{C_{eq}^f} = \frac{1}{C_{graphene}^f} + \frac{1}{C_{electrode}^f} \quad (6.5)$$

Therefore;

$$\Delta R = R_{eq}^f + R_{eq}^i \quad (6.6)$$

$$\frac{1}{C_{eq}^i} - \frac{1}{C_{eq}^f} = \frac{C_{eq}^f - C_{eq}^i}{C_{eq}^f C_{eq}^i} = \frac{\Delta C}{C_{eq}^f C_{eq}^i} \quad (6.7)$$

$$\Delta C = C_{eq}^f C_{eq}^i - \left(\frac{1}{C_{eq}^i} - \frac{1}{C_{eq}^f} \right) \quad (6.8)$$

where R_{eq} , $R_{electrode}$, C_{eq} , $C_{electrode}$ and $C_{graphene}$ are equivalent resistance, resistance of electrode, equivalent capacitance, capacitance of electrode, and capacitance of graphene network, respectively. Meanwhile, ΔR and ΔC are the resistance and capacitance change in a response to change in applied pressure, respectively.

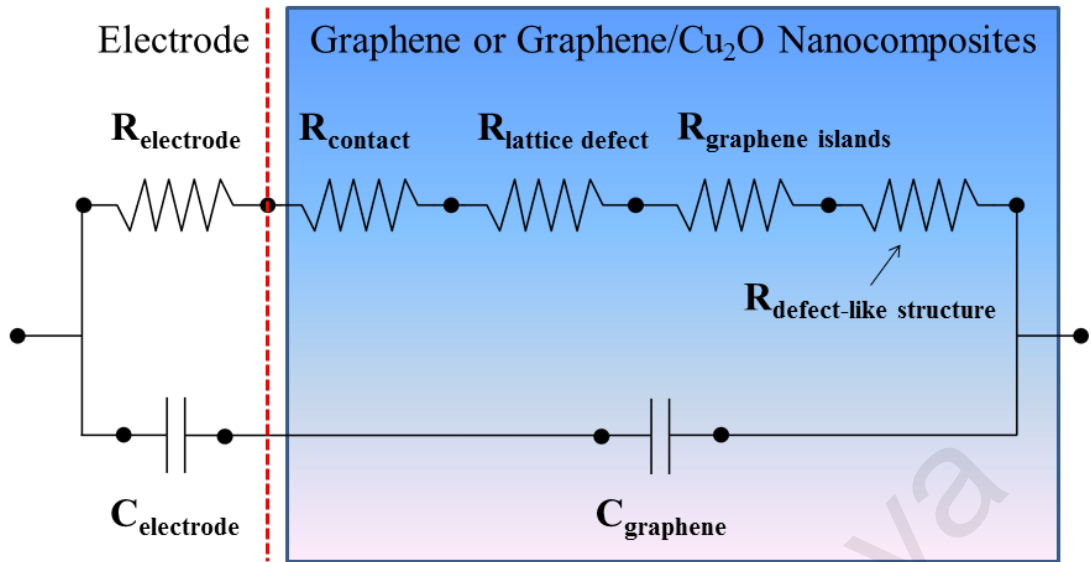


Figure 6.17: Schematic representation of circuit model for graphene-based flexible pressure sensor.

It should be noted that due to very low gauge factor of metal (Window et al., 1992), the resistance change of the electrode component ($\Delta R_{\text{electrode}}$) is possibly not significant and thus can be neglected in the model. Under the DC testing, the influence of capacitance on the electrode can also assumed to be negligible during the measurement due to the large gap (electrode gap = 200 μm) between the electrode fingers. In addition, there is also a possibility that changes in resistance may come from the graphene that is directly touching the IDE which can result in contact resistance changes when pressure is applied to the flexible substrate. However, if the contact resistance effect is significant enough as compared to the resistance produced by the difference in defect density in graphene, the response of the pressure sensor may not be linearly dependent on the applied pressure (see **Fig. 6.10**) and no multi-cycle of repeated loading and unloading at different pressures (see **Fig. 6.11**) could be achieved (Yao et al., 2013). Thus, the contact resistance effect as a function of applied pressure can be neglected in the discussion.

At a growth temperature of 750 °C, the deformation produced by the high defect density is more significant on the resistance changes compared to that of perfect graphene due to the enhancement in quantum confinement effects from the presence of point defects and line disruption defects. The high dependence of the resistance changes in the high defect density of the graphene networks on the structural deformation could be attributed to the creation of charge carrier scattering. Under the application of pressure, the tunneling distortion among the overlapping and adjacent graphene islands and defect-like structures become more significant thus increased the density of the tunneling per graphene area. This led to a higher probability of electron scattering in the percolating networks, which further reduced the density of the conducting paths, thereby effectively increasing the rate of the resistance change.

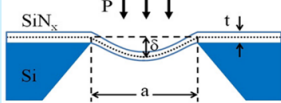
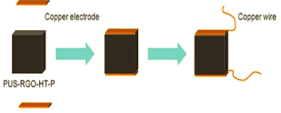
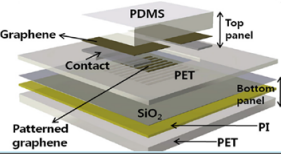
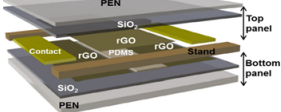
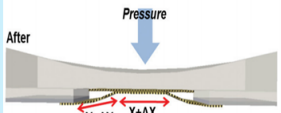
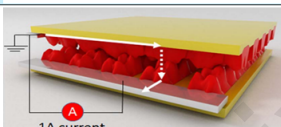
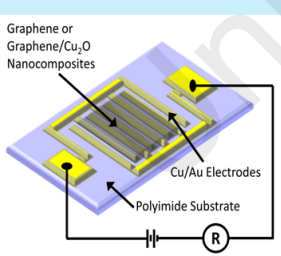
6.6 Comparison of Graphene-based Pressure Sensor in Literature

Up to now, many kinds of graphene-based pressure sensor have been reported in the literature. Therefore, performance comparisons between graphene-based flexible pressure sensors presented in this work and the one reported by others are presented in **Table 6.2**. One of the pioneer works reported by Zhu et al. (2013), demonstrated that high-quality, multilayer, polycrystalline graphene obtained by CVD process can be used as a pressure sensor. The fabricated sensor shows a high sensitivity within a wide pressure range from 0 to 70 kPa as the graphene is suspended on a rigid silicon nitride substrate and not fully supported by the substrate. However, the problem of suspended-graphene configuration addressed by Sorkin et al., in which two distinct types of mechanical failure were identified; 1) A complete detachment of the suspended graphene from the substrate edges via breaking the covalent bonds between the carbon atoms of the graphene and the atoms of the substrate. 2) A rupture of the graphene structure via breaking the C-C bonds within the graphene itself (Sorkin et al., 2011). From the work of Yao et al. (2013), the reduced graphene oxide is coated onto

polyurethane (PU) sponge which realized a significantly higher detection limit at 0.009 kPa. The high detection limit is due to a significant change of PU microstructure towards a small deformation. However, the sensing range is observed to be limited from 0 to 10 kPa due to the limit of elastic region for PU microstructure which avoided a plastic deformation region.

University of Malaya

Table 6.2: Performance comparisons between graphene-based flexible pressure sensors presented in this work and reported by others.

Material	Sensor Structure	Pressure Range	Sensitivity	Detection Limit	Gauge Factor	Comment	Reference
High-quality Graphene on silicon nitride		0-70 kPa	$8.5 \times 10^{-2} \text{ kPa}^{-1}$	5 kPa	1.6	-Wide sensing range -Vary low GF -Not flexible	Zhu et al. (2013) Applied Physics Letter
Reduced Graphene Oxide on Polyurethane (PU) sponge		0-10kPa	$3.0 \times 10^{-2} \text{ kPa}^{-1}$	0.009 kPa	-	-Narrow sensing range -High sensitivity -Non-linear response -Bulky	Yao et al. (2013) Advanced Materials
Stacked Graphene/ Patterned Graphene on Polydimethylsiloxane (PDMS)		0-14 kPa	$3.9 \times 10^{-8} \text{ kPa}^{-1}$	1 kPa	-	-Narrow sensing range -Vary low sensitivity -Complicated fabrication process	Chun et al. (2014) Applied Physics Letter
Reduced Graphene Oxide Flakes on Polyethylene Naphthalate (PEN)		0-20 kPa	$7.0 \times 10^{-3} \text{ kPa}^{-1}$	0.039 kPa	-	-Narrow sensing range -Non-linear response -Complicated fabrication process	Chun et al. (2015) Carbon
Double-layered Graphene on PDMS		1-10 kPa	$3.9 \times 10^{-2} \text{ kPa}^{-1}$	0.0003 kPa	-	-Narrow sensing range -High sensitivity -Non-linear response	Chun et al. (2015) Nanoscale
Stacked Laser-Scribed Graphene on Polyethylene Terephthalate (PET)		10-50 kPa	$5.0 \times 10^{-3} \text{ kPa}^{-1}$	-	-	-Wide sensing range -Complicated fabrication process	Tian et al. (2015) Scientific Reports
High-quality Graphene Islands Films on Polyimide		0-50 kPa	$1.2 \times 10^{-3} \text{ kPa}^{-1}$	-	15	-Wide sensing range -Linear response -Medium GF	Controlled sample
High-defect Graphene/Cu ₂ O Nanocomposite on Polyimide			$4.5 \times 10^{-3} \text{ kPa}^{-1}$	0.24 kPa	50	-Wide sensing range -Linear response -High GF -Controllable sensitivity	THIS WORK

Chun's group (2014; 2015a) has actively worked on graphene-based flexible pressure sensor using graphene and reduced graphene oxide with a complicated design of the sensor structure. This would drive a higher piezoresistive character due to the contact resistance between two graphene layers and the electromechanical properties of graphene itself. However, the design which sandwiched the graphene or graphene oxide sample between the Polyethylene Naphthalate (PEN) or Polydimethylsiloxane (PDMS) layers restricted the slip motion. Therefore, the sensitivity of the sensor is observed to be low even within a small pressure range (0 to 14 kPa). The disadvantage of this sensor structure has been overcome by the introduction of a pressure-amplifying structure in the improved sensor design (Chun et al., 2015b). They reported that the new sensor sensitivity and detection limit reached up to $3.9 \times 10^{-2} \text{ kPa}^{-1}$ and 0.0003 kPa, respectively. However, the sensing range is reported to be narrower with a non-linear response observed when the pressure exceeded 10 kPa limits.

The use of imperfection of a graphene network to increase the piezoresistive effect upon deformation has been reported by Kim et al. (2011) and Hempel et al. (2012). Recently, Tian et al. reported a significant increase in the pressure sensing range from 10 to 50 kPa and high sensitivity at $5.0 \times 10^{-3} \text{ kPa}^{-1}$ by using patterned laser-scribed reduced graphene oxide (LSG) (Tian et al., 2015). Two layers of LSG are stacked on each other with the patterns arranged in perpendicular to each other to form a cross-bar structure. Upon applying pressure, a compressive deformation can enhance the contact between the two LSG lines and reduce the interlayer distance of LSG, resulting in more electrical path ways through the crossbar structure.

In comparison, this work has shown the development of a pressure sensor which is sensitive within a wide pressure range from 0 to 50 kPa with a linear sensing response using high-quality graphene films. The sensitivity of the sensor is measured to be at $1.2 \times 10^{-3} \text{ kPa}^{-1}$ which is comparable to a discrete pressure sensor. Since the sample has been formed with the graphene islands merging together to form a continuous films, the calculated gauge factor (GF) is significantly increased to 15 as compared to the high-quality, multilayer, polycrystalline graphene at $\text{GF} = 1.6$ as reported by Zhu et al. (2013). The sensitivity of the sensor is further increased to $4.5 \times 10^{-3} \text{ kPa}^{-1}$ and shows a moderate detection limit of 0.24 kPa while maintaining its wide sensing range with a linear response when high-defect density graphene/Cu₂O nanocomposites is used. The GF of the sample fabricated at 750 °C is calculated to be of 50, which are 3.3 and 31.3 times higher compared to the high-quality graphene islands films (controlled sample) and high-quality graphene on silicon nitride (Zhu et al, 2013), respectively. Furthermore, the sensitivity of the sensor could be easily tuned by controlling the growth temperature of the graphene/Cu₂O nanocomposite.

6.6 Summary

In summary, a one-step process to grow graphene-copper oxide nanocomposites (graphene/Cu₂O nanocomposites) using hot-filament thermal chemical vapour deposition (HFTCVD) technique has been successfully demonstrated. The growth temperature resulting in the formation of graphene/Cu₂O nanocomposites are shown to be in the region of 750 and 850 °C which induced the re-deposition of the sublimated trapped Cu vapour inside the alumina tube onto the graphene layer. However, at growth temperature of 1000 °C, the formation of nanocomposites on the graphene layer is minimized due to higher rate of re-evaporation of the Cu₂O nanoparticles. It is also observed that the presence of defect-like structures such as wrinkles and Cu₂O nanoparticles are more prominent in the graphene grown at 750 °C as compared to the one grown at 850 and 1000 °C. A linear piezoresistive effect has been observed for the applied pressure within the range of 0 to 50 kPa. The sensitivity of the fabricated pressure sensor could easily be modified by varying the substrate temperature. The sensing mechanism of graphene and graphene/Cu₂O nanocomposites pressure sensor based on the variation of percolation schemes through specific type of defects has been presented and the correlation through the corresponding morphological analysis has been discussed systematically. The best sensor performance with the; sensitivity of 0.0045 kPa⁻¹, limit of detection of 0.24 kPa, and gauge factor of 50, are achieved for the device fabricated using the graphene/Cu₂O nanocomposite grown at substrate temperature of 750 °C. This investigation provides a better understanding of the use of graphene in highly sensitive piezoresistive-based flexible pressure sensors.

CHAPTER 7: CONCLUSION AND FUTURE WORKS

7.1 Conclusion

This thesis has successfully reported a PhD journey on the fabrication, characterization and application of graphene grown by both the top-down and bottom-up approach. The top-down approach involved the growth of graphene oxide (GO) by the modified Hummers technique and reducing it to reduced graphene oxide (rGO) by hydrogen plasma treatment. Two sets of hydrogen plasma treatment process parameters had been systematically studied which included the effect of plasma treatment time and hydrogen flow rate. The quality of rGO was found to be dependent on the reduction time and pressure inside the reaction chamber during the hydrogen plasma treatment process. It was found that the removal of oxygen functional groups by the hydrogen plasma treatment effectively healed the imperfections within the carbon basal plane and increases the in-plane sp^2 crystallite size, L_a . The highest reduction obtained resulted in rGO sample with C/O ratio of 7.9 where the reduction process time and the chamber pressure was fixed at 20 s and 0.8 mbar respectively.

In gas sensor application study, rGO was deposited on a sensor platform. The CO_2 gas sensor using the rGO with the highest degree of reduction showed the highest sensitivity towards CO_2 gas in the range of 0 to 1500 ppm when tested in 1 atm N_2 environment at 23°C with 37% RH. The sensitivity dropped from 54% to 10% at 750 ppm CO_2 when further tested at higher humidity set at 68% RH (air environment). However, it showed good repeatability performance with a sensing and recovery time of about 4 min when exposed to 750 and 769 ppm CO_2 concentration in air environment at 68% RH without an external assisted recovery. The sensing mechanism of this CO_2 gas sensor involved CO_2 molecules acting as electron donors contributing to a decrease in the resistance detected.

The non-linear sensing response produced was deduced to be related to the rate of adsorption of the CO₂ gas molecules on the sp² crystallite sites (adsorption active sites) which increased after undergoing hydrogen plasma treatment and the sensitivity increased with higher degree of reduction of the rGO. The capability of the sensor to recover without any external assistance was attributed to the weak interaction between the graphene and CO₂ gas molecules. The sensing performance of this rGO sensor is very encouraging for practical applications like indoor CO₂ gas sensor considering the room temperature reduction process and the high sensitivity sensing capability and low cost fabrication.

The novel technique developed in this work, the hot-filament thermal chemical vapour deposition (HFTCVD) is shown to be capable of growing high quality graphene and graphene/Cu₂O nanocomposites which has been successfully tested for application in a flexible pressure device. A common fabrication technique of Cat-CVD had been modified to adopt the vapour trapping mechanism by adding an alumina tube (one end sealed) which then coiled around using tungsten filament. Two sets of parameters had been systematically studied which covered the effect of growth duration and hydrogen flow rates. It was found that the Cu₂O nanoparticles nucleation size acted as nucleation sites for monolayer and multi-layer graphene growth. The presence of hydrogen would trim the edges of graphene and modify the surface kinetic reaction to obtain controllable graphene layers and defect densities. A high-quality graphene was then realized by the synergistic effect of the quasi-static condition inside the alumina tube as well as the catalytic dissociation of CH₄ and H₂ precursors by the hot-filament. A growth mechanism was then proposed to explain the growth of high-quality graphene using the HFTCVD technique.

The HFTCVD system demonstrated its versatility and capability of fabricating graphene/Cu₂O nanocomposites simultaneously (one-step process), by altering the

capture-controlled regime and desorption-controlled regime near the surface of Cu foils. This had been shown to be possible only by simply controlling the deposition temperature of graphene growth. It was found that at low growth temperature, the Cu₂O nucleation density would be significantly increased which resulted in a higher probability of overlapping event between graphene islands. The remaining trapped copper vapour inside the alumina tube would then be re-deposited in the form of Cu₂O nanoparticles onto the grown graphene layer to result in the graphene/Cu₂O nanocomposites. In addition, this would also sacrifice the high-quality graphene structure due to the surface kinetic factors of precursor's gases. Interestingly, variation of percolation conducting schemes through specific type of defects (i.e. overlapping between graphene islands, decorated Cu₂O nanoparticles, wrinkles and structural points defects) were found to be able to significantly enhance the piezoresistive effect in graphene structure for flexible pressure sensor application. A linear piezoresistive effect was observed for applied pressure within the range of 0 to 50 kPa with a high sensitivity of $4.5 \times 10^{-3} \text{ KPa}^{-1}$, limit of detection at 0.24 kPa and GF of 50, had been successfully achieved in this work. Furthermore, performance comparisons between graphene-based flexible pressure sensors that had been reported by others in literatures were discussed to highlight the significance of the findings of this work. Finally, the sensing mechanism was proposed to provide a better understanding of the use of graphene in highly sensitive piezoresistive-based flexible pressure sensors.

7.2 Summary of Contributions

The novelty and important findings acquired in this work can be summarized as follows;

- 1) Environmentally friendly, room-temperature reduction process and efficient method of removing oxygen functional groups for the reduction of graphene oxide (GO) by hydrogen plasma.
- 2) Evaluation of reduced graphene oxide capability in room-temperature sensing and recovery of CO₂ gas sensor which envision for practical use in indoor air quality monitoring.
- 3) Fabrication of high-quality graphene on Cu foils by hot-filament thermal chemical vapour deposition (HFTCVD) technique.
- 4) Proposed a growth mechanism for the fabrication of high-quality graphene on Cu foils by hot-filament thermal chemical vapour deposition (HFTCVD) technique.
- 5) One-step process growth of graphene/Cu₂O nanocomposites by hot-filament thermal chemical vapour deposition (HFTCVD) technique.
- 6) Evaluation of graphene-based flexible pressure sensor with an enhancement in terms of gauge factor for a wide range of pressure.
- 7) Proposed a sensing mechanism of graphene-based flexible pressure sensor by employing piezoresistive effect in graphene/Cu₂O nanocomposites materials.

7.3 Future Works

Envisioned future of graphene fabrication and application towards industrial-scale production was found to be advancing so fast. Therefore, the scientific understanding of the reduced graphene oxide, graphene and graphene/Cu₂O nanocomposites materials as well as its application in gas and pressure sensor has been explored in this PhD works for the future in graphene-based industry. Despite of the successful development of the reduction of graphene oxide by hydrogen plasma at room temperature and its capability as CO₂ gas sensor, fabrication of high-quality graphene in modified Cat-CVD technique and the one-step process of growing graphene/Cu₂O nanocomposites for the enhancement of graphene-based flexible pressure sensors, further improvement for future works was then suggested as follows;

7.3.3 Plasma Doping of rGO for Enhancement in Gas Sensor Selectivity

Tuneable physicochemical properties by chemical modification of materials become necessary in graphene applications especially in gas sensor devices which controlled the selectivity of target gases. One way of achieving this control is by elemental doping, a method widely used in semiconductor silicon technology. Nitrogen and Boron doping is widely employed to modify silicon properties in electronic devices. It will certainly be of great interest for the processing of future graphene-based gas sensor devices using widespread technologies like plasma doping process. Therefore, a facile approach is proposed as future works as to reduce and doped the rGO by employing a PECVD technique. The plasma doping process of nitrogen or boron atoms will promotes the selectivity of environmental polluting or toxic gas molecules such as CO₂, CO, NO₂ and NO. Furthermore, bulk quantities rGO could be doped with a controllable level of nitrogen or boron atoms can be achieved. This also allows a one-pot process which is completely dry and, thus, eliminates the re-aggregation of solution process doping of graphene oxide.

7.3.3 Transfer-free of Graphene Fabrication Assisted by Trapped

Copper-Vapour

High-quality graphene suffered some degradation during the transfer process. This was found to be a major hindrance to cope with the quality optimization and the cost reduction in the future of graphene manufacturing industry. To retain the optimum quality of as prepared graphene, a transfer-free of graphene should be explored. To avoid the Cu etching step in graphene transfer process, a remote catalysis method using HFTCVD technique has been proposed (see Appendix 2). The trapped subliming copper vapour was inferred to act as a remote catalysis due to the circumfluence flow inside the alumina tube (one end sealed). With the aids of precursor's dissociation at the hot-filament as well as vapour trapping mechanism, a high-quality transfer-free graphene could be possibly achieved.

7.3.3 Electronic Skin

Recognition of tactile information will be very important for future applications in medical, robotics, human-machine interfaces and artificial intelligence fields which can be used as electronics skin. An important step to obtain good artificial electronic skin was to fabricate large-area pressure sensors with a high mechanical flexibility and tunability. A part from that, producing a highly sensitive pressure sensor with sufficient detection limit in both medium- (10-100 kPa, suitable for object manipulation) and low-pressure regimes (<10 kPa, comparable to gentle touch) as well as fast response time (in the range of ms to μ s) were crucial. The tuneable piezoresistive sensing mechanism of graphene-based material with a high detection limit has been established in this thesis, which paves the way for one of the diverse electronic skin applications. The rapidly increasing innovations in this area, especially graphene-based materials will be important to the scientific community and to the future of human life.

REFERENCES

- Abergel, D. S. L., Apalkov, V., Berashevich, J., Ziegler, K., & Chakraborty, T. (2010). Properties of graphene: a theoretical perspective. *Advances in Physics*, 59(4), 261-482.
- Akhavan, O. (2010). The effect of heat treatment on formation of graphene thin films from graphene oxide nanosheets. *Carbon*, 48(2), 509-519.
- Almassri, A. M., Wan Hasan, W. Z., Ahmad, S. A., Ishak, A. J., Ghazali, A. M., Talib, D. N., & Wada, C. (2015). Pressure sensor: state of the art, design, and application for robotic hand. *Journal of Sensors*, 2015, 1-12.
- Ashruf, C. M. A. (2002). Thin flexible pressure sensors. *Sensor Review*, 22(4), 322-327.
- Bae, S., Kim, H., Lee, Y., Xu, X., Park, J. S., Zheng, Y., ... & Kim, Y. J. (2010). Roll-to-roll production of 30-inch graphene films for transparent electrodes. *Nature Nanotechnology*, 5(8), 574-578.
- Bae, S., Kim, S. J., Shin, D., Ahn, J. H., & Hong, B. H. (2012). Towards industrial applications of graphene electrodes. *Physica Scripta*, 2012(T146), 014024, 1-8.
- Baraket, M., Walton, S. G., Wei, Z., Lock, E. H., Robinson, J. T., & Sheehan, P. (2010). Reduction of graphene oxide by electron beam generated plasmas produced in methane/argon mixtures. *Carbon*, 48(12), 3382-3390.
- Barlian, A. A., Park, W. T., Mallon Jr, J. R., Rastegar, A. J., & Pruitt, B. L. (2009). Review: Semiconductor piezoresistance for microsystems. *Proceedings of The IEEE*, 97(3), 513-552.
- Basu, S., & Bhattacharyya, P. (2012). Recent developments on graphene and graphene oxide based solid state gas sensors. *Sensors and Actuators B: Chemical*, 173, 1-21.
- Batrakov, K., Kuzhir, P., Maksimenko, S., Paddubskaya, A., Voronovich, S., Lambin, P., ... & Svirko, Y. (2014). Flexible transparent graphene/polymer multilayers for efficient electromagnetic field absorption. *Scientific Reports*, 4(7191), 1-5.
- Bauer, E. (2014). *Surface microscopy with low energy electrons*. Springer.
- Baughman, R. H., Zakhidov, A. A., & de Heer, W. A. (2002). Carbon nanotubes--the route toward applications. *Science*, 297(5582), 787-792.
- Bhavaripudi, S., Jia, X., Dresselhaus, M. S., & Kong, J. (2010). Role of kinetic factors in chemical vapor deposition synthesis of uniform large area graphene using copper catalyst. *Nano Letters*, 10(10), 4128-4133.
- Biroju, R. K., & Giri, P. K. (2014). Defect enhanced efficient physical functionalization of graphene with gold nanoparticles probed by resonance Raman spectroscopy. *The Journal of Physical Chemistry C*, 118(25), 13833-13843.

- Blakely, J. M., Kim, J. S., & Potter, H. C. (1970). Segregation of carbon to the (100) surface of nickel. *Journal of Applied Physics*, 41(6), 2693-2697.
- Boehm, HP, Clauss, A., Fischer, GO, & Hofmann, U. (1962). The adsorption behavior of very thin carbon foils. *Journal of Polymer Science*, 316 (3-4), 119-127.
- Boland, C. S., Khan, U., Backes, C., O'Neill, A., McCauley, J., Duane, S., ... & Coleman, J. N. (2014). Sensitive, high-strain, high-rate bodily motion sensors based on graphene–rubber composites. *ACS Nano*, 8(9), 8819-8830.
- Bogue, R. (2014). Graphene sensors: a review of recent developments. *Sensor Review*, 34(3), 233-238.
- Borini, S., White, R., Wei, D., Astley, M., Haque, S., Spigone, E., ... & Ryhanen, T. (2013). Ultrafast graphene oxide humidity sensors. *ACS Nano*, 7(12), 11166-11173.
- Brodie, B. C. (1859). On the atomic weight of graphite. *Philosophical Transactions of the Royal Society of London*, 149, 249-259.
- Cai, W., Huang, Y., Wang, D., Liu, C., & Zhang, Y. (2014). Piezoresistive behavior of graphene nanoplatelets/carbon black/silicone rubber nanocomposite. *Journal of Applied Polymer Science*, 131(3), 39778-39783.
- Cançado, L. G., Jorio, A., Ferreira, E. M., Stavale, F., Achete, C. A., Capaz, R. B., ... & Ferrari, A. C. (2011). Quantifying defects in graphene via Raman spectroscopy at different excitation energies. *Nano Letters*, 11(8), 3190-3196.
- Celebi, K., Cole, M. T., Choi, J. W., Wyczisk, F., Legagneux, P., Rupesinghe, N., ... & Park, H. G. (2013). Evolutionary kinetics of graphene formation on copper. *Nano Letters*, 13(3), 967-974.
- Chan, J., Venugopal, A., Pirkle, A., McDonnell, S., Hinojos, D., Magnuson, C. W., ... & Vogel, E. M. (2012). Reducing extrinsic performance-limiting factors in graphene grown by chemical vapor deposition. *ACS Nano*, 6(4), 3224-3229.
- Chen, J. H., Jang, C., Xiao, S., Ishigami, M., & Fuhrer, M. S. (2008). Intrinsic and extrinsic performance limits of graphene devices on SiO₂. *Nature Nanotechnology*, 3(4), 206-209.
- Chen, W., Yan, L., & Bangal, P. R. (2010). Preparation of graphene by the rapid and mild thermal reduction of graphene oxide induced by microwaves. *Carbon*, 48(4), 1146-1152.
- Chen, Z., Ren, W., Gao, L., Liu, B., Pei, S., & Cheng, H. M. (2011). Three-dimensional flexible and conductive interconnected graphene networks grown by chemical vapour deposition. *Nature Materials*, 10(6), 424-428.

- Cheneler, D., Vervaeke, M., & Thienpont, H. (2014). Light-modulating pressure sensor with integrated flexible organic light-emitting diode. *Applied Optics*, 53(13), 2766-2772.
- Chun, S., Jung, H., Choi, Y., Bae, G., Kil, J. P., & Park, W. (2015a). A tactile sensor using a graphene film formed by the reduced graphene oxide flakes and its detection of surface morphology. *Carbon*, 94, 982-987.
- Chun, S., Kim, Y., Jung, H., & Park, W. (2014). A flexible graphene touch sensor in the general human touch range. *Applied Physics Letters*, 105(4), 41907-41911.
- Chun, S., Kim, Y., Oh, H. S., Bae, G., & Park, W. (2015b). A highly sensitive pressure sensor using a double-layered graphene structure for tactile sensing. *Nanoscale*, 7(27), 11652-11659.
- Chung, D. D. L. (2002). Review graphite. *Journal of Materials Science*, 37(8), 1475-1489.
- Cookson, J. W. (1935). Theory of the piezo-resistive effect. *Physical Review*, 47(2), 194-195.
- Debbichi, L., Marco de Lucas, M. C., Pierson, J. F., & Kruger, P. (2012). Vibrational properties of CuO and Cu₄O₃ from first-principles calculations, and Raman and infrared spectroscopy. *The Journal of Physical Chemistry C*, 116(18), 10232-10237.
- Dubale, A. A., Su, W. N., Tamirat, A. G., Pan, C. J., Aragaw, B. A., Chen, H. M., ... & Hwang, B. J. (2014). The synergetic effect of graphene on Cu₂O nanowire arrays as a highly efficient hydrogen evolution photocathode in water splitting. *Journal of Materials Chemistry A*, 2(43), 18383-18397.
- Dubin, S., Gilje, S., Wang, K., Tung, V. C., Cha, K., Hall, A. S., ... & Kaner, R. B. (2010). A one-step, solvothermal reduction method for producing reduced graphene oxide dispersions in organic solvents. *ACS Nano*, 4(7), 3845-3852.
- Duong, D. L., Han, G. H., Lee, S. M., Gunes, F., Kim, E. S., Kim, S. T., ... & Chae, S. J. (2012). Probing graphene grain boundaries with optical microscopy. *Nature*, 490(7419), 235-239.
- Eckmann, A., Felten, A., Verzhbitskiy, I., Davey, R., & Casiraghi, C. (2013). Raman study on defective graphene: effect of the excitation energy, type, and amount of defects. *Physical Review B*, 88(3), 35426-35437.
- Eda, G., & Chhowalla, M. (2010). Chemically derived graphene oxide: towards large-area thin-film electronics and optoelectronics. *Advanced Materials*, 22(22), 2392-2415.
- Erdmann, C. A., & Apte, M. G. (2004). Mucous membrane and lower respiratory building related symptoms in relation to indoor carbon dioxide concentrations in the 100-building BASE dataset. *Indoor Air*, 14(s8), 127-134.

- Fan, L., Wang, K., Wei, J., Zhong, M., Wu, D., & Zhu, H. (2014). Correlation between nanoparticle location and graphene nucleation in chemical vapour deposition of graphene. *J. Mater. Chem. A*, 2(32), 13123-13128.
- Felten, A., Flavel, B. S., Britnell, L., Eckmann, A., Louette, P., Pireaux, J. J., ... & Casiraghi, C. (2013). Single-and double-sided chemical functionalization of bilayer graphene. *Small*, 9(4), 631-639.
- Ferrari, A. C., & Basko, D. M. (2013). Raman spectroscopy as a versatile tool for studying the properties of graphene. *Nature nanotechnology*, 8(4), 235-246.
- Ferrari, A. C., Bonaccorso, F., Fal'Ko, V., Novoselov, K. S., Roche, S., Bøggild, P., ... & Garrido, J. A. (2015). Science and technology roadmap for graphene, related two-dimensional crystals, and hybrid systems. *Nanoscale*, 7(11), 4598-4810.
- Gan, L., & Luo, Z. (2013). Turning off hydrogen to realize seeded growth of subcentimeter single-crystal graphene grains on copper. *ACS Nano*, 7(10), 9480-9488.
- Gan, L., Zhang, H., Wu, R., Zhang, Q., Ou, X., Ding, Y., ... & Luo, Z. (2015). Grain size control in the fabrication of large single-crystal bilayer graphene structures. *Nanoscale*, 7(6), 2391-2399.
- Ganguly, A., Sharma, S., Papakonstantinou, P., & Hamilton, J. (2011). Probing the thermal deoxygenation of graphene oxide using high-resolution in situ X-ray-based spectroscopies. *The Journal of Physical Chemistry C*, 115(34), 17009-17019.
- Gao, J., Liu, F., Liu, Y., Ma, N., Wang, Z., & Zhang, X. (2010). Environment-friendly method to produce graphene that employs vitamin C and amino acid. *Chemistry of Materials*, 22(7), 2213-2218.
- Gao, L., Ren, W., Zhao, J., Ma, L. P., Chen, Z., & Cheng, H. M. (2010). Efficient growth of high-quality graphene films on Cu foils by ambient pressure chemical vapor deposition. *Applied Physics Letters*, 97(18), 183109.
- Gau, C., Ko, H. S., & Chen, H. T. (2009). Piezoresistive characteristics of MWNT nanocomposites and fabrication as a polymer pressure sensor. *Nanotechnology*, 20(18), 185503-185514.
- Geim, A. K. (2012). Graphene prehistory. *Physica Scripta*, 2012(T146), 14003-14007.
- Gómez-Navarro, C., Weitz, R. T., Bittner, A. M., Scolari, M., Mews, A., Burghard, M., & Kern, K. (2007). Electronic transport properties of individual chemically reduced graphene oxide sheets. *Nano Letters*, 7(11), 3499-3503.
- Gorantla, S., Bachmatiuk, A., Hwang, J., Alsalman, H. A., Kwak, J. Y., Seyller, T., ... & Rummeli, M. H. (2014). A universal transfer route for graphene. *Nanoscale*, 6(2), 889-896.

- Grant, J. T., & Haas, T. W. (1970). A study of Ru (0001) and Rh (111) surfaces using LEED and Auger electron spectroscopy. *Surface Science*, 21(1), 76-85.
- Gupta, A., Sakthivel, T., & Seal, S. (2015). Recent development in 2D materials beyond graphene. *Progress in Materials Science*, 73, 44-126.
- Hafiz, S. M., Chong, S. K., Huang, N. M., & Rahman, S. A. (2015). Fabrication of high-quality graphene by hot-filament thermal chemical vapor deposition. *Carbon*, 86, 1-11.
- Hafiz, S. M., Ritikos, R., Whitcher, T. J., Razib, N. M., Bien, D. C. S., Chanlek, N., ... & Rahman, S. A. (2014). A practical carbon dioxide gas sensor using room-temperature hydrogen plasma reduced graphene oxide. *Sensors and Actuators B: Chemical*, 193, 692-700.
- Han, G. H., Güneş, F., Bae, J. J., Kim, E. S., Chae, S. J., Shin, H. J., ... & Lee, Y. H. (2011). Influence of copper morphology in forming nucleation seeds for graphene growth. *Nano Letters*, 11(10), 4144-4148.
- Hao, Y., Wang, Y., Wang, L., Ni, Z., Wang, Z., Wang, R., ... & Thong, J. T. (2010). Probing layer number and stacking order of few-layer graphene by Raman spectroscopy. *Small*, 6(2), 195-200.
- Hawaldar, R., Merino, P., Correia, M. R., Bdikin, I., Grácio, J., Méndez, J., ... & Singh, M. K. (2012). Large-area high-throughput synthesis of monolayer graphene sheet by hot filament thermal chemical vapor deposition. *Scientific Reports*, 2(682), 1-9.
- Hazra, K. S., Rafiee, J., Rafiee, M. A., Mathur, A., Roy, S. S., McLauhlin, J., ... & Misra, D. S. (2010). Thinning of multilayer graphene to monolayer graphene in a plasma environment. *Nanotechnology*, 22(2), 25704-25710.
- Hempel, M., Nezich, D., Kong, J., & Hofmann, M. (2012). A novel class of strain gauges based on layered percolative films of 2D materials. *Nano Letters*, 12(11), 5714-5718.
- Hibino, H., Kageshima, H., & Nagase, M. (2010). Epitaxial few-layer graphene: towards single crystal growth. *Journal of Physics D: Applied Physics*, 43(37), 374005-374019.
- Hibino, H., Kageshima, H., Maeda, F., Nagase, M., Kobayashi, Y., Kobayashi, Y., & Yamaguchi, H. (2008). Thickness determination of graphene layers formed on SiC using low-energy electron microscopy. *e-Journal of Surface Science and Nanotechnology*, 6, 107-110.
- Homma, Y., Liu, H., Takagi, D., & Kobayashi, Y. (2009). Single-walled carbon nanotube growth with non-iron-group “catalysts” by chemical vapor deposition. *Nano Research*, 2(10), 793-799.

- Hsieh, Y. P., Hofmann, M., & Kong, J. (2014). Promoter-assisted chemical vapor deposition of graphene. *Carbon*, 67, 417-423.
- Huang, M., Pascal, T. A., Kim, H., Goddard III, W. A., & Greer, J. R. (2011). Electronic– mechanical coupling in graphene from in situ nanoindentation experiments and multiscale atomistic simulations. *Nano Letters*, 11(3), 1241-1246.
- Hummers Jr, W. S., & Offeman, R. E. (1958). Preparation of graphitic oxide. *Journal of the American Chemical Society*, 80(6), 1339-1339.
- Hwang, C., Yoo, K., Kim, S. J., Seo, E. K., Yu, H., & Biró, L. P. (2011). Initial stage of graphene growth on a Cu substrate. *The Journal of Physical Chemistry C*, 115(45), 22369-22374.
- Ito, T., Yamaguchi, H., Okabe, K., & Masumi, T. (1998). Single-crystal growth and characterization of Cu₂O and CuO. *Journal of Materials Science*, 33(14), 3555-3566.
- Jariwala, D., Sangwan, V. K., Lauhon, L. J., Marks, T. J., & Hersam, M. C. (2013). Carbon nanomaterials for electronics, optoelectronics, photovoltaics, and sensing. *Chemical Society Reviews*, 42(7), 2824-2860.
- Jin, C., Lan, H., Peng, L., Suenaga, K., & Iijima, S. (2009). Deriving carbon atomic chains from graphene. *Physical Review Letters*, 102(20), 205501-205505.
- Jing, Z., Guang-Yu, Z., & Dong-Xia, S. (2013). Review of graphene-based strain sensors. *Chinese Physics B*, 22(5), 57701-57710.
- Jung, I., Dikin, D., Park, S., Cai, W., Mielke, S. L., & Ruoff, R. S. (2008). Effect of water vapor on electrical properties of individual reduced graphene oxide sheets. *The Journal of Physical Chemistry C*, 112(51), 20264-20268.
- Kang, J., Hwang, S., Kim, J. H., Kim, M. H., Ryu, J., Seo, S. J., ... & Choi, J. B. (2012). Efficient transfer of large-area graphene films onto rigid substrates by hot pressing. *ACS Nano*, 6(6), 5360-5365.
- Kasap, S., Khaksaran, H., Celik, S., Ozkaya, H., Yank, C., & Kaya, I. I. (2015). Controlled growth of large area multilayer graphene on copper by chemical vapour deposition. *Physical Chemistry Chemical Physics*, 17(35), 23081-23087.
- Kataria, S., Patsha, A., Dhara, S., Tyagi, A. K., & Barshilia, H. C. (2012). Raman imaging on high-quality graphene grown by hot-filament chemical vapor deposition. *Journal of Raman Spectroscopy*, 43(12), 1864-1867.
- Kim, H., Mattevi, C., Calvo, M. R., Oberg, J. C., Artiglia, L., Agnoli, S., ... & Saiz, E. (2012). Activation energy paths for graphene nucleation and growth on Cu. *ACS Nano*, 6(4), 3614-3623.

- Kim, S. J., Choi, T., Lee, B., Lee, S., Choi, K., Park, J. B., ... & Hone, J. (2015). Ultraclean patterned transfer of single-layer graphene by recyclable pressure sensitive adhesive films. *Nano letters*, 15(5), 3236-3240.
- Kim, Y. J., Cha, J. Y., Ham, H., Huh, H., So, D. S., & Kang, I. (2011). Preparation of piezoresistive nano smart hybrid material based on graphene. *Current Applied Physics*, 11(1), S350-S352.
- Kochat, V., Pal, A. N., Sneha, E. S., Sampathkumar, A., Gairola, A., Shivashankar, S. A., ... & Ghosh, A. (2011). High contrast imaging and thickness determination of graphene with in-column secondary electron microscopy. *Journal of Applied Physics*, 110(1), 014315.
- Kusunoki, M., Norimatsu, W., Bao, J., Morita, K., & Starke, U. (2015). Growth and features of epitaxial graphene on SiC. *Journal of the Physical Society of Japan*, 84(12), 121014-121028.
- Lee, S. W., Mattevi, C., Chhowalla, M., & Sankaran, R. M. (2012). Plasma-assisted reduction of graphene oxide at low temperature and atmospheric pressure for flexible conductor applications. *The Journal of Physical Chemistry Letters*, 3(6), 772-777.
- Leenaerts, O., Partoens, B., & Peeters, F. M. (2008). Adsorption of H₂O, NH₃, CO, NO₂, and NO on graphene: A first-principles study. *Physical Review B*, 77(12), 125416-125422.
- Leenaerts, O., Partoens, B., & Peeters, F. M. (2009). Adsorption of small molecules on graphene. *Microelectronics Journal*, 40(4), 860-862.
- Li, D. M., Hernberg, R., & Mäntylä, T. (1998). Catalytic dissociation of hydrogen on a tantalum carbide filament in the HFCVD of diamond. *Diamond and Related Materials*, 7(11), 1709-1713.
- Li, Q., Chou, H., Zhong, J. H., Liu, J. Y., Dolocan, A., Zhang, J., ... & Cai, W. (2013). Growth of adlayer graphene on Cu studied by carbon isotope labeling. *Nano Letters*, 13(2), 486-490.
- Li, X., Cai, W., An, J., Kim, S., Nah, J., Yang, D., ... & Banerjee, S. K. (2009a). Large-area synthesis of high-quality and uniform graphene films on copper foils. *Science*, 324(5932), 1312-1314.
- Li, X., Cai, W., Colombo, L., & Ruoff, R. S. (2009c). Evolution of graphene growth on Ni and Cu by carbon isotope labeling. *Nano Letters*, 9(12), 4268-4272.
- Li, X., Magnuson, C. W., Venugopal, A., Tromp, R. M., Hannon, J. B., Vogel, E. M., ... & Ruoff, R. S. (2011b). Large-area graphene single crystals grown by low-pressure chemical vapor deposition of methane on copper. *Journal of the American Chemical Society*, 133(9), 2816-2819.

- Li, X., Zhang, R., Yu, W., Wang, K., Wei, J., Wu, D., ... & Ruoff, R. S. (2012). Stretchable and highly sensitive graphene-on-polymer strain sensors. *Scientific Reports*, 2 (870), 1-6.
- Li, X., Zhu, Y., Cai, W., Borysiak, M., Han, B., Chen, D., ... & Ruoff, R. S. (2009b). Transfer of large-area graphene films for high-performance transparent conductive electrodes. *Nano Letters*, 9(12), 4359-4363.
- Li, Z., Wu, P., Wang, C., Fan, X., Zhang, W., Zhai, X., ... & Hou, J. (2011a). Low-temperature growth of graphene by chemical vapor deposition using solid and liquid carbon sources. *ACS Nano*, 5(4), 3385-3390.
- Lin, H. C., Chen, Y. Z., Wang, Y. C., & Chueh, Y. L. (2015). The essential role of Cu vapor for the self-limit graphene via the Cu catalytic CVD method. *The Journal of Physical Chemistry C*, 119(12), 6835-6842.
- Liu, X., Cheng, S., Liu, H., Hu, S., Zhang, D., & Ning, H. (2012). A survey on gas sensing technology. *Sensors*, 12(7), 9635-9665.
- Llobet, E. (2013). Gas sensors using carbon nanomaterials: A review. *Sensors and Actuators B: Chemical*, 179, 32-45.
- López, V., Sundaram, R. S., Gómez-Navarro, C., Olea, D., Burghard, M., Gómez-Herrero, J., ... & Kern, K. (2009). Chemical vapor deposition repair of graphene oxide: A route to highly-conductive graphene monolayers. *Advanced Materials*, 21(46), 4683-4686.
- Losurdo, M., Giangregorio, M. M., Capezzuto, P., & Bruno, G. (2011). Graphene CVD growth on copper and nickel: role of hydrogen in kinetics and structure. *Physical Chemistry Chemical Physics*, 13(46), 20836-20843.
- Lu, A. Y., Wei, S. Y., Wu, C. Y., Hernandez, Y., Chen, T. Y., Liu, T. H., ... & Juang, Z. Y. (2012). Decoupling of CVD graphene by controlled oxidation of recrystallized Cu. *RSC Advances*, 2(7), 3008-3013.
- Lu, G., Ocola, L. E., & Chen, J. (2009). Gas detection using low-temperature reduced graphene oxide sheets. *Applied Physics Letters*, 94(8), 83111-83114.
- Lu, X., Yu, M., Huang, H., & Ruoff, R. S. (1999). Tailoring graphite with the goal of achieving single sheets. *Nanotechnology*, 10(3), 269-272.
- Luo, Z., Yu, T., Kim, K. J., Ni, Z., You, Y., Lim, S., ... & Lin, J. (2009). Thickness-dependent reversible hydrogenation of graphene layers. *ACS Nano*, 3(7), 1781-1788.
- Magnuson, C. W., Kong, X., Ji, H., Tan, C., Li, H., Piner, R., ... & Ruoff, R. S. (2014). Copper oxide as a “self-cleaning” substrate for graphene growth. *Journal of Materials Research*, 29(03), 403-409.

- Malard, L. M., Pimenta, M. A., Dresselhaus, G., & Dresselhaus, M. S. (2009). Raman spectroscopy in graphene. *Physics Reports*, 473(5), 51-87.
- Marquardt, D., Beckert, F., Pennetreau, F., Tölle, F., Mülhaupt, R., Riant, O., ... & Janiak, C. (2014). Hybrid materials of platinum nanoparticles and thiol-functionalized graphene derivatives. *Carbon*, 66, 285-294.
- Massera, E., La Ferrara, V., Miglietta, M., Polichetti, T., Nasti, I., & Di Francia, G. (2011). Gas sensors based on graphene. *Chemistry Today*, 29(1), 39-41.
- Matsumura, T., & Sato, Y. (2010). A theoretical study on Van der Pauw measurement values of inhomogeneous compound semiconductor thin films. *Journal of Modern Physics*, 1(05), 340.
- Mattevi, C., Kim, H., & Chhowalla, M. (2011). A review of chemical vapour deposition of graphene on copper. *Journal of Materials Chemistry*, 21(10), 3324-3334.
- Mendoza, F., Limbu, T. B., Weiner, B. R., & Morell, G. (2015). Large-area bilayer graphene synthesis in the hot filament chemical vapor deposition reactor. *Diamond and Related Materials*, 51, 34-38.
- Mertens, R. (2012, August 18). Nokia patents a graphene-based photo detector. Retrieved April 19, 2016, from <http://www.graphene-info.com/nokia-patents-graphene-based-photo-detector>
- Ming, H. N. (2010). Simple room-temperature preparation of high-yield large-area graphene oxide. *International Journal of Nanomedicine*, 6, 3443-3448.
- Nasibulin, A. G., Ahonen, P. P., Richard, O., Kauppinen, E. I., & Altman, I. S. (2001). Copper and copper oxide nanoparticle formation by chemical vapor nucleation from copper (II) acetylacetonate. *Journal of Nanoparticle Research*, 3(5), 383-398.
- Nasibulin, A. G., Richard, O., Kauppinen, E. I., Brown, D. P., Jokiniemi, J. K., & Altman, I. S. (2002). Nanoparticle synthesis by copper (II) acetylacetonate vapor decomposition in the presence of oxygen. *Aerosol Science & Technology*, 36(8), 899-911.
- Neto, A. C., Guinea, F., & Peres, N. M. (2006). Drawing conclusions from graphene. *Physics World*, 19(11), 33, 1-5.
- Nie, S., Wu, W., Xing, S., Yu, Q., Bao, J., Pei, S.-s., & McCarty, K. F. (2012). Growth from below: bilayer graphene on copper by chemical vapor deposition. *New Journal of Physics*, 14(9), 93028-93037.
- Norimatsu, W., & Kusunoki, M. (2014). Epitaxial graphene on SiC {0001}: advances and perspectives. *Physical Chemistry Chemical Physics*, 16(8), 3501-3511.

- Novoselov, K. S. A., Geim, A. K., Morozov, S., Jiang, D., Katsnelson, M., Grigorieva, I., ... & Firsov, A. (2005). Two-dimensional gas of massless Dirac fermions in graphene. *Nature*, 438(7065), 197-200.
- Novoselov, K. S., Geim, A. K., Morozov, S. V., Jiang, D., Zhang, Y., Dubonos, S. A., ... & Firsov, A. A. (2004). Electric field effect in atomically thin carbon films. *Science*, 306(5696), 666-669.
- Okpalugo, T. I. T., Papakonstantinou, P., Murphy, H., McLaughlin, J., & Brown, N. M. D. (2005). High resolution XPS characterization of chemical functionalized MWCNTs and SWCNTs. *Carbon*, 43(1), 153-161.
- Osaklung, J., Euaruksakul, C., Meevasana, W., & Songsirittthigul, P. (2012). Spatial variation of the number of graphene layers formed on the scratched 6H-SiC (0001) surface. *Applied Surface Science*, 258(10), 4672-4677.
- Othman, M., Ritikos, R., Hafiz, S. M., Khanis, N. H., Rashid, N. M. A., & Rahman, S. A. (2015). Low-temperature plasma-enhanced chemical vapour deposition of transfer-free graphene thin films. *Materials Letters*, 158, 436-438.
- Pacakova, B., Vejpravova, J., Repko, A., Mantlikova, A., & Kalbac, M. (2015). Formation of wrinkles on graphene induced by nanoparticles: atomic force microscopy study. *Carbon*, 95, 573-579.
- Paredes, J. I., Villar-Rodil, S., Solis-Fernandez, P., Martinez-Alonso, A., & Tascon, J. M. D. (2009). Atomic force and scanning tunneling microscopy imaging of graphene nanosheets derived from graphite oxide. *Langmuir*, 25(10), 5957-5968.
- Park, C. S., Kang, B. S., Lee, D. W., & Choi, Y. S. (2006). Single carbon fiber as a sensing element in pressure sensors. *Applied physics letters*, 89(22), 223516.
- Pei, S., & Cheng, H. M. (2012). The reduction of graphene oxide. *Carbon*, 50(9), 3210-3228.
- Peleg, R. (2015, June 26). Graphene breakthrough as Bosch creates magnetic sensor 100 times more sensitive than silicon equivalent. Retrieved April 19, 2016, from <http://phys.org/news/2015-06-graphene-breakthrough-bosch-magnetic-sensor.html>
- Pereira, V. M., & Neto, A. C. (2009). Strain engineering of graphene's electronic structure. *Physical Review Letters*, 103(4), 46801-46805.
- Piner, R., Li, H., Kong, X., Tao, L., Kholmanov, I. N., Ji, H., ... & Chen, S. (2013). Graphene synthesis via magnetic inductive heating of copper substrates. *ACS Nano*, 7(9), 7495-7499.
- Pirkle, A., Chan, J., Venugopal, A., Hinojos, D., Magnuson, C. W., McDonnell, S., ... & Wallace, R. M. (2011). The effect of chemical residues on the physical and electrical properties of chemical vapor deposited graphene transferred to SiO₂. *Applied Physics Letters*, 99(12), 122108.

- Pumera, M., Ambrosi, A., Bonanni, A., Chng, E. L. K., & Poh, H. L. (2010). Graphene for electrochemical sensing and biosensing. *Trends in Analytical Chemistry*, 29(9), 954-965.
- Qi, X., Guo, X., & Zheng, C. (2012). Density functional study the interaction of oxygen molecule with defect sites of graphene. *Applied Surface Science*, 259, 195-200.
- Rathod, P. B. (2015). Graphene/Nanoparticles Composites synthesis and Application. *IJAR*, 1(7), 752-758.
- Reina, A., Jia, X., Ho, J., Nezich, D., Son, H., Bulovic, V., ... & Kong, J. (2008). Large area, few-layer graphene films on arbitrary substrates by chemical vapor deposition. *Nano Letters*, 9(1), 30-35.
- Robertson, J. (1986). Amorphous carbon. *Advances in Physics*, 35(4), 317-374.
- Robinson, Z. R., Ong, E. W., Mowll, T. R., Tyagi, P., Gaskill, D. K., Geisler, H., & Ventrice, C. A. (2013). Influence of chemisorbed oxygen on the growth of graphene on Cu (100) by chemical vapor deposition. *The Journal of Physical Chemistry C*, 117(45), 23919-23927.
- Rümmeli, M. H., Gorantla, S., Bachmatiuk, A., Phieler, J., Geißler, N., Ibrahim, I., ... & Eckert, J. (2013). On the role of vapor trapping for chemical vapor deposition (CVD) grown graphene over copper. *Chemistry of Materials*, 25(24), 4861-4866.
- Schedin, F., Geim, A. K., Morozov, S. V., Hill, E. W., Blake, P., Katsnelson, M. I., & Novoselov, K. S. (2007). Detection of individual gas molecules adsorbed on graphene. *Nature Materials*, 6(9), 652-655.
- Schropp, R. E. I. (2009). Frontiers in HWCVD. *Thin Solid Films*, 517(12), 3415-3419.
- Seah, C. M., Chai, S. P., & Mohamed, A. R. (2014). Mechanisms of graphene growth by chemical vapour deposition on transition metals. *Carbon*, 70, 1-21.
- Seibert, K., Cho, G. C., Kütt, W., Kurz, H., Reitze, D. H., Dadap, J. I., ... & Malvezzi, A. M. (1990). Femtosecond carrier dynamics in graphite. *Physical Review B*, 42(5), 2842.
- Seo, H. K., Ansari, S. G., Kim, G. S., Kim, Y. S., & Shin, H. S. (2004). Effect of tungsten/filament on the growth of carbon nanotubes in hot filament chemical vapor deposition system. *Journal of Materials Science*, 39(18), 5771-5777.
- Shen, J., Li, T., Long, Y., Shi, M., Li, N., & Ye, M. (2012). One-step solid state preparation of reduced graphene oxide. *Carbon*, 50(6), 2134-2140.
- Shi, Y. G., Wang, D., Zhang, J. C., Zhang, P., Shi, X. F., & Hao, Y. (2014). Fabrication of single-crystal few-layer graphene domains on copper by modified low-pressure chemical vapor deposition. *Crystal Engineering Communication*, 16(32), 7558-7563.

- Soler, V. M. F., Badia-Canal, J., Roca, C. C., Miralles, E. P., Serra, E. B., & Bella, J. L. A. (2013). Hot-wire chemical vapor deposition of few-layer graphene on copper substrates. *Japanese Journal of Applied Physics*, 52(1S), 1AK02-1AK08.
- Sorkin, V., & Zhang, Y. W. (2011). Graphene-based pressure nano-sensors. *Journal of Molecular Modeling*, 17(11), 2825-2830.
- Sprinkle, M., Siegel, D., Hu, Y., Hicks, J., Tejeda, A., Taleb-Ibrahimi, A., ... & Chiang, S. (2009). First direct observation of a nearly ideal graphene band structure. *Physical Review Letters*, 103(22), 226803.
- Sreeprasad, T. S., Rodriguez, A. A., Colston, J., Graham, A., Shishkin, E., Pallem, V., & Berry, V. (2013). Electron-tunneling modulation in percolating network of graphene quantum dots: fabrication, phenomenological understanding, and humidity/pressure sensing applications. *Nano Letters*, 13(4), 1757-1763.
- Stankovich, S., Dikin, D. A., Piner, R. D., Kohlhaas, K. A., Kleinhammes, A., Jia, Y., ... & Ruoff, R. S. (2007). Synthesis of graphene-based nanosheets via chemical reduction of exfoliated graphite oxide. *Carbon*, 45(7), 1558-1565.
- Staudenmaier, L. (1898). A process for the presentation of graphite acid. *Journal of the American Chemical Society*, 31 (2), 1481-1487.
- Stojanović, D., Woehrl, N., & Buck, V. (2012). Synthesis and characterization of graphene films by hot filament chemical vapor deposition. *Physica Scripta*, 2012(T149), 14068-14071.
- Takagi, D., Kobayashi, Y., Hibino, H., Suzuki, S., & Homma, Y. (2008). Mechanism of gold-catalyzed carbon material growth. *Nano letters*, 8(3), 832-835.
- Tao, L., Lee, J., Chou, H., Holt, M., Ruoff, R. S., & Akinwande, D. (2012). Synthesis of high quality monolayer graphene at reduced temperature on hydrogen-enriched evaporated copper (111) films. *ASC Nano*, 6(3), 2319-2325.
- Thomson, W. (1856). On the electro-dynamic qualities of metals:--effects of magnetization on the electric conductivity of nickel and of iron. *Proceedings of the Royal Society of London*, 8, 546-550.
- Tian, H., Shu, Y., Wang, X. F., Mohammad, M. A., Bie, Z., Xie, Q. Y., ... & Ren, T. L. (2015). A graphene-based resistive pressure sensor with record-high sensitivity in a wide pressure range. *Scientific Reports*, 5, 8603-8609.
- Timoshenko, S. P., & Woinowsky-Krieger, S. (1959). *Theory of plates and shells*. McGraw-hill.
- Tiwana, M. I., Redmond, S. J., & Lovell, N. H. (2012). A review of tactile sensing technologies with applications in biomedical engineering. *Sensors and Actuators A: Physical*, 179, 17-31.

- Topsakal, M., Şahin, H., & Ciraci, S. (2012). Graphene coatings: An efficient protection from oxidation. *Physical Review B*, 85(15), 155445.
- Tour, J. M. (2013). Top-down versus bottom-up fabrication of graphene-based electronics. *Chemistry of Materials*, 26(1), 163-171.
- Tsen, A. W., Brown, L., Levendorf, M. P., Ghahari, F., Huang, P. Y., Havener, R. W., ... & Park, J. (2012). Tailoring electrical transport across grain boundaries in polycrystalline graphene. *Science*, 336(6085), 1143-1146.
- Van der Pauw, L. J. (1958). A method of measuring specific resistivity and Hall effect of discs of arbitrary shape. *Philips Research Reports*, 13, 1-9.
- Voigtländer, B. (2015). *Scanning probe microscopy: Atomic force microscopy and scanning tunneling microscopy*. Springer.
- Viculis, L. M., Mack, J. J., Mayer, O. M., Hahn, H. T., & Kaner, R. B. (2005). Intercalation and exfoliation routes to graphite nanoplatelets. *Journal of Materials Chemistry*, 15(9), 974-978.
- Vlassioug, I., Regmi, M., Fulvio, P., Dai, S., Datskos, P., Eres, G., & Smirnov, S. (2011). Role of hydrogen in chemical vapor deposition growth of large single-crystal graphene. *ACS Nano*, 5(7), 6069-6076.
- Vlassioug, I., Smirnov, S., Regmi, M., Surwade, S. P., Srivastava, N., Feenstra, R., ... & Dai, S. (2013). Graphene nucleation density on copper: fundamental role of background pressure. *The Journal of Physical Chemistry C*, 117(37), 18919-18926.
- Wang, B. B., Zheng, K., Cheng, Q. J., Wang, L., Zheng, M. P., & Ostrikov, K. (2014). Formation and electron field emission of graphene films grown by hot filament chemical vapor deposition. *Materials Chemistry and Physics*, 144(1), 66-74.
- Wang, C. Y., Mylvaganam, K., & Zhang, L. C. (2009). Wrinkling of monolayer graphene: a study by molecular dynamics and continuum plate theory. *Physical Review B*, 80(15), 155445-15450.
- Wang, C., Chen, W., Han, C., Wang, G., Tang, B., Tang, C., ... & Chang, S. (2014). Growth of millimeter-size single crystal graphene on cu foils by circumfluence chemical vapor deposition. *Scientific Reports*, 4, 4537-4542.
- Wang, L., Dimitrijević, S., Fissel, A., Walker, G., Chai, J., Hold, L., ... & Iacopi, A. (2016). Growth mechanism for alternating supply epitaxy: the unique pathway to achieve uniform silicon carbide films on multiple large-diameter silicon substrates. *RSC Advances*, 6(20), 16662-16667.
- Wang, L., Ding, T., & Wang, P. (2009). Thin flexible pressure sensor array based on carbon black/silicone rubber nanocomposite. *IEEE Sensors Journal*, 9(9), 1130-1135.

- Wang, S. J., Geng, Y., Zheng, Q., & Kim, J. K. (2010). Fabrication of highly conducting and transparent graphene films. *Carbon*, 48(6), 1815-1823.
- Wang, Y., Yang, R., Shi, Z., Zhang, L., Shi, D., Wang, E., & Zhang, G. (2011). Super-elastic graphene ripples for flexible strain sensors. *ACS Nano*, 5(5), 3645-3650.
- Webb, M. J., Palmgren, P., Pal, P., Karis, O., & Grennberg, H. (2011). A simple method to produce almost perfect graphene on highly oriented pyrolytic graphite. *Carbon*, 49(10), 3242-3249.
- Window, A. L. (1992). *Strain Gauge Technology*: Springer Netherlands.
- Woo, S. J., Kong, J. H., Kim, D. G., & Kim, J. M. (2014). A thin all-elastomeric capacitive pressure sensor array based on micro-contact printed elastic conductors. *Journal of Materials Chemistry C*, 2(22), 4415-4422.
- Wood, J. D., Schmucker, S. W., Lyons, A. S., Pop, E., & Lyding, J. W. (2011). Effects of polycrystalline Cu substrate on graphene growth by chemical vapor deposition. *Nano Letters*, 11(11), 4547-4554.
- Wu, W., Liu, Z., Jauregui, L. A., Yu, Q., Pillai, R., Cao, H., ... & Pei, S. S. (2010). Wafer-scale synthesis of graphene by chemical vapor deposition and its application in hydrogen sensing. *Sensors and Actuators B: Chemical*, 150(1), 296-300.
- Xu, S., Man, B., Jiang, S., Wang, J., Wei, J., Xu, S., ... & Li, H. (2015). Graphene/Cu nanoparticle hybrids fabricated by chemical vapor deposition as surface-enhanced Raman scattering substrate for label-free detection of adenosine. *ACS Applied Materials & Interfaces*, 7(20), 10977-10987.
- Yang, D., Velamakanni, A., Bozoklu, G., Park, S., Stoller, M., Piner, R. D., ... & Ruoff, R. S. (2009). Chemical analysis of graphene oxide films after heat and chemical treatments by X-ray photoelectron and Micro-Raman spectroscopy. *Carbon*, 47(1), 145-152.
- Yang, F., Liu, Y., Wu, W., Chen, W., Gao, L., & Sun, J. (2012). A facile method to observe graphene growth on copper foil. *Nanotechnology*, 23(47), 475705-475714.
- Yang, S., & Lu, N. (2013). Gauge factor and stretchability of silicon-on-polymer strain gauges. *Sensors*, 13(7), 8577-8594.
- Yao, H. B., Ge, J., Wang, C. F., Wang, X., Hu, W., Zheng, Z. J., ... & Yu, S. H. (2013). A flexible and highly pressure-sensitive graphene-polyurethane sponge based on fractured microstructure design. *Advanced Materials*, 25(46), 6692-6698.
- Yavari, F., & Koratkar, N. (2012). Graphene-based chemical sensors. *The Journal of Physical Chemistry Letters*, 3(13), 1746-1753.

- Yi, M., & Shen, Z. (2015). A review on mechanical exfoliation for the scalable production of graphene. *Journal of Materials Chemistry A*, 3(22), 11700-11715.
- Yoon, H. J., Yang, J. H., Zhou, Z., Yang, S. S., & Cheng, M. M. C. (2011). Carbon dioxide gas sensor using a graphene sheet. *Sensors and Actuators B: Chemical*, 157(1), 310-313.
- Zhang, J., Yang, H., Shen, G., Cheng, P., Zhang, J., & Guo, S. (2010). Reduction of graphene oxide via L-ascorbic acid. *Chemical Communications*, 46(7), 1112-1114.
- Zhang, W., Wu, P., Li, Z., & Yang, J. (2011). First-principles thermodynamics of graphene growth on Cu surfaces. *The Journal of Physical Chemistry C*, 115(36), 17782-17787.
- Zhang, X., Ning, J., Li, X., Wang, B., Hao, L., Liang, M., ... & Zhi, L. (2013). Hydrogen-induced effects on the CVD growth of high-quality graphene structures. *Nanoscale*, 5(18), 8363-8366.
- Zhang, X., Xu, S., Jiang, S., Wang, J., Wei, J., Xu, S., ... & Liu, H. (2015). Growth graphene on silver-copper nanoparticles by chemical vapor deposition for high-performance surface-enhanced raman scattering. *Applied Surface Science*, 353, 63-70.
- Zhang, Y., Small, J. P., Pontius, W. V., & Kim, P. (2004). Fabrication and electric field dependent transport measurements of mesoscopic graphite devices. *Applied Physics Letters*, 86(7), 73104- 73107.
- Zhang, Y., Tan, Y. W., Stormer, H. L., & Kim, P. (2005). Experimental observation of the quantum Hall effect and Berry's phase in graphene. *Nature*, 438(7065), 201-204.
- Zhang, Y., Zhang, L., & Zhou, C. (2013). Review of chemical vapor deposition of graphene and related applications. *Accounts of Chemical Research*, 46(10), 2329-2339.
- Zhang, Y., Zhang, L., Kim, P., Ge, M., Li, Z., & Zhou, C. (2012). Vapor trapping growth of single-crystalline graphene flowers: synthesis, morphology, and electronic properties. *Nano Letters*, 12(6), 2810-2816.
- Zhu, S. E., Ghatkesar, M. K., Zhang, C., & Janssen, G. C. A. M. (2013). Graphene based piezoresistive pressure sensor. *Applied Physics Letters*, 102(16), 161904-161907.
- Zhu, Y., Murali, S., Cai, W., Li, X., Suk, J. W., Potts, J. R., & Ruoff, R. S. (2010). Graphene and graphene oxide: synthesis, properties, and applications. *Advanced Materials*, 22(35), 3906-3924.

Zuraimi, M. S., Tham, K. W., Chew, F. T., & Ooi, P. L. (2007). The effect of ventilation strategies of child care centers on indoor air quality and respiratory health of children in Singapore. *Indoor air*, 17(4), 317-327.

University of Malaya